BOUNDARY-LAYER ANALYSIS AND MEASUREMENT OF NEWTONIAN AND NON-NEWTONIAN FLUIDS

by

BYUNG KYU KIM

Dissertation submitted to the Graduate Faculty of the Virginia Polytechnic Institute and State University in partial fulfillment of the requirements for the degree of

DOCTOR OF PHILOSOPHY

in

Materials Engineering Science

APPROVED:

D. P. Telionis, co-chairman

M. S. Cramer, co-chairman

L. C. Burton

T. E. Diller

D. G. Baird

K. L. Reifsnider

J. E. McGrath

December, 1984

Blacksburg, Virginia

BOUNDARY-LAYER ANALYSIS AND MEASUREMENT OF NEWTONIAN AND NON-NEWTONIAN FLUIDS

Byung K. Kim

(ABSTRACT)

The velocity fields around a circular cylinder in a crossflow of drag-reducing polymeric solutions and water were experimentally investigated using a laser-Doppler velocimeter. Measured boundary -layer velocity profiles indicated that the flow parameter controlling the drag on a bluff body in drag-reducing flows is the turbulence intensity rather than the Reynolds number. For turbulence intensity less than 0.7% polymer addition induced delayed separation. For turbulence intensity over 1% the opposite effect was true. Time-averaged velocity profiles of water did not show any significant difference between self-induced and forced oscillatory flows.

Heat, mass and momentum transfer of Newtonian and power-law non-Newtonian fluids were theoretically investigated using an implicit finite-difference scheme. The results clearly indicated that shear-depedent non-Newtonian viscosity controls the entire transport processes of the power-law fluids. For the major portion of the boundary layer, it was found that the more shear thinnig the material exhibits, the lower the skin friction and the higher the heat transfer result. Accounting for the motion of the stagnation point provided an improved prediction of heat transfer for Newtonian fluid.

ACKNOWLEDGEMENTS

I would like to express my sincere gratitude to Dr. D. P. Telionis for his continuous guidance, understanding and assistance through the entire phase of the preparations. I express my heartfelt gratitude to Dr. M. S. Cramer who, with skills of scientific investigations, guided me in the entire phase of the theoretical developments, especially for the preparation of chap. 3.

My deep appreciations are directed to Dr. T. E. Diller for his valuable suggestions, cooperations and sharp criticisms. I am also deeply indebted to Dr. L. C. Burton, Dr. J. E. McGrath and Dr. D. G. Baird for their contributions to my graduate education, valuable suggestions and guidance as committee members. A gentlemanly guidance and constructive suggestions by Dr. K. L. Reifsnider for my graduate education should be sincerely acknowledged.

Thanks are also due to the ESM shop personnels for their good job in preparing the model cylinders, and our fluid lab friends for their cooperations, especially D. Mathioulakis for his time spent in the lab.

My mother's understanding and my mife, Kyung Hee's real help and encouragements are also highly appreciated.

The support of the major part of the research as part of the contract # DE-AS 05-82E 12022 under the direction of Dr. Oscar Manley of the Office of Basic Energy Research, Department of Energy is gratefully acknowledged.

TABLE OF CONTENTS

NOMENCLATURE

Symbol	Meaning
A_i	= coefficients of the outer flow equation
a_i	= coefficients of the differential momentum equation (see Eqs. 2.3.16 - 20)
a	= coefficient of the outer flow equation pertinent to the plane stagnation flow (see Eq. 3.1.1)
b_i	= coefficient of the differential thermal energy equation (see Eqs. 2.3.21- 24)
b	= velocity amplitude imposed on the stagnation region outer flow (see Eq. 3.1.1)
C	= concentration of diffusant, dimensional
C_D	= pressure drag coefficient, time averaged
C_D'	= pressure drag coefficient, fluctuating
Cp	= pressure coefficient, time averaged
ci	= coefficient of the differential mass transfer equation (see Eqs. 2.3.25-28)
Cp'	= pressure coefficient, fluctuating
c_p	= specific heat = time-mean pressure coefficient(see Eq. 4.3.1)
D	= binary diffusion coefficient
F	= normalized tangential velocity(see Eq.2.3.8)
F, G, H	= stagnation region velocity functions in y coordinate
f, g, h	= stagnation region velocity functions in y coordinate
f_d	= driving frequency
fs	= shedding frequency
k	= thermal conductivity

k = reduced frequency($= \omega/a$)

L = characteristic length, radius

m = consistency, power-law fluid

n = flow behavior index, power-law fluid

p = static pressure

p' = fluctuating pressure

p_s = stagnation pressure

r = radius of cylinder

T = temperature, dimensional

t = time, dimensional

t_1 = time, dimensionless

u = streamwise velocity, dimensional

u_1 = streamwise velocity, nondimensional

U_e = outer flow velocity, dimensional

U_{e1} = outer flow velocity, nondimensional

V = modified normal velocity(see Eq. 2.3.9)

v = velocity normal to the surface, dimensional

v_1 = velocity normal to the surface, nondimensional

X = concentration of diffusant, nondimensional (see Eq. 2.2.9)

x = streamwise coordinate, dimensional

x_1 = streamwise coordinate, nondimensional

y = normal coordinate, dimensional

y_1 = normal coordinate, nondimensional

Dimensionless Groups

Pr = Prandtl number($=c_p \nu/k$)

Pr,p = generalized Prandtl number(see Eq. 2.2.14)

Re = Reynolds number($=Lu_c/\nu$)

Re,p = generalized Reynolds number(see p. 20)

Sc = Schmidt number(ν/D)

Sc,p = generalized Schmidt number(see Eq. 2.2.16)

St = Strouhal number($=fsD/u_o$)

Greek Letters

α = thermal diffusity

β = velocity amplitude

γ = rate of shear

χ = deformation tensor

η = transformed normal coordinate(see Eq. 2.3.1)
= non-Newtonian viscosity(see Eq. 2.1.7)

θ = temperature, dimensionless($=T_1$)
= angle measured from the stagnation point

μ = Newtonian viscosity

ν = dynamic viscosity

ξ = transformed tangential coordinate(see Eq. 2.3.2)

ρ = density

τ = transformed time(see Eq. 2.3.3)

$\underline{\underline{T}}$ = Stress tensor

τ_{ij} = shear stress, component

Subscripts

e = condition at boundary-layer edge

o = condition in freestream

s = condition in the stagnation region

w = condition at the wall surface

LIST OF FIGURES AND TABLES

INTRODUCTION

The classical definition of a Newtonian fluid is to postulate that the stress tensor is directly proportional to the rate of strain tensor. The proportionality factor is called viscosity; this is a pure physical property which is constant at given temperature, pressure and composition. Any departure from this is called non-Newtonian behavior(Coleman and Noll 1961). For low molecular-weight liquids and for all gases the Newtonian postulate has been verified experimentally.

It is nowadays well known, however, that many industrially important fluids such as molten plastics, pulps, slurries, solutions of organic macromolecules etc., do not obey the Newtonian postulate. For these non-Newtonian fluids the concept of Newtonian viscosity is not applicable and therefore a realistic viscosity function or, more generally, a comprehensive constitutive equation should be sought to relate the local stress to the hydrodynamic variables of the system. Useful rheological models have been reviewed by Coleman and Noll(1961), Hershey and Zakin(1967) and Bird et al(1977a). Although fairly general rheological models have been developed in the past, the chief difficulty in the theoretical study of non-Newtonian fluids and in the correct interpretation of experimental results is that so far no definite relationship between the stress tensor and the deformation tensor valid for all kinds of non-Newtonian fluids, like the Navier-Stokes equation for Newtonian fluids, has been discovered. The theoretical studies in this area are therefore limited not so much by the

mathematical complexity as by the lack of well-established governing equations.

Fortunately, certain simple problems in this area can be successfully attacked, either theoretically or experimentally, and these thereby provide a basis for the analysis of more complicated physical problems which are usually encountered in practice.

The internal flow problems of various non-Newtonian fluids have been primarily studied in the past; this is perhaps due to its importance and relative simplicity. These problems are well treated in standard texts(Han 1976, Bird, Armstrong and Hassager 1977, Middleman 1977, Tadmor and Gogos 1979). It is surprising to note, however, that not much of external flow has been investigated for non-Newtonian fluid. A series of works by Acrivos et al(Acrivos, Shah and Petersen 1960, Shah, Acrivos and Petersen 1962, Acrivos, Shah and Petersen 1965) are the pioneering works in the area of external flows of power-law fluids. This was initiated by recognizing that the well-known Newtonian laminar boundary-layer equations may be easily extended to include power-law fluids. In the literature, the laminar boundary-layer equations of power-law fluids are referred to as generalized laminar boundary-layer equations.

A particular case of the external flow past a circular cylinder in crossflows will be briefly mentioned here as it relates to the present research. A conventional method of approach to the solution of continuity and momentum equations is based on momentum-integral method, namely von Karman-Pohlhausen integral procedure(Acrivos,

Shah, Petersen 1960, Shah, Acrivos and Petersen 1962, Bizzell and Slattery 1962). Aside from the limitations on the type of power-law fluids that can be treated, the accuracy of this integral method is nevertheless unexpectedly poor(Bizzel and Slattery 1962, Acrivos, Shah and Petersen 1965). Other methods of approach involve similarity solutions(Wells 1964), the combination of similarity transformation and asymptotic expansion(Acrivos, Shah and Petersen 1965) and series solutions(Luikov, Schulman and Berkovsky 1966, Wolf and Szewczyk 1966). Generally, the validity of the solutions by the above methods is , however, limitted locally due either to breakdown of similarity or to the number of terms available in the series expansion.

Where the heat transfer is concerned, the solution to the thermal energy equation was either for a large value of generalized Prandtl number(Shah, Acrivos and Petersen 1962) or limited to a finite number of terms in series expansion of temperature(Wolf and Szewczyk 1966, Luikov, Schulman and Berkovsky 1966). The results predicted by these methods are apparently not in good agreement even in their tendency. A very limited number of experimental works in this area (Shah, Acrivos and Petersen 1962, Takahashi 1979) also pose a difficulty for comparision.

It is surprising to find that no numerical solution of the generalized laminar boundary-layer equations for 2-D(two-dimensional) external flow has so far been published. This solution, exact within the limit of the boundary-layer approximation, may closely describe the transport behavior of the non-Newtonian fluids obeying the power-law

for a wide range of conditions provided the boundary layer remains attached. This is one of the motivations and contributions of the present research.

The first phase of the present research is the formulation of the 2-D unsteady laminar boundary-layer equations of heat, mass and momentum transfer for power-law fluids in a finite-difference form followed by a numerical analysis of these equations. Unlike all earlier studies, no limitation on the range of the generalized Prandtl number or flow-behavior index has been made. The problem is formulated in chapter 2, and the results of the numerical analysis are presented in chapter 5.

The second phase of the present research is an experimental investigation of the flow field of dilute polymeric solution around a circular cylinder in crossflows. The polymers added to water are well-known drag reducing agents, i.e., Polyox-1005(polyethylene oxide, Mw=900,000) and Separan-AP30(polyacrylamide, Mw=1,000,000).

It has recently been discovered that a drastic drag reduction, up to approximately 75% of that of the solvent, may be realized by adding only a minute amount of certain linear polymers. The potential application of drag reduction phenomenon is well documented in a review paper by Hoyt(1972). Continuous efforts have been made to further understand this phenomenon, and also to better organize the various experimental observations in a number of important review papers (Lumley 1969, Patterson, Zakin and Rodriguez 1969, Virk 1975, Berman 1978). The focus of this area of studies, mainly experimental, was

previously confined to flows past a flat plate and internal flows in the turbulence regime. The main issue of the majority of the earlier investigations was to obtain Prandtl type empirical correlation of the friction factor with Reynolds number from pressure drop measurements with different type of polymers in varying concentrations.

A number of possible mechanisms have been suggested for the drag-reducing polymeric solutions. So far, none has been universially accepted or directly verified experimentally. Historically, Toms(1949) first suggested the existence of a shear-thinning wall layer which, by virtue of a reduced viscosity, would give lower frictional resistance than the pure solvent. However, rheograms of polyethylene oxide which became available later did not verify the existence of shear-thinning layer. The shear thinning model was dealt a final blow by the work of Walsh(1967) who showed that the dilute solutions of dilatent materials were also strongly drag reducing in alkaline condition.

The possibility of an absorbed layer of polymer molecules on the wall has also once been postulated. This absorbed layer would creat a slippage effect and prevent the initiation of vorticity at the wall. However, it was concluded that the absorbed polymer layer was not related to the drag reducing effect(Hoyt 1972).

All of the polymer-solvent combinations that display drag reduction also display, at higher concentrations, viscoelastic effect(Lumley 1973). Solutions that do not show viscoelastic effects at any concentrations do not produce drag reduction. Therefore, it may be concluded that fluid elasticity is essential for the drag-reducing phenomena(Metzner and

Park 1964).

Molecular stretching or extensional viscosity model for drag-reducing mechanism may be the one which has received a widespread attention over 20 years(Tulin 1966, Lumley 1969, 1973, 1976, Berman 1978). The stretching of polymer molecules is a result of the extensional flow which, by virtue of the increased viscosity i.e., extensional viscosity, gives a thickened sublayer. The velocity gradient near the wall therefore becomes small and a reduced skin drag results. Lumley(1969,1973,1976) may be the only author who, with a penetrating physical intuition and patience, made a consistent effort to elucidate the mechanism of drag reduction. His extensional viscosity model was apparently successful, at least qualitatively, in explaining some of the anomalies observed in velocity and heat transfer measurements in drag-reducing flows. However, the extensional viscosity model was never successfully tested experimentally.

With regard to the progress of phenomelogical understanding of drag reduction, Wells and Spangler(1967) may be the first who conclusively demonstrated that the drag reduction is a wall phenomenon. They injected a polymer solution at the center-line of the pipe and observed no drag reduction until the polymer diffused into the wall region. Polymer injection experiments followed by other investigators repeatedly verified this boundary-layer phenomenon. However, it is still not clearly understood whether the drag reduction is an entirely boundary-layer phenomenon, or the boundary layer simply serves the onset junction for drag reduction and therefore the real drag-reducing

flow region is further extended beyond the boundary layer. Following the former picture, the interpretation of the observed drag reduction is a straightforward procedure like the Newtonian by assuming the drag-reducing polymeric solution thickenes the viscous sublayer. The thickened viscous sublayer natually gives a smaller velocity gradient near the wall and hence reduces drag. As a matter of fact the idea of thickened viscous sublayer prevailed overwhelmingly up to approximately 1973. It is also surprising to note that many of the velocity measurements, using either hot-element probe or laser Doppler velocimeter(LDV) which were reported by then showed the thickened viscous sublayer(Mayer 1966, Rudd 1969, Virk 1971, Wang 1972).

Recent velocity measurements(Scrivener 1974, Reischman and Tiederman 1975, Mizushina and Usui 1977) indicated no evidence of thickened viscous sublayer. However, the change caused by the polymer additive occured in the buffer region, which appeared thickened. At the present state of art, it may not be so feasible to derive a clean conclusion.

Measurements on the bluff bodies submerged in the external flow of polymeric solution were limited to the global characteristics of sphere. To the knowledge of the present author, no work for a circular cylinder in a crossflow has appeared in the literature. Results for sphere indicated that in an extreme case the drag could be increased by Polyox addition. Below the critical Reynolds number, Polyox solutions(10 to 120 wppm) reduced the drag on sphere up to approximately by an half at high concentrations above 100 wppm(White

1969, Lang and Patrick 1966). It should also be mentioned that the reduced drag was also observed in the complex soap solutions. However, at transient and supercritical Reynolds numbers, the drag has been increased by Polyox solution(White 1966, 1969).

A further look at this phenomenon from a molecular point of view may be desirable. The drag reduction phenomenon from the molecular point of view is also rather empirical but some important facets are clear. Hoyt and Fabula(1964), using a standardized rotating-disc apparatus, extensively measured drag reduction in dilute polymeric solution of many natural and synthetic polymers. They found that the most effective polymer structures for drag reduction were those with a linear structure having no or few side chains. This result may be interpreted in terms of main chain flexibility when the polymer is resisting against the external force. In a good solvent the polymer-solvent interactions are favored over polymer-polymer interactions so that the polymer is relatively extended in three dimensions. When this dilute polymeric solution is set in motion due to flow, the polymer molecules may prefer to be oriented along the flow direction with a disturbance due to the local rotational motion of the fluid. If this is true, the drag reduction phenomenon may find a close analogy in solvent-induced polymer orientation like a moving web system in film-forming operation, and the extensional viscosity may be responsible for the reduced drag as first suggested by Lumley(1973).

With the above in mind the present experiment in drag-reducing flow has been performed as follows. The velocity field has been

measured at three characteristic angular positions of a circular cylinder in crossflows. These positions correspond to the potential flow around the stagnation point, the boundary layer and separated flows around the separation point, and in the completely turbulent region of the wake. In view of the fact that the drag reduction experiments have conventionally been parameterized with the Reynolds number, some of the experiments were done for a relatively wide range of Reynolds numbers. Flow visualization in polymeric solution has also been carried out to confirm the above measurements, and to monitor the motion of the point of separation visually. In addition, shedding frequency and turbulence intensity both in the free stream and boundary layer have been measured. In all of the above velocity measurements, a two-channel LDV allowing a simultaneous measurement of two components of vector velocity has been used. The experimental facilities and procedures are described in Chapter 1, and the results are plotted in Chapter 4 with discussions.

The third phase of the present research is a Newtonian study. The purpose of the Newtonian study was twofold, namely to guide the Non-Newtonian study, and to confirm the experimental and analytical tools that have been developed in the present research are reliable by comparing the present Newtonian results with existing data or theoretical predictions. Such comparisons were not possible for the non-Newtonian results due to the lack of published data.

This part of the research is both theoretical and experimental. The theoretical investigation includes the development of 2-D unsteady

stagnation region solutions for heat, mass and momentum transfer. A fundamental difficulty for the numerical study of unsteady flows in the past was the lack of accurate and complete schemes of the unsteady analysis. The governing equations developed represent coupled nonlinear boundary value problems, and have subsquently been solved numerically using a collocation method. The analytical and numerical solutions of stagnation region flow are the topic of chapter 3.

These numerical solutions, valid for a small region near the stagnation point, subsquently provided initial conditions for the boundary-layer code. The boundary-layer code adopted for the present research was originally developed by Werle and Davis(1972) for steady calculations, and was extended for unsteady problems by Telionis et al(Telionis, Tsahalis, and Werle 1973, Telionis and Werle 1973, Telionis 1981) with a fair amount of modifications. A major contribution by this group was to clarify the criterion for unsteady separation(Sears and Telionis 1975). This program, in the present research, has been modified to rigorously provide the initial conditions to the x-plane from the stagnation region analysis mentioned above. Furthermore, this program has been expanded to include the unsteady thermal energy equation and the convective mass transfer equation. Subsquently, the unsteady laminar boundary-layer heat, mass and momentum transfer has been worked out. The formulation of this problem and the results of numerical analysis are shown in chapters 2 and 5, respectively.

Experimental studies in Newtonian fluids are those for velocity measurement and flow visualization in water, and surface pressure

measurement in air streams. The boundary-layer velocity distribution is an indirect indication of heat transfer under forced convection assumption, and pressure drag is the dominating part of the total drag for bluff body submerged in a high Reynolds number flow.

For Re>200 a regular vortex shedding, characterized by the Strouhal number, has long been observed experimentally. This natural shedding induces oscillatory flow in boundary layer as well which, in the literature, is referred to as *self-induced oscillatory flow*(Dwyer and McCroskey 1973). As a result of this, the point of separation as well as the point of stagnation suffers an excursion which, in nature, is periodic. Boundary-layer velocity profiles have sometimes been measured in the past for self-induced oscillatory flow(Dwyer and McCroskey 1973) and for purely steady flow(Varty and Currie 1984). However, boundary-layer velocity measurements for forced oscillatory flow are rare.

In the present experiment, boundary-layer velocity profiles have been measured for self-induced and forced oscillatory flows for at least two different Reynolds numbers. Particular attention has been paid to the measurement about the point of separation where the velocity profiles have been measured every one degree. It was also attempted to find signs of boundary-layer formation in the wake region of the cylinder surface from velocity measurement. Dye injection experiment was also performed to confirm the above measurements.

The mean surface pressure distribution over a circular cylinder has been measured in the past for self-induced oscillatory flows for a

wide range of Reynolds numbers (Roshko 1961, Achenbach 1968, Okamoto and Yagita 1973, Meyer, Kreplin and Fang 1981). For forced oscillatory flows, however, no measurements have so far appeared in the literature. In the present experiment surface pressure distributions i.e., time-mean and fluctuating component of pressure all around the cylinder have been measured at a given Reynolds number of 43,000. The driving frequency has been varied about the measured natural shedding frequency of 31.5 Hz.

The scope of the present work has been already mentioned in this introduction following discussions of related earlier groups of works. For completeness, the major contributions of the present investigations will be provided again.

1. Experiments with drag-reducing polymeric solutions were conducted for the first time for external flows over a two-dimensional body. No information on velocity profiles is available in literature. In the present study, experimental data for developing and separating boundary layers for non-Newtonian and Newtonian fluids have been provided.

2. Earlier investigations are mainly concerned with the effect of polymer on fully-developed turbulent flows. Here, the effect of the ploymer on laminar and transitional boundary layers and separation including the influence of the free-stream turbulence has been considered. Based on the data obtained, meaningful physical explanations are provided on the erratic behavior of the drag with Reynolds number.

3. Due to the extremely thin thickness of the boundary layer near the stagnation point, it was not possible to measure the boundary-layer velocity profiles in this region. However, measured velocity profiles near the boundary-layer edge indicated a weak sign of the extensional flow.

4. Momentum, heat and mass transfer of power-law non-Newtonian fluids has been analyzed via the boundary-layer approximation. The governing transport equations have been derived and subsquently worked out numerically. The shear-dependent velocity and temperature fields, and thereby the skin friction and heat transfer for power-law materials were predicted. To the knowledge of the author, this is the first numerical scheme which can solve exactly such problems, removing the limitations on parameters like the flow-behavior index, Prandtl and Schmidt numbers, or the geometrical configuration of the problem.

5. For unsteady flow problems, no detailed experimental data on velocity profiles exist. The present study provides data on a thick measuring grid, which can serve as a base for later comparisons of numerical calculations.

6. For unsteady flows, the stagnation region poses a formidable problem to numerical analysts. An asymptotic expansion solving the coupled nonlinear equations, valid for a small region near the mean stagnation location, was obtained. The governing set of equations were then solved numerically to provide initial conditions for the boundary-layer calculations.

7. Steady and unsteady heat transfer was calculated. In all earlier

calculations of steady heat transfer over a circular cylinder, the natural unsteadiness was neglected. Taking this effect into account, the present results provided an explanation of the poor prediction of all earlier methods of solution.

CHAPTER 1

EXPERIMENTAL METHODS AND DATA REDUCTION

In this chapter the experimental facilities, procedures and the data acquisition system employed in the present experiments are described. Velocity measurements and flow visualization in the flow of water and dilute polymeric solutions were carried out in the ESM water tunnel which was recently modified to provide a wide range of flow parameter values and accurate flow control. On the other hand, the surface pressure distribution was measured in a specially designed wind tunnel in the Mechanical Engineering Department. Both facilities were extensively calibrated before any of the present experiments were undertaken.

1.1 Tunnels and Flow Systems

The ESM water tunnel, depicted in Fig. 1.1, is a pump-driven, closed system with test section dimensions, 30cm x 25cm and an internal working volume of approximately 2.15 m^3. A false wall to control the boundary-layer suction and reduce the wall boundary-layer thickness was installed in the test section. Mean flow oscillations are introduced by a rotating vane mounted on the top of the tunnel(see Fig.1.1).

A circular cylinder, 5cm in diameter yielding a tunnel blockage of 16.7%, was tightly mounted on the side walls in the middle of the test section. This cylinder was used for the velocity measurements and flow visualization. Reynolds numbers up to 100,000 based on the cylinder

diameter, and 600,000 based on the equivalent diameter of the rectangular cross section were achieved.

The wind tunnel is an open system with a series of rotating shatters, as depicted in Fig. 1.2. The cylinder for surface pressure measurements, 5.7cm in diameter corresponding to a 20% tunnel blockage, was mounted in the middle of the test section like in the water tunnel. By controlling the intake opening, Reynolds numbers over 100,000 were obtained. Some of the important calibration data for both facilities will be given in chapter 4.

1.2 Special Cares for Polymeric Solutions

The polymers tested in the present experiments were Separan AP-30(polyacrylamide, Mw=1,000,000) and Polyox WSR-1105(polyethylene oxide, Mw=900,000). The commercial grade of these polymers was used without any further purifications. One hundred ppm by weight (214 g in a 2.15 m^3 of tunnel volume) of each of the polymer was first dissolved in a 30 liters of water with mild agitation. It took about 10 hours for Separan and 6 hours for Polyox to completely dissolve in water. The relatively high concentration of 100 ppm was believed to encounter possible mechanical degradation during the experiment. This solution was then fed to water tunnel followed by a slow free run for 10 min to homogenize the solution. Velocity was measured within the next three hours. The polymer solution was then discharged and the tunnel was washed with water several times for the next run.

Though no intrinsic viscosity change has directly been measured during the experiment, the free stream velocity of the polymeric

solution has been measured as a function of the run time at a given control setting of the tunnel. The time dependent velocity of the polymeric solution was then compared with the constant velocity of the water at the same control setting. Measurements in polymeric solutions were done only when the difference between the two was significant to ensure that the polymer data were obtained in a drag-reducing condition.

1.3 LDA Measurements

The basic principle of LDA(laser-Doppler anemometer) is to measure the Doppler shifted frequency of laser scattered by small particles. The Doppler frequency is proportional to a single component of the fluid vector velocity. This presumes at most single scattering from each particle, and that the particle follows the flow accurately.

As a non-invasive instrument, the LDA has a number of advantages over the conventional impact-type devices such as Pitot-tube, heat-transfer and hot-element probes. This is especially true for velocity measurements in drag-reducing polymeric solutions. The impact-type device, when employed to polymeric solution, is subject to inherent errors due to i) the influence of the normal stress term; ii) the fluctuating stresses are not simply related to velocity distribution; iii) the boundary-layer thickness on the pressure probe may be large compared to the probe size. Depending on the position of measurement and velocity, errors as large as 15% with Pitot-tube were reported by Smith et al(1967). Serious difficulties were also encountered by Friehe and Schwarz(1969) in the process of angular calibration of a hot-film

probe. Lumley(1973) offers a detailed account of specific measuring problems in viscoelastic solutions.

In the present experiments two LDA systems, a DISA and a TSI, were used simultaneously. The former, arranged in forward scattering mode monitored the free stream velocity at a fixed upstream position and the latter, in a backward scattering mode, measured the boundary-layer velocity. The optical arrangement of the TSI, shown in Fig. 1.3, was such that the two normal components of the velocity vector were measured simultaneously. Moreover, the use of two Bragg cells permitted the recording of positive or negative values of the two velocity components. The entire optical set was rotated around the axis of the cylinder to provide the maximun burst at each angular position being measured.

The measuring volume was traversed by a specially designed traversing mechanism(Fig. 1.4). The train of the TSI optics was mounted on a linear translator which allows the entire system to move in the horizontal direction. The parallel beams from the LDA were reflected twice from the mirrors and passed through a lens to converge at the measuring volume. The upper mirror together with the lens translated in the vertical direction. Both the linear translator and the upper mirror were controlled by stepping motors interfaced with a laboratory computer(MINC II). In this way, steps as small as 0.05 mm were implemented with a precision of ±0.01 mm. The LDA signal was processed with three TSI counters. These instruments were equiped with digital to analogue converters. To get an ensemble average, a

trigger signal was generated at the tip of the rotating vane and fed into the computer. The on-line data acquisition system is shown schematically in Fig. 1.5.

1.4) Flow Visualization

The flow visualization has been carried out both in water and polymeric solutions. The cylinder for dye injection was painted white. Dye was injected at two locations on the cylinder surface, upstream and downstream of separarion, respectively. Straight line segments were drawn at fixed intervals in the spanwise direction to provide spatial locations for reference. The instantaneous streaklines were monitored by a video system.

1.5 Pressure Measurement and Other Instruments

The cylinder for pressure measurement was specially designed and fabricated. This model(Fig. 1.6) has nine pressure taps. Two of them located at the same angular position were used in the present experiment. One was connected to a manometer to read the mean pressure and the other was connected to B & K microphone to read the instantaneous value of the pressure. By rotating the cylinder around the axis, the pressure distribution was measured at various azimuthal locations. The signal from the microphone was fed to a signal analyzer after passing through a preamplifier. A power spectrum integration method using HP 5420, a FFT-based time-and frequency-domain analyzer, together with an rms voltmeter(Schlumberge JM1860) was employed.

The pressure distribution was measured at a Reynolds number of 43,000. The driving frequency was given values around the natural shedding frequency. These two frequencies have been sensed by a linearized hot-wire anemometer(TSI IFA—100), and monitored by the HP 5420. The HP was externally triggered by a phase signal from the rotating shatters to obtain the ensemble average.

CHAPTER 2

MOMENTUM, HEAT AND MASS TRANSFER FOR NON-NEWTONIAN POWER-LAW FLUIDS

The governing equations of momentum, heat and mass transfer of two-dimentional unsteady laminar boundary-layer flow of power-law fluids are formulated in this chapter. The Newtonian counterparts of the governing equations are readily obtained by simply letting the flow behavior index(n) equal to 1 in the generalized equations.

Forced convection with no viscous dissipation has been assumed. The mass transfer problem is limitted to convective transport of a nonreacting-binary system of dilute solution, which still has a plenty of applications(Bird, Steward, and Lightfoot 1960).

2.1 The Governing Equations

The dimensional form of the governing equations in terms of conventional notation for the flow of an incompressible continuum in two dimension(see the coordinate system in Fig. 2.1) read

continuity:

$$\frac{\partial u}{\partial x} + \frac{\partial v}{\partial y} = 0 \qquad (2.1.1)$$

momentum:

$$\frac{\partial u}{\partial t} + u \frac{\partial u}{\partial x} + v \frac{\partial u}{\partial y} = - \frac{1}{\rho} \frac{\partial p}{\partial x} + \frac{1}{\rho} \left(\frac{\partial \tau_{xx}}{\partial x} + \frac{\partial \tau_{yx}}{\partial y} \right) \qquad (2.1.2)$$

$$\frac{\partial v}{\partial t} + u \frac{\partial v}{\partial x} + v \frac{\partial v}{\partial y} = - \frac{1}{\rho} \frac{\partial p}{\partial y} + \frac{1}{\rho} \left(\frac{\partial \tau_{xy}}{\partial x} + \frac{\partial \tau_{yy}}{\partial y} \right) \qquad (2.1.3)$$

thermal energy:

$$\frac{\partial T}{\partial t} + u \frac{\partial T}{\partial x} + v \frac{\partial T}{\partial y} = \alpha \left(\frac{\partial^2 T}{\partial x^2} + \frac{\partial^2 T}{\partial y^2} \right) \qquad (2.1.4)$$

continuity of diffusant:

$$\frac{\partial C}{\partial t} + u \frac{\partial C}{\partial x} + v \frac{\partial C}{\partial y} = D \left(\frac{\partial^2 C}{\partial x^2} + \frac{\partial^2 C}{\partial y^2} \right) \qquad (2.1.5)$$

The initial and boundary conditions considered are:

$$u(x,0,t) = v(x,0,t) = 0 \qquad (2.1.6)$$

$$T(x,0,t) = T_w \qquad (2.1.7)$$

$$C(x,0,t) = C_w \qquad (2.1.8)$$

$$u(x,\infty,t) = U_e(x) \qquad (2.1.9)$$

$$T(x,\infty,t) = T_e \qquad (2.1.10)$$

$$C(x,\infty,t) = C_e \qquad (2.1.11)$$

$$u(0,y,t) = u_s(y,t) \qquad (2.1.12)$$

$$v(0,y,t) = v_s(y,t) \qquad (2.1.13)$$

$$T(0,y,t) = T_s(y,t) \qquad (2.1.14)$$

$$C(0,y,t) = C_s(y,t) \qquad (2.1.15)$$

In the above equations, subscripts w and e denote the applied conditions at the wall and the edge of the domain, respectively. For boundary-layer flow studies, the edge of the domain is the edge of the boundary layer. In the present research, constant wall temperature

and concentration conditions have been assumed. The subscript s in Eqs. 2.1.12 to 15 designates conditions near the stagnation point. The governing equations in this region will subsquently be developed and solved numerically in chapter 3. The steady counterparts of the governing equations can be obtained by letting $\partial/\partial t = 0$.

For Newtonian fluids it is postulated that the stress tensor is directly proportional to the deformation tensor, and viscosity is a pure physical property. For power-law fluids, however, the viscosity is a function of the second invariant of the deformation tensor, leading to a constitutive equation of the form

$$\underline{\underline{\tau}} = \eta \, \underline{\underline{\dot{\gamma}}} \qquad (2.1.16)$$

In this equation η is a non-Newtonian viscosity and for a power-law fluid

$$\eta = m|\dot{\gamma}|^{n-1} \qquad (2.1.17)$$

in which $m(N\ s^n/m^2)$ and the dimensionless quantity, n are constants characteristics of each polymer and polymer solution. For 2-D boundary-layer flow, from an arguement on the order of magnitude, the magnitude of deformation tensor is easily approximated as

$$\dot{\gamma} = \left|\frac{\partial u}{\partial y}\right| \qquad (2.1.18)$$

Then,

$$\tau_{xx} = - m\left|\frac{\partial u}{\partial y}\right|^{n-1} \frac{\partial u}{\partial y} \qquad (2.1.19)$$

$$\tau_{yy} = - m\left|\frac{\partial u}{\partial y}\right|^{n-1} \frac{\partial v}{\partial y} \qquad (2.1.20)$$

$$\tau_{xy} = \tau_{yx} = - n\left|\frac{\partial u}{\partial y}\right|^{n-1} \frac{\partial u}{\partial y} \qquad (2.1.21)$$

Upon substituting these relationships into Eqs. 2.1.2 and 3 yields

$$\frac{\partial u}{\partial t} + u \frac{\partial u}{\partial x} + v \frac{\partial u}{\partial y} + \frac{1}{\rho} \frac{\partial p}{\partial x}$$

$$= \frac{m}{\rho} \left\{\frac{\partial}{\partial x} \left[\left(\frac{\partial u}{\partial y}\right)^{n-1}\left(\frac{\partial u}{\partial x}\right)\right] + \frac{\partial}{\partial y} \left(\frac{\partial u}{\partial y}\right)^{n}\right\} \qquad (2.1.22)$$

$$\frac{\partial v}{\partial t} + u \frac{\partial v}{\partial x} + v \frac{\partial v}{\partial y} + \frac{1}{\rho} \frac{\partial p}{\partial y}$$

$$= \frac{m}{p} \frac{\partial}{\partial x} \left(\frac{\partial u}{\partial y}\right)^{n} + \frac{\partial}{\partial y} \left[\left(\frac{\partial u}{\partial y}\right)^{n-1}\left(\frac{\partial v}{\partial y}\right)\right] \qquad (2.1.23)$$

A negative velocity gradient would have been considered in removing the absolute sign in Eq. 2.1.18. However, this case has purposely been excluded on the basis of physical consideration namely, the power-law may no longer be valid for very small rates of shear.

2.2 Boundary-Layer Approximation

The above set of equations(Eqs.2.1.1, 4, 5, 22 and 23) are highly nonlinear and coupled. Useful solutions can be obtained by simplifying these equations via the boundary-layer approximation. The standard procedure to this approximation is first to rewrite the governing equations in a stretched coordinate system by letting

$$t = Lt_1/u_o \qquad (2.2.1)$$

$$x = Lx_1 \tag{2.2.2}$$

$$y = Ly_1/R_{e,p}^{\frac{1}{n+1}} \tag{2.2.3}$$

$$u = u_o u_1 \tag{2.2.4}$$

$$v = u_o v_1/R_{e,p}^{\frac{1}{n+1}} \tag{2.2.5}$$

$$p = \rho u_o^2 p_1 \tag{2.2.6}$$

$$U_e = u_o U_{e1} \tag{2.2.7}$$

$$\theta = (T_2 - T)/(T_w - T_e) \tag{2.2.8}$$

$$X = (C_w - C)/(C_w - C_e) \tag{2.2.9}$$

In the above, $Re,p = \frac{\rho u_o^{2-n} L^n}{m}$ is the generalized Reynolds number(Takahashi and Maeda 1979).

The governing equations in boundary-layer coordinates read

continuity:

$$\frac{\partial u_1}{\partial x_1} + \frac{\partial v_1}{\partial y_1} = 0 \tag{2.2.10}$$

momentum:

$$\frac{\partial u_1}{\partial t_1} + u_1 \frac{\partial u_1}{\partial x_1} + v_1 \frac{\partial u_1}{\partial y_1} = \frac{\partial U_{e1}}{\partial t_1} + U_{e1} \frac{\partial U_{e1}}{\partial x_1} + R_{e,p}^{\frac{-2}{n+1}} \frac{\partial}{\partial x_1} \left(\frac{\partial u_1}{\partial y_1}\right)^{n-1} \frac{\partial u_1}{\partial x_1} + \frac{\partial}{\partial y_1}\left[\frac{\partial u_1}{\partial y_1}\right]^n \tag{2.2.11}$$

$$R_{e,p}^{\frac{-2}{n+1}} \left[\frac{\partial v_1}{\partial t_1} + u_1 \frac{\partial v_1}{\partial x_1} + v_1 \frac{\partial v_1}{\partial y_1}\right] + \frac{\partial p_1}{\partial y_1} = R_{e,p}^{\frac{-2}{n+1}} \left[\frac{\partial}{\partial x_1} \left(\frac{\partial u_1}{\partial y_1}\right)^n + \frac{\partial}{\partial y_1} \left\{\left(\frac{\partial u_1}{\partial y_1}\right)^{n-1} \left(\frac{\partial v_1}{\partial y_1}\right)\right\}\right] \tag{2.2.12}$$

thermal energy:

$$\frac{\partial\theta}{\partial t_1} + u_1 \frac{\partial\theta}{\partial x_1} + v_1 \frac{\partial\theta}{\partial y_1} = \frac{1}{P_{r,p}} \left[R_{e,p}^{\frac{-2}{n+1}} \frac{\partial^2\theta}{\partial x_1^2} + \frac{\partial^2\theta}{\partial y_1^2} \right] \qquad (2.2.13)$$

where

$$P_{r,p} = \frac{C_p \rho L u_o}{k \, R_{e,p}^{\frac{2}{n+1}}} = P_r \frac{R_e}{R_{e,p}^{\frac{2}{n+1}}} \qquad (2.2.14)$$

continuity of diffusant:

$$\frac{\partial X}{\partial t_1} + u_1 \frac{\partial X}{\partial x_1} + v_1 \frac{\partial X}{\partial y_1} = \frac{1}{S_{c,p}} \left[R_{e,p}^{\frac{2}{n+1}} \frac{\partial^2 X}{\partial x_1^2} + \frac{\partial^2 X}{\partial y_1^2} \right] \qquad (2.2.15)$$

and

$$S_{c,p} = \frac{L u_o}{R_{e,p}^{\frac{2}{n+1}}} = S_c \frac{R_e}{R_{e,p}^{\frac{2}{n+1}}} \qquad (2.2.16)$$

The boundary conditions are

$$u_1(x_1, 0, t) = v_1(x_1, 0, t) = 0 \qquad (2.2.17)$$

$$u_1(x_1, \infty, t) = U_e \qquad (2.2.18)$$

$$\theta(x_1, 0, t) = 0 \qquad (2.2.19)$$

$$\theta(x_1, \infty, t) = 1 \qquad (2.2.20)$$

$$X(x_1, 0, t) = 0 \qquad (2.2.21)$$

$$X(x_1, \infty, t) = 1 \qquad (2.2.22)$$

In the above equations Re, Pr and Sc are the Reynolds number, Prandtl number and Schmidt number, respectively. Also in the above equations, Pr,p is called the generalized Prandtl number. In an

analogy to the generalized Reynolds number and generalized Prandtl number, Sc,p may be called the generalized Schmidt number.

At this stage of derivation an order of magnitude analysis is pertinent. For $O(R_{e,p}) >> O(1)$, the terms divided by $R_{e,p}^{\frac{2}{n+1}}$ may be neglected. The result is the first order boundary-layer approximation or simply the boundary-layer equation. They are

continuity:

$$\frac{\partial u_1}{\partial x_1} + \frac{\partial v_1}{\partial y_1} = 0 \tag{2.2.23}$$

momentum:

$$\frac{\partial u_1}{\partial t_1} + u \frac{\partial u_1}{\partial x_1} + v_1 \frac{\partial u_1}{\partial y_1} = \frac{\partial U_{e1}}{\partial t_1} + U_{e_1} \frac{\partial U_{e1}}{\partial x_1} + \frac{\partial}{\partial y_1} \left(\frac{\partial u_1}{\partial y_1}\right)^n \tag{2.2.24}$$

thermal energy:

$$\frac{\partial p_1}{y_1} = 0 \tag{2.2.25}$$

$$\frac{\partial \theta}{\partial t_1} + u_1 \frac{\partial \theta}{\partial x_1} + v_1 \frac{\partial \theta}{\partial y_1} = \frac{1}{P_{r,p}} \frac{\partial^2 \theta}{\partial y_1^2} \tag{2.2.26}$$

continuity of diffusant:

$$\frac{\partial X}{\partial t_1} + u_1 \frac{\partial X}{\partial x_1} + v_1 \frac{\partial X}{\partial y_1} = \frac{1}{S_{c,p}} \frac{\partial^2 X}{\partial y_1^2} \tag{2.2.27}$$

The second momentum equation essentially dictates that there is no significant pressure variation across the boundary layer, even for power-law fluids. This presumes high Re,p but is valid for all kinds

of fluids that may be approximated by power-law constitutive equation.

It should also be mentioned that the above three generalized parameters i.e., Re,p, Pr,p and Sc,p are all reduced to those of Newtonian flow by letting n=1. The same is also true for the generalized laminar boundary-layer equations. With n=1 these equations are the familiar laminar boundary-layer equations for Newtonian fluids.

In applying the power-law boundary-layer analysis, however, certain limitations should be considered. The Re,p is proportional to u_e with a power of (2-n). It follows then that if and only if $n<2$ Re,p is a monotonically increasing function of u_e and only then the laminar boundary-layer flows are established at high Reynolds number. With $n>2$, on the contrary, a high Re,p can be obtained at low u_e. However, then the power-law may no longer be valid due to the insignificance of shear rate, and consequently a Newtonian boundary-layer configuration may be established. Therefore, for $n>2$ there may be still certain range of the Reynolds number where the boundary-layer approximation is valid.

2.3 A Goertler-Type Transformation and Finite Difference Approximation

Traditionally the numerical solution of laminar boundary-layer equations has been performed in a similarity variable domain. In such a domain, the numerical grid approximately follows the growth of the boundary layer. The boundary layer around a circular cylinder is only locally similar. Therefore, a certain modified form of similarity variable should be employed for this geometry. The one introduced here is a Goertler-type variable which has been proved very useful in Newtonian

flow investigation(Werle and Davis 1972, Telionis 1981).

$$\xi = \xi(x_1,t_1) = \int_0^{x_1} U_{e1}(x_1,t_1)dx_1 \qquad (2.3.1)$$

$$\eta = \eta\ (x_1,y_1,t_1) = \frac{U_{e1}(x_1,t_1)}{\sqrt{2\xi}} \qquad (2.3.2)$$

$$\tau = \tau(t_1) = t_1 \qquad (2.3.3)$$

A straightforward application of the chain rule followed by a finite difference approximation of the time derivative leads to the following form of the governing equations

$$2\xi F_\xi + F + V_\eta = 0 \qquad (2.3.4)$$

$$a_0F_{\eta\eta} + a_1F_\eta + a_2F + a_3 + a_4F_\xi = 0 \qquad (2.3.5)$$

$$\theta_{\eta\eta} + b_1\theta_\eta + b_2\theta + b_3 + b_4\theta_\xi = 0 \qquad (2.3.6)$$

$$X_{\eta\eta} + c_1X_\eta + c_2X + c_3 + c_4X_\xi = 0 \qquad (2.3.7)$$

where F is the normalized viscous velocity defined by

$$F = \frac{u}{U_e} \qquad (2.3.8)$$

and

$$V = 2\xi \frac{\partial \eta}{\partial x_1} F + \frac{\sqrt{2\xi}}{U_{e1}} v_1 \qquad (2.3.9)$$

The boundary conditions are

$$F(\xi,0,\tau) = V(\xi,0,\tau) = 0 \qquad (2.3.10)$$

$$F(\xi,\infty,\tau) = 1 \qquad (2.3.11)$$

$$\theta(\xi,0,\tau) = 0 \qquad (2.3.12)$$

$$\theta(\xi,\infty,\tau) = 1 \qquad (2.3.13)$$

$$X(\xi,0,\tau) = 0 \qquad (2.3.14)$$

$$X(\xi,\infty,\tau) = 1 \qquad (2.3.15)$$

The variable coefficients in the momentum equation are

$$a_0 = n\left[\frac{U_{e1}}{2\xi} F_\eta\right]^{n-1} \qquad (2.3.16)$$

$$a_1 = \left[\frac{2\xi}{U_{e1}^3} \frac{\partial U_{e1}^3}{\partial t_1} + \frac{1}{U_{e1}^2} \int_0^{x_1} \frac{\partial U_{e1}}{\partial t_1} dx_1\right]\eta - v \qquad (2.3.17)$$

$$a_2 = -\frac{2\xi}{U_{e1}^3} \frac{\partial U_{e1}}{\partial t_1} - \beta F - \frac{2\xi}{U_{e1}^2} \frac{1}{\Delta\tau}, \quad \beta \equiv \frac{2\xi}{U_{e1}} \frac{\partial U_{e1}}{\partial \xi} \qquad (2.3.18)$$

$$a_3 = \frac{2\xi}{U_{e1}^3}\frac{\partial U_{e1}}{\partial t_1} + \beta + \frac{2\xi}{U_{e1}^2}\frac{F^{i-1}}{\Delta\tau} \tag{2.3.19}$$

$$a_4 = \frac{2\xi}{U_{e1}^2}\int_0^{x_1}\frac{\partial U_{e1}}{et_1}\,dx_1 - 2\xi F \tag{2.3.20}$$

Those in the thermal energy equations are

$$b_1 = a_1 P_{r,p} \tag{2.3.21}$$

$$b_2 = -\frac{2\xi}{U_{e1}^2}\frac{P_{r,p}}{\Delta\tau} \tag{2.3.22}$$

$$b_3 = \frac{2\xi}{U_{e1}^2}\frac{P_{r,p}}{\Delta\tau}\,\theta^{i-1} \tag{2.3.23}$$

$$b_4 = a_4 P_{r,p} \tag{2.3.24}$$

and, those in the mass transfer equation are

$$c_1 = a_1 S_{c,p} \tag{2.3.25}$$

$$c_2 = -\frac{2\xi}{U_{e1}^2}\frac{S_{c,p}}{\Delta\tau} \tag{2.3.26}$$

$$c_3 = \frac{2\xi}{U_{e1}^2} \frac{S_{c,p}}{\Delta\tau} X^{i-1} \qquad (2.3.27)$$

$$c_4 = a_4 S_{c,p} \qquad (2.3.28)$$

In the above equations, F^{i-1}, T^{i-1} and X^{i-1} denote the corresponding quantities at the previous time step. The governing unsteady equations reduce essentially in this way to their equivalent steady forms. By simply eliminating terms including values of the previous time step, and letting $\partial Ue/\partial t=0$, the above set of equations reduce to their steady counterparts. The Newtonian counterparts of the above equations correspond to n=1 which subsquently reduces the nonlinearity and therefore the computation time.

The above governing equations have been numerically integrated using finite difference method. Central difference with a variable grid spacing based on a geometric progression has been used for the approximation of the η derivatives. The fine structures of the velocity and temperature/concentration fields near the wall were thereby obtained by taking a very small grid spacing near the wall. For the ξ derivative approximations, backward, and a mixed difference, namely, the upwinding technique were employed. The latter has been proved very successful for boundary-layer calculation with partially reversed flows(Telionis, Werle and Tsalalis 1973). The results of the numerical analysis for both Newtonian and power-law fluid are given in chapter 5.

CHAPTER 3

THE STAGNATION REGION SOLUTIONS

Ordinary differential equations governing the momentum, heat and mass transfer in oscillating plane stagnation flow will be set up, and solved numerically in this chapter.

3.1 Derivation of the Governing Equations

Consider a steady 2-D stagnation flow of a viscous incompressible fluid in the upper x, y plane depicted in Fig. 4.1. Let the flow be directed towards and limited by a plate in the plane y=0, with the stagnation point at x=y=0. The velocity distribution of the outer potential flow is a function of only geometry(Acrivos, Shah, and Petersen 1960); the inner viscous flow velocity distribution is linear in x, and asymptotically linear in y. This is the well-known Hiemenz stagnation profile(Schlichting 1979).

Now consider a periodic disturbance of the inner viscous flow. Physically the disturbance may be introduced externally such as by disturbing the wall, or may naturally occure due, for example, to the natural shedding from a bluff body submerged in a crossflow. Mathematically, aside from introducing unsteady terms in the differential equations, both cases modifiy the boundary conditions, namely the former at wall and the latter at boundary-layer edge. The former case, wall oscillation has in the past been investigated by Rott(1958). The latter case is of interest here and will be examined.

First, by superposing a periodic disturbance on the mean flow in the streamwise direction, the boundary conditions far from the plate become

$$u = ax + b\cos\omega t + o(1) \tag{3.1.1}$$

$$v = - ay + o(y) \tag{3.1.2}$$

$$p/\rho = b\omega x\sin\omega t - ax\, b\cos\omega t - \frac{a^2}{2}[x^2+y^2] + H(t) + o(1) \tag{3.1.3}$$

as $x^2 + y^2 \dashrightarrow \infty$

where H(t) is an arbitrary function of time.

The boundary conditions at wall are no-sleep and no-penetration i.e.,

$$u = v = 0 \text{ at } y = 0 \tag{3.1.4}$$

The above pressure distribution has been obtained by integrating the Euler equation with respect to x and y, followed by a differentation with respect to t.

The inner viscous flow solutions are postulated to be

$$u = xf'(y) + g(y)\cos\omega t + h(y)\sin\omega t \tag{3.1.5}$$

$$v = - f(y) \tag{3.1.6}$$

For a Newtonian fluid, the full Navier-Stokes equations for two-dimensional unsteady flow reduce to

$$u_x + v_y = 0 \tag{3.1.7}$$

$$u_t + uu_x + vu_y + p_x/\rho = \nu(u_{xx} + u_{yy}) \tag{3.1.8}$$

$$v_t + uv_x + vv_y + p_y/\rho = \nu(v_{xx} + v_{yy}) \tag{3.1.9}$$

It is seen at once that the above postulated velocity distribution satisfy the continuity equation. Upon substituting Eqs. 3.1.5 and 6 into the Navier-Stokes equations and integrating once, the pressure distribution is obtained as

$$p/\rho = (x^2/2)(ff'' + \nu f''' - f'^2)$$
$$+ x(\nu g'' - \omega h - f'g + fg')\cos\omega t$$
$$+ x(\nu h'' + fh' - f'h + \omega g)\sin\omega t + c_1(y,t) \qquad (3.1.10)$$

and

$$p/\rho = - \nu f' - f^2/2 + c_2(x,t) \qquad (3.1.11)$$

The former is from x-momentum equation and the latter is from the y-momentum equation. The arbitray function of integration in the above equation is determined by comparing these two equations

$$c_1(y,t) = - \nu f' - f^2/2 + m(t) \qquad (3.1.12)$$

The final form of the pressure distribution is therefore

$$p/\rho = x^2(ff'' = \nu f''' - f')/2$$
$$+ x(\nu g'' - \omega h - f'g + fg')\cos\omega t$$
$$+ x(\nu h'' + fh' - f'h + \omega g)\sin\omega t \qquad (3.1.13)$$
$$- \nu f' - f^2/2 + m(t)$$

Let the undetermined function in Eq. 3.1.3 be $H(t) = (b^2/2)\cos^2 \omega t$. Then, the three unknown functions, f, g, and h satisfy the following ordinary differential equations.

$$ff'' + f'''' - f'^2 + a^2 = 0 \qquad (3.1.14)$$

$$\nu g'' + fg' - f'g - wh + ab = 0 \qquad (3.1.15)$$

$$\nu h'' + fh' - f'h + \omega(g - b) = 0 \qquad (3.1.16)$$

The boundary conditions for these auxiliary functions are obtained by comparing Eqs. 3.1.1, 2 and 4 with Eqs. 3.1.5 and 6 to be

$$f'(\infty) = a \qquad (3.1.17)$$

$$g(\infty) = b \qquad (3.1.18)$$

$$h(\infty) = 0 \qquad (3.1.19)$$

$$f(0) = f'(0) = g(0) = h(0) = 0 \qquad (3.1.20)$$

3.2) Temperature and Concentration Distributions

Under the forced convection and convective mass transfer assumption the temperature and concentration distributions are readily obtained by substituting the velocity distributions into corresponding governing equations. Upon substituting eqs. 3.1.5 and 6 into the boundary-layer thermal energy equation (Eq. 2.1.4), the governing thermal energy equation in the stagnation region is obtained as

$$T_t + (xf' + g\cos\omega t + h\sin\omega t)T_x - fTy = (T_{xx} + T_{yy})/\alpha \qquad (3.2.1)$$

$$(3.2.2)$$

where α is the thermal diffusivity. By postulating T=T(y) in a small stagnation region, the above equations become

$$T_{yy} + fT_y\,\alpha = 0 \qquad (3.2.3)$$

$$\omega/T(0) = To,\ T(\infty) = T_e \qquad (3.2.4)$$

Similarily, the governing equation for continuity of the diffusant is obtained as

$$C_{yy} + fC_y D = 0 \tag{3.2.5}$$

$$\omega/C(0) = C_\omega,\ C(\infty) = C_0 \tag{3.2.6}$$

3.3 Numerical Solution

Since the differential equations that have been set up in the previous section are all nonlinear, a numerical solution is generally necessary. In order to solve them numerically it is convenient to do the following transformations.

$$y = (\nu/a)^{1/2}\,\hat{y} \tag{3.3.1}$$

$$f(y) = (\nu/a)^{1/2} F(\hat{y}) \tag{3.3.2}$$

$$g(y) = bG(\hat{y}) \tag{3.3.3}$$

$$h(y) = wbH(\hat{y})/a \tag{3.3.4}$$

$$\theta(\hat{y}) = \frac{T - T_w}{T_e - T_w} \tag{3.3.5}$$

$$X(\hat{y}) = \frac{C - C_w}{C_e - C_w} \tag{3.3.6}$$

The governing equations are now rewritten in terms of $\hat{y}$ coordinate as follows.

$$F''' + FF'' - F'^2 + 1 = 0 \tag{3.3.7}$$

$$\omega/F(0) = F'(0) = 0,\ F'(\infty) = 1. \tag{3.3.8}$$

$$G'' + FG' - F'G - k^2H + 1 = 0 \tag{3.3.9}$$

$$H'' + FH' - F'H + G - 1 = 0 \tag{3.3.10}$$

$$\omega/G(0) = H(0) = H(\infty) = 0,\ G(\infty) = 1 \tag{3.3.11}$$

$$\alpha\theta'' + F\theta' = 0 \qquad (3.3.12)$$

$$\omega/\theta(0) = 0,\ \theta(1) = 1 \qquad (3.3.13)$$

$$DX + FX = 0 \qquad (3.3.14)$$

$$\omega/X(0) = 0,\ X(1) = 1 \qquad (3.3.15)$$

In Eq. 3.3.9 $k = \omega/a$ is a reduced frequency. Since the function F is known(Equation. 3.3-7 is uncoupled so that it can be solved independently.) the exact solution for G and H can be found for k=0. This case corresponds to a steady superposition on the mean flow, or may be regarded as a quasi-steady state.

The nondimensional form of the outer flow equation and the proper value of the parameter, k in eq. 3.3.9 are obtained as follows. The outer flow equation for a two-dimensional symmetric body with a stagnation point should be in the form of

$$u_{e1} = A_1 x_1 + A_3 x_1^3 + A_5 x_1^5 + \beta\cos\omega t \qquad (3.3.16)$$

where x =0 is the mean stagnation point. In this equation the leading linear term is to ensure a stagnation flow and terms only of odd order are necessary to guarantee the symmetry of the flow.

The dimensional constants a and b are determined by comparing the above equation with Eq. 3.1.1 as

$$a = A_1 u_o/r \qquad (3.3.17)$$

$$b = \beta u_o \qquad (3.3.18)$$

The dimensionless quantities of frequency, ω_1 and time, t_1 are introduced as

$$\omega = \omega_1\omega_0 = \omega_1 u_0/r = 2\pi f \qquad (3.3.19)$$

$$t = t_1 r/u_0 = t_1/\omega_0 \qquad (3.3.20)$$

In terms of these quantities, the reduced frequency(k) and the Strouhal number(S_t) become

$$k = \pi S_t/A_1 = \omega_1/A_1 \qquad (3.3.21)$$

$$S_t = \omega_1/\pi \qquad (3.3.22)$$

These boundary value problems have been numerically solved using a collocation method based on the method of lines with cubic Hermit basis functions. Shown in Table 4.1 is the present numerical solution to Eq. 3.3.7 which corresponds to steady plane stagnation flow. Also shown in the same table is the numerical solution to the same equation by Howarth (Schlichting 1979) who made an improvement over Hiemenz' original solution. Up to the forth decimal unit, the precision reported by Howarth, the two solutions are almost identical upon truncating the present results at the fifth decimal unit.

Shown in Fig. 3.2 are the steady and quasi-steady velocity profiles. The latter corresponds to k=0. The relative magnitude of each velocitity and its distribution across the boundary layer can be deduced. The general behavior is an asymptotic one, an important characteristic of the boundary layer. The numerical solutions to the unsteady problems (simultaneous set of Eqs. 3.3.7 to 11) are shown in Figs. 3.3 to 6 as a function of the Strouhal frequency. When these functional values are substituted into Eqs. 3.1.5, the result describes

time dependent velocity distributions in the stagnation region.

Finally the steady stagnation region temperature/concentration profile is shown in Fig. 3-7. Again an asymptotic behavior is seen. The relative thickness between the velocity and temperature/concentration boundary-layers will depend on the Prandtl/Schmidt number of the material system under investigation.

The actual solutions to the viscous velocity, pressure , temperature and concentration distributions have been obtained by recasting the numerical solutions obtained in the $\hat{y}$ coordinate(F, G, H etc) into those of the y coordinate(f, g, h etc) via Eqns. 3.3.1 through 6. The solutions thereby obtained provided the initial conditions to the x plane in the boundary-layer calculations that have already been described in chapter 2.

CHAPTER 4

EXPERIMENTAL RESULTS

In this chapter the results obtained from the present experiments are presented with a special emphasis on the fundamental phenomena. The experimental results obtained in water, and surface pressure measurements in air stream will first be displayed to ensure that the present results are comparable with existing data, or with the well-established theory of Newtonian fluid mechanics.

Such a direct comparison, or a straightforward interpretation was not possible for the results obtained in polymeric solutions. This was mainly due to the lack of published experimental data for the particular geometry and flow adopted in the present experiment. Therefore, measurements in polymeric solutions were accompanied by the present measurements in the solvent of water at the same conditions. The effect of the added polymer on the flow field has thereby been elucidated upon comparing the two results.

4.1 Facility Calibrations

Extensive calibrations of the water tunnel and the wind tunnel have first been performed. The purpose of calibration was to ensure the facility performance, to estimate the range of the experiments that could be done using the facility and most importantly to investigate the values of the parameters corresponding to optimum conditions for the desired experiments. The calibration included measurements of the flow

uniformity in the test section, velocity range achievable, turbulence level and oscillatory flow characteristics such as velocity waveform and amplitude for a variety of frequencies that have been imposed. In both facilities, Reynolds numbers up to 100,000 based on the cylinder diameter, minimum turbulence level of 0.2-0.4 % and velocity amplitude up to 10-12 % (peak to peak) at certain conditions were achieved. The thickness of the wall boundary layer in test section was generally less than 1cm in both facilities.

Measurements were made in the uniform flow region to avoid any 3-D effects. The bulk of the calibration-type measurements is recorded in earlier reports(Tavakoli, Kim, Borell, Diller and Telionis 1983, Telionis, Matioulakis, Kim 1984). Typical velocity waveforms and corresponding frequency spectra are shown in Figs. 4.1 and 2. In a power frequency spectrum analysis, the power value of the superimposed driving frequency generally exceeded 80% of the total value for the majority of the present experimental range covered.

4.2 Basic Phenomena

Certain essential features concerning the transport phenomena over a circular cylinder in crossflows may first be considered to provide basic background for the material of this and the following chapters.

The velocity field around a circular cylinder, with an oncoming flow normal to its axis, may conveniently be divided into three characteristic regions: the outer potential flow, the inner viscous boundary-layer flow and the wake downstream of the cylinder. The role of the outer potential flow in transport processes is to directly

control the configuration of the boundary layer attached to the body surface, and to interactively govern the vortex shedding and the wake which is turbulent but almost inviscid.

The boundary layer which is of major concern here starts at the front stagnation point where the fluid particles first attach to the body surface. The boundary layer grows in thickness as it flows downstream reaching its maximum near the point of separation, the thickness being proportional to the reciprocal square root of the Reynolds number. For $500<Re<200,000$, due to eventual unbalance between the inertia forces and viscous forces, the attached boundary layer separates from the body surface to form a free-shear layer. The free-shear layers roll up to form large vortical structures. The frequency of the formation of such vortices is a function of the freestream velocity. This phenomenon, characterized by the Strouhal number, is referred to as the natural vortex shedding in literature.

The Strouhal number, defined by fD/u_0 (f=natural shedding frequency, D=cylinder diameter, and u_0 =free stream velocity), is approximately a constant value of 0.20 in the subcritical range of the Reynolds number. The critical Reynolds number is approximately 200,000. Beyond this is the transition range where the Karman vortex street is no longer regular. It is only for $Re>4,000,000$, the supercritical region, that a regular pattern forms again. In this range, the Strouhal number is higher ranging from 0.26 to 0.32 compared to 0.2 in the subcritical range. Though the above values are generally observed, there is some variation depending on the external flow

conditions. With a significant free–stream turbulence intensity or with a higher blockage, the transition occurs at lower Reynolds numbers.

The self-induced oscillatory flow in the boundary layer results in periodic excursions of the separation point as well as the stagnation point. The stagnation point motion poses a significant difficulty in boundary-layer analysis of heat and mass transfer. Aside from the error due to the neglect of this motion in boundary-layer calculations, an account for the motion of the hydrodynamic stagnation point is highly desirable to disclose the effect of oscillatory flow on the transport processes.

The motion of the separation point, on the other hand, sheds an insight into the local fluctuations of pressure, heat and mass transfer around this point, in addition to the oscillation of the boundary layer as a whole. Experimental results by Dwyer and McCroskey(1973) demonstrated that the separation point oscillates over 10 degrees at Re=53,000. Points on the surface of the cylinder contained within the limits of the traveling separation will sometimes be in the boundary layer and in the wake for the rest of a cycle. The local heat and mass transfer from this region of surface will be therefore governed by two entirely different mechanisms, namely the one controlled by the boundary layer and the other controlled by the turbulence of the wake. The overall governing mechanism may not simply be the weighted average of the two.

Some discussion is pertinent here on the time-averaged location of the point of separation. The motion of separation found its significance

in transport processes. However, the time-averaged point of separation(will be referred to as simply 'point of separation' from now on) finds its extreme importance in relation to the forces exerted by the fluid on the submerged body, in particular the drag. With delayed separation, for example, the size of the wake is small and therefore reduction in form drag results. The form drag is the dominant part of the total drag for bluff bodies submerged in high Reynolds number flows. Therefore, the point of separation will actually govern the total drag of submerged bodies in high-Reynolds-number flows.

As far as the major part of the attached boundary layer is concerned, an oscillatory motion induced by the natural shedding affects the rate of the transport process, either directly, by introducing an additional mechanism which in nature should be unsteady, or indirectly by changing the outer flow velocity distribution. The latter case will be more likely true when the Reynolds number is high(Evans 1974).

By considering the self-induced oscillation in boundary layers, the classically steady problem becomes more complicated but certainly provides a more realistic picture of the transport process. More interesting results are expected with an externally imposed disturbance on the oncoming upstream, i.e., with a forced oscillation in addition to the self-induced oscillation. The boundary layer response to the freestream oscillation should depend on the relative magnitude and frequency of the two oscillations, the natural and the externally imposed.

In addition to the above rather universal aspects an unpredictable complication may be expected with a polymer additive in a Newtonian solvent. Yet, in contrast to numerous experimental works for internal flows and streamlined bodies, little definitive information has so far been reported in the literature for external flows.

The effect of added polymer in reducing the drag on a submerged body is complicated by several factors. With well-streamlined geometries such as flat plates and slender bodies, the drag reduction due to polymer additive is effected just as in internal flows, namely by reducing the skin friction drag. With bluff geometries such as circular cylinders and spheres in crossflows , however, the total drag consists primarily of form drag as was mentioned earlier. The typical polymers that have been added to solvent for drag reduction essentially reduce the skin friction by thickening the viscous sublayer or buffer region. In other words, they induce a steeper slope on the boundary-layer velocity profile. The effect will lead to a decreased boundary-layer velocity gradient, induce an earlier separation and therefore a larger wake for polymeric solutions compared with the Newtonian solvent results. As a result, the polymeric solution will reduce the skin drag in the attached flow region but increase the form drag in the separated flow region.

The transport processes that have briefly been discussed in this section in connection with some important phenomena will later be expanded upon in chapter 5, where the heat and mass transfer is the major topic. However, it should be emphasized here that these two

additional transport processes are mainly governed by momentum transfer for a given material system at certain condition. The momentum transfer, in principle, is uniquely determined by the velocity distribution in laminar viscous flow as long as the Reynolds number is over approximately 1,000.

4.3 Pressure Measurements in Wind Tunnel

The time-mean and fluctuating surface pressure distributions have been measured at a particular Reynolds number of 36,600 which is within the subcritical range. The driving frequency has been varied about the measured shedding frequency of 31.5 Hz. The total drag of the circular cylinder consists of frictional drag and pressure drag. For Re>10,000, however, drag due to friction is less than 2% of the total drag(Okamoto and Yogita, 1973). Therefore, the total drag may be expressed approximately in terms of the measured surface pressure distribution

$$Cp=2(P-Ps)/\rho u^2 \qquad (4.3.1)$$

and,

$$Cd=\int_0^{\pi} Cp(\theta)\ \cos\theta\ d\theta \qquad (4.3.2)$$

where Cp and Cd are the time-mean pressure, and the pressure drag coefficients, respectively. The fluctuating counterparts are obtained upon replacing p by p', the fluctuating component of pressure.

The time-mean and rms values of pressure coefficients for different driving frequencies(fd) are shown in Figs. 4.3 and 4, respectively. Also shown in Fig. 4.3 are recent measurements by other investigators

for self-induced oscillatory flow at Re=30,000(West and Apelt, 1982). The present results for self-induced oscillatory flow(fd=0) show a fairly good agreement with those of West and Apelt. A small deviation is perhaps due to the difference in blockage in the two experiments, i.e., presently a 20% compared to a 15.2% in West and Apelt. Obviously, higher blockage will induce higher pressure drag.

Apparently, the mean pressure coefficient is independent of the driving frequency up to about θ= 45 degrees from the stagnation point. There may be some physical justification for this and the fact that the pressure coefficient up to this angle is independent of the Reynolds number(Achenbach 1968). A significant difference is found from the minimum pressure coefficient position which preceeds by a few degrees the point of separation. The pressure drag coefficients for forced oscillatory flows are thereby higher by 3-5% compared with those of self-induced oscillatory flow, with a maximum at fd=fs. The fluctuating component of surface pressure apparantly increases monotonically with increasing frequency but is not related directly to the amplitude(see Table 4.1).

An interesting feature of the rms pressure distribution appears to be the influence of the driving frequency on the variation along the peripheral direction. For self-induced oscillatory flow, the maximum value of the rms pressure is found near the point of separation, or perhaps, a little upstream. This is a clear indication of the locally strong effect of the free shear layer oscillation near this point. The effect of the free shear layer oscillation becomes relatively weaker as

the driving frequency is increased. With fd>fs the rms pressure distribution of the attached boundary layer is governed by the driving frequency; the decreasing tendency of the rms pressure along the downstream direction of the attached flow region indicates this fact. It is also interesting to see that the maximum local disturbance of rms pressure near the point of separation is found at fd=fs. Time-averaged rates of heat transfer measured at the same tunnnel also indicated serious fluctuations near the point of separation(Borell, Kim, Ekhaml, Diller, and Telionis 1983).

4.4 Velocity Measurements in Water

Experimentally measured velocity profiles in water will be presented here. In the present experiments, the thickness of the boundary layer was about 0.1 mm near the stagnation point, and was the order of 1 mm near the separation point. In view of the extremely thin boundary layer, boundary-layer velocity measurements have been centered around the point of separation.

Velocity profiles over a fairly wide range of angular positions are shown in Figs. 4.5 and 6 for self-induced oscillatory flows, and in Figs. 4.7, 8 and 9 for forced oscillatory flows. For the first two cases of forced oscillatory flows the driving frequency has been matched to the natural shedding frequency (fd=fs), and the last case corresponds to fd=1.2fs assuming the Strouhal number is 0.20. The boundary-layer velocity profile generally follows a conventional laminar boundary-layer behavior at the given range of the Reynolds number. It grows continuously in its thickness for increasing θ or decreasing Reynolds

numbers. The magnitude of normal velocity is approximately one order lower than that of tangential velocity. The normal velocity grows downstream or as the Reynolds number is decreased.

It should be noticed that, near the point of separation, the normal velocity is not quite one order lower compared to the tangential velocity. An implication of this may raise a question on the validity of *boundary-layer approximation near the point of separation*. The boundary-layer approximation is based on the assumption that $|v/u|<<1$ and resulted in a constant pressure across the boundary layer. The present velocity measurements near the point of separation indicate that the normal velocity is quite significant.

For forced oscillations, whether the driving frequency is matched to the natural shedding frequency or not, time-averaged velocity profiles of boundary layer appear to be similar with the profiles of self-induced oscillatory flows. However, the dynamic behavior of the two cases is different.

As discussed earlier in this chapter the motion of the point of separation, in addition to the boundary-layer oscillations as a whole, has an important influence on the local heat and mass transfer. To study carefully this phenomenon, velocity measurements were obtained at 1 degree intervals for both self-induced and forced oscillatory flows(Figs. 4.10 and 11). The driving frequency has been matched to the natural shedding frequency in the latter case. The first appearance of the time-averaged flow reversal seems indistinguishable between the two cases. However, the process of separation appears

significantly different. Up to about θ=81 degrees there appears to be no difference between the two families of profiles. Approaching the point of separation, however, a lot more retarded flows are introduced due to the forced oscillation.

The motion of the separation point, analyzed by the sign of the instantaneous tangential velocity measured at y=0.1mm, covered a spatial variation of 85±3 degrees for forced oscillatory flows.

4.5 Measurements in Polymeric Solutions

4.5.1 Fundamental measurements

Certain fundamental measurements in polymeric solutions will first be displayed and discussed to define the conditions for which the velocity profiles have been measured.

Since the polymer is subjected to the shear degradation in turbulent flows, measurements on the mechanical degradation of polymer are desirable to ensure that the measurements in polymeric solutions are obtained under drag-reducing conditions. Peterson and Abernathy(1970) carried out a systematic measurements on the shear degradation in turbulent pipe flow of dilute Polyox solutions by monitoring the intrinsic viscosity of the solution. According to these authors, the major part of the degradation, a function of shear rate as well as the polymer type and concentration, occured in the first approximately ten seconds, and remained almost unchanged beyond this. At a wall shear stress of 55 dyne/cm^2, for example, the intrinsic viscosity of the originally 50 wppm Polyox solution has been reduced by 5%.

In the present experiments such a rigorous degradation measurement was not undertaken. Instead, the free-stream velocity of the polymeric solution was measured as a function of run time and was compared with that of water measured at the same control settings of the tunnel(Fig. 4.12). The effect of the polymer in reducing flow resistance, thereby increasing the free stream velocity, is relatively small due ,perhaps, to the small contribution of the skin friction resistance to the total head in the present flow system. The velocity of the polymeric solution decreases as the run time elapses due to the mechanical degradation of the polymer. However, up to approximately four hours of run time the velocity of the polymeric solution is fairly high compared to that of water. Any measurements in polymeric solution have therefore been performed within the first three hours after the solution is charged and homogenized.

It has universally been accepted that the skin drag reduction due to the polymer addition is a turbulence-aided wall phenomenon. Therefore, the drag reduction experiments have conventionally been parametrized in terms of the Reynolds number. Apparently, for internal flows and external flows along flat plates and streamlined bodies, the reported drag reduction has generally been increased monotonically as the Reynolds number increased. This may be due to the increased turbulence at high Reynolds number, a normal characteristic of internal flow or a fully developed turbulent boundary layers.

For bluff bodies submerged in a large duct such as in a wind

tunnel or water tunnel, the boundary-layer turbulence intensity is not exclusively related to the Reynolds number i.e., the free-stream velocity. It is mainly related to the free-stream turbulence intensity and roughness of the surface. A case of extremely low free stream turbulence intensity may be obtained by dropping a smooth sphere in a large and deep tank of a still medium that is of interest. The boundary layer thereupon formulated is fairly laminar up to the critical Reynolds number.

For geometries other than the sphere, this approach is neither practical nor industrially important. Moreover, a moving model makes it impossible to obtain local measurements.

Generally a certain level of free-stream turbulence is inevitable for most of the experimental work on bluff bodies. For this reason, it is imperative that the turbulence intensity be carefully examined. This is especially true for the measurements in drag reducing polymeric solutions since the well-known drag reducing polymer is very sensitive to the turbulence intensity and it reduces skin drag only when the flow is significatly turbulent.

Direct turbulence measurements in drag reducing flows have also been reported by some other investigators in the past, however the reported effects of the added polymer on the turbulence intensity is inconsistent for many reasons. Earlier investigators were rather concerned theoretically the role of polymer in turbulent flow or vice verse. Some comprehensive and representative earlier ideas on the the mechanism involved attribute the phenomenon to the reduced generation

of turbulence(Astarita 1965), or to the stored turbulence energy in polymer chains, thus prohibiting the loss due to dissipation(Walsh 1967).

Experimental measurements of turbulence intensity in drag reducing flows, reported later, actually contradict the above hypotheses. Logan(1971) and Rudd(1971)(see also Virk 1975), from LDV measurements in square duct, have shown that the turbulence intensity was increased near the wall but was identical in the core region for polymeric solution compared to that of Newtonian solvent. However, more recent measurements in channel and pipe flows did not confirm the above results(Reischman and Tiedman 1975, Mizushina and Usui 1977), namely the turbulence for polymeric solution was lower near the wall compared to solvent, and rather inconsistent near the center. Especially, measurements in square duct identified secondary flows that were not detected by turbulence measurement. Bearman(1978) expressed doubts whether or not the turbulence intensity is ever higher than the Newtonian case at any radial position.

The best approach is perhaps to measure the turbulence at the same conditions where the drag reduction and velocity profiles are measured in order to provide a reliable interpretation. This may be especially true for the external flow over a bluff body since the point of separation and therefore the total drag is very sensitive to to the free-stream turbulence intensity.

Shown in Fig. 4.13 is the free-stream turbulence intensity measured in the present experiment. A notable contradiction to the

conventional understanding is seen in the inverse proportionality of turbulence intensity to the Reynolds number. This is however a characteristic of the present control setting of the flow system. The freestream turbulence intensity of polymeric solution is lower than that of water at low Reynolds numbers, but no difference is evident at higher Reynolds numbers. Alternatively, this should be interpreted in terms of turbulence intensity of the water rather than the Reynolds number. The added polymer reduces the turbulence intensity of water when the turbulence intensity that the water would have had without polymer is significantly high. A power spectrum analysis has been performed to indicate the frequency band that has been screened by the polymeric solution. Typical freestream spectra of water and polymeric solution taken at relatively low Reynolds numbers are shown in Figs. 4.14 and 15. It appears that the added polymer reduces the turbulence intensity of the solution for the entire frequency band that has been examined presently when the turbulence intensity of the solvent is high.

In an attempt to indirectly verify the measured turbulence intensity and to understand the shedding phenomenon of the drag-reducing polymeric solution, the natural shedding frequency has been measured using a power spectrum analyzer(HP2640). The polymeric solution defined the natural shedding identically well with Newtonian fluid(Figs. 4.16 and 17). No anomaly in shedding spectrum due presumably to the phase lag between shear stress and rate of strain for small amplitude oscillatory flow of viscoelastic fluid is seen. The

shedding frequencies measured in a wide range of Reynolds number are shown in Fig. 4.18. As was discussed earlier in this chapter, the Strouhal number for the subcritical region of Reynolds number is approximately 0.2 for Newtonian fluids. The present Strouhal number for water is slightly higher than 0.2, and fluctuates at low Reynolds number. Both of these two facets are the characteristics of turbulence effect. The Strouhal number for polymeric solution shows a similar tendency but with a lower value than that of water at low Reynolds number, a clear verification of lowered turbulence. Both Strouhal number distributions, however, tend to smooth out and become indistinguishable as the Reynolds number is increased.

A boundary-layer turbulence intensity has been measured at θ=82, Re=27,500(Fig. 4.19). The measured turbulence intensity distribution is typical for transitional boundary-layer flow. For fully turbulent flow, the turbulence intensity exceeds the value of 10% within the boundary layer. The turbulence intensity of polymeric solution is significantly lower than that of water all the way across the boundary layer. This is consistent in tendency with recent measurements by others(Mizushina and Usui 1977, Berman 1978). It may have been noticed that boundary-layer turbulence intensity near the boundary-layer edge is somehow higher than that of freestream measured at the same Reynolds number for both water and polymeric solution(Fig. 4.13). Most likely, the reason may be the strong effect of the free shear layer oscillation due to vortex shedding. This sheds more light on the strong influence of the vortex shedding on the velocity field around the point of

separation which has extensively been discussed earlier in this chapter.

The experiments conducted here were grouped in two categories. The first group of experiments was conducted with freestream turbulence intensity between 1% and 3.5%. The freestream turbulence intensity decreasd monotonically with the Reynolds number. For this range of the freestream turbulence, intensity and at the Reynolds number tested, the boundary layer flow of the Newtonian fluid entered the transitional regime and separation was turbulent. The experimental results obtained at the above condition are discussed in Section 4.5.2.

Experiments were also conducted at freestream turbulence intensities lower than 0.6% which, at the present Reynolds number range, do not disturb the boundary-layer flow. The boundary layers were therefore kept laminar and separation was laminar. The experimental results obtained at this condition are discussed in Section 4.5.3.

4.5.2 Transitional flow velocity profiles

The velocity profiles measured in polymeric solutions near the stagnation point will be displayed first. The corresponding velocity profiles for water have also been measured to provide a comparison for the measurements in polymeric solution. The velocity profiles near the stagnation point are shown in Figs. 4.20 through 23 for two different Reynolds numbers.

The velocity profiles for water are not boundary-layer profiles. The measurements extend far out into the potential flow region. In these angular positions, a close geometrical similarity between the flat

plate and circular cylinder is doubtless. The boundary-layer velocity profiles should generally follow the familiar stagnation profile that has been discussed in chapter 3. In short, this profile describes a negative linearity between normal velocity, v and and normal distance, y i.e., v=-y. The present results show a positive normal velocity in a small region near the stagnation point, especially at low Reynolds number(Fig. 4.20). As the Reynolds number is doubled and as the measuring volume traverses downstream, the positive region of normal velocity disappears(Fig. 4.21, 22 and 23). The positive normal velocity designating the outer flow near the frontal surface should be discussed to some extent. Traditionally, experimental velocity measurements notably neglected the stagnation region for some obvious reason. Perhaps uniquely, Sadeh et al(1977) measured the velocity profile in this region in air and found a rotational flow there introduced by the free stream turbulence. Since the impinging free stream has its major turbulence in the direction normal to the wall, the local rotational flow near the stagnation point may preferably be introduced on the horizontal plane normal to the surface. Therefore, the local rotationality of flow is more likely to influence the normal velocity rather than the tangential velocity.

Following the above observation by Sadeh et al, the present result may be easily interpreted at least qualitatively. The free stream turbulence intensities of water at Reynolds number of 41,200 and 20,875 are less than 1% and over 1.5%, respectively(Fig. 4.13). Therefore, local rotational flow might have been introduced measurably near the

stagnation point in the latter, but not in the former case. Relatively small difference in turbulence intensity of the two cases may be argued. However, one percent difference in the turbulence intensity of the free stream changed the measured heat transfer by a factor of two at low turbulence level(Lowery and Vachon 1978). The effect of polymer on turbulence intensity, as discussed earlier, is to reduce the turbulence intensity only when the turbulence intensity of water is relatively high. It is also seen in the same figures that this hypothesis qualitively explains the measurements in polymeric solution. With low turbulence intensity of water, added polymer is inactive(Figs. 4.21 ,22 and 23). However when the turbulence intensity of water is relatively high, the added polymer reduced free stream turbulence intensity resulting also in reduction of the rotational flow in the stagnation region(Fig. 4.20).

Following Lumley(1973) the impinging flow around the stagnation point is viewed as an irrotational contraction. Therefore, a close analogy to extensional flow should be expected. Presently measured velocity profiles at high Reynolds number may be regarded as irrotational flows. Therefore, the velocity profiles around this point may be useful to test the extensional viscosity model of drag reduction mechanism, discussed in chapter 1. Apparently no sign of shearing effect is seen in either of the Reynolds numbers both for polymeric solution like water. With extensional viscosity at work, the polymer is extended in shear-free flow, the viscosity increases, therefore the boundary layer for polymeric solution should be thicker than that of water. However, this presumably thickened boundary layer is still

thinner than 0.1mm in the stagnation region and therefore inaccessible to the present measuring volume. However, with a thickened boundary layer the outer potential flow should follow the geometry at an extended distance from the surface.

The present velocity profiles measured at a low Reynolds number show a significant increase in magnitude of the normal velocity for polymeric solution. However, the tangential velocity is identical with that of water(Fig. 4.20). By adding the two components of the velocity vector, a narrowed down streamtube for polymeric solution results.

Velocity profiles measured at doubled Reynolds number, at the same angular position show essentially the same tendency. However, the difference in normal velocity between the two kinds of fluids has been reduced(Fig. 4.21). A rather interesting feature is found in the velocity profiles measured futher downstream, but still not far from the stagnation point. The velocity profiles of water and polymeric solution cross each other both in tangential and normal components. The crossing point near the point of stagnation is nearer to the wall than at stations further downstream. The velocity for polymeric solution is now larger in tangential direction but smaller in normal direction near the wall. A direct interpretation of this is: the streamtubes for polymeric solutions are narrower away from the surface. However, they follow the geometry at an extended distance from the surface. This may at once be regarded to confirm the extensional viscosity model of drag reduction.

The boundary-layer velocity profiles have been measured only near

the separation point but for a wide range of Reynolds numbers. Having only a few measuring points in the thinner boundary layer elsewhere would have the comparison with water data more difficult. There are a few more reasons dictating measurements near the point of separation such as i) single station velocity profile generally signifies the characteristic of the whole attached boundary layer, ii) velocity profile near the separation point implicitely describes the separation behavior, and iii)response to wide variations in Reynolds number is much more pronounced than that of angular position in elucidating the effect of added polymer.

The measured boundary-layer velocity profiles in 100 ppm Separan solution at θ=82 degrees are shown in a series of figures, Figs. 4.24 through 31 in an order of increasing Reynolds numbers. Apparently the drag reducing effect of polymer, namely the thickened boundary layer or a steeper tangential velocity profile for polymeric solution compared to water is more pronounced at lower Reynolds numbers. Unless specified from now on the 'tangential velocity', 'tangential velocity profile' etc will be referred to as 'velocity', 'velocity profile' etc. The maximum skin drag reduction, based on the slope of the measured velocity profile across the boundary layer, corresponded to the lowest Reynolds number, 6750 encountered in the present expriment(Fig. 4.24). However, the two velocity profiles of water and polymeric solution tend to become identical as the Reynolds number increases, or an alternating tendency may be expected with a further increase in Reynolds number.

The Reynolds number dependence of the skin friction drag reduction is exactly the opposite of the conventional internal flow data reported by many other investigators. This apparently inverse Reynolds number dependence is not believed to be due to the different geometry effect, i.e., presently a 2-D external flow compared to the conventional internal flows in a circular pipe or rectangular duct. Indeed for a flat plate increased skin drag reductions have been reported at increased Reynolds number. A realistic interpretation should therefore be attributed to something else, namely turbulence effect. In the present case, the measured turbulence intensity was a monotonically decreasing function of the Reynolds number within the major part of the present experimental range. With the turbulence intensity distribution in mind, a consistent tendency is seen in the measured velocity profiles. The skin friction drag reduction is almost a monotonically increasing function of turbulence intensity when the free-stream turbulence intensity exceeds a certain value.

It is observed in Figs. 4.24-31 that whenever the tangential velocity of the polymeric solution was smaller than that of water the same was true for the normal velocity. However, when the difference in normal velocity between water and polymeric solution is divided by the difference in tangential velocity, the result is always smaller than unity. This is a consistent evidence for the thickened boundary layer for polymeric solution as is seen in the figures.

With a steeper boundary-layer velocity profile for polymeric solutions compared to water at relatively high turbulence intensity, an

earlier separation may be expected. The velocity profiles measured around the point of separation are shown in Fig. 4.32. A steeper wall velocity gradient followed by an earlier separation and a larger wake for polymeric solution have been observed in a series of velocity profiles measured along the downstream direction. As a matter of fact certain anomalies in separation behavior such as delayed separation due to elasticity effect or vortex reattachment were expected. The observed separation behavior for polymeric solution did not indicate any sign of such anomalies. The behavior of the separation process is qualitatively similar to the Newtonian flow separation except that the polymeric solution separates earlier than the Newtonian solvent.

Finally, cross-wake velocity profiles have been measured by traversing the upper half of the wake with its origin at 1.2 times the cylinder diameter downstream of the rear stagnation point. The velocity profiles measured in the wake show a much more significant influence of the polymer compared to the boundary layer data. This is attributed to the turbulent nature of the wake. The vertical component of the wake velocity is very small in its magnitude and no significant differences can be found between water and polymeric solution. Apparently, a significant difference between the two kinds of fluids is measured in horizontal velocity while traversing vertically(Fig. 4.33). The horizontal position of the vertical traversing is within the time-averaged backflow region of the water wake, but outside of the wake of the polymeric solution. The wake of the polymeric solution is larger in vertical dimension and smaller in horizontal dimension compared to the

water wake. The wake of water is therefore stretched in the axial direction compared to the wake of the polymeric solution. The tendency has been expected from the earlier separation for polymeric solution.

4.5.3 Laminar flow velocity profiles

Although the polymer-aided skin drag reduction has only been observed in turbulent flow, it is also interesting to examine the laminar velocity field under the influence of polymer.

Shown in Figs. 4.34 through 40 are the boundary-layer velocity profiles of polymeric solution(100 wppm Polyox) measured at θ=75, 80 and 82 degrees. The turbulence intensity of the water for these measurements was fairly low and was in the range of 0.3-0.7%, again controlled by the flow system setting. The turbulence intensity in this case was generally increased with the Reynolds number. Nevertheless, for these Reynolds numbers, no turbulence amplification occurs in the boundary layer. The turbulence intensity of polymeric solution was not measured in this case. However, when the turbulence intensity of water is low, the added polymer is inactive and the turbulence intensity of the polymeric solution is almost the same with that of water(see Fig. 4. 13). At this fairly low turbulence level the boundary layer is laminar. The measured boundary-layer velocity profiles for the polymeric solutions are significantly fuller compared to those of water. The same is true qualitatively for the normal velocity. However, when the difference in normal velocity between the polymeric solution and water is divided by the difference in tangential velocity, the result is less than unity evidencing a thinner boundary layer for the polymeric

solution compared with water as shown in the figures. This is exactly the opposite trend to what was discussed in the previous section. A similar result has been reported in the tangential flow between two concentric cylinders in which the inner one is rotating while the outer one is fixed(Rubin and Elata 1969, Denn and Roisman 1969). As the rpm is increased a secondary flow, known as 'Taylor vortices' is developed. The torque for polymeric solution is reduced compared with Newtonian fluids as the Taylor number is increased before the onset of turbulence. This is apparently associated with the reduction of the intensity of the secondary flow(Hoyt, 1972). Apparently the added polymer signifies its shear thinning or elasticity effect in laminar flow. The boundary-layer velocity profiles for polymeric solution become increasingly fuller as the Reynolds number is increased up to 27,500. However, they remain constant beyond this value. This may correspond to the maximum drag reducing Reynolds number of approximately 50,000 for internal flows(Berman 1978).

An important implication of the fuller boundary-layer velocity profile for polymeric solution near the point of separation is a delayed separation. The delayed separation will result in a smaller wake and reduced form drag for solution compared to water. The former was also confirmed by the flow visualization.

4.6 Flow visualization

The flow visualization has been carried out to confirm the above measurements visually. Dye was injected from the surface of the cylinder, upstream of separation. The instantaneous streaklines

monitored by a video system generally confirmed the above measurements with regard to the point of separation and its motion, the effect of the freestream turbulence intensity on separation, and the opposite effect of the added polymer on separation depending on the freestream turbulence intensity. The time averaged point of separation and its motion are shown in Table. 4-2. It is seen from the table that the time-averaged point of separation for water has been delayed by approximately 5 degrees as the free stream turbulence intensity is increased from 0.8 to 3.4%. The added polymer induced an earlier separation compared to water when the free stream turbulence intensity was significant, however delayed separation by approximately three degrees when the free stream was fairly laminar.

4.5.5 Measurements on sphere - an interpretation

Measurements by White for sphere, mentioned in "introduction", may also be explained in terms of free stream turbulence rather than the Reynolds number. Indirect drag measurements by White(1968) were obtained by dropping a sphere through a deep tank(7m) of water and polymeric solution. The terminal velocities were measured near the bottom of the tank and the drag coefficients were then calculated. As was mentioned earlier, the free stream is idealy laminar up to the critical Reynolds number in this case. As the Reynolds number is nearing the critical value from the below, turbulence is generated both in boundary layer and free stream. The elasticity-caused delayed laminar separation is now counterbalanced with the turbulence-polymer interacted earlier separation. The drag coefficients of water and

polymeric solution therefore cross each other at about the critical Reynolds number(Fig. 4.42). Further increase in Reynolds number adds the turbulence in free stream resulting in the reattachment of separated flow onto the body surface and apparently delaying the point of separation tremendously. However, the added polymer is most effective in a fully turbulent flow as a skin drag reducing agent. Then the boundary-layer velocity profile will be steepened inducing an earlier separation. The earlier separation will obviously induce a larger wake and increase the form drag. The total drag of the sphere in the supercritical region of the Reynolds number therefore becomes higher for polymeric solution compared to that of water.

CHAPTER 5

NUMERICAL RESULTS

The numerical results of the laminar boundary-layer analyses of momentum, heat and mass transfer, formulated in chapter 2, are presented in this chapter. The stagnation region solutions, developed in chapter 3, provided the initial conditions to the x plane for Newtonian problems. For power-law non-Newtonian problems the Hiemenz solution has been assumed at x=0 with a very small grid spacing in x direction near the stagnation point.

The steady heat and mass transfer over a circular cylinder in Newtonian crossflows has been studied extensively in the past, both theoretically and experimentally. The present Newtonian studies focused on the unsteady problems. However, a rigorous numerical analysis of the steady Newtonian problem has also been provided to confirm the present numerical scheme upon comparing the present results with existing ones. It should also be mentioned that no numerical analysis based on the finite difference has so far been published, even for the steady heat transfer problem.

In contrast to the numerous theoretical and experimental works established for Newtonian fluids, few have so far been evolved for relatively simple and easily accessible power-law non-Newtonian fluids. The present numerical results for power-law fluids, though limited to the steady problems, disclosed certain important facets of power-law fluids that have not been exposed by analytical approximations.

5.1 Results of Newtonian Analysis

5.1.1 Outer flow equation and basic wall quantities

The boundary-layer calculations proceede by first providing the outer flow information in terms of velocity distribution at the edge of the boundary layer which, in principle, is a function of only geometry but not function of materials involved. The outer flow equation implicitely represents the configuration of the body, and provides the velocity boundary conditions at the edge. Aside from the difference in mathematical formulation, the uncertainty of the outer flow equation in the representation of real flow has been a serious source of error in predicting the additional transport rates. Therefore, a most reliable outer flow equation should be adopted, and any comparisons of results thereby obtained should be made using the same outer flow equation.

Several outer flow velocity distributions that have widely been employed for boundary-layer calculation in the past are given in Table 5.1 in algebraic form, and shown in Fig. 5.1. Some fundamental wall quantities i.e., wall velocity gradient, skin friction and wall temperature gradient distributions calculated by the present numerical scheme are shown in Figs. 5.2, 3 and 4. Obviously different outer flow equations yield significantly different wall quantities, and the differences are amplified as one moves in the downstream direction. This is due to the increasing significance of the higher order terms in the outer flow equation. The uncertainty involved in the experimental determination of the outer flow, especially near the point of separation

provides a possible physical explanation of the deviation. An exception to the above general tendency is the local rate of heat transfer ; a significant difference between the potential flow theory and the experimentally determined outer flow equations are found from the stagnation point.

5.1.2 Steady heat and mass transfer

Shown in Fig. 5.5 is the local rate of heat transfer using the different outer flow equations given above. The local rate of heat transfer i.e., the local Nusselt number is normalized by the square root of Reynolds number. This is to eliminate the Reynolds number dependence of the heat transfer. The implication is an approximately inverse linearity between the rate of heat transfer and boundary-layer thickness due to the linear nature of the conduction resistance across the laminar boundary layer.

The predicted local rate of heat transfer at the stagnation point using the two different experimental outer flow equations is essentially the same. However, the one predicted from potential flow theory is higher by approximately 5% compared with the other two. The same tendency is consistently found downstream in the boundary layer. This is contrasted to the predicted wall quantities which are essentially the same at the stagnation point for three of the cases. The local heat transfer coefficient, however, is proportional to the ratio of the wall temperature gradient to the temperature gradient across the boundary layer. To account for the interaction of the inviscid flow with the boundary layer, further calculations will preceed using experimental

outer flow, mainly the Himenz 3-term equation which was obtained from the experimental data by Schmidt and Wenner(1942).

Shown in Figs. 5.6 are theoretically estimated rates of heat transfer by many different methods of boundary-layer approximation calculated using the same outer flow equation, namely the Eckert equation. The details of the methods of prediction and references are found in the original paper by Spalding and Pun(1962); they are mainly based on locally similar solution or power series expansions. Also shown in the same figures are the present numerical results and experimental data by Schmidt and Wenner(1942), and by Andraka and Diller(1985). The former experimental data have widely been employed for comparison for over one quarter century.

Spalding and Pun reviewed over 18 methods of predictions that were available by 1962 and rated the methods of prediction by comparing the results with the exact solution by Frossling up to 45 degrees from the stagnation point, and with the experimental data by Schmidt and Wenner beyond this range. The present results show an excellent agreement with those of Spalding and Pun. However, the majority of the theoretical results including the present one underestimate the heat transfer compared with the experimental data by Schmidt and Wenner. A better agreement between the majority of the theoretical predictions and experimental data is found with the experimental data by Andrake and Diller. However, the outer flow equation for all of the theoretical predictions including the present numerical solution is from the experimental data by Schmidt and

Wenner. Further discussions will be based on the experimental data by Schmidt and Wenner. At least three possible reasons may be considered for this common discripancy between the theoretical prediction and experimental data; the constant-property assumption, the free stream turbulence effect and the unsteadiness effect introduced by the natural shedding. The latter two effects have so far been completely neglected in laminar boundary-layer analysis, and the constant property assumption is the premise of the forced convection. The turbulence intensity was not directly measured in the experiment by Schmidt and Wenner, however, it is presumbly not insignificant (Kestin and Wood 1971). Accounting of the natural shedding in the boundary-layer analysis is the topic of the subsquent section.

The convective mass transfer over a circular cylinder is also an industrially important transport process which is frequently been encountered in heterogeneous catalytic processes. The case analyzed here is a sublimation process of cylindrical naphthalene into air. The Schmidt number for this system is about 2.5. The present numerical results are shown in Fig.5.7 together with the experimental data by Sogin and Subramanian(1961). Also shown in this figure is the analytical approximation using Merk's method by the same authors. A common outer flow equation (Sogin and Subramanian 2-term equation) has been used. The present results show a fairly good agreement with the one obtained by Merk's method. However, both the present numerical result and analytical solution by these authors overestimate the rate of mass transfer up to about 45 degrees and underestimate it

beyond this region. The discrepancies between the theoretical calculations and the experimental mass transfer data show the opposite tendency with those of heat transfer up to about 45 degrees, however, the same are found beyond this range.

5.1.3 Unsteady results

The unsteady problem to be considered here is the naturally occuring unsteady flow due to natural vortex shedding, namely a self-induced oscillatory flow. The motion of the stagnation point as well as the point of separation has been investigated experimentally by Dwyer and McCroskey(1973). In their numerical calculations these authors employed a moving coordinate system to account for the motion of the stagnation point.

The novel aspect of the present numerical analysis of self-induced oscillatory flow is to incorporate the motion of the stagnation point by employing an aysmptotic expansion of the solution to the full Navier-Stokes equation for oscillating stagnation flow, described in chapter 3. The solution has been matched to the boundary-layer code and provided the initial condition for the boundary-layer calculation.

In the present numerical analysis the frequency and amplitude of the velocity oscillation have been matched to the experimental values, namely the Strouhal frequency of 0.21 and amplitude of around 10% have been assigned.

Shown in Fig. 5.8 is the periodic mean rate of the heat transfer with a 10% velocity amplitude. Also shown in the same figure are several reference data for comparison. Apparently, the present time-averaged

unsteady results represent an improvement over all steady results and fit the experimental data fairly accurately, especially near the stagnation point. This is presumbly due to the rigorous treatment of the unsteady motion of the hydrodynamic stagnation point. However, a notable deviation from the experimental data is still found neat the point of separation. As discussed in chapter 4, the effect of the free-shear layer oscillation is extremely strong around this point, and this would give an effect on heat transfer in addition to the boundary-layer oscillation as a whole.

The effect of the free stream amplitude on the local rate of heat transfer is displayed in Fig. 5.9. The Strouhal frequency of 0.21 has been assumed. Up to approximately 45 degrees from the stagnation point, the heat transfer monotonically increases with the velocity amplitude. However, the opposite tendenscy is seen beyond this point.

The fine structure of the unsteady velocity field and heat transfer along the boundary layer have been examined for self-induced oscillatory flow with Strouhal frequency of 0.21 and free-stream amplitude of 10%. The periodic variations of skin friction and local heat transfer are shown in Figs. 5.10 and 11. Corresponding to the outer flow variation of Fig. 5.12 the expanded structure of the periodic variations of skin friction and heat transfer for some selected angular positions are given in Figs. 5.13 and 14, respectively. The skin friction varies in phase with the outer flow with an almost constant amplitude along the downstream direction. No phase lag along the downstream direction is found as well as across the boundary layer.

The boundary-layer oscillates uniformly under the given conditions. This is an agreement with Lighthill's(1954) asymptotic theory for low frequency parameters.

The calculated heat transfer, however, shows certain variations. The periodic fluctuation of heat transfer is minimum about θ=45 degrees from the stagnation point, and amplified along upstream and downstream directions with its maximum amplitude near the point of separation. Experimentally measured time-averaged rate of heat transfer also showed a serious fluctuation near the point of separation(Borell, Kim, Ekhaml, Diller, and Telionis 1983).

The unsteady velocity and temperature profiles across the boundary layer are shown in Figs. 5.15 through 22 for the above selected angular positions. The temperature boundary layer is significantly thicker than the velocity boundary layer at this Prandtl number(0.7). It should be emphasized here that the temperature boundary conditions both at the wall and the freestream were steady. Therefore, the temperature fluctuations are due to nonlinear effects. The velocity fluctuations are not quite significant in all of the above figures. However, the temperature fluctuation is discernable at θ=45 degrees and become more significant further downstream.

5.2 Results of Power-Law Non-Newtonian Analysis

5.2.1 Basic calculations

The numerical solutions to the boundary-layer equations for power-law non-Newtonian fluids, formulated in chapter 3, will be presented here. The present numerical solution to the boundary-layer equation may be considered exact. There was no limitations on the generalized Prandtl number and the flow behavior index of the power-law fluid. Therefore, any anomalous transport behavior of different power-law fluids are entirely due to the different characteristics of the non-Newtonian materials. There was no additional difficulty in running the power-law program compared to the Newtonian case except for the increased computation time, approximately 30 - 50 % depending on the flow behavior index and generalized Prandtl number.

The global rate of heat transfer will first be presented to ensure that the present numerical scheme for nonlinear constitutive equations is reliable upon comparing the present results with the earlier analytical approximations. A significantly different response of the non-Newtonian boundary layer to the outer flow equation will next be shown by examining several wall quantities predicted with different outer flow equations. Finally, the fine scale of the non-Newtonian boundary layer will be examined for a most reliable outer flow equation.

Shown in Fig 5.23 is the presently calculated heat transfer for $n = 0.8$, and $Pr,p = 10$. Also shown in the same figure are analytical approximations by other investigators. The predicted heat transfer shows a considerable deviation among them. Aside from the present

numerical solution, the two other analytical approximations for n=0.8 show a significant difference even in tendency. The approximation by Shah et al(1962) is based on an asymptotic expansion for large Prandtl number, i.e. Pr,p ->∞ . Physically, this case corresponds to an extremely thin thermal boundary layer compared to the momentum boundary layer. The velocity profile covering the extremely thin thermal boundary may presumbly be linear. The analytical solution by Wolf and Szewczyk(1966) was based on Blausius type series expansions of velocity and temperature, and hence was not limited to large Prandtl number. A generalized Prandtl number of 10, certainly realistic, has been used by these authors. The thermal boundary-layer thickness and hence, the wall temperature gradient for Pr,p = 10 should be much thicker and smaller, respectively, resulting in a decreased heat transfer compared to those of Pr,p ->∞ .

The above described Prandtl number effect on heat transfer is well understood and experimentally proven for Newtonian fluids, and the same should be true for purely viscous non-Newtonian fluids. This is clearly seen in Figs. 5.24 and 25. The local heat transfer of the power-law fluid is doubled as the Prandtl number is increased by 10 times (Fig. 5.25). The calculated wall temperature gradient again confirms this (Fig 5.24). However, the opposite is seen in Fig. 5.23 between the two different analytical solutions. The reason for this opposite tendency may, in part, be due to the different boundary conditions and different outer flow equation. The prediction by Wolf and Szewczyk is based on potential outer flow, and the one by Shah was based on

experimental outer flow obtained by the same authers. The outer flow distribution will certainly influence the transport processes across the boundary layer as was seen earlier in this chapter for the Newtonian case. However, the tendency should not be changed. This topic will subsequently be discussed to some extent. The different boundary conditions at wall i.e., constant heat flux and constant temperature give identically the same rate of heat transfer up to θ = 30 degrees from the front stagnation point (Zukauskas 1978). Therefore, it seems appropriate to mention here that the two analytical methods which have shown a fairly good agreement for Newtonian fluids (see Spalding and Pun 1962) predict the opposite tendency of heat transfer for power-law non-Newtonian fluids.

Following Shah et al, their theoretical prediction was in exceptionally good agreement with the experimental data. The present numerical solution, using the outer flow equation by Shah et al, shows a similar tendency with the one predicted by them. However, relatively lower values were obtained, especially away from the stagnation point. This may reasonably be explained, at least qualitatively, from the different Prandtl number and boundary conditions employed for each of the predictions. The presently adopted Prandtl number of 14 will surely predict a lower heat transfer all the way compared to Pr,p ->∞ by Shah et al, as was shown in Fig. 5.23. As was mentioned earlier, the constant wall temperature condition (present B.C.) gives identically the same heat transfer compared to constant heat flux condition at upstream. However, the temperature gradient near the wall will drop at

downstream due to the transferred heat at upstream resulting also in the drop of driving force for heat transfer for constant wall temperature problem but not for constant heat flux problem. The above two tendencies are seen in Fig. 5.23.

5.2.2 Skin friction and heat transfer

The skin friction and heat transfer have been calculated for both pseudoplastic (n < 1) and dilatant (n>1) materials. A relatively wide range of flow behavior index has been tested for pseudoplastic materials. This is due to the practical importance of these materials. Two types of external flows i.e., the potential flow and experimentally determined Hiemenz' 3-term equation have been tested. This was so designed to avoid any possible peculiarities due to the outer flow equation. Shown in Fig 5.26 and 27 are the skin friction of the power-law materials for the two different outer flow equations mentioned above. No experimental data or theoretical works are available for comparison. The skin friction distributions of the power-law materials are significantly different from those of Newtonian fluid, and this is especially true for flow behavior index(n) far from the Newtonian value of unity. The skin friction of pseudoplastic materials are higher than that of Newtonian (n=1) up to about 30 degrees from the stagnation point, and lower beyond this range. Exactly the opposite is shown in the same figures for dilatant material. Since the same tendency has been found for both of the outer flow equations, it is believed that the above tendency is a consistant characteristic of power-law materials.

The skin friction and, therefore, the rate of shear near the wall is

maximum at about θ = 50 - 60 degrees and tends to become zero at the point of separation for Newtonian fluid. The exact point of maximum skin friction depends on the external flow condition. Potential outer flows do not show separation. Instead, the wall velocity gradient at the stagnation point is zero, also resulting in the zero skin friction at that point. The experimentally determined outer flow equation, on the contrary, reflects the viscous effect and therefore shows laminar separation at approximately θ = 80 degrees. The point of maximum skin friction surely moves upstream compared to potential flow theory, and also the skin friction at the stagnation point is not necessarily zero. All of these important facets are clearly shown in the same figures.

As far as the skin friction for power law non-Newtonian fluids is concerned, again the results are very clear. The Newtonian viscosity of pseudoplastic material, that is the viscosity of the pseudoplastic materials before the onset of shear thinning, is presumably higher compared to the Newtonian fluid. However, once the rate of shear exceeds certain value as it flows downstream on the cylinder, the shear thinning viscosity works, and eventually the skin friction of the pseudoplastic material will become smaller than that of the Newtonian fluid. Apparantly the maximum shear thinning effect will occur at maximum rate of shear location.

Exactly the opposite argument may be applied to the dilatant material, namely the Newtonian viscosity of the dilatant material is presumably smaller compared to Newtonian. However, as the rate of shear increases the non-Newtonian viscosity of dilatant material

increases with its maximum at the location of maximum rate of shear. The above described skin friction variation of power-law materials is clearly seen in the same figures (Figs. 5.26 and 27). A slight difference between the two figures may be due to the different external flow condition described earlier.

The presently predicted heat transfer for power-law fluids is shown in Figs. 5.28 and 29 for two different outer flows. The outer flow equations and the power-law fluids concerned here are the same with the ones considered earlier. A more significant difference is found for heat transfer compared to the skin friction between the power-law fluids and the Newtonian fluid. Though the general tendencies seem similar to each other, a notable difference is also found between the two different outer flows. It was mentioned earlier in this chapter that the potential flow is not a realistic input for Newtonian heat transfer calculations. It was also mentioned that the predicted heat transfer for power-law fluid using potential flow showed the opposite in tendency (see fig 5-23) compared to those predicted using experimental outer flows. Especially the predicted heat transfer using the potential flow for n = 0.6 tends to become infinite near the stagnation point, which is not realistic. Therefore, from the heuristic point of view further discussions will be limited to the experimental outer flow equation, namely the Hiemenz' equation.

The heat transfer of the pseudoplastic materials is higher than that of Newtonian which on the other hand, is higher compared to dilatant materials for a large portion of the attached boundary layer.

The heat transfer of the pseudoplastic materials becomes higher as the flow behavior index decreases, i.e. as the material becomes more and more shear-thinning. Although only one case of the dilatant materials is presented here, exactly the opposite tendency is easily expected, namely a further decrease in heat transfer is expected for a more shear-thickening material. The opposite tendency may be claimed near the stagnation point and separation. This tendency has also been predicted under constant heat flux conditions by Shah et al (see Fig. 5.23). A consistent tendency is also found in the wall temperature gradient(Figs. 5.30 and 31). For the wide range of the attached boundary layer, the wall temperature gradient increases as the flow behavior index(n) decrease across the Newtonian value.

A clear conceptual distinction should be made here between the Newtonian and non-Newtonian fluid. The skin friction of pseudoplastic material was lower compared to water, say at θ = 40 degrees (see Fig. 5.27). A straightforward Newtonian interpretation will designate a lower velocity gradient, lower temperature gradient and therefore a lower heat transfer for pseudoplastic materials compared to the Newtonian. This interpretation should be avoided for power-law fluids. For Newtonian fluid, the skin friction is linearly determined by the velocity gradient for given material system at given temperature and pressure. However, for power-law fluid the non-Newtonian viscosity is a function of shear rate in addition to the other variables controling Newtonian viscosity. The non-Newtonian viscosity is nonlinear with respect to the magnitude of the rate of shear.

The skin friction of the power-law fluid is further complicated by the velocity field like the Newtonian, however, in a different way. With shear-thinning viscosity onset, for example , the viscosity of the pseudoplastic material may become lower compared to the Newtonian value, under other conditions the same, resulting in a fuller velocity profile. The skin friction of the pseudoplastic material is now decreased by the decreased viscosity and increased by the increased velocity gradient. The actual skin friction of power-law materials may be smaller or larger than that of Newtonian fluid depending on the relative significance of these two opposite contributions.

5.2.3 Boundary-layer velocity and temperature profiles

The temperature field and therefore the heat transfer is not directly related to the non-Newtonian viscosity, but uniquely determined by the velocity field as far as the fluid is a purely viscous material. The connection between the temperature distribution and non-Newtonian viscosity comes into play only through the velocity field.

The increased and decreased heat transfer for pseudoplastic and dilatant materials, respectively is a direct result of the velocity field near the wall for those materials. This will now be clearly demonstrated by displaying the velocity and temperature distributions across the boundary layer. The velocity and temperature fields of power-law materials have been examined with a most reliable outer flow equation, namely, with the Hiemenz outer flow equation. Shown in a series of figures, 5-30 through 37, are the boundary layer velocity and temperature profiles at three angular positions.

A consistent and notable difference between the velocity and temperature boundary layers is that the latter is much thinner than the former, a direct result of the large Prandtl number of 14 that is presently being employed.

A very interesting structure of the velocity field of power-law fluids is noticed in the velocity profiles (Figs. 5.32, 34, and 36). The viscous velocity of pseudoplastic materials is fuller near the wall and smaller near the free stream compared to Newtonian fluid. On the contrary, the viscous velocity of the dilatant material is smaller near the wall and larger near the edge compared to Newtonian fluid. These are most clearly seen in Fig 5.34 and 36, namely at θ= 45 or 60 degrees. The same tendency was also reported for flat plate (Acrios et al 1960). It is not difficult to understand this overlapping velocity profiles across the flow behavior indices and boundary layer. At a given angular position, the local rate of shear across the boundary layer is maximum near the wall, and minimum near the edge where it tends to zero. In between these two it is natural to believe that there is certain onset value of shear dependent viscosity to work depending upon the characteristics of the material. Therefore, the shear rate dependent non-Newtonian viscosity is most effective near the wall, and becomes less effective while nearing the edge. Eventually the Newtonian viscosity dominates.

The angular variation of the shear rate dependent velocity field is also easily explained in terms of skin friction. The skin friction around θ= 60 degrees is much higher than at θ = 20 degrees. Therefore, the

shear rate dependent boundary layer velocity profiles are dominant at θ=60 degrees.

The boundary-layer temperature profile, under the forced convection assumption, is uniquely determined by the velocity field with their relative thickness dependent on the Prandtl number of the material system. The thermal boundary layer is much thinner compared to the momentum boundary layer. The velocity field covering the thermal boundary layer is within the shear rate dependent velocity field. Therefore, the boundary-layer temperature profile for pseudoplastic materials is fuller compared to the Newtonian fluid, and the opposite is true for dilatant materials(Figs. 5.33, 35, and 37). As a result, the wall temperature gradient, and hence the heat transfer for pseudoplastic materials is favored over Newtonian fluid. Exactly the opposite argument may be applied for dilatant material. These are clearly seen in the same figures.

CHAPTER 6

CONCLUSIONS

In the present research fundamental measurements in drag-reducing external flows of polymeric solutions and solvent, and finite-difference analyses of laminar boundary-layer flows of heat, mass and momentum for Newtonian and power-law non-Newtonian fluids have been performed. The experimental results disclosed certain unusual aspects of drag-reducing flow, and certain important aspects of the boundary layer flow of power-law fluids have been exposed through the numerical analysis.

In the past investigations on the polymer-aided drag reduction have been focused on the internal flows and streamlined bodies. It was surprising to find that the circular cylinder in crossflow has so far not been considered. Present measurements in polymeric solutions disclosed certain important facets concerning the bluff body submerged in conventionally-drag-reducing flow of polymeric solutions.

Velocity measurements in Separan solution showed that the boundary-layer velocity profiles for polymeric solutions were significantly steeper compared with the Newtonian solvent which resulted in an earlier separation. Unexpectedly, the opposite tendency was found at high Reynolds number range. The Reynolds number dependence of the present polymer velocity profile was apparently the opposite to the typical velocity profile measured in drag reducing internal flows and flows parallel to a flat plate.

Velocity measurements in Polyox solution, on the contrary, showed

a significantly fuller boundary-layer velocity profile for polymeric solution compared to water for the entire Reynolds number ranges encountered. Apparently, the skin friction has been increased due to the Polyox addition, a contradiction to findings in internal flows and flows parallel to a flat plate.

The above velocity measurements in both of the polymeric solutions alone do not allow any acceptable interpretations of the present results based on the earlier measurements. Therefore, we must find some other controlling parameter governing the non-Newtonian flow over a bluff body submerged in a high Reynolds number flow. This was made possible by measuring the turbulence intensities of the free stream and boundary layer. Measurements in Separan solutions were conducted at tunnel settings such that the free stream turbulence intensity was high enough to induce transition in boundary layer in the low Reynolds number range. Moreover, for these settings, the turbulence intensity decreased monotonically with the Reynolds number. The drag-reducing polymer works only with a significant level of turbulence. The present velocity measurements at low Reynolds number showed a steeper velocity gradient near the wall compared to water ; a direct indication of the reduced skin drag for polymeric solution. As the Reynolds number increased, i.e., the turbulence intensity decreased, the velocity profiles of the polymeric solution and Newtonian solvent tend to become indistinguishable.

Measurements in Polyox solutions were done with a fairly low free-stream turbulence intensity. The boundary layers at such conditions are

laminar. The measured velocity profiles for polymeric solutions were significantly fuller compared to the Newtonian solvent. Indeed, it was verified from the flow visualization that the point of separation for polymeric solution has been delayed significantly in laminar flow, a direct indication of fuller velocity profile for polymeric solution.

From the present measurements in polymeric solutions, it may be concluded that i) in transition boundary-layer flows, polymers reduce the skin drag just as in internal flow, and induce earlier separation resulting thereby in an increased form drag; ii) in laminar boundary-layer flows, skin friction increases due to polymer addition. However, with a significantly delayed separation, a reduction of form drag results.

The total drag of a bluff body submerged in a high Reynolds number flow is dominated by the form drag. Therefore, with a total drag reduction as the objective, the polymer should be added only in laminar flows.

Laminar boundary-layer analysis of power-law non-Newtonian fluids clearly disclosed the dependence of velocity and temperature on the rate of shear. This is the result of shear-dependent non-Newtonian viscosity. The skin friction of the pseudoplastic materials was higher compared to the Newtonian fluid up to approximately 30 degrees from the front stagnation point, and was lower beyond this range. Exactly the opposite was found for dilatant materials. The wall shear stress monotonically increases up to approximately θ = 50 degrees, and decreases beyond this, regardless of the materials involved. The rate

of shear corresponding to the crossing point of skin friction curves should therefore correspond to a critical value. Before this critical value of shear, the viscosity of the pseudoplastic materials(whether it is Newtonian or shear dependent non-Newtonian viscosity) would be higher than that of Newtonian fluid. Exactly the opposite arguement may be applied to the dilatant materials.

The velocity distributions across the boundary layer again showed crossing points between the Newtonian and non-Newtonian materials due to the shear rate distribution across the boundary layer. For all materials the local rate of shear is maximum near the wall and asymptotically tends to zero near the boundary-layer edge. The boundary-layer velocity profiles of pseudoplastic and dilatant materials were fuller and thinner, respectively near the wall compared to the Newtonian fluid due to the shear dependent non-Newtonian viscosity effect. As the local rate of shear decreases approaching the edge, the shear dependent non-Newtonian viscosity becomes less effective. Again a critical rate of shear exists, depending on the flow behavior index, whereby the velocity profiles cross each other. Beyond this range, the shear dependent non-Newtonian viscosity becomes less effective and eventually the Newtonian viscosity of the power-law materials governs the velocity profiles.

The boundary-layer temperature distribution is entirely determined by the velocity field with the relative thickness depending on the generalized Prandtl number. This number for the majority of the power-law materials is the order of 10, and was chosen 14 for the present

case. The thermal boundary layer is therefore much thinner compared to the momentum boundary layer. The presently calculated temperature profiles for pseudoplastic materials were fuller compared to Newtonian fluid all the way across the thermal boundary layer. The opposite was true for dilatant material. No crossing in temperature profile was seen between the Newtonian and non-Newtonian fluids. Obviously, this is due to the extremely thin thermal boundary layers of power-law materials which are spatially limitted to the shear controlled range of the velocity field.

The heat transfer is uniquely determined by the temperature profile which, on the other hand, is indirectly governed by the non-Newtonian viscosity via the velocity distribution. For the major portion of the attached boundary layer, the rate of heat transfer is increased as the flow behavior index decreases, namely the more shear thinning the material, the higher the heat transfer.

Measurements in Newtonian fluids also disclosed certain new aspects of the field, or confirmed the earlier findings by others. The mean and rms pressure measurements in wind tunnel showed that i) the mean pressure coefficient for forced oscillatory flow was slightly higher than that of self-induced oscillatory flow, especially in the wake, or when fd = fs. ii) the rms pressure was a monotonically increasing function of the driving frequency, with its maximum spatial disturbance near the point of separation, especially when fd = fs.

The boundary-layer velocity measurements in the water tunnel showed no substantial difference between self-induced and forced

oscillatory flows; whether the driving frequency was matched to the natural shedding frequency or not. A significant difference was found near and after separation. Both the velocity and pressure measurements in Newtonian fluids showed a strong effect of the free-shear layer oscillation near the point of separation.

The unsteady laminar boundary-layer analysis of Newtonian fluids explained in part why all of the earlier steady calculations underpredicted the heat transfer, especially near the front stagnation point. The partial success of the present method hinges critically on initial conditions which were obtained independently in the form of an asymptotic expansion.

REFERENCE CITED

E. Achenbach, "Distribution of Local Pressure and Skin Friction Around a Circular Cylinder in Cross-Flow up to Re=5,000,000," J. Fluid Mech., 34, 625(1968)

A. Acrivos, M. J. Shah and E.E.Petersen, "On the Solution of Two-Dimensional Boundary-Layer Flow Equations for Non-Newtonian Power-Law Fluids", Chem. Engr. Sci., 20, 101(1965)

A. Acrivos, M. J. Shah, and E.E.Petersen, "Momentum and Heat Transfer in Laminar Boundary-Layer Flows of Non-Newtonian Fluid Past External Surfaces", A.I.Ch.E.J., 6, 410(1960)

C. E. Andrake, and T. E. Diller, "Heat Transfer Distribution Around a Cylinder in Pulsating Crossflow," paper accepted for presentation at Int'l Gas Turbine Conf., Houston, May 1985

P. W. Bearman, "On Vortex Shedding from a Circular Cylinder in the Critical Reynolds Number Regime", J. Fluid Mech., 37, 577(1969)

N. S. Berman, " Drag Reduction by Polymers," Ann. Rev. Fluid Mech." 10, 47(1978)

R. B. Bird, R. C. Armstrong, and O. Hassager, "Dynamics of Polymeric Liquids", Vol.1, "Fluid Mechanics", John Wiley and Sons, Inc., New York(1977a)

R. B. Bird, R. C. Armstrong, and O. Hassager, "Dynamics of Polymeric Liquids", Vol.2, "Kinetic Theory", John Wiley and Sons, Inc., New York(1977b)

G. D. Bizzel, and J. C. Slattery, "Non-Newtonian BoundaryLayer Flow", Chem. Engr. Sci., 17, 777(1962)

G. J. Borell, B. K. Kim, W. Ekhaml, T. E. Diller, and D. P. Telionis, "Pressure and Heat Transfer Measurements Around a Circular Cylinder in Pulsating Crossflows," Presented at 1984 ASME Fluid Engr. Conf., New Orleans, Feb. 1984. Also appeared in the Proceeding

B. D. Colman and W. Noll, Ann. Rev. Fluid Mech., Acad. Sci., 89, 672(1961)

G. A. Davis, and A. B. Ponter, "Turbulent Flow Properties of Dilute Polymeric Solutions," Nature, Vol. 212, 66(1966)

R. M. Debrule, and R. H. Sabersky, Int. J. Heat Mass Transfer, 17, 529(1974)

M. M. Denn and J. J. Roisman, "Rotational Stability and Measurements of Normal Stress Functions in Dilute Polymeric Solutions," A.I.Ch.E.J., 15, 459(1969)

G. L. Donohue, W. G. Tiederman, and M. M. Reischman, "Flow Visualization of the Near-Wall Region in a Drag Reducing Channel Flows", J. Fluid Mech., 56, 559(1972)

H. A. Dwyer, and W. J. McCroskey, "Oscillating Flow Over a Cylinder at Large Reynolds Number," J. Fluid Mech., 61, 753(1973)

H. L. Evans, "Laminar Boundary-Layer Theory," Addision-Wesly, 1968

C. A. Friehe, and W. H. Schwarz, "The Use of Pitot Static Tubes *and Hot-Film Anemometers in Dilute Polymeric Solutions," in C. W. Wells* ed., "Viscous Drag Reduction," Plenum Press, 281(1969)

C. D. Han, "Rheology in Polymer Processing," Academic Press, 1976

H. C. Hershey, and J. L. Zarkin, Ind. Eng. Chem., Fundamentals, 6, 381(1967)

M. Hiwada, K. Niwa, M. Kumada, and I. Mabuchi, "Effect of Tunnel Blockage on Local Mass Transfer From a Circular Cylinder in Crossflows", Heat Transfer-Japanese Research, 8, 37(1980)

J. W. Hoyt, "The Effect of Additives on Fluid Friction," ASME J., Basic Engr., 94, 258(1972)

J. W. Hoyt, and A. G. Fabula, "The Effect of Additive on Fluid Friction," Proc. 10th Int'l. Towing Tank Conf., Teddingtone, 1963

J. W. Hoyt, and A. G. Fabula, "The Effect of Additives on Fluid Friction," Pro. 5th Symp. on Naval Hydrodynamics, Bergen, Norway, ONR ACR-112, 947(1964)

H. Ishigaki, "Heat Transfer in a Periodic Boundary Layer near a Two-Dimensional Stagnation Point," J. Fluid Mech., 60, 401(1972)

J. Kestin and R. T. Wood, "The Influence of Turbulence on Mass Transfer from Cylinder," J. Heat Transfer, 321(1971)

B. K. Kim, G. J. Borell, M. S. Cramer, T. E. Diller, and D. P. Telionis, "Pulsating Flow and Heat Transfer Over a Circular Cylinder," Proc. Symp. on Nonlinear Problems in Energy Engr., DOE Conf-830313, 96(1983)

B. K. Kim, D. VandenBrink, M. S. Cramer, D. P. Telionis,

"Unsteady Heat Convection Over Circular Cylinders," presented at 1984 ASME-AIChE National Heat Transfer Conf., Niagara, August, 1984 Paper # 84-HT-100

T. G. Lang and H. V. L. Patrick, "Drag of Blunt Bodies in Polymer Solutions," ASME preprint 66-WA/FE-33, 1966

M. J. Lighthill, "The Response of Laminar Skin Friction and Heat Transfer to Fluctuations in the Stream Velocity," Proc. Roy. Soc. A 224, 1(1954)

C. W. Lowery, and R. I. Vachon, "The Effect of Turbulence on Heat Transfer for Heated Cylinder," Int'l. J. Heat Mass Transfer, 18, 1229(1975)

A. V. Luicov, Z. P. Schulman, and B. M. Berkovsky, "Heat and Mass Transfer in a Boundary-Layer of Non-Newtonian Fluids," Third Int'l Heat Transfer Conf., Chicago, Paper#38

J. L. Lumley, "Drag Reduction by Additives," Ann Rev. Fluid Mech., 1, 366(1969)

J. L. Lumley, "Drag Reduction in Turbulent Flow by Polymer Additive," J. Polymer Sci., Macromol. Rev., 7, 263(1973)

J. L. Lumley, "Two Phase and Non-Newtonian Flow", in Turbulence ed. P. Bradshaw, pp. 290-324, New York: Springer. 335pp

D. J. Maull, and R. A. Young, "Vortex Shedding from Bluff Bodies in a Shear Flow," J. Fluid Mech., 60, 619(1973)

A. B. Metzner, and M. G. Park, J. Fluid Mech., 20, 291(1964)

S. Middleman, "Fundamentals of Polymer Processing," McGraw-Hill, New York(1977)

T. Mizushina, and H. Usui, "Reduction of Eddy Diffusion for Momentum and Heat in Viscoelastic Fluid in a Circular Tube," Phys. Fluid, Suppl., 20, 222(1977)

W. A. Meyer, "A Correlation of the Frictional Characteristics for Turbulent Flow of Dilute Viscoelastic Non-Newtonian Fluids in Pipe Flows, A.I.Ch.E.J., 12, 522(1966)

T. Okamoto and M. Yagita, "The Experimental Investigation on the Flow Past a Circular Cylinder of Finite Length Placed Normal to the Plane Surface in a Uniform Flow Stream," Bulletin JSME 16, 805(1973)

G. K. Patterson, J. L. Zakin, and J. M. Rodriguez, "Drag

Reduction: Polymer Solutions, Soap Solutions and Solid Particle Suspension in Pipe Flows," Ind. Eng. Chem., 61, 22(1969)

M. M. Reischman, and W. G. Tiederman, "Laser-Doppler Anemometer Measurements in Drag Reducing Channel Flows," J. Fluid Mech., 70, 369(1975)

A. Roshko, "Experiments on the Flow Past a Circular Cylinder at very High Reynolds Numbers," J. Fluid Mech., 10, 345(1961)

N. Rott, "Unsteady Viscous Flow in the Vicinity of a Stagnation Point," Quart. J. Appl. Math., 13, 444(1956)

H. Rubin and C. Eleta, "Stability of Couette Flow of Dilute Polymer Solutions," Phys. Fluid, 9, 1929(1966)

M. J. Rudd, "Measurements Made on Drag Reducing Solution with a Laser Velocimeter", Nature, 224, 587(1969)

W. Z. Sadeh, H. J. Brauer, and J. A. Garrison, "Visualization Study of Vorticity Amplification in Stagnation Flow," Technical Report at Colorado State University, CSU-1-PU, October, 1977

H. Schlichting, "Boundary-Layer Theory,,7th ed., McGraw-Hill, New-York, 1979

O. Scrivener, "A Contribution on Modifications of Velocity Profiles and Turbulence Structure in a Drag Reducing Solution," St Johns College, Cambridge, ed. N. G. Coles, C6-70, 1974

M.J.Shah, A.Acrivos and E.E.Petersen, "Heat Transfer from a Circular Cylinder to a Power-Law Non-Newtonian Fluids," A.I.Ch.E.J., 8, 542(1962)

K. A. Smith, E. W. Merrill, H. S. Mickley, and P. S. Virk, "Anomalous Pitot Tube and Hot Film Measurements in Dilute Polymeric Solutions," Chem. Engr. Sci., 22, 619(1967)

H. H. Sogin, and V. S. Subramanian, "Local Mass Transfer from Circular Cylinders in Crossflow," Trans. ASME., J. Heat Transfer, 83, 483(1961)

W. R. Sears, and D. P. Telionis, "Boundary Layer Separation in Unsteady Flow," SIAM J. Appl. Math., 28, 215(1975)

A. Tabakoli, B. K. Kim, G. J. Borell, T. E. Diller, and and D. P. Telionis, "Design and Evaluation of a Pulsating Flow Wind Tunnel," VPI-E-83-41

Z. Tadmor, and C.G.Gogos, "Principles of Polymer Processing,"

John Wiley and Sons, Inc., New York(1979)

D. P. Telionis, D. Mathioulakis, and B. K. Kim, "The ESM Water Tunnel Calibrations," Reported at VPI & SU, spring, 1984

D. P. Telionis, D. T. Tsahalis, and M. J. Werle, "Numerical Investigation of Unsteady Boundary-Layer Separation," Phys. Fluids., 16, 968(1973)

D. P. Telionis, "Unsteady Viscous Flow", Springer-Verlag, New York, 1981

D. P. Telionis, and D. T. Tsahalis, "Impulsively Started Flow Over a Cylinder," Acta. Astron., 1, 1487(1974)

D. P. Telionis and M. J. Werle, "Boundary-Layer Separation From Moving Boundaries," J. Appl. Mech., 40, 369(1973)

B. A. Toms, "Some Observations on the Flow of Linear Polymer Solutions Through Straight Tubes at Large Reynolds Numbers," Proc. Int'l Cong on Rheology, Vol II, North Holland Publishing Co., Amsterdam, 135(1949)

K. Takahashi, and M. Maeda, "Experimental Study on Heat Transfer from a Cylinder Submerged in a Non-Newtonian Fluid," Proc. 6th Int'l Heat Transfer Conference, New-York, 335(1979)

R. L. Varty, and I. G. Curie, "Measurements near a Laminar Separation Point," J. Fluid Mech., 138, 1(1984)

P. S. Virk, "Drag Reduction in Rough Pipes", J. Fluid. Mech., 45, 225(1971)

P. S. Virk, "Drag Reduction Fundamental," A.I.Ch.E. J. 21, 625(1975)

C. B. Wang, "Correlation of the Friction Factor for Turbulent Pipe Flows of Dilute Polymer Solution", Ind. Eng. Chem., Fundamental, 11, 546(1972)

C. S. Wells, and J. G. Spangler, Phys. Fluids, 10, 1890(1976)

M. Walsh, "On the Turbulent Flow of Dilute Polymeric Solutions," Ph. D. Thesis, California Institute of Technology, 1967

S. C. Welle, "Similar Solution of the Boundary-Layer Equations for Purely Viscous Non-Newtonian Fluids", NASA TN D-2262(1964)

M. J. Werle, and R. T. Davis, "Incompressible Laminar Boundary Layers on a Parabola at an Angle of Attack: A Study of the Separation

Point,"J. Appl. Mech., 39, 7(1978)

G. S. West, and C. J. Apelt, "The Effect of Tunnel Blockage and Aspect Ratio on the Mean Flow Past a Circular Cylinder With Reynolds Numbers Between 10,000 and 100,000," J. Fluid Mech., 114, 361(1982)

A. White, "Some Observations on the Flow Characteristics of Certain Dilute Macromolecular Solutions," in C. W. Wells ed., "Viscous Drag Reduction," Plenum Press, 297(1969)

a. White, "Effect of Polymer Additive on Boundary Layer Separation and Drag of Submerged Bodied," Nature, 211, 1309(1966)

J. C. Wolf, and A. A. Szewczyk, "Laminar Heat Transfer to Power-Model Non-Newtonian Fluids from Arbitrary Cylinders", Third Int'l Heat Transfer Conf., Chicago, Paper#37

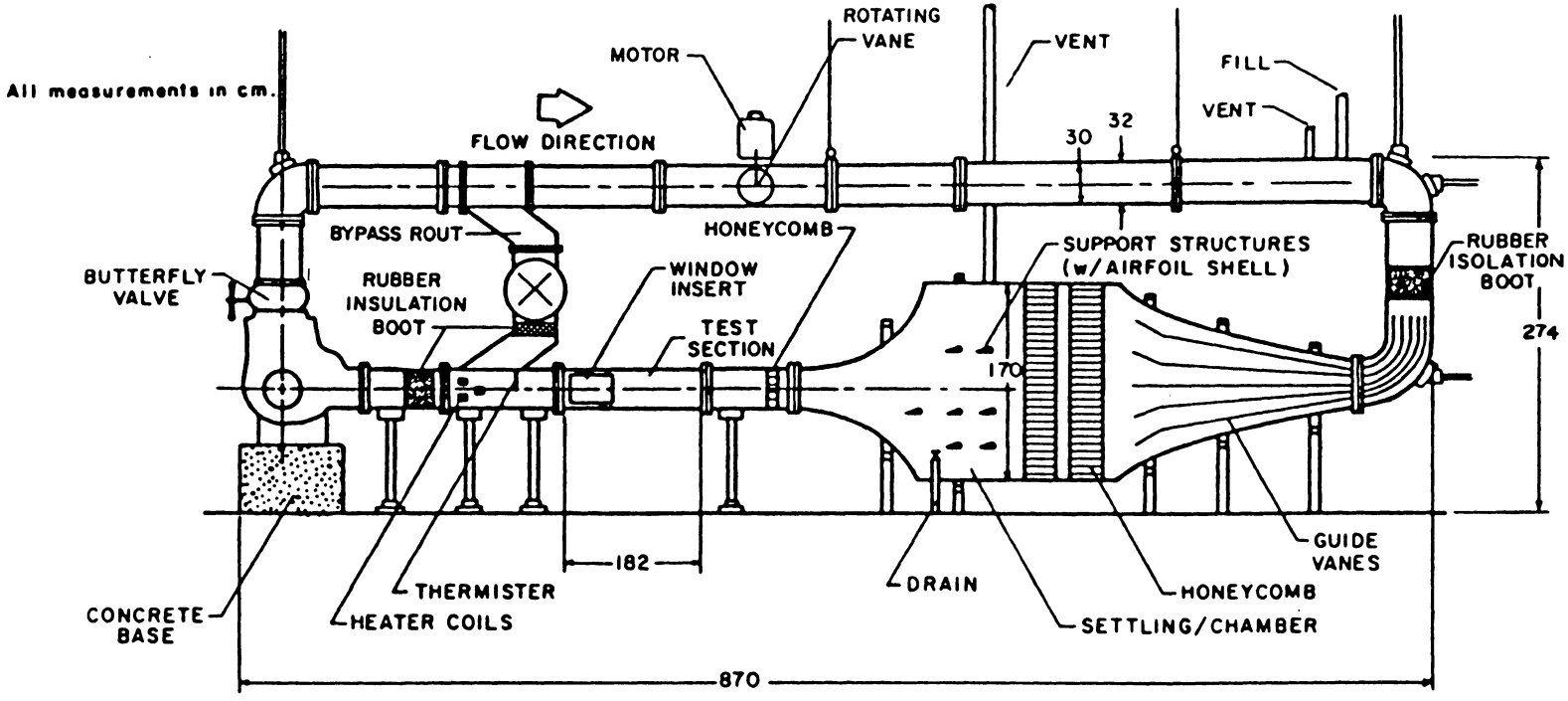

Figure 1.1 Schematic of water tunnel

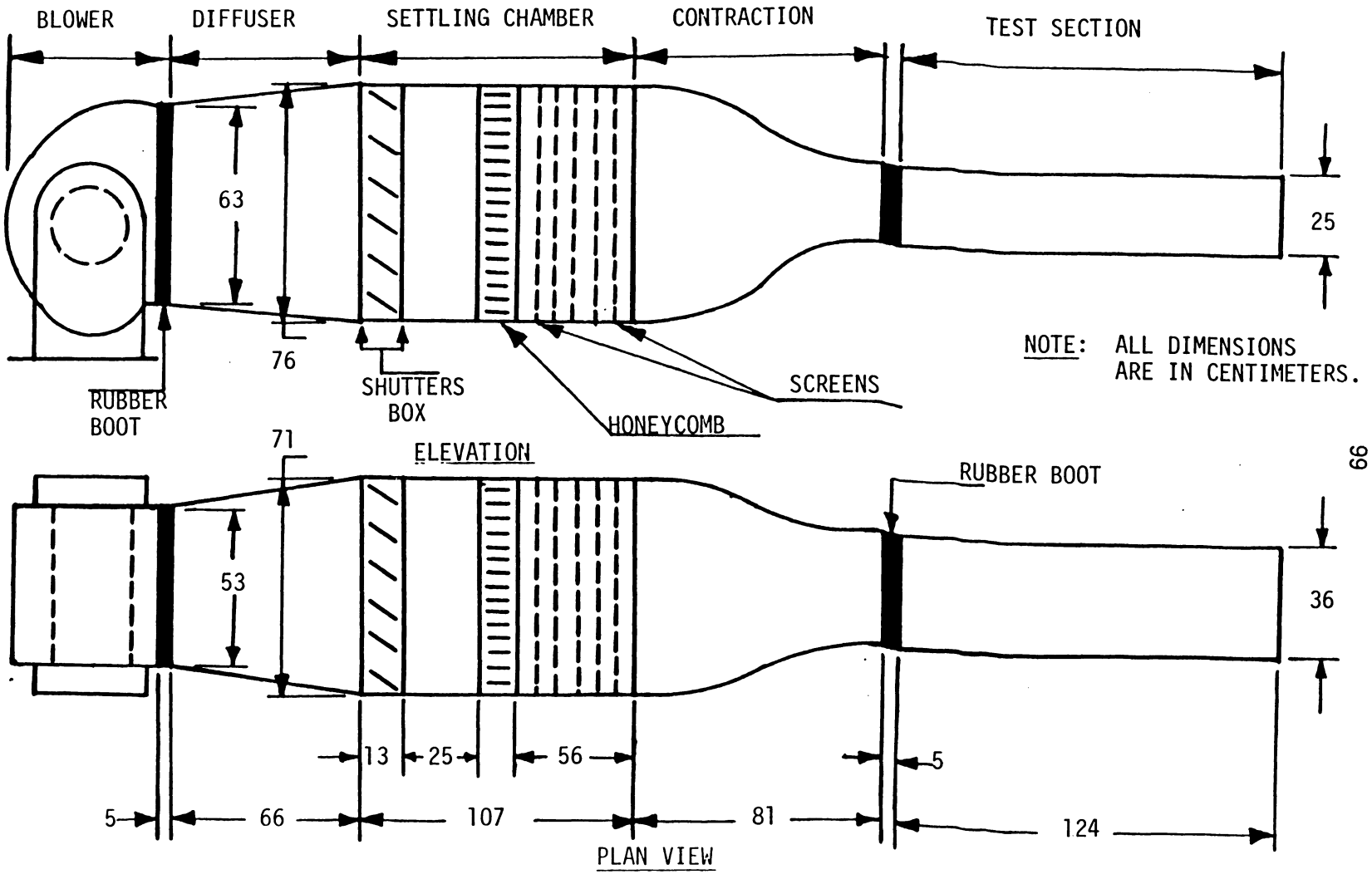

Figure 1.2 Schematic of wind tunnel

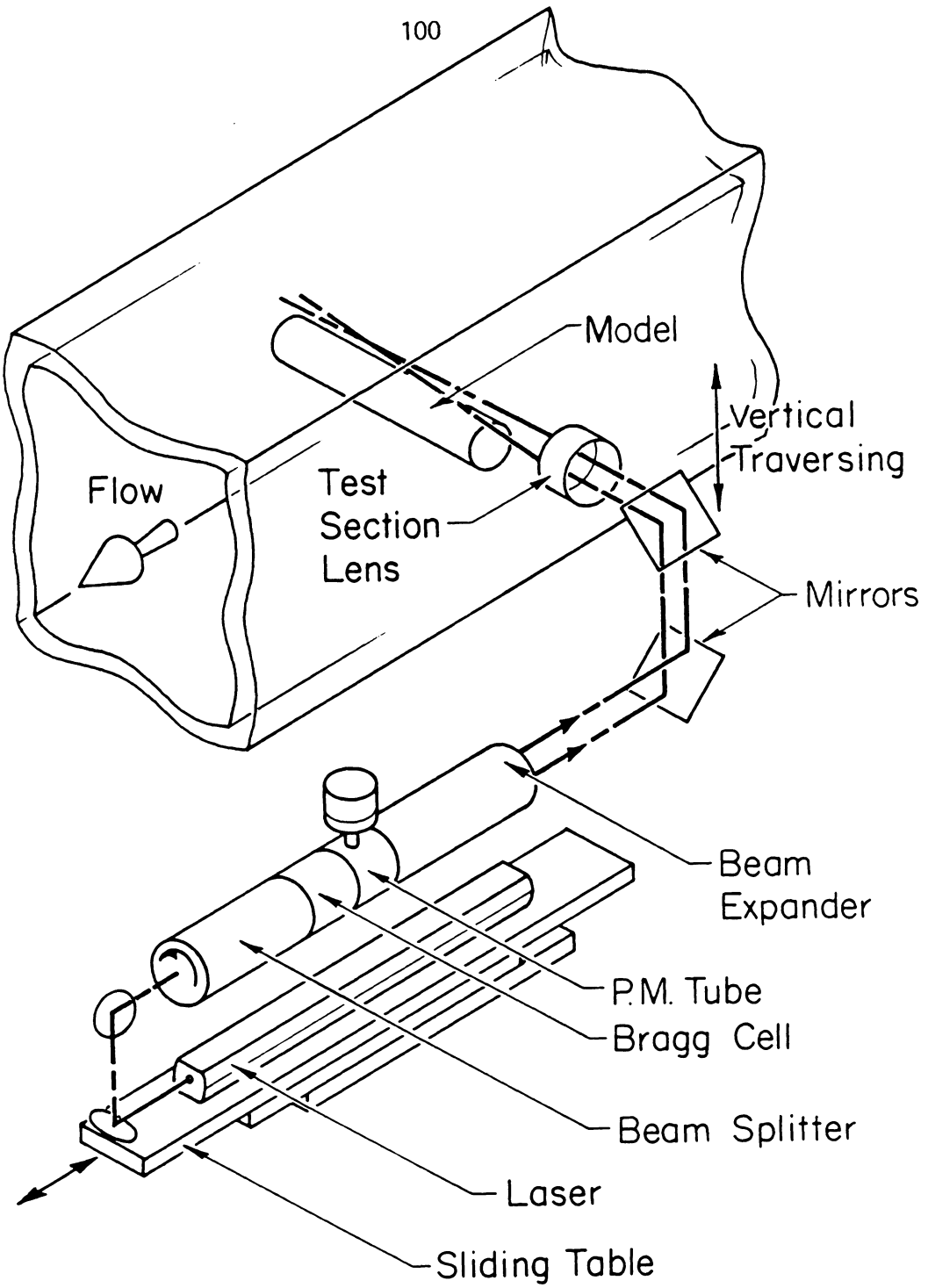

Figure 1.3 The optical arrangement of TSI anemometry

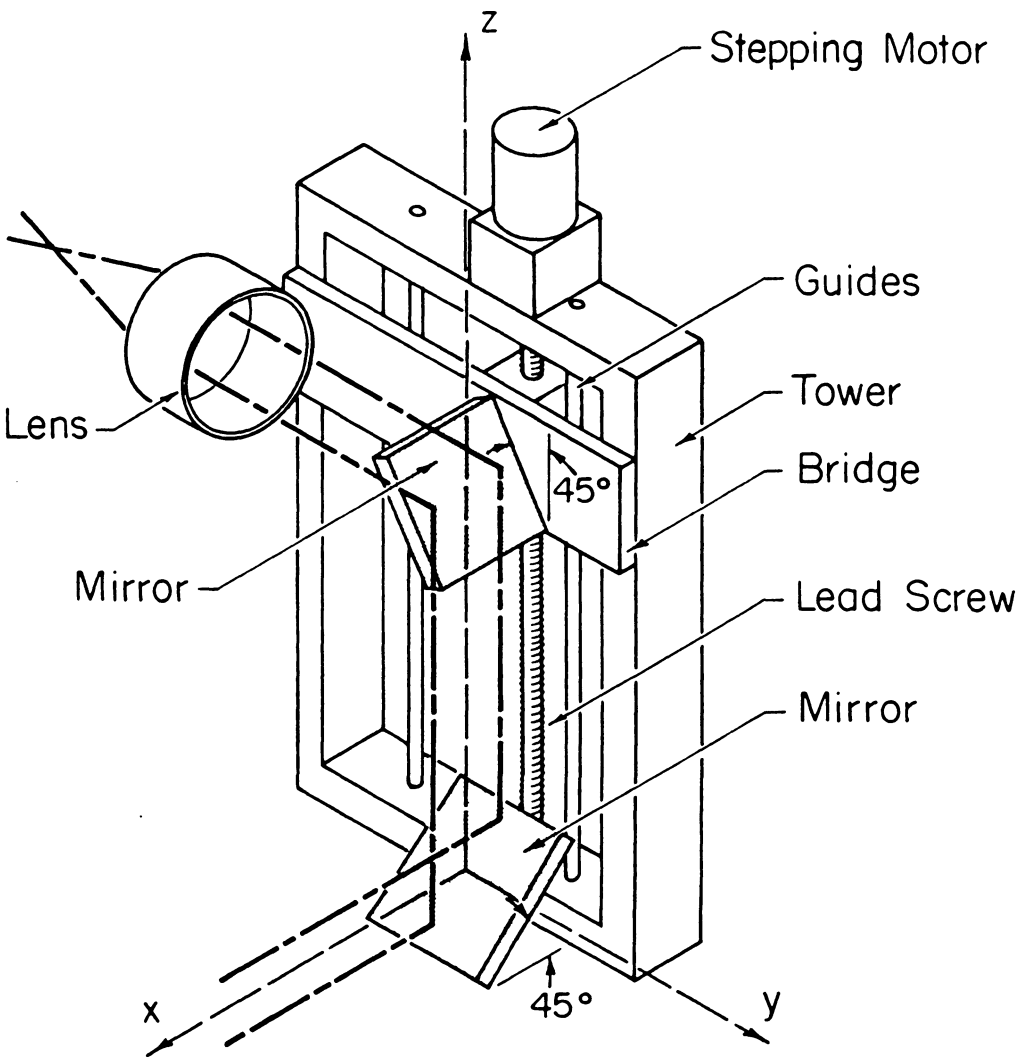

Figure 1.4 Traversing mechanism

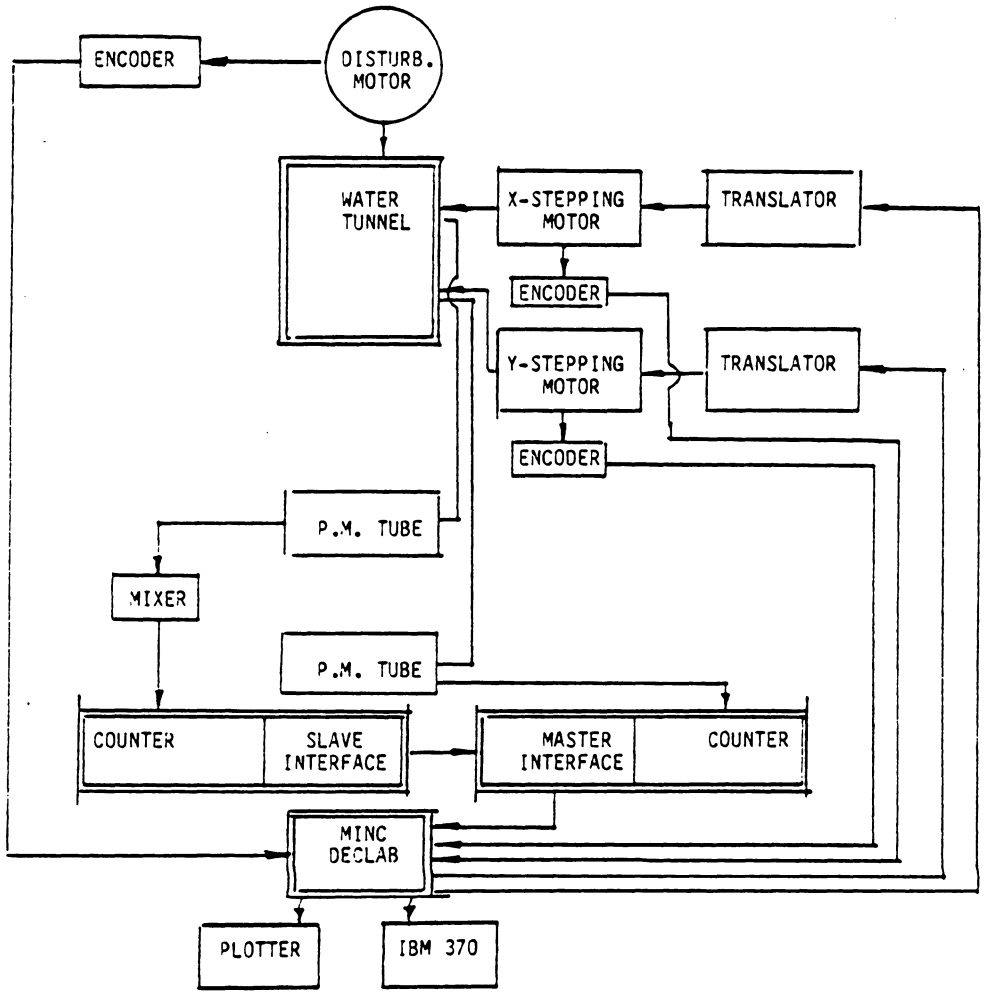

Figure 1.5 The online data acquisition system

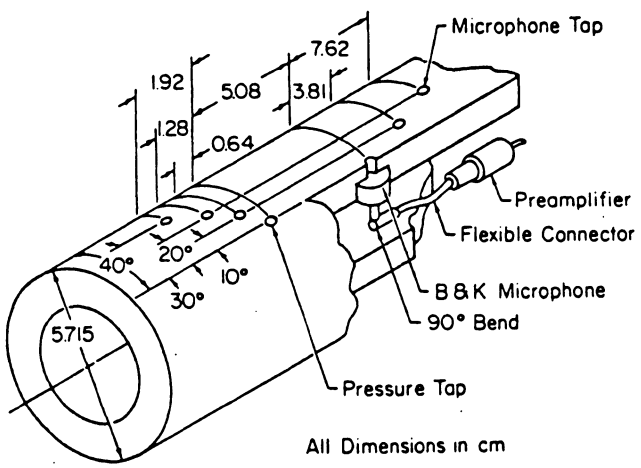

Figure 1.6 Test cylinder for pressure measurement

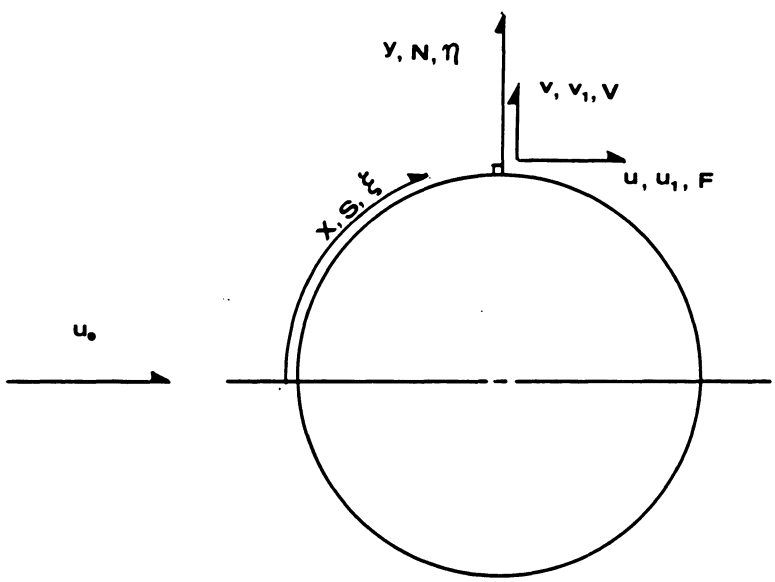

Figure 2.1 Boundary-layer coordinate system

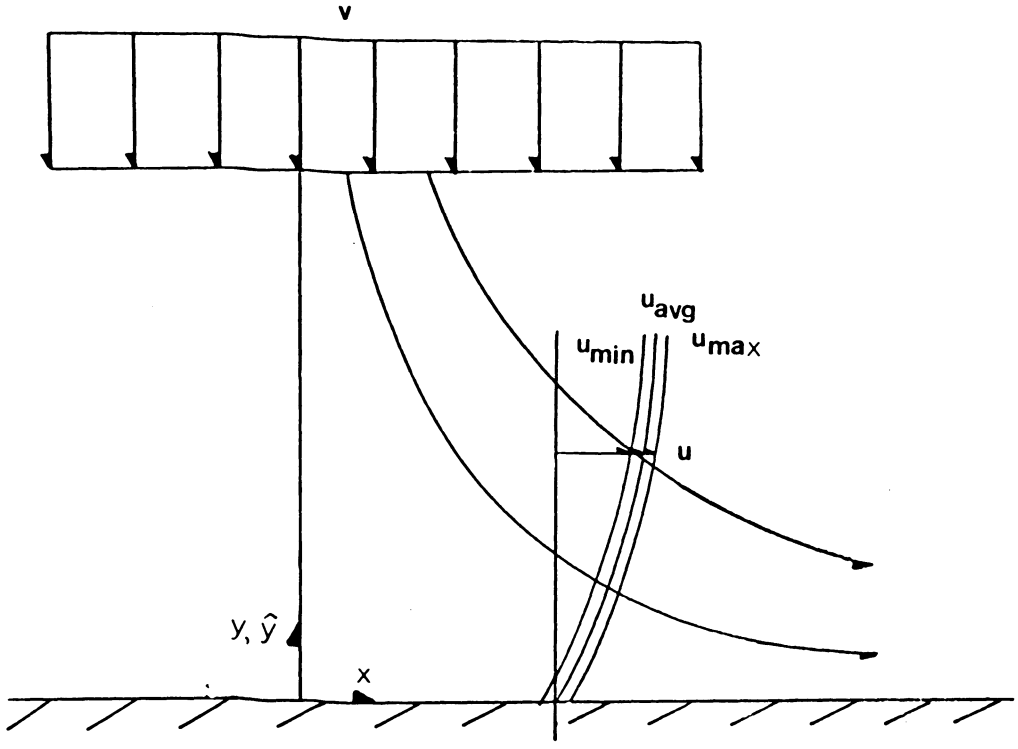

Figure 3.1 Plane stagnation flow

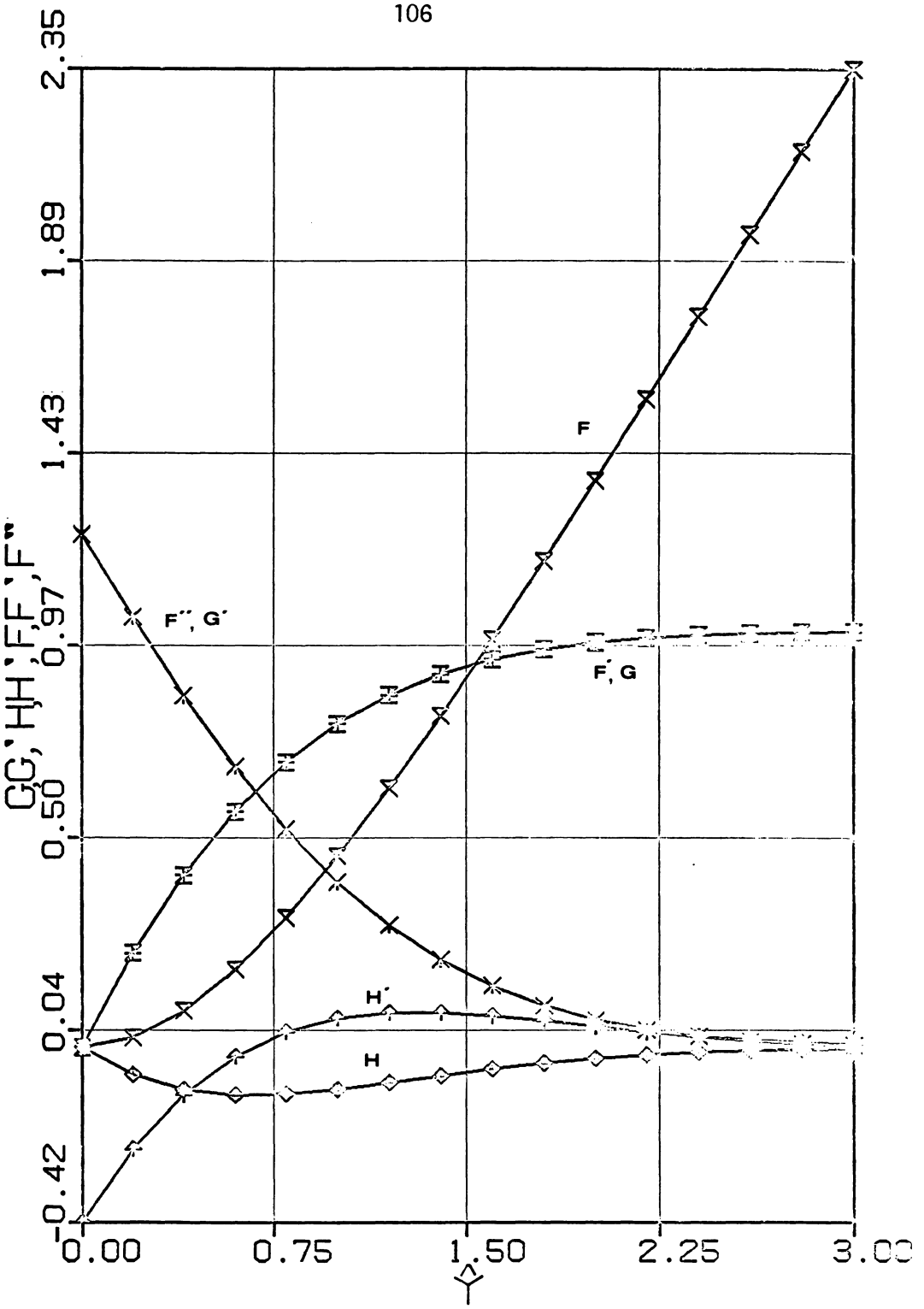

Figure 3.2 Steady and quasi-steady velocity profiles

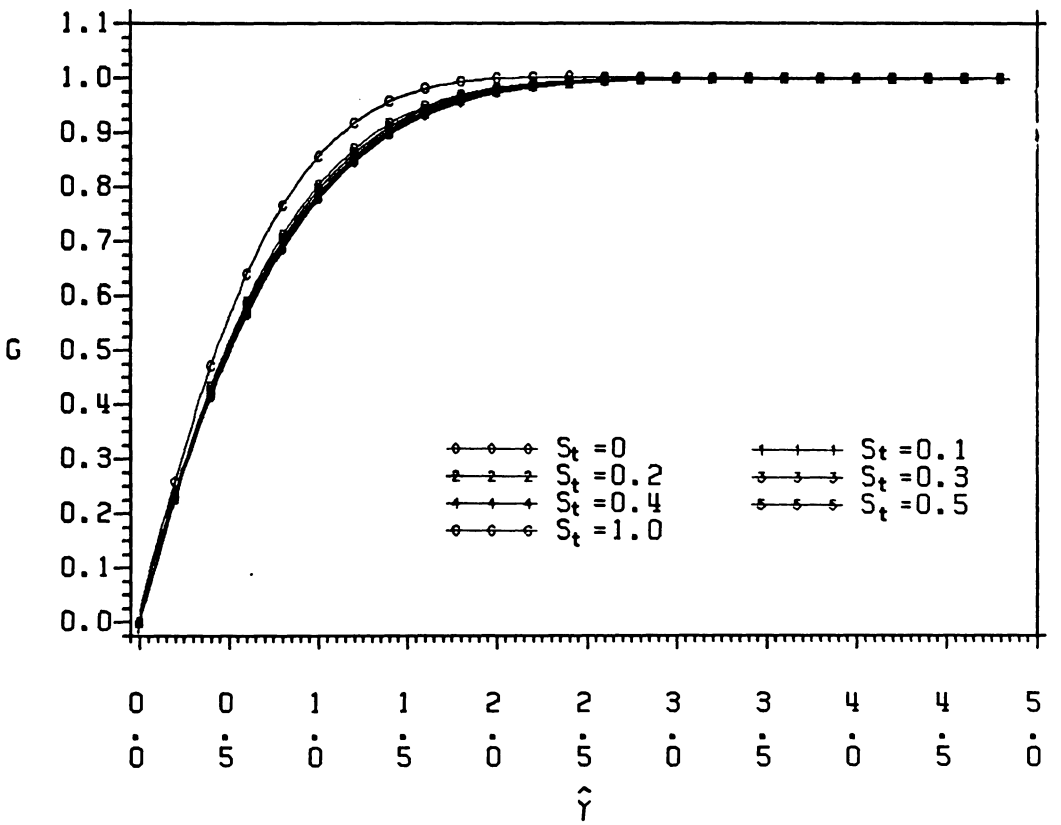

Figure 3.3 G profiles

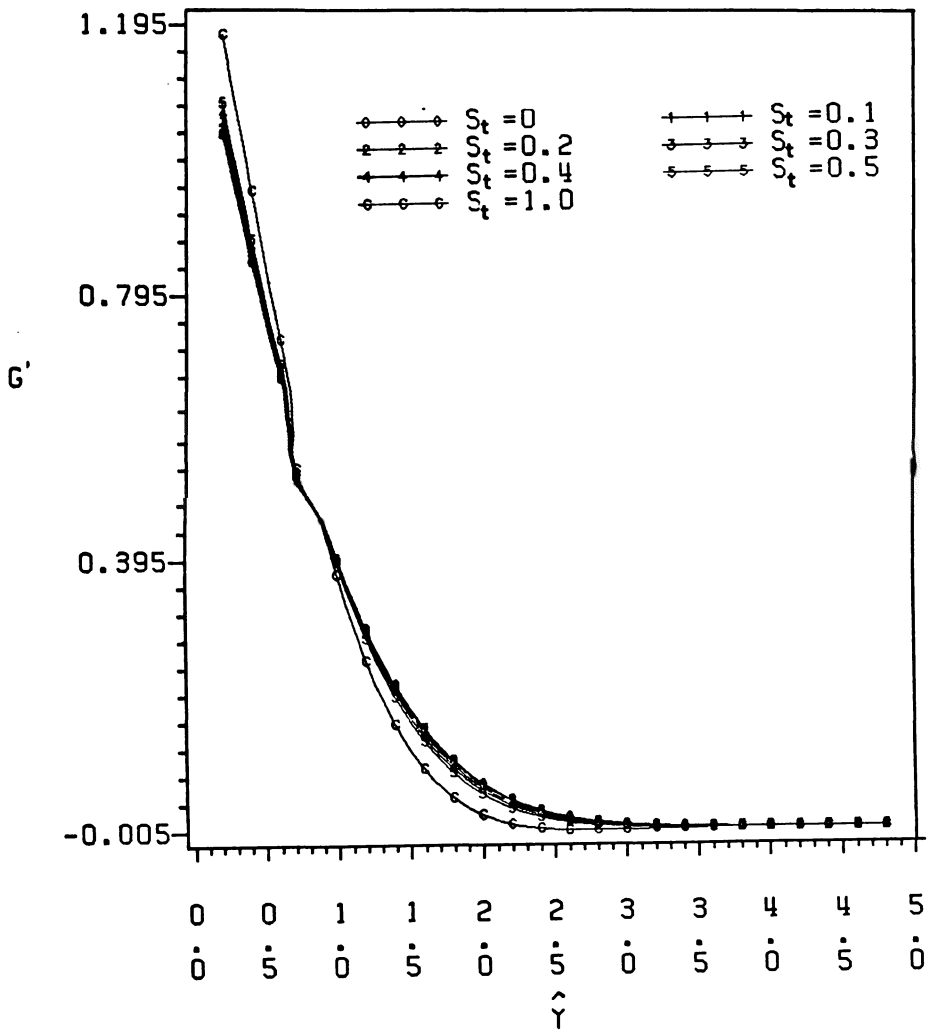

Figure 3.4 G' profiles

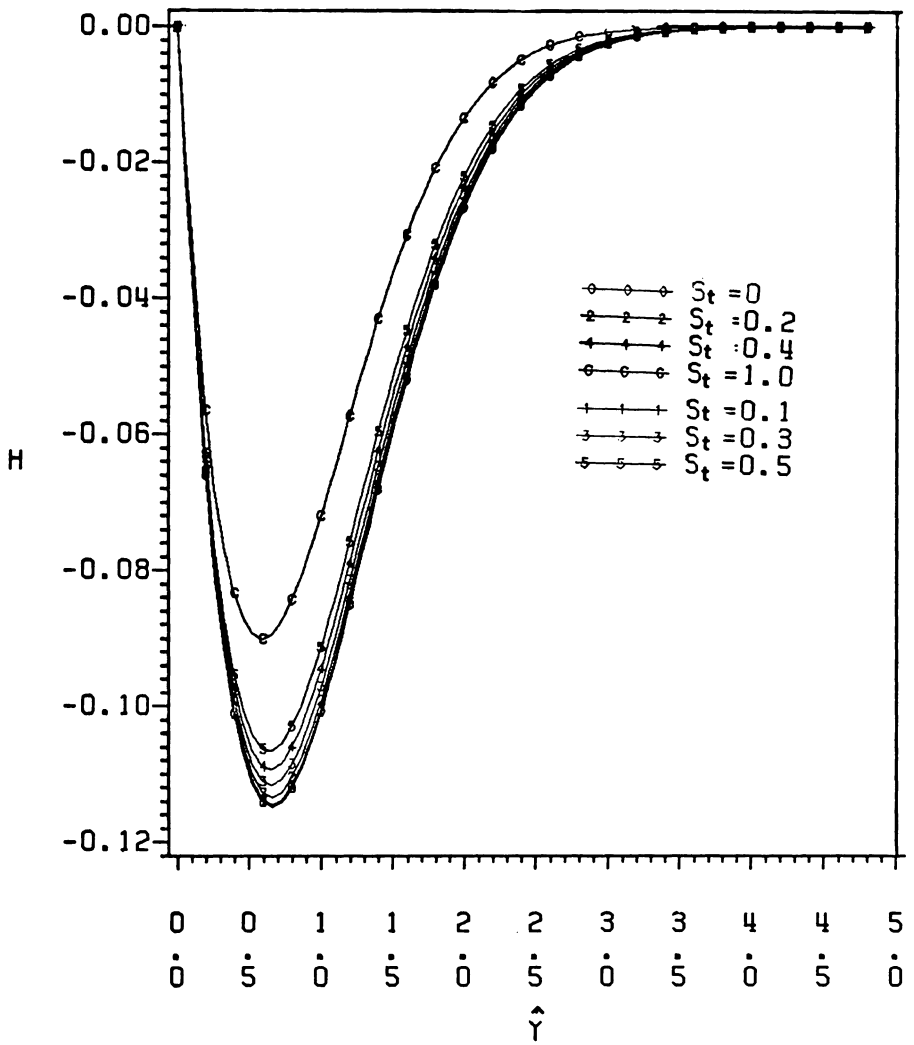

Figure 3.5 H profiles

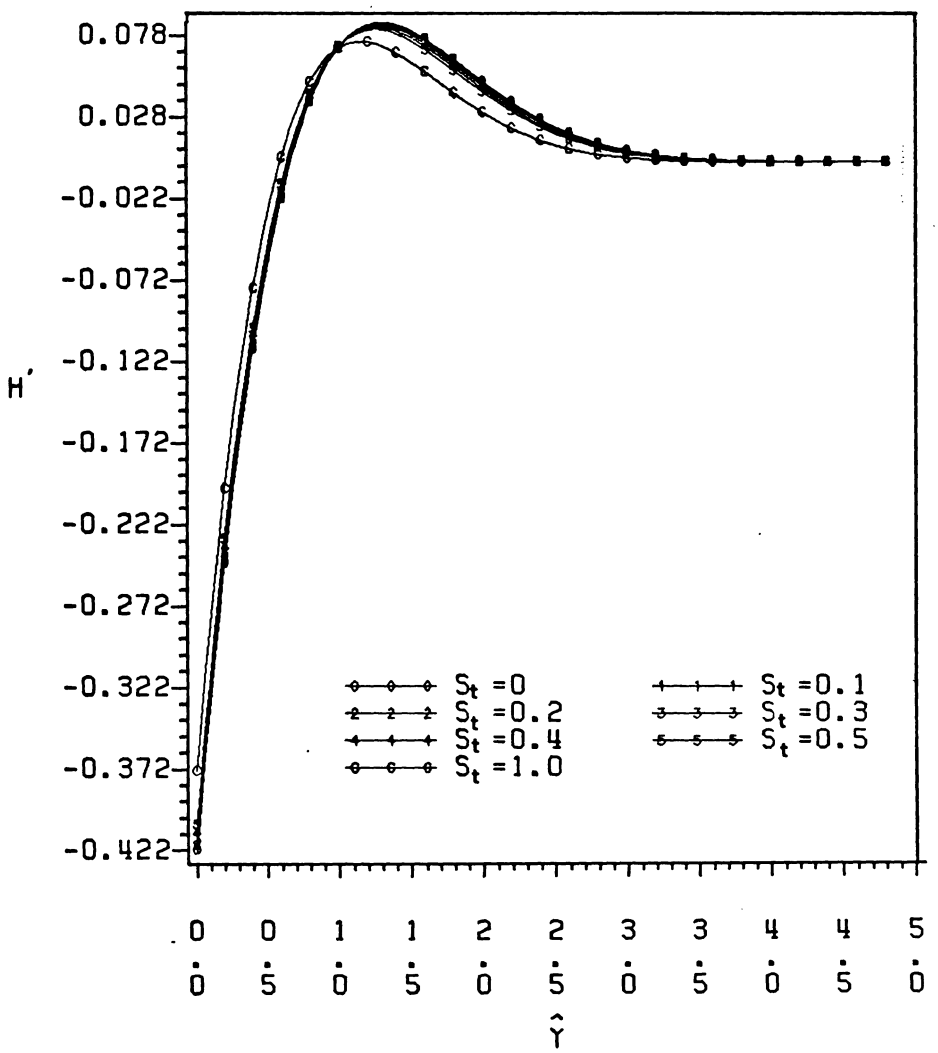

Figure 3.6 H' profiles

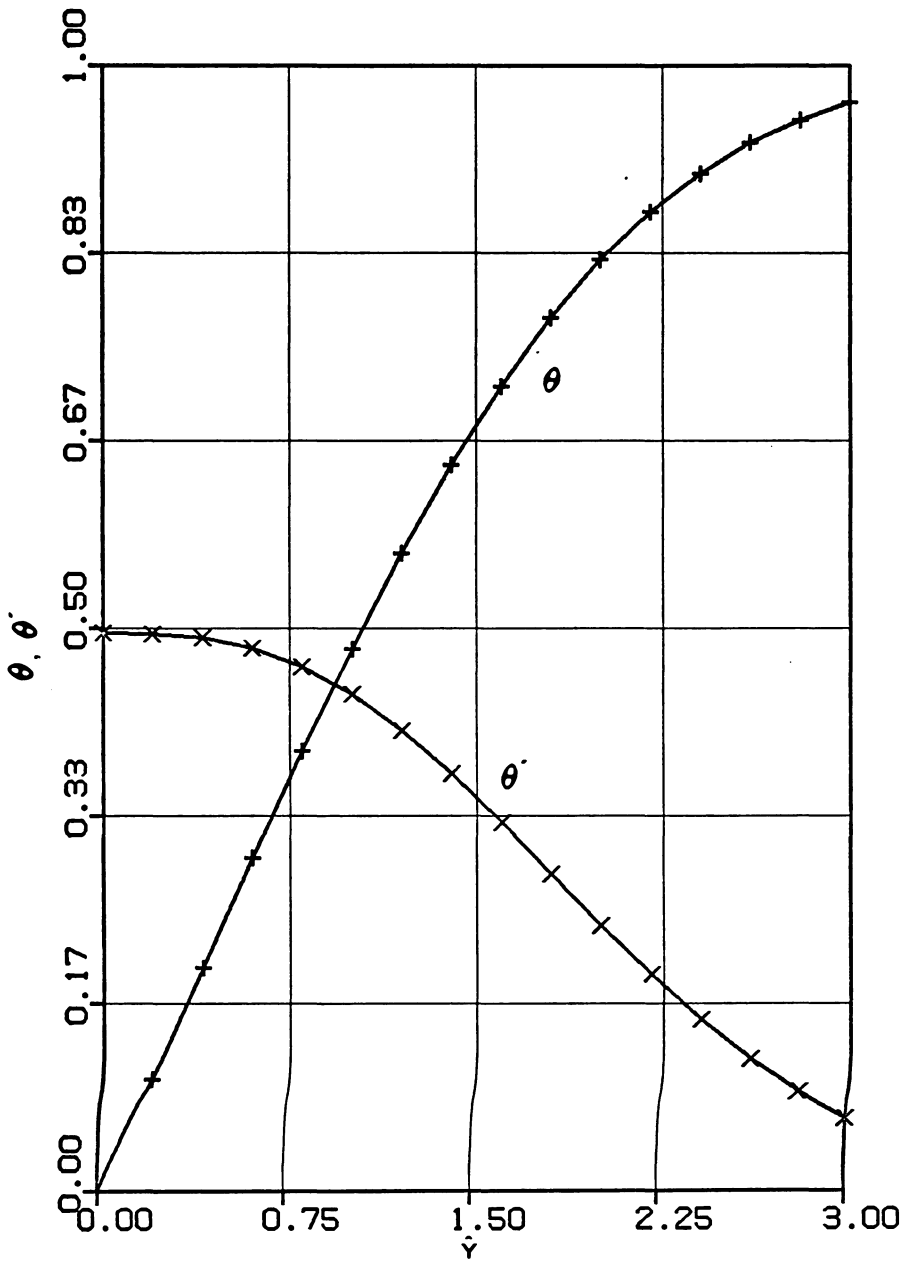

Figure 3.7 Steady temperature profile

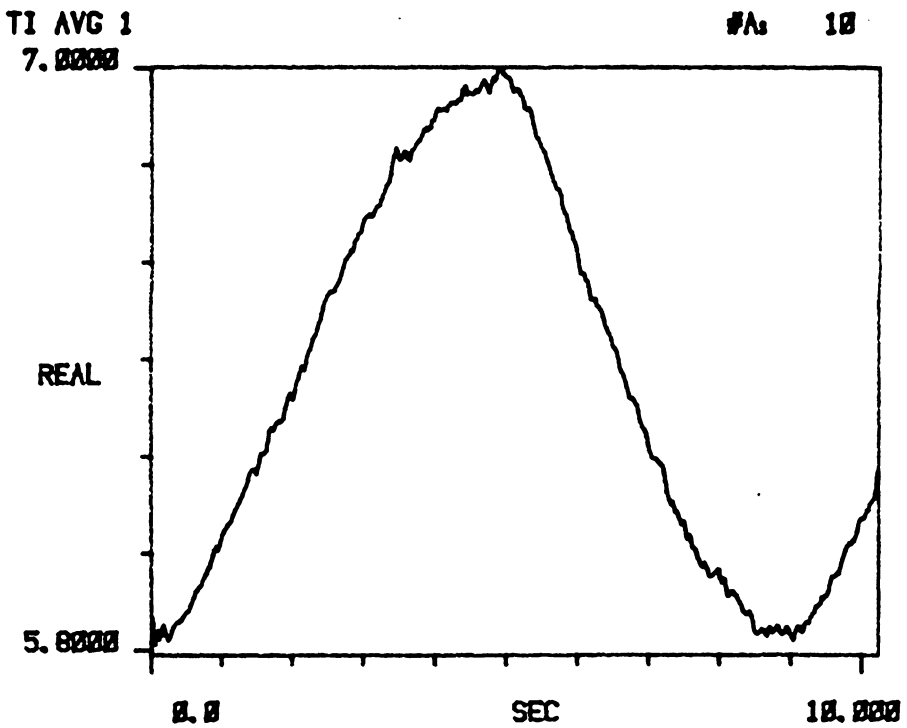

Figure 4.1 Typical velocity waveform obtained in the water tunnel (u_0 = 25 cm/s)

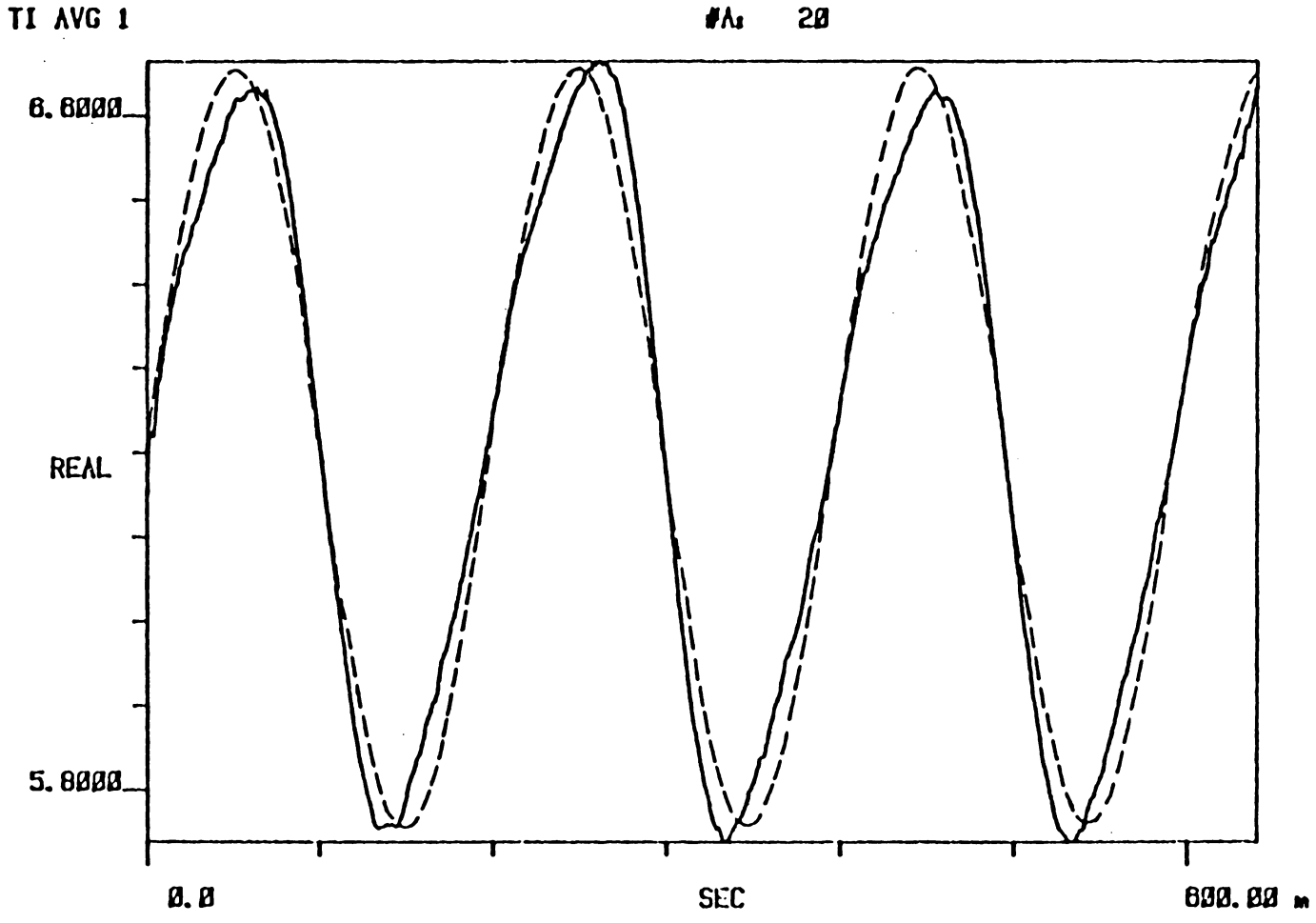

Figure 4.2a Typical velocity waveform obtained in the wind tunnel(u_0 = 17 m/s)

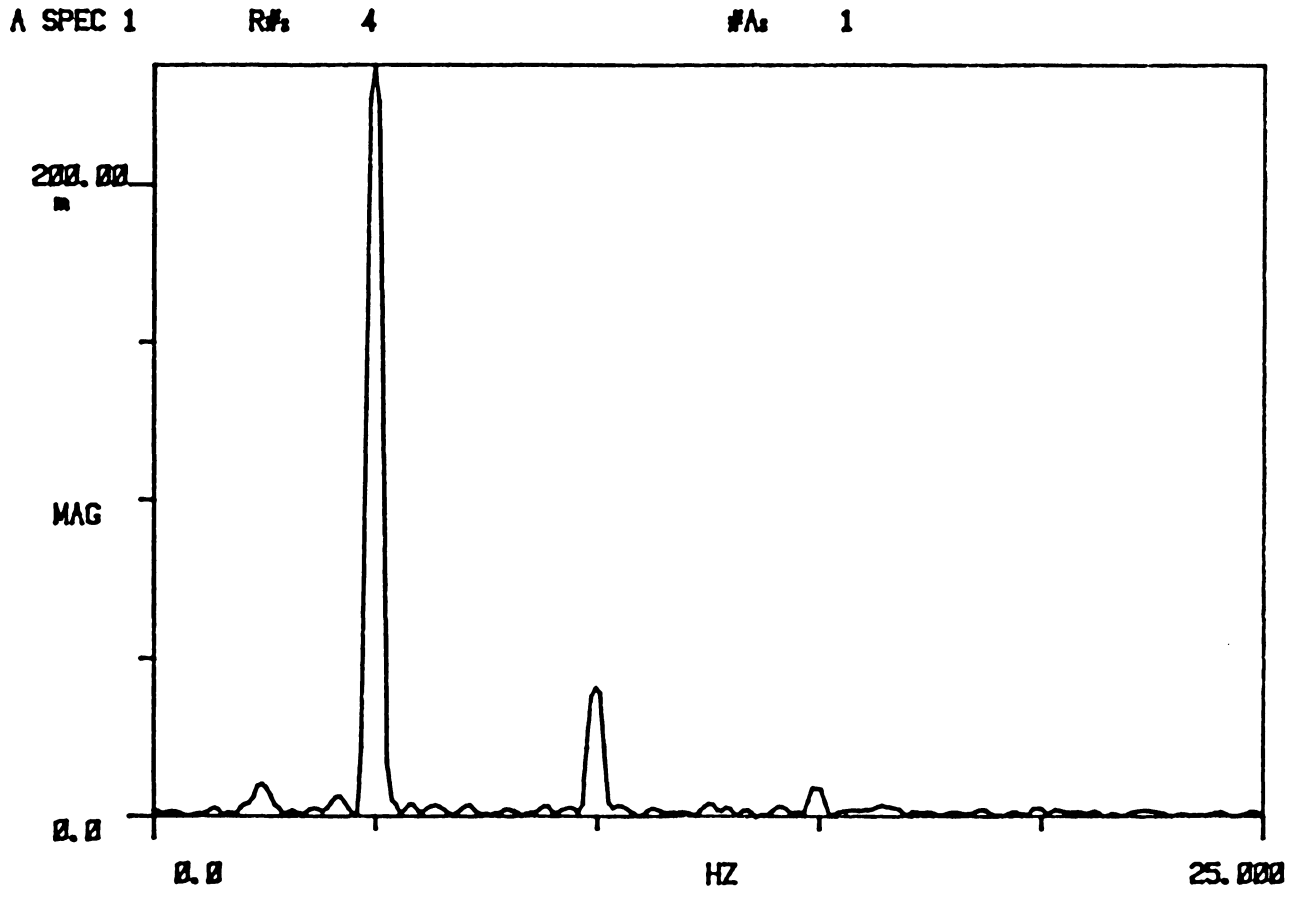

Figure 4.2b The corresponding frequency spectrum of Fig. 4.2a

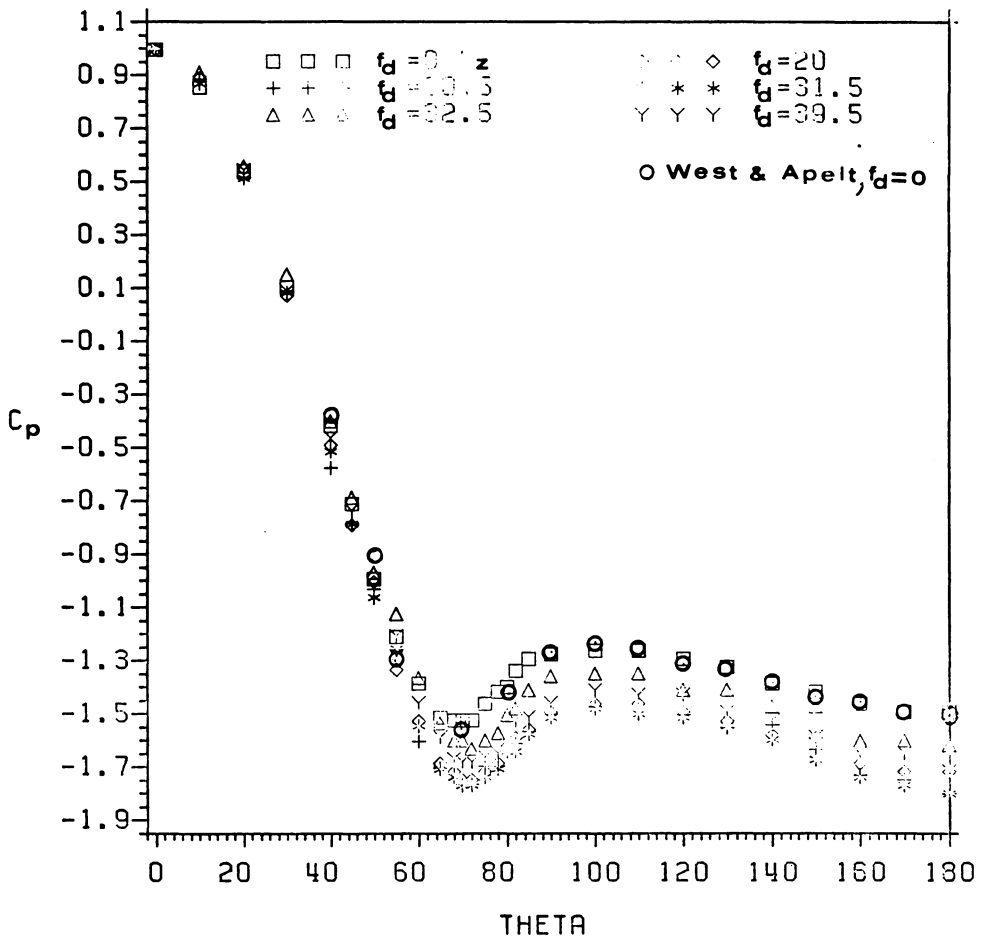

Figure 4.3 The time-mean pressure distribution around a circular cylinder with various driving frequencies at Re=36,600

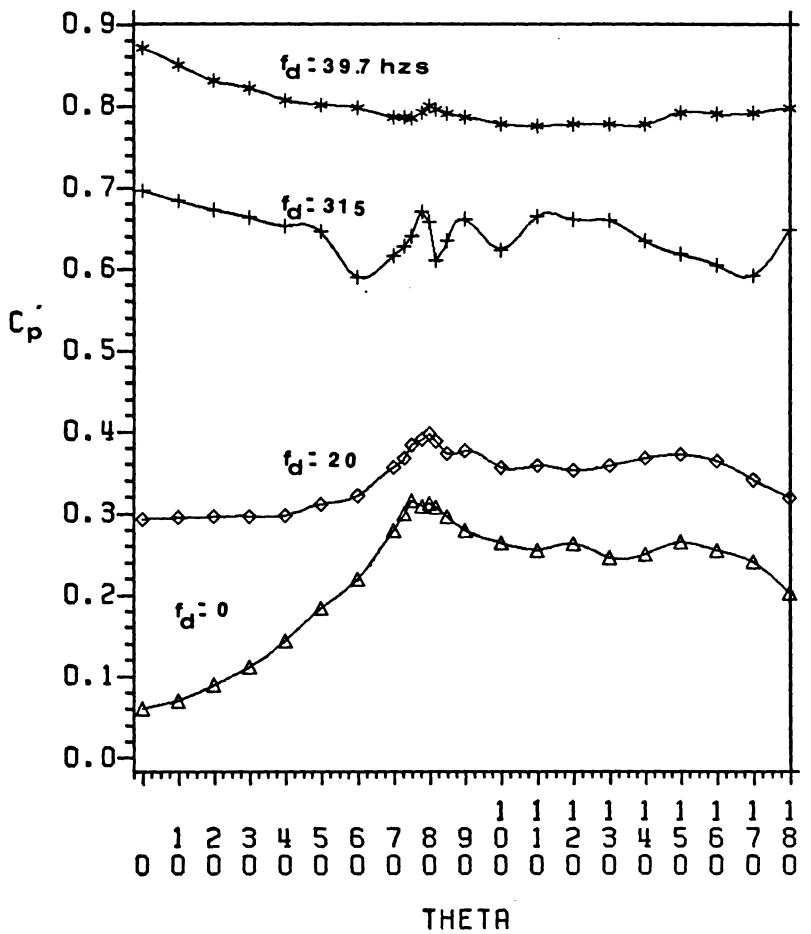

Figure 4.4 The rms pressure distribution around a circular cylinder with various driving frequencies at Re=36,600

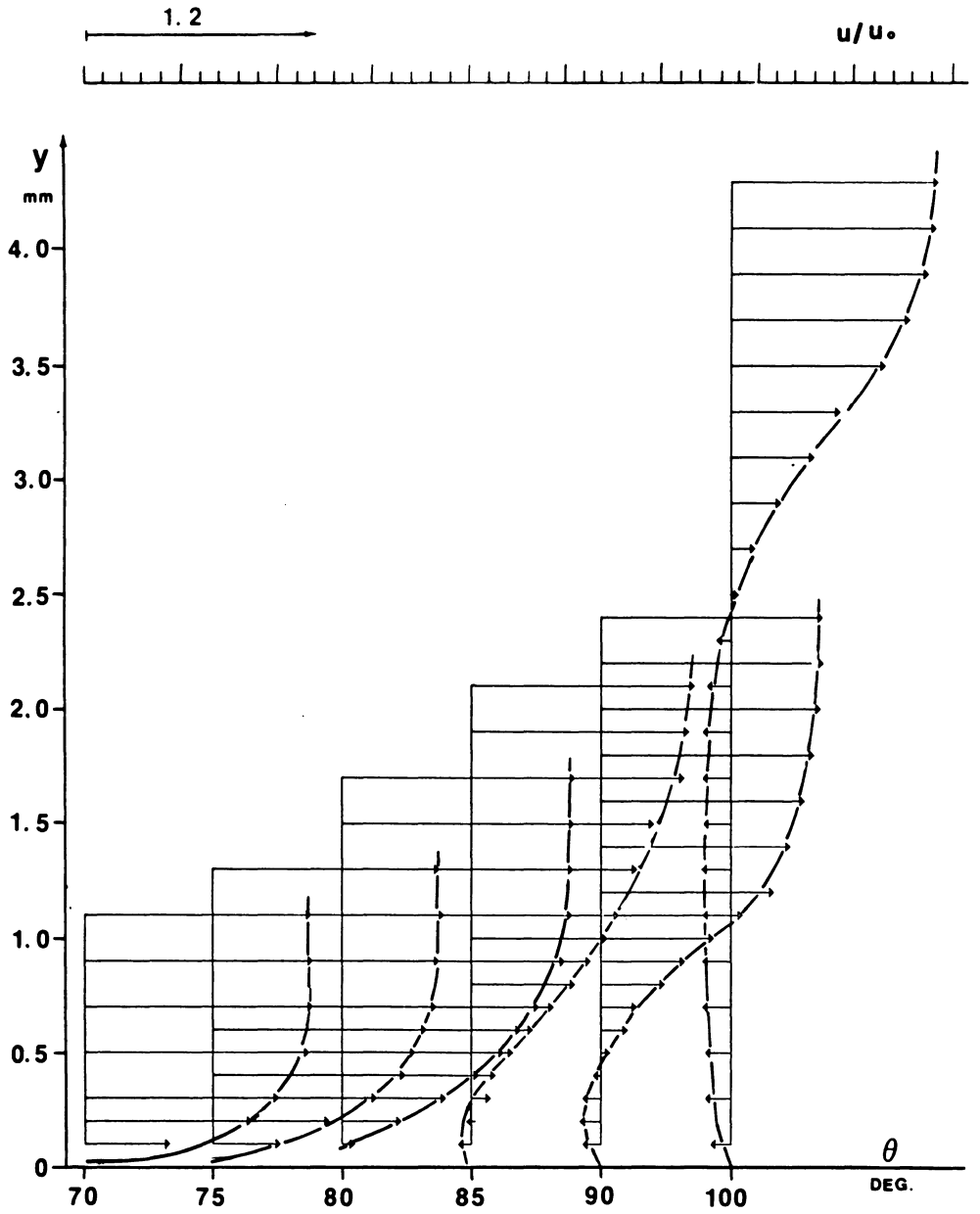

Figure 4.5a u -velocity profiles over a wide angular positions (self-induced oscillatory flow, u_0 =18 cm/sec)

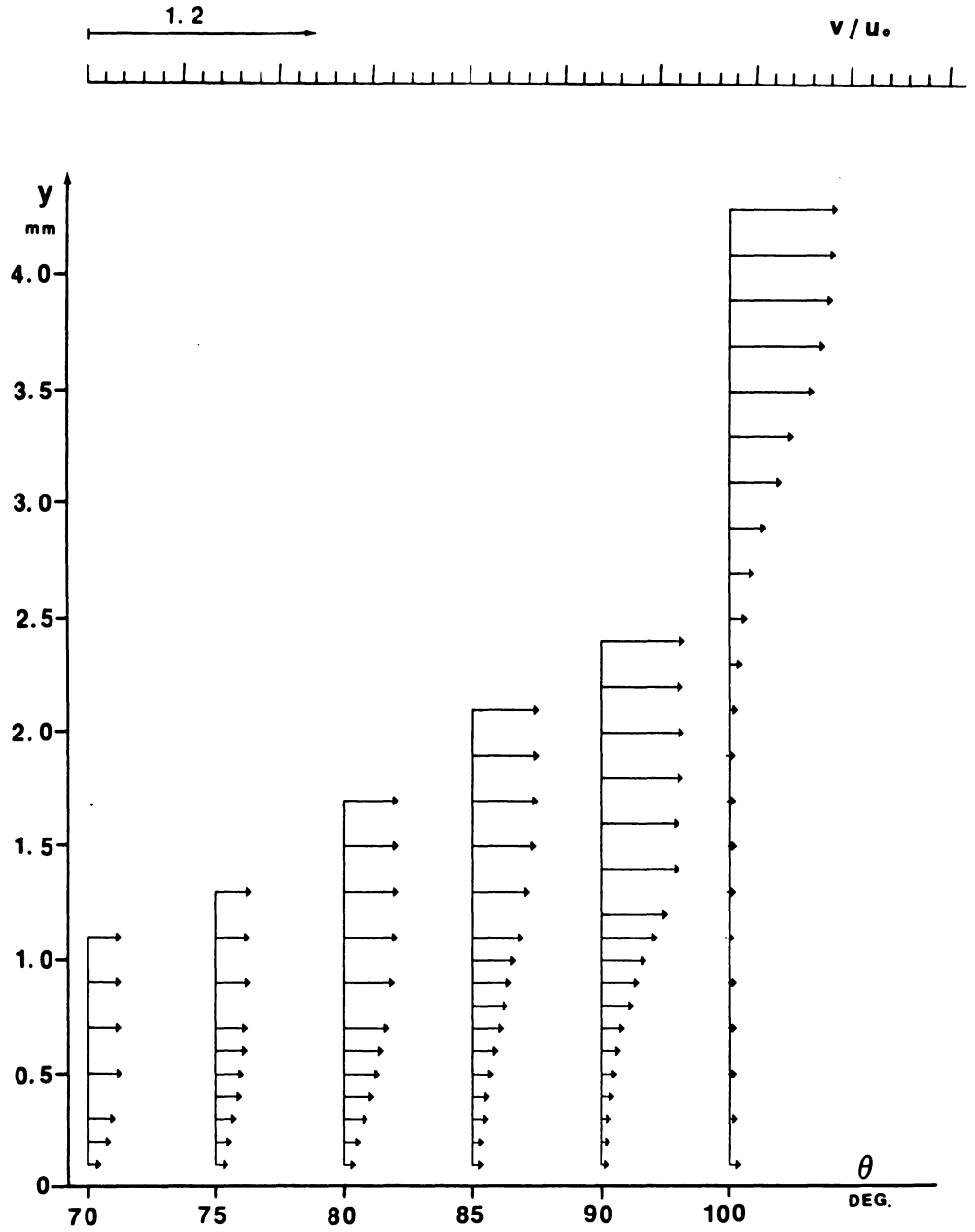

Figure 4.5b v -velocity profiles over a wide angular positions (self-induced oscillatory flow, u_0 =18 cm/sec)

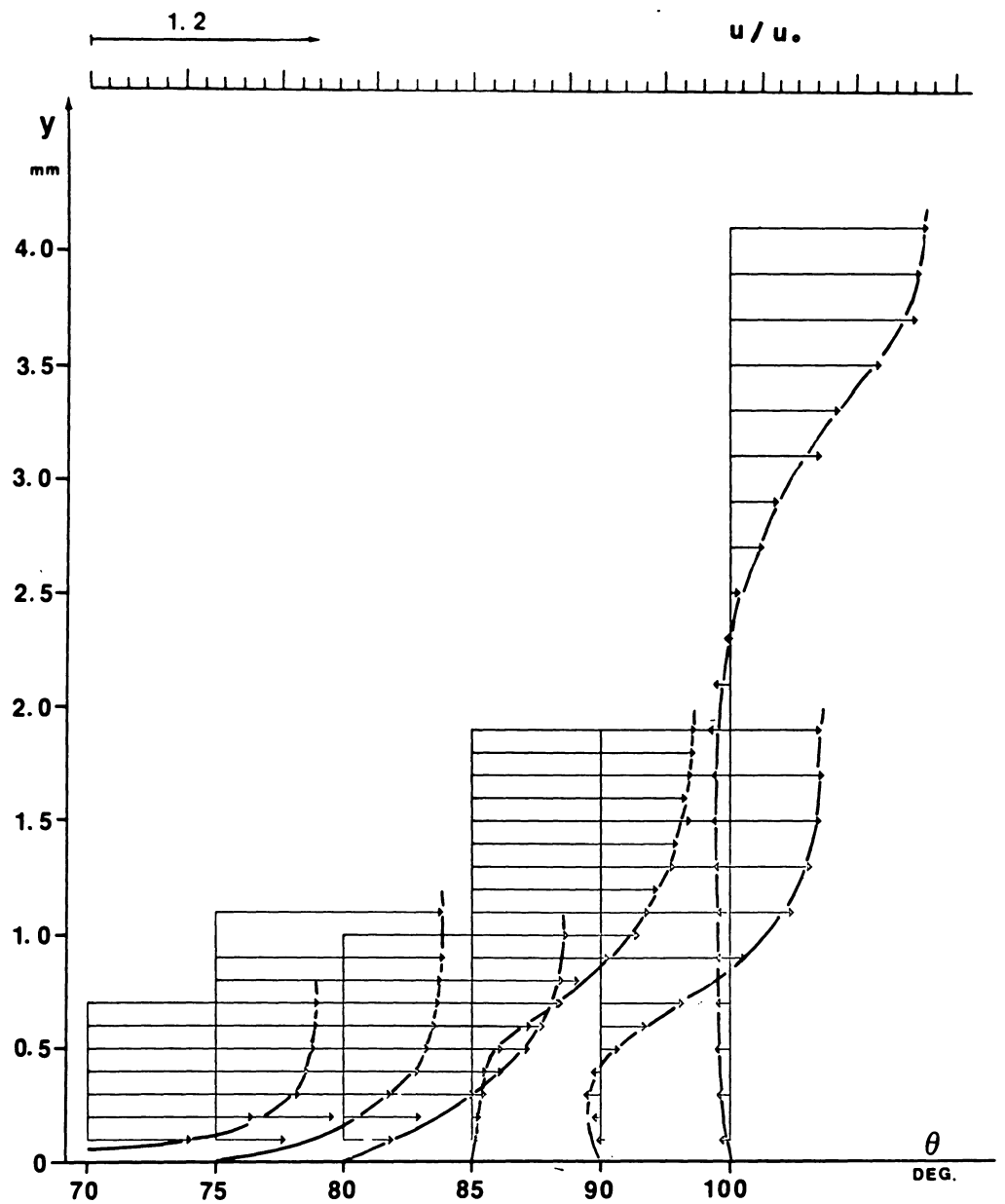

Figure 4.6a u -velocity profiles over a wide angular positions (self-induced oscillatory flow, u_0=36 cm/sec)

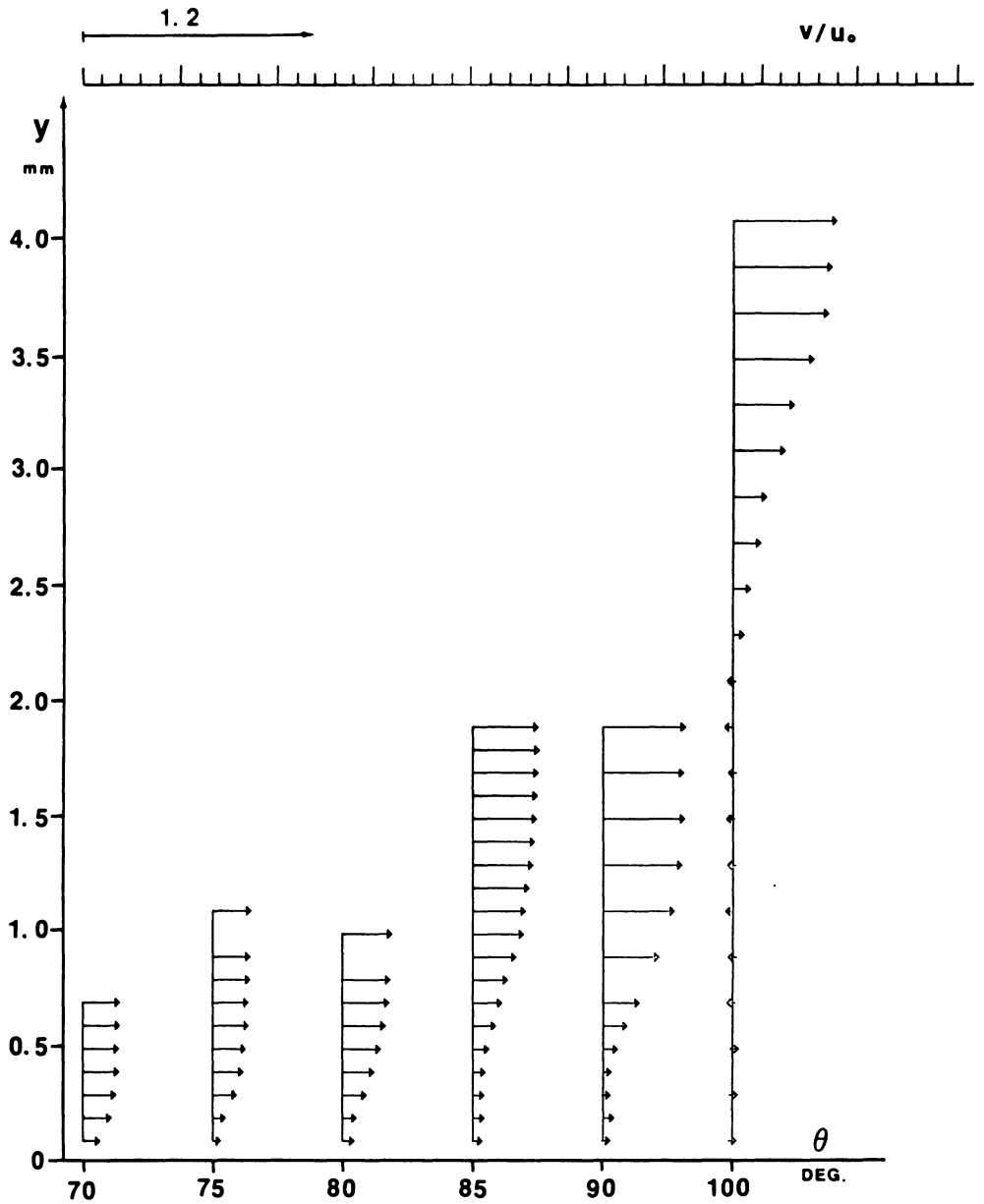

Figure 4.6b v -velocity profiles over a wide angular positions (self-induced oscillatory flow, u_0 =36 cm/sec)

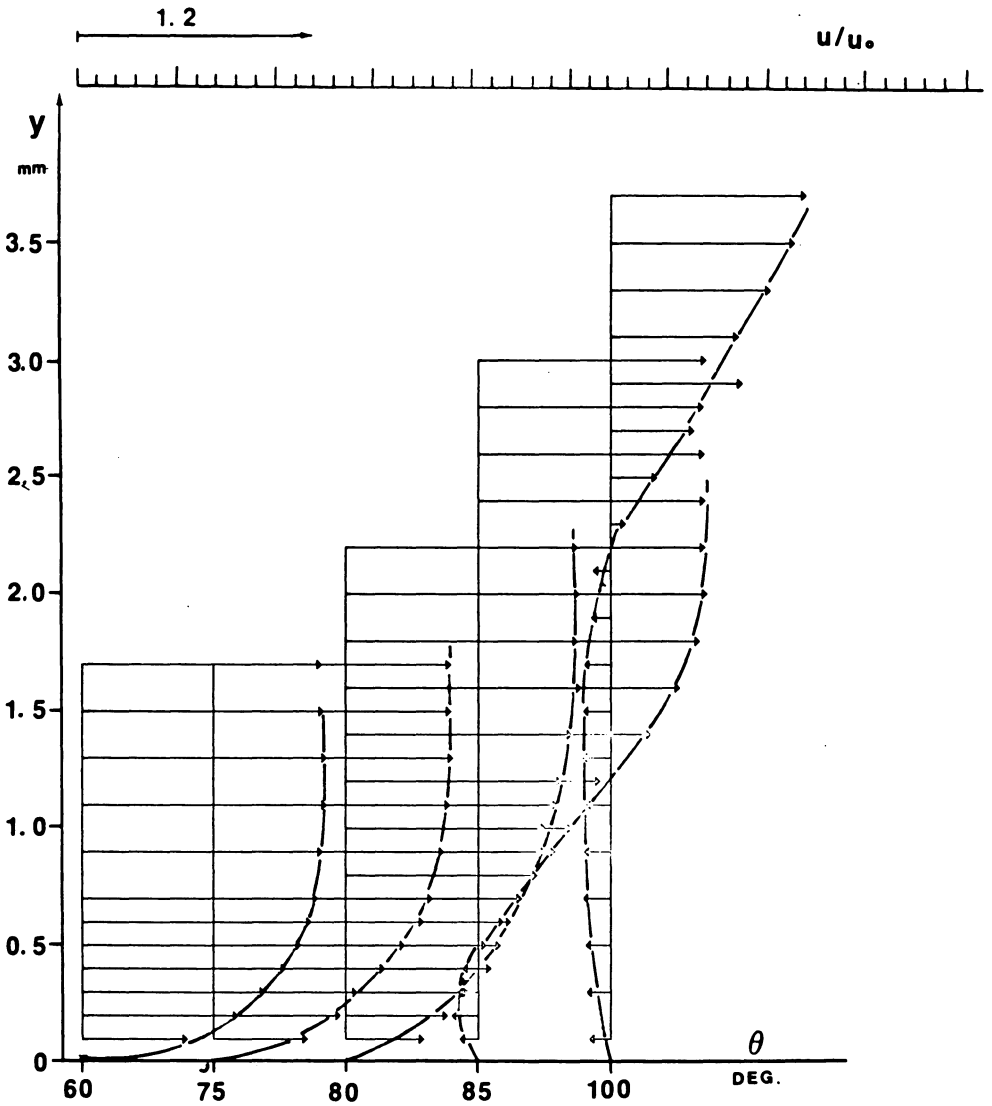

Figure 4.7a u -velocity profiles over a wide angular positions (forced oscillatory flow, fd=fs, u_0=18 cm/sec)

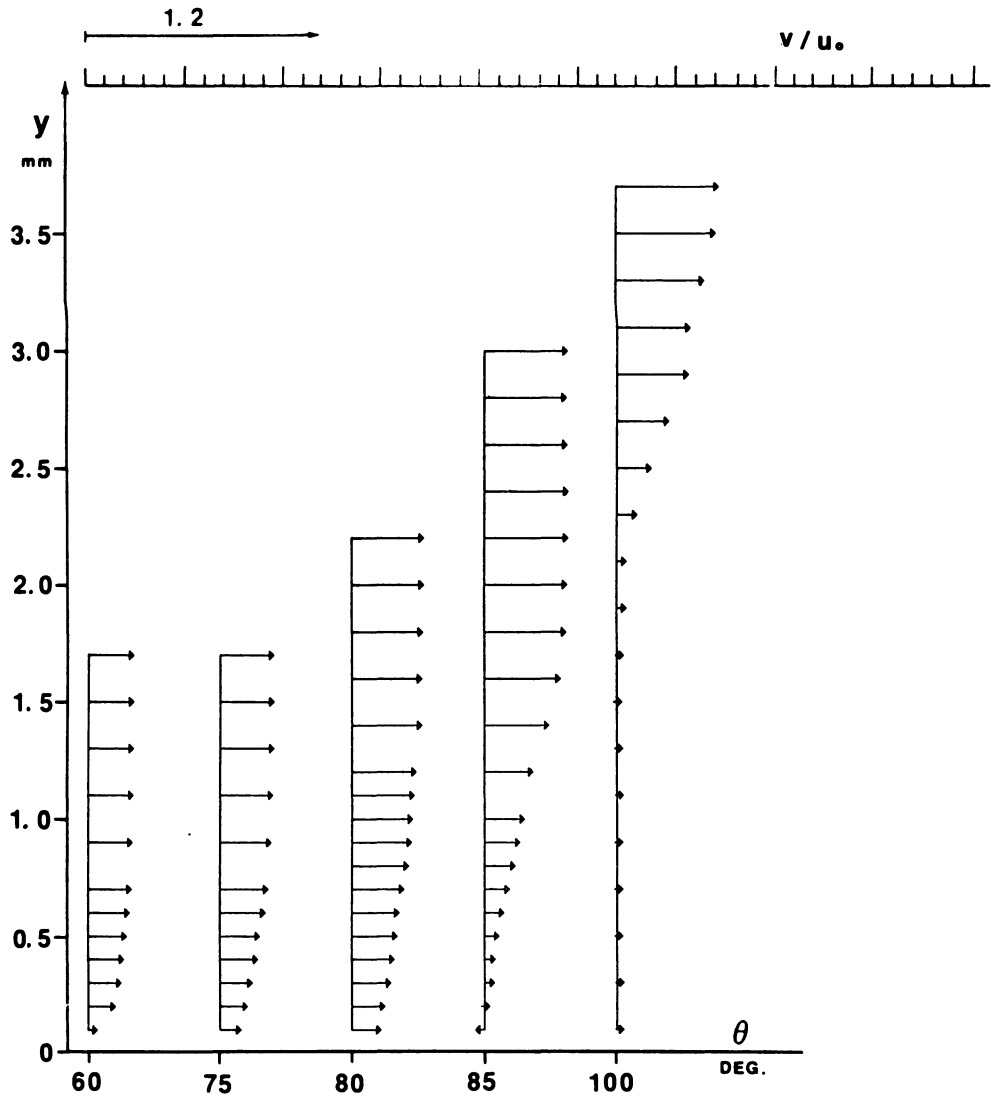

Figure 4.7b v -velocity profiles over a wide angular positions (forced oscillatory flow, fd=fs, u_0=18 cm/sec)

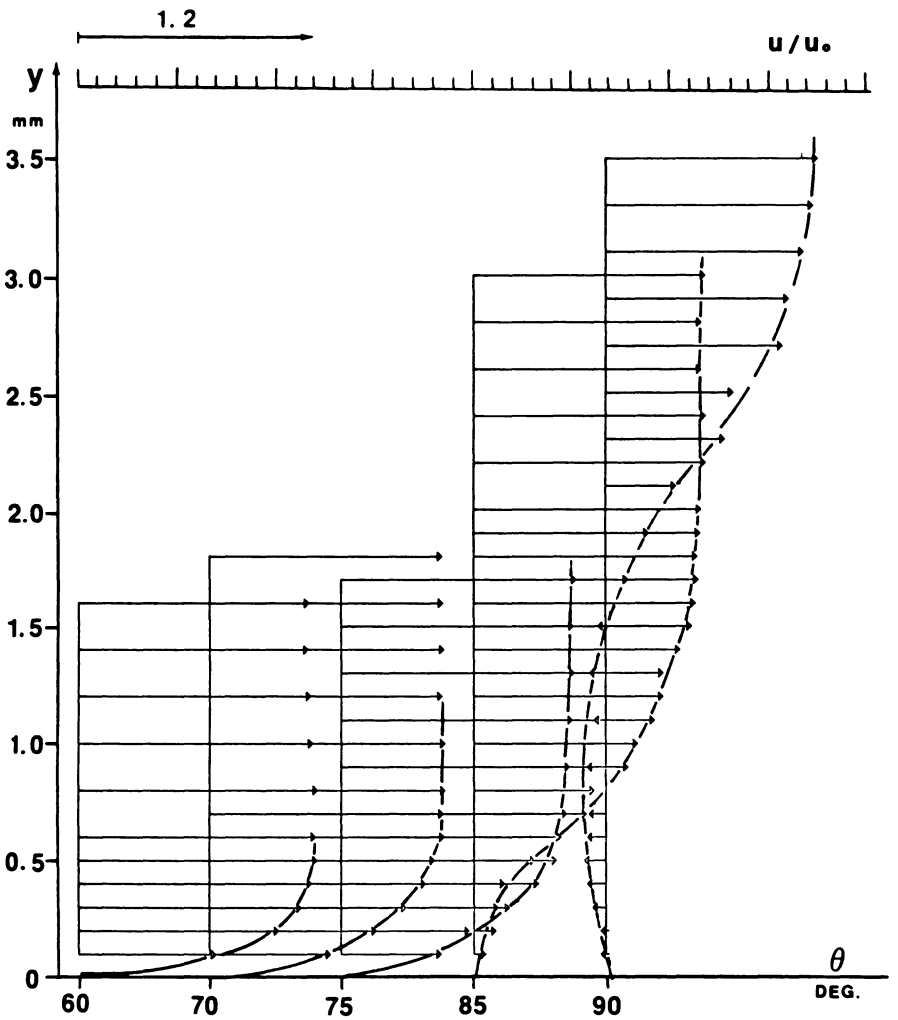

Figure 4.8a u -velocity profiles over a wide angular positions (forced oscillatory flow, fd=fs, u_0 =36cm/sec)

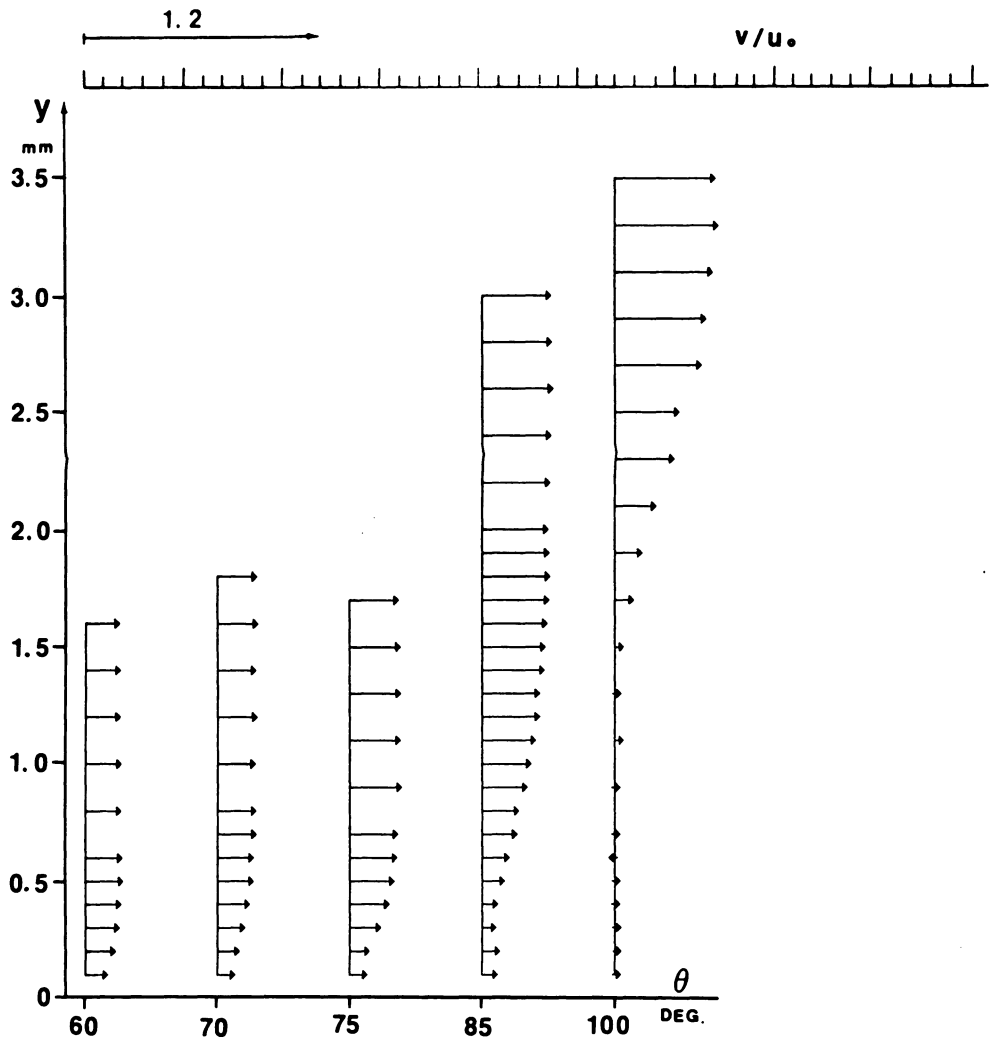

Figure 4.8b v -velocity profile over a wide angular positions (forced oscillatory flow, fd=fs, u_0 =36cm/sec)

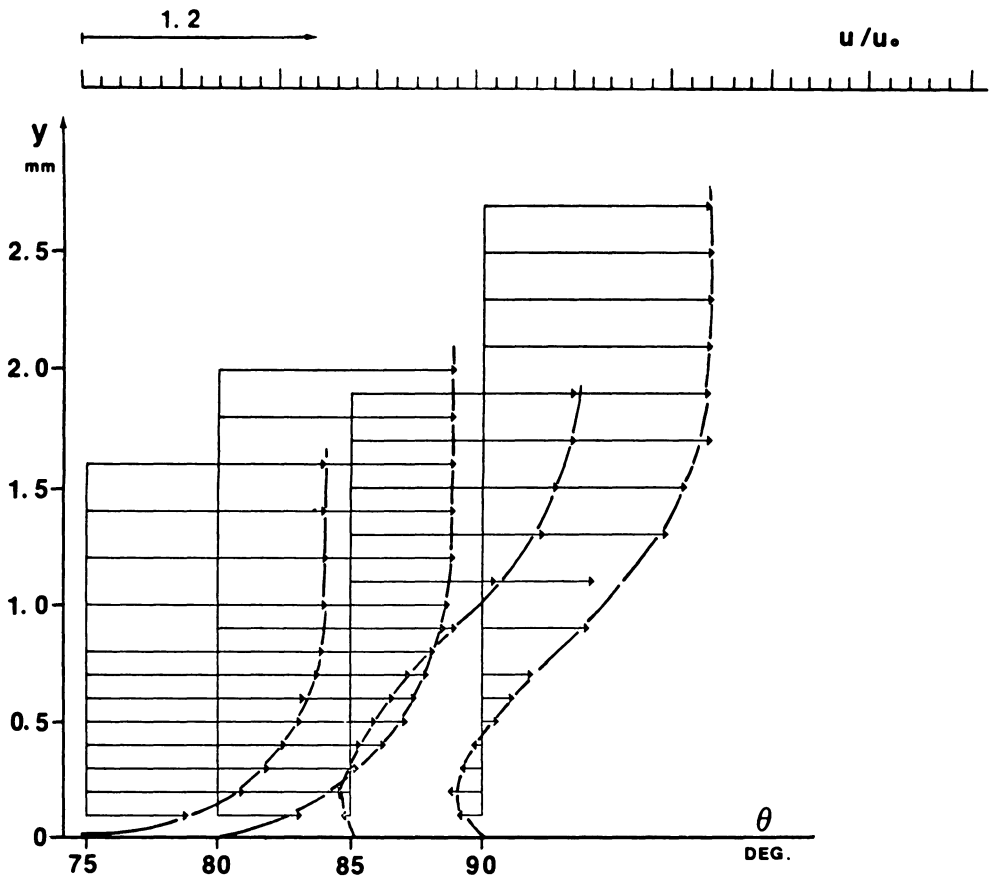

Figure 4.9a u -velocity profiles over a wide angular positions (forced oscillatory flow, fd=1.2fs, u_0=18cm/sec)

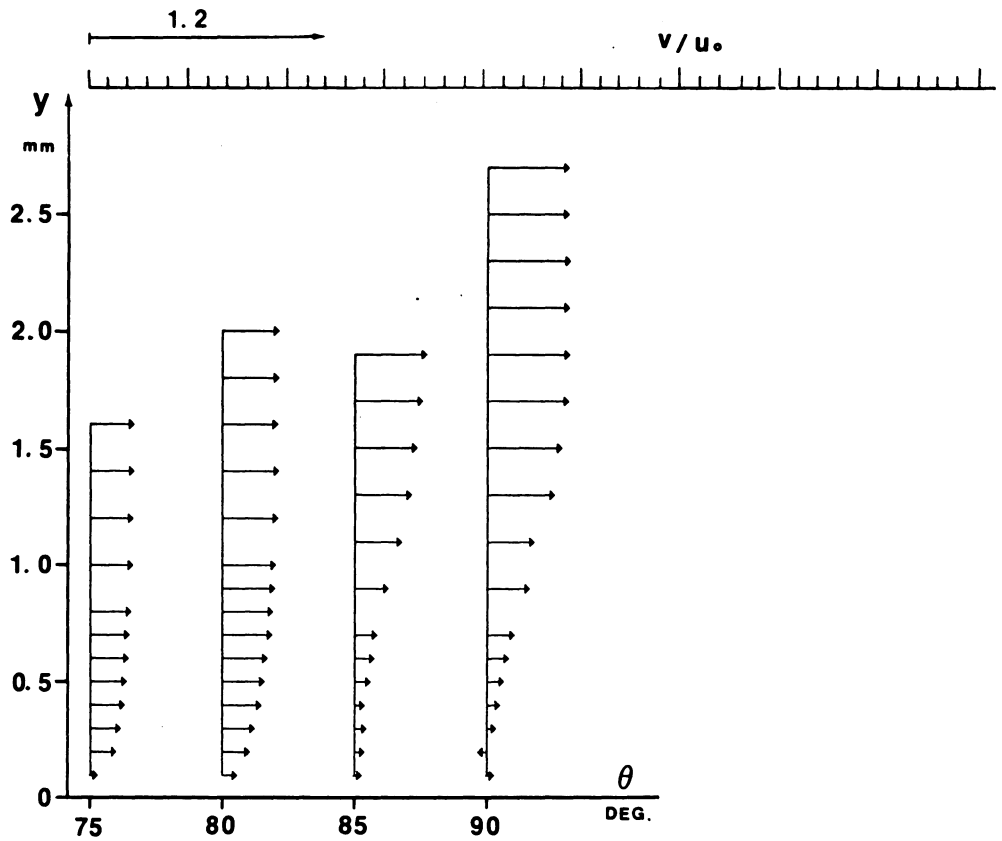

Figure 4.9b v -velocity profile over a wide angular positions (forced oscillatory flow, fd=1.2fs, u_0 =18cm/sec)

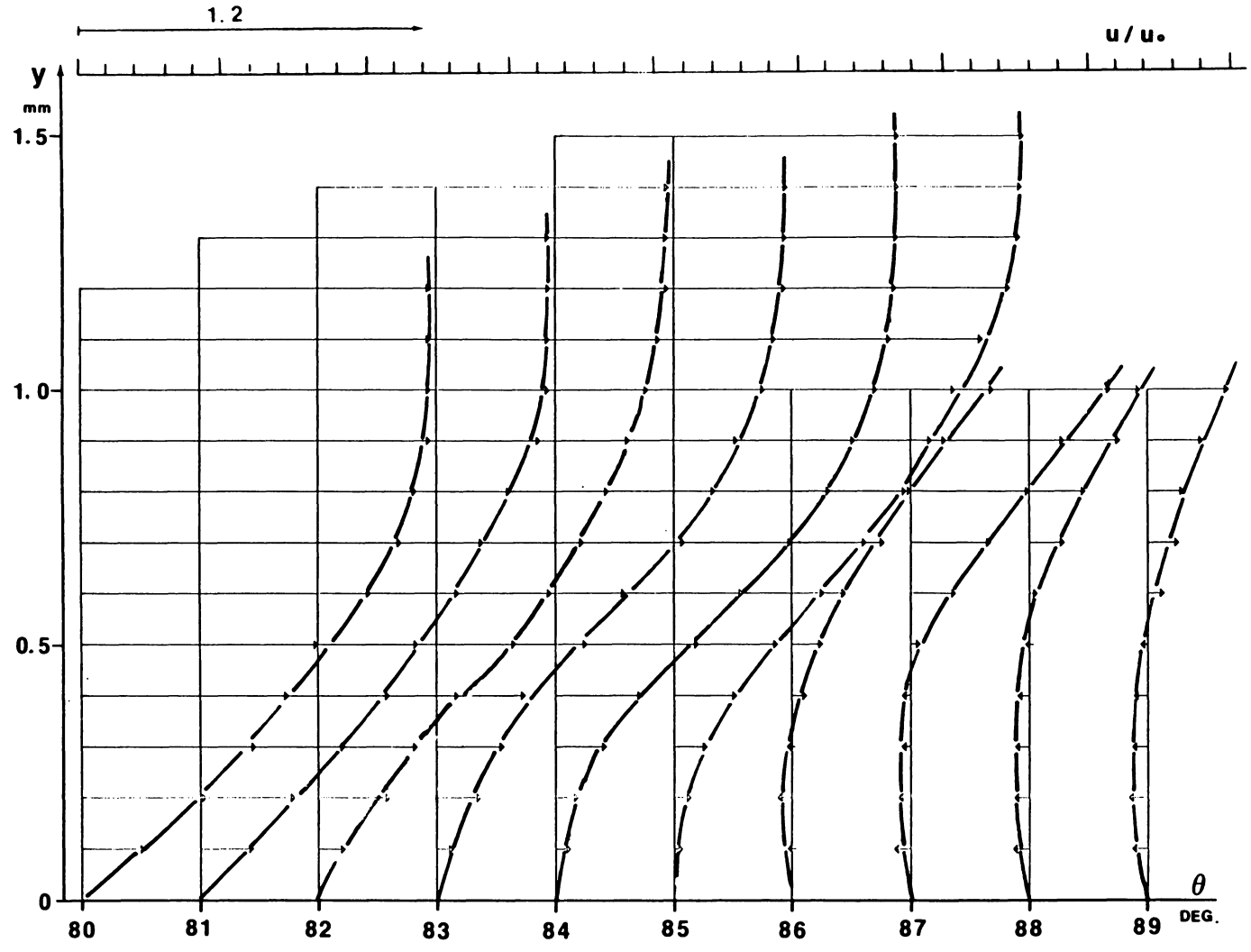

Figure 4.10a u -velocity profiles in the Separation region
(self-induced oscillatory flow, u_0 =70cm/sec)

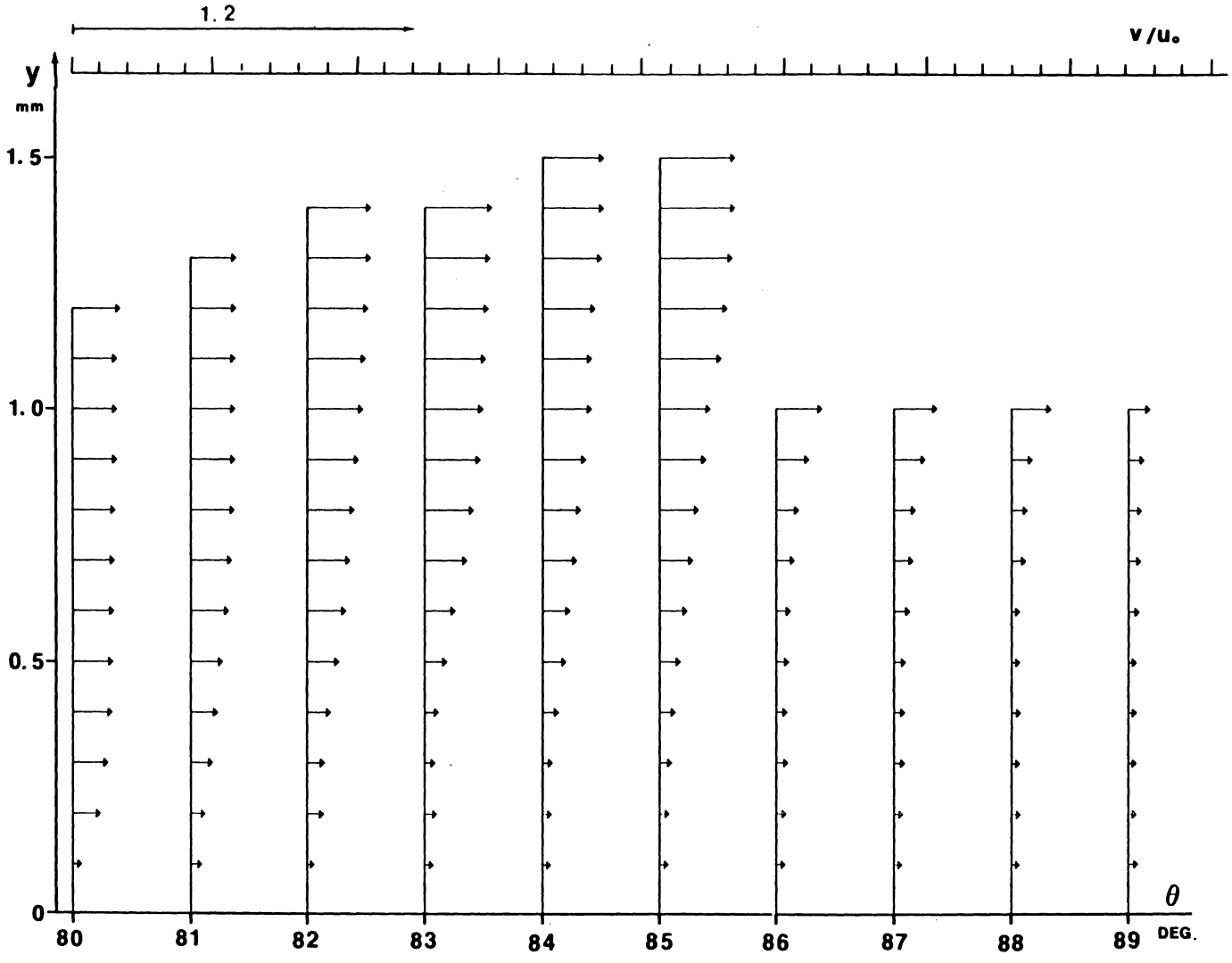

Figure 4.10b v -velocity profiles in the Separation region
(self-induced oscillatory flow, u_0=70cm/sec)

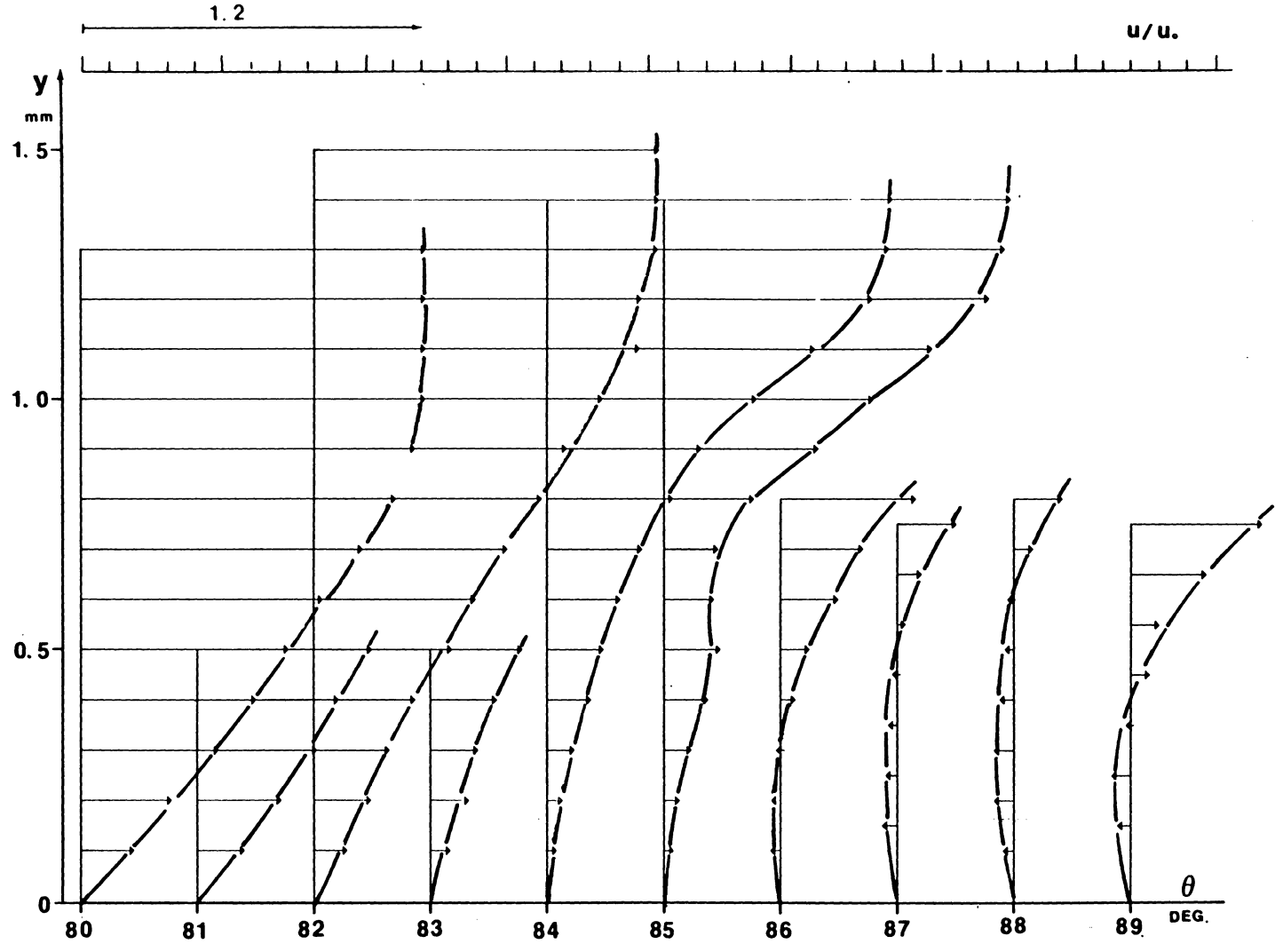

Figure 4.11a u -velocity profiles in the stagnation region
(forced oscillatory flow, fd=fs, u_0=70cm/sec)

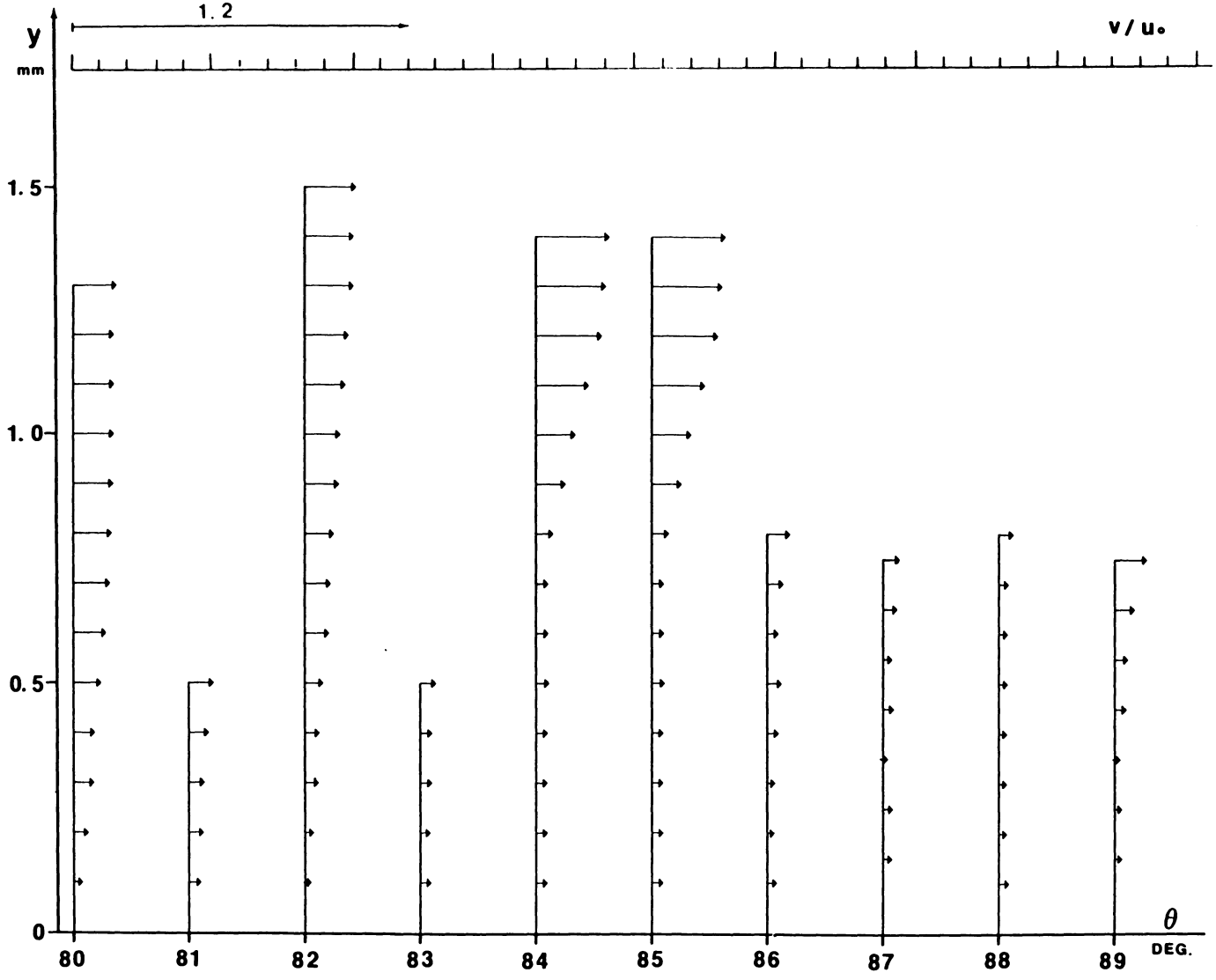

Figure 4.11b v -velocity profiles in the separation region
(forced oscillatory flow, fd=fs, u_0=70cm/sec)

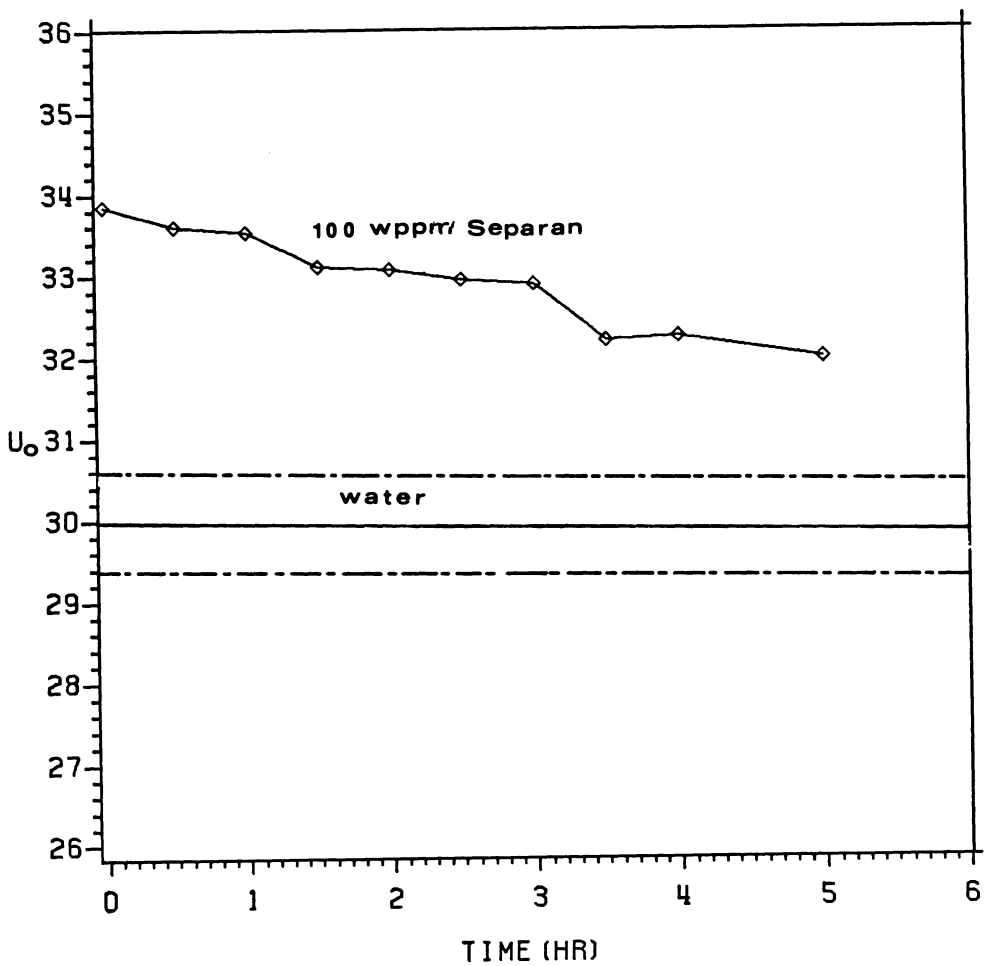

Figure 4.12 Time dependent velocity of polymeric solution (100 wppm Separan)

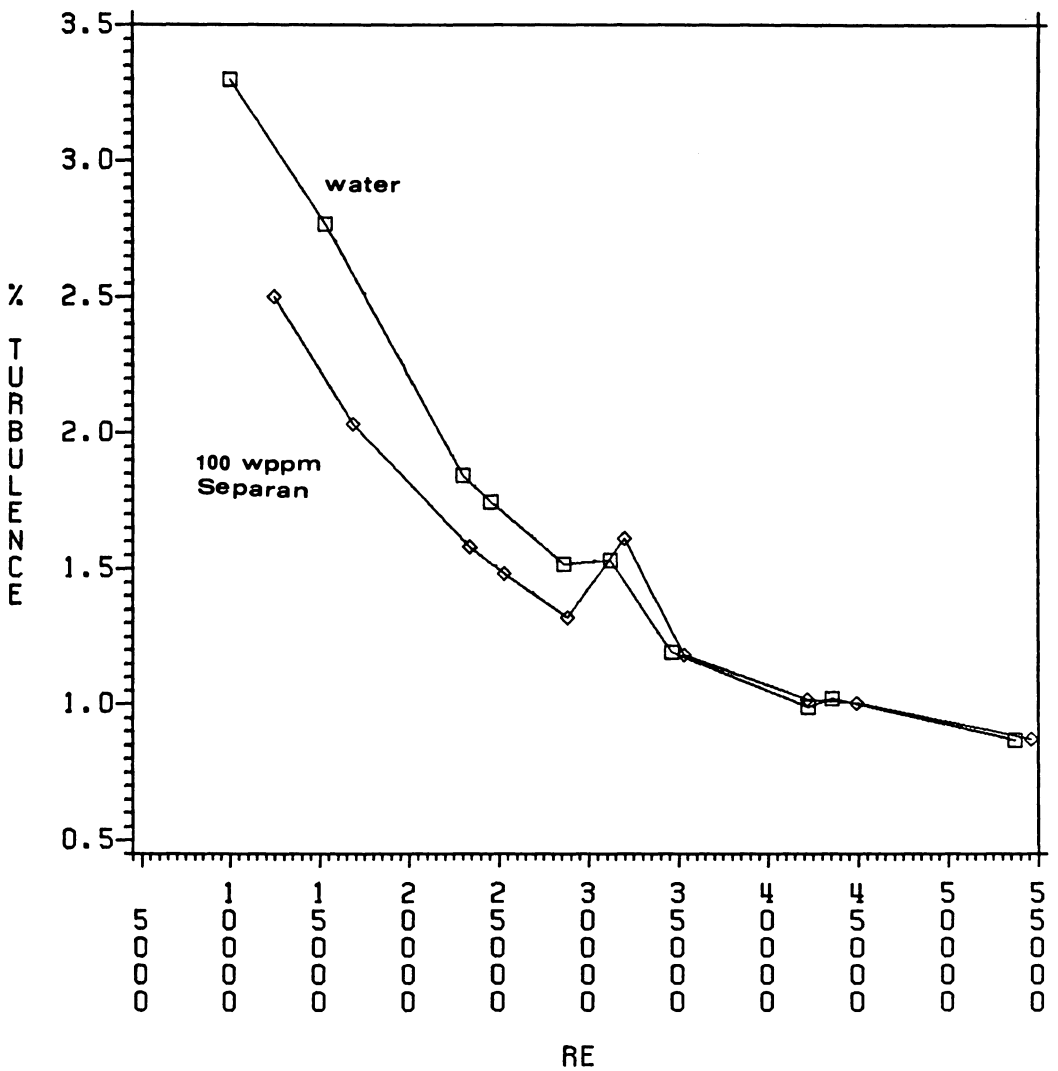

Figure 4.13 Free stream turbulence intensity
(water and 100 wppm Separan solution)

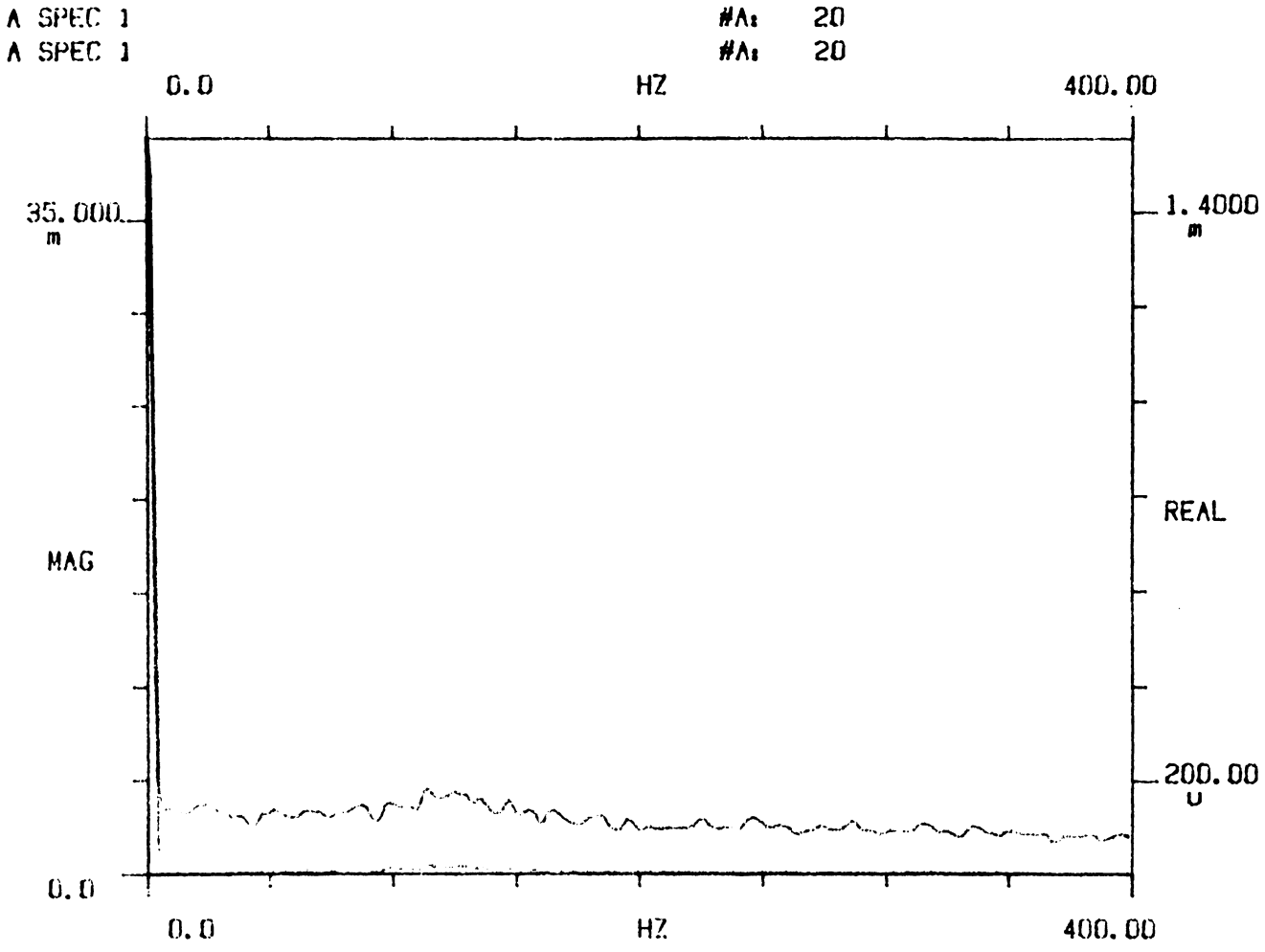

Figure 4.14 Free stream velocity spectrum of water
(u = 35cm/sec)

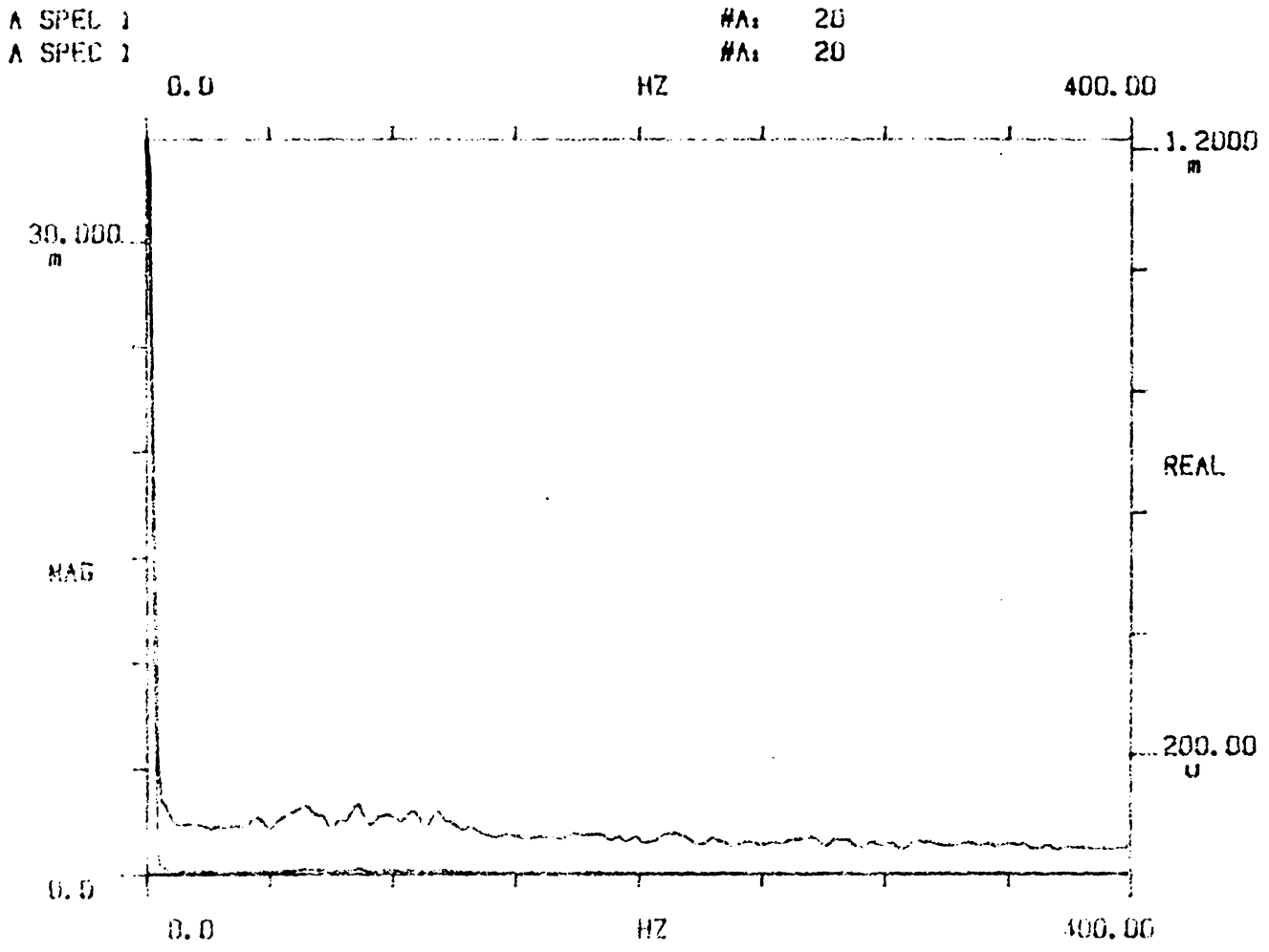

Figure 4.15 Free stream velocity spectrum of polymeric solution
(100 wppm Separan, u =35 cm/sec)

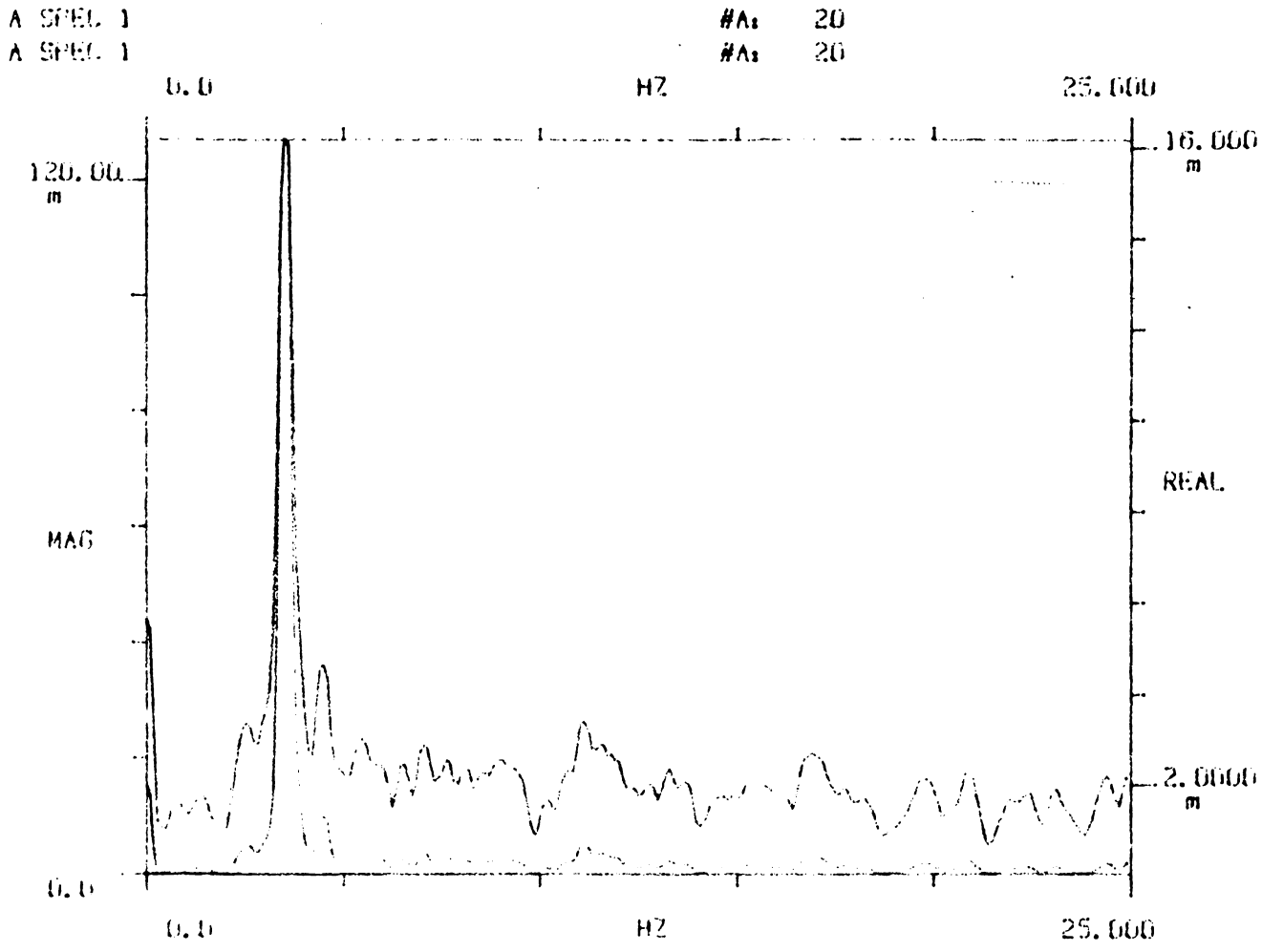

Figure 4.16 Natural shedding spectrum of water
(u =82 cm/sec)

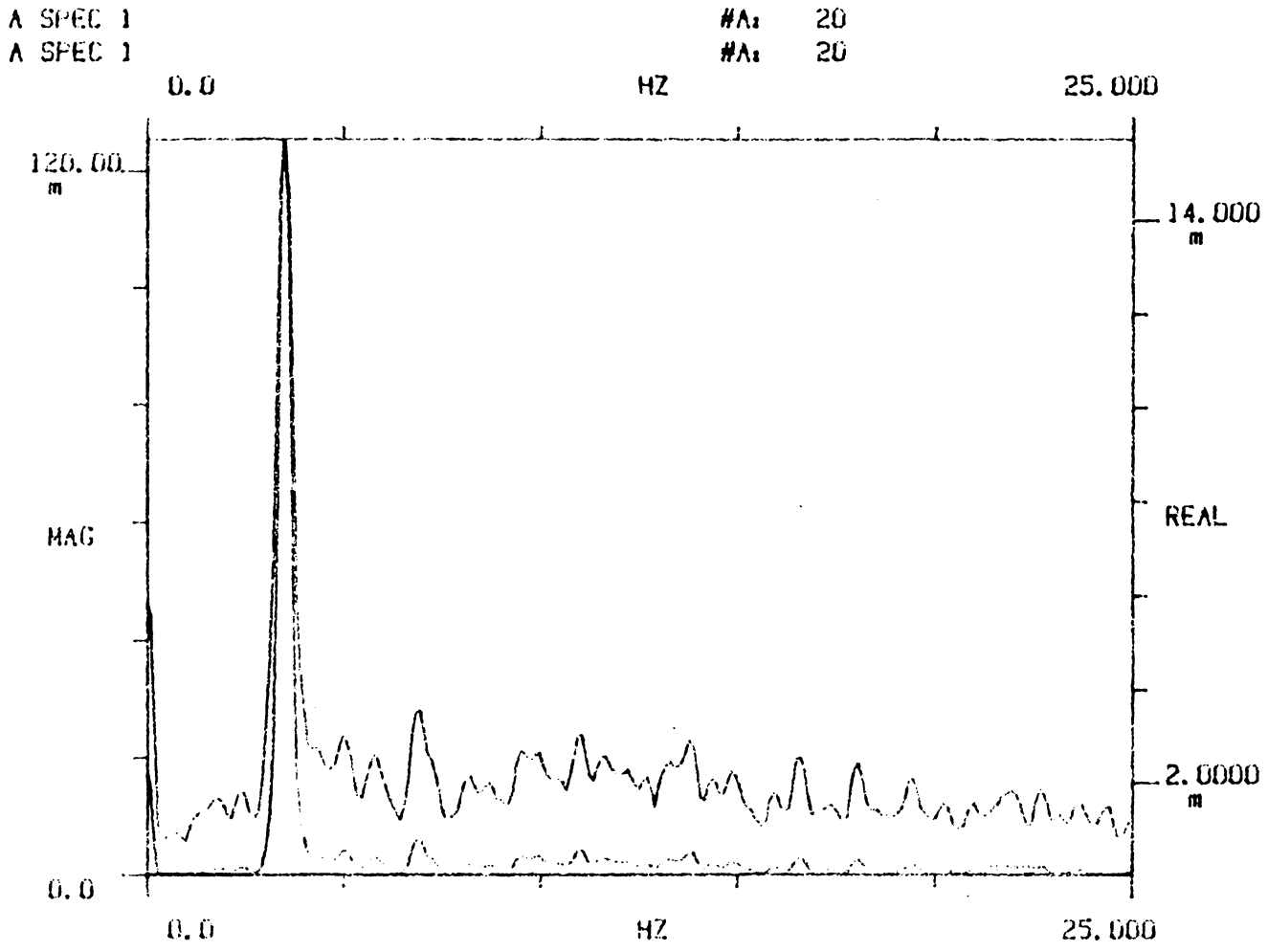

Figure 4.17 Natural shedding spectrum of polymeric solution
(100 wppm Separan, u =84 cm/sec)

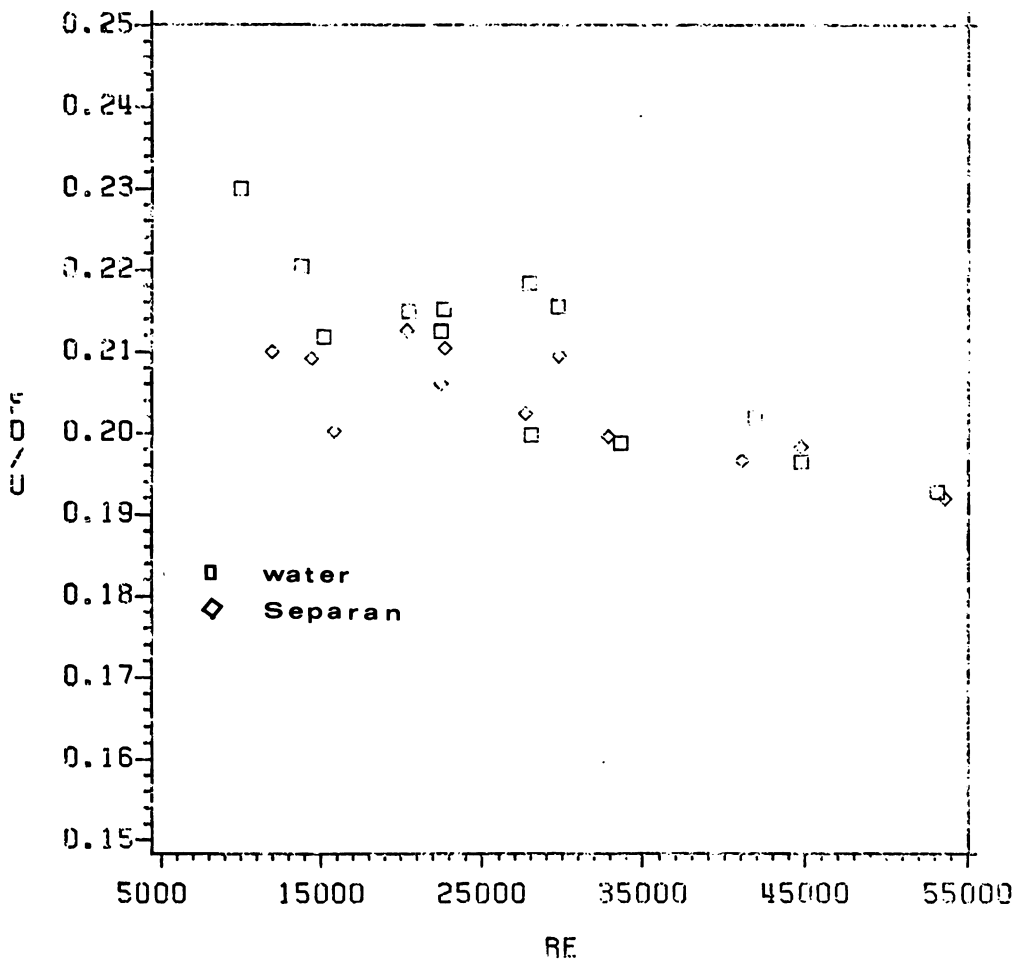

Figure 4.18 Natural shedding frequency
(water and 100 wppm Separan)

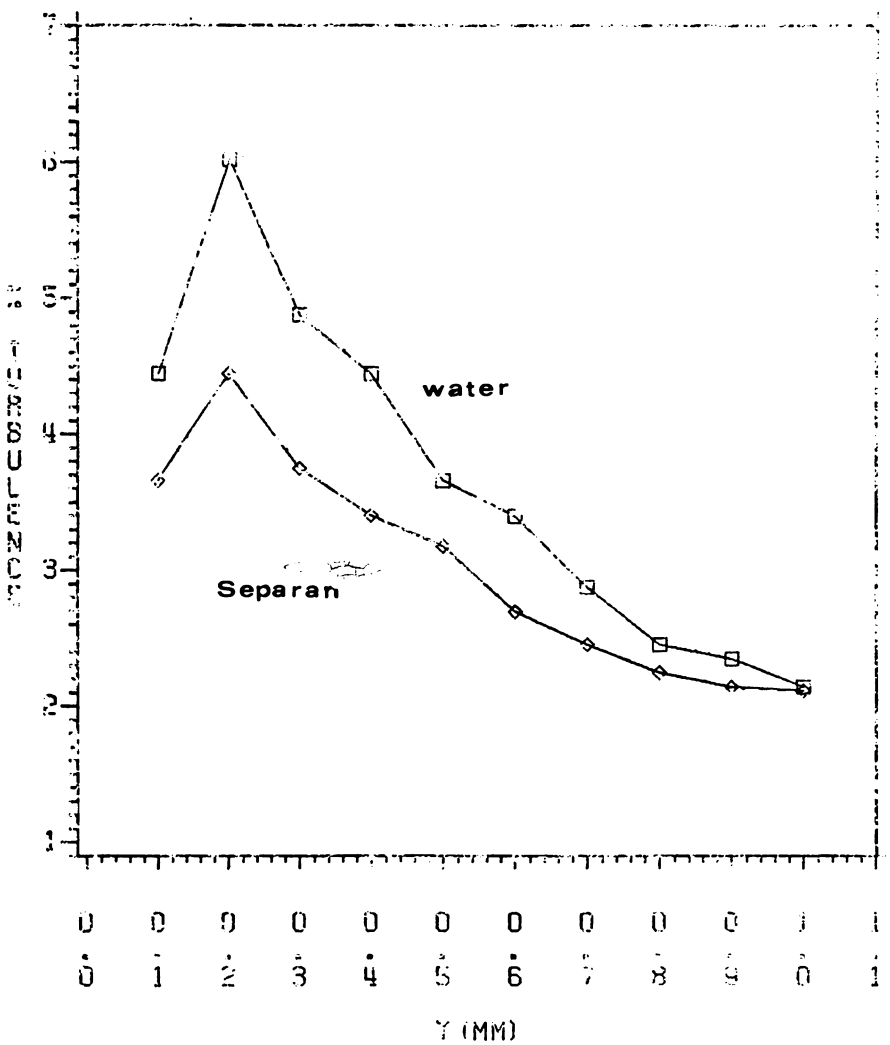

Figure 4.19 Boundary-layer turbulence intensity distributions (water and 100 wppm Separan, θ=80 degrees)

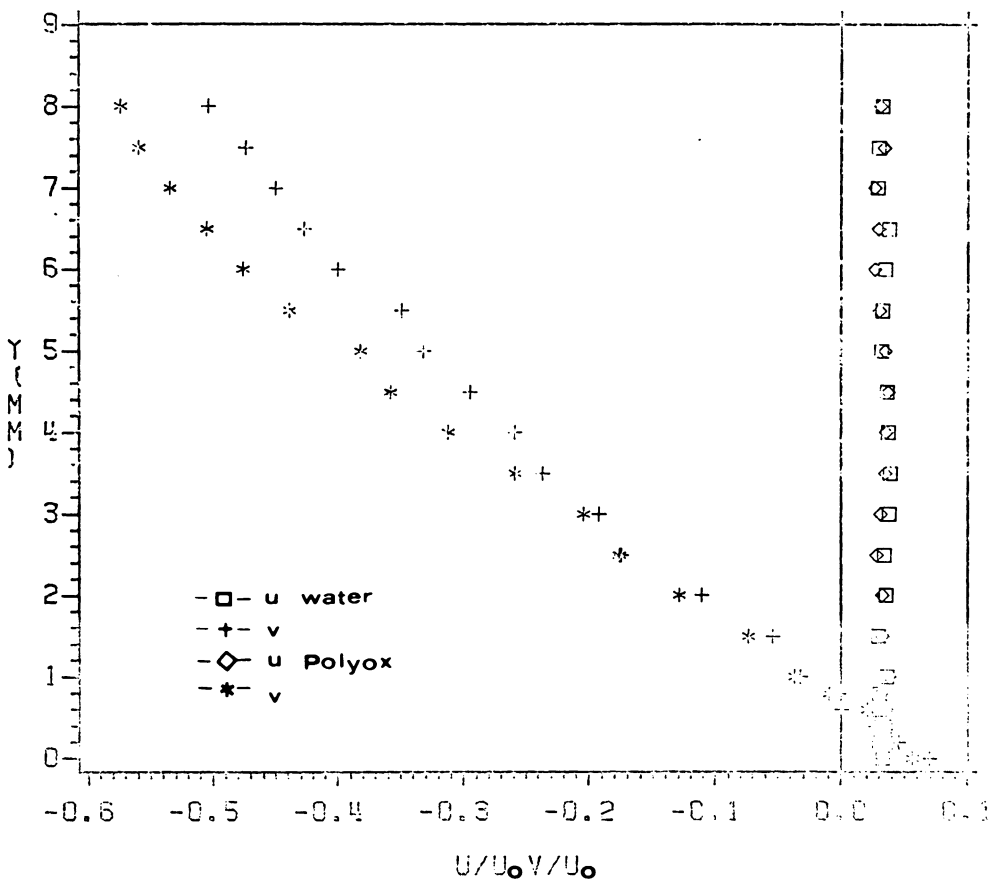

Figure 4.20 Stagnation region velocity profiles at θ=0.5 degree (water and 100 wppm Polyox, u =42 cm/sec)

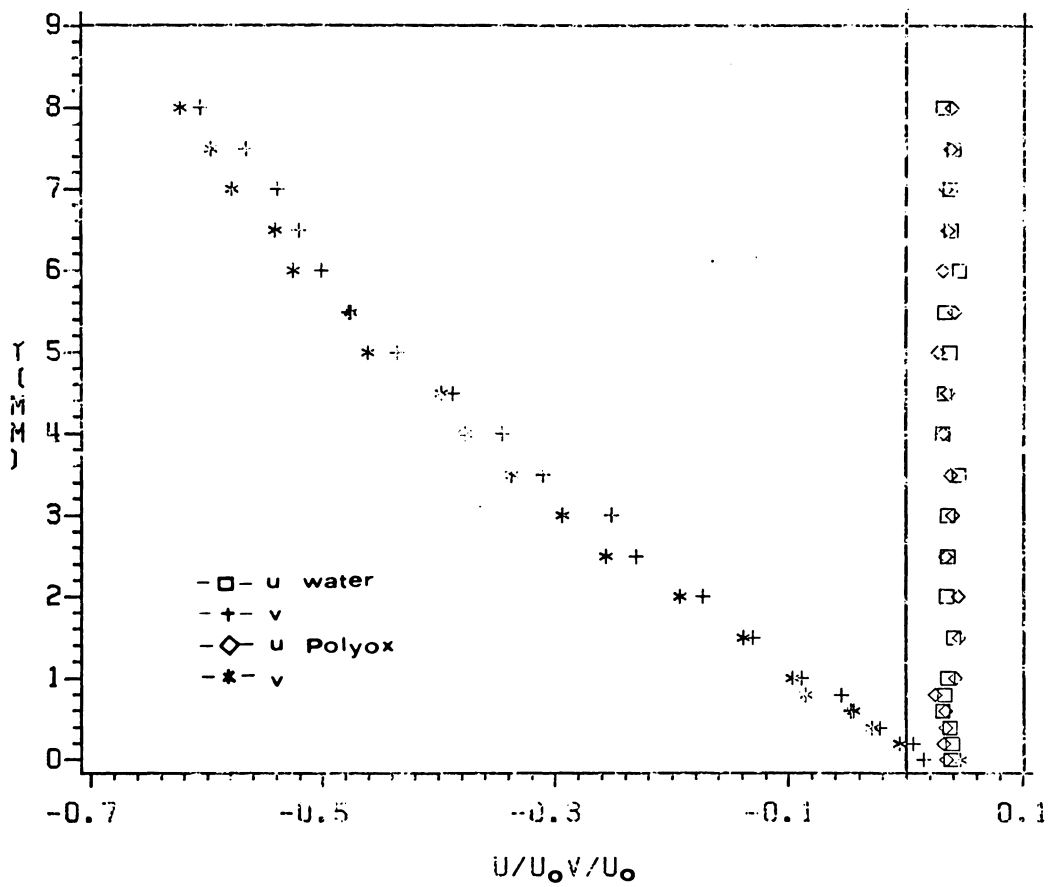

Figure 4.21 Stagnation region velocity profiles at θ=0.5 degree (water and 100 wppm Polyox, u =84 cm/sec)

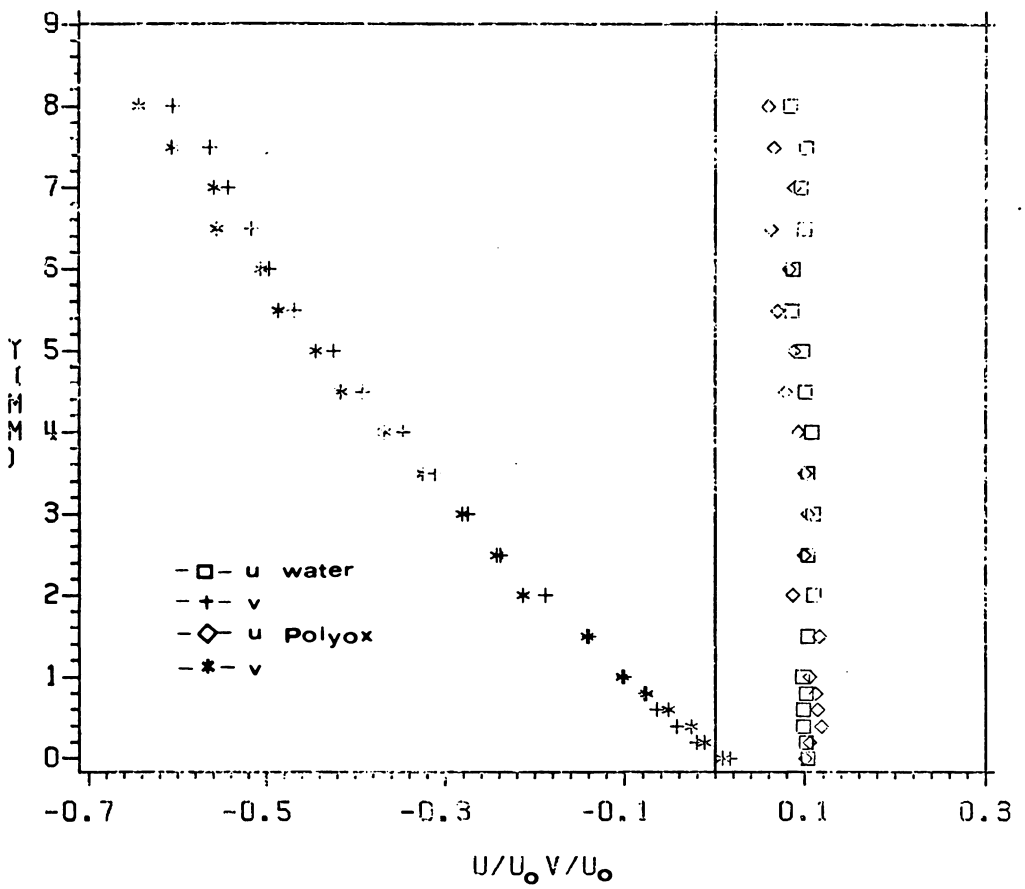

Figure 4.22 Stagnation region velocity profiles at θ=2 degrees (water and 100 wppm Polyox, u =84 cm/sec)

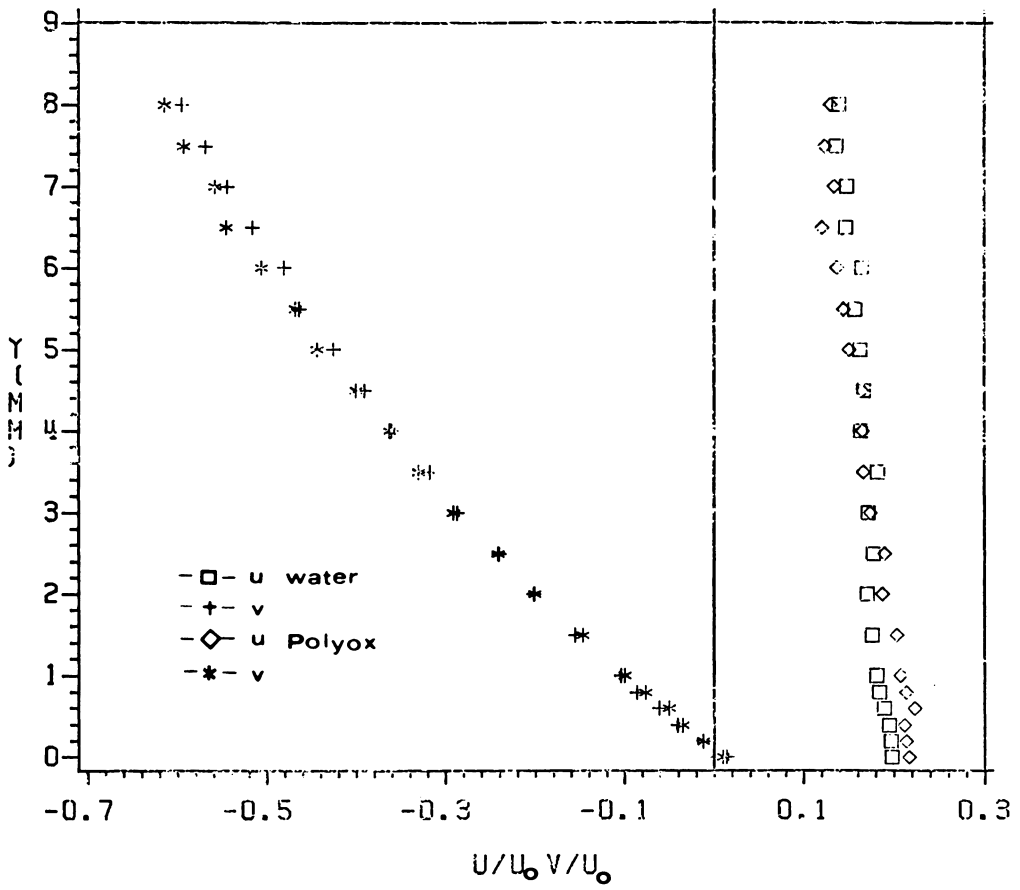

Figure 4.23 Stagnation region velocity profiles at θ=4 degrees (water and 100 wppm Polyox, u =84 cm/sec)

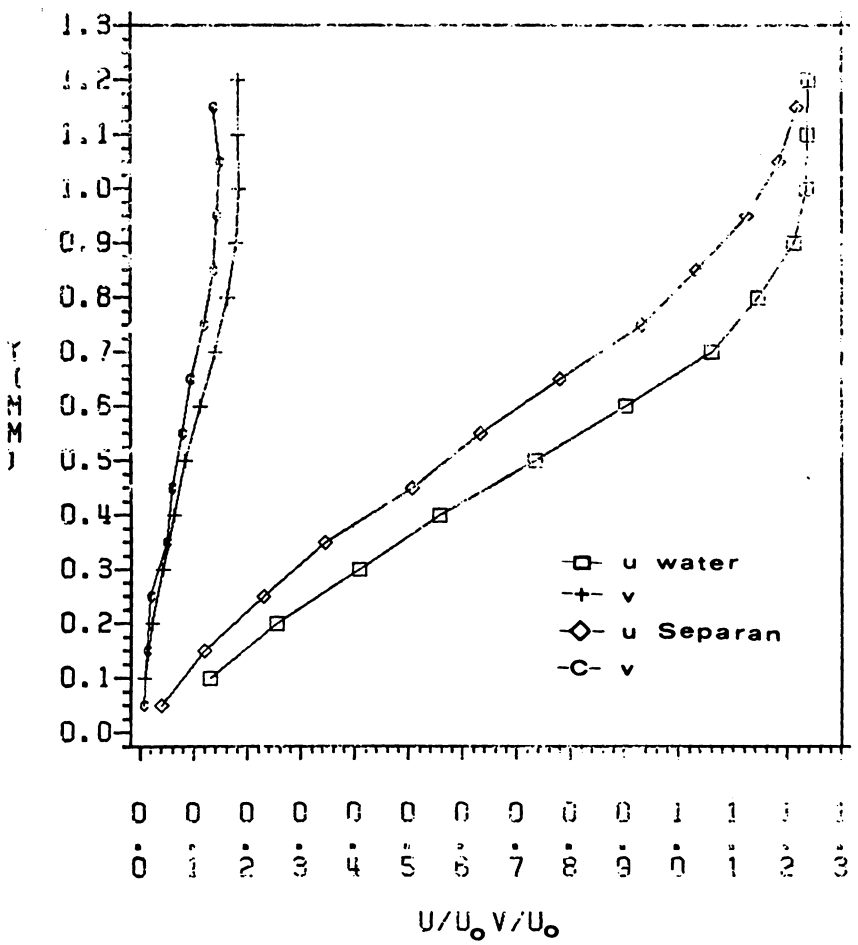

Figure 4.24 Boundary-layer velocity profiles at θ=82 degrees-Re=6,750 (water and 100 wppm Separan)

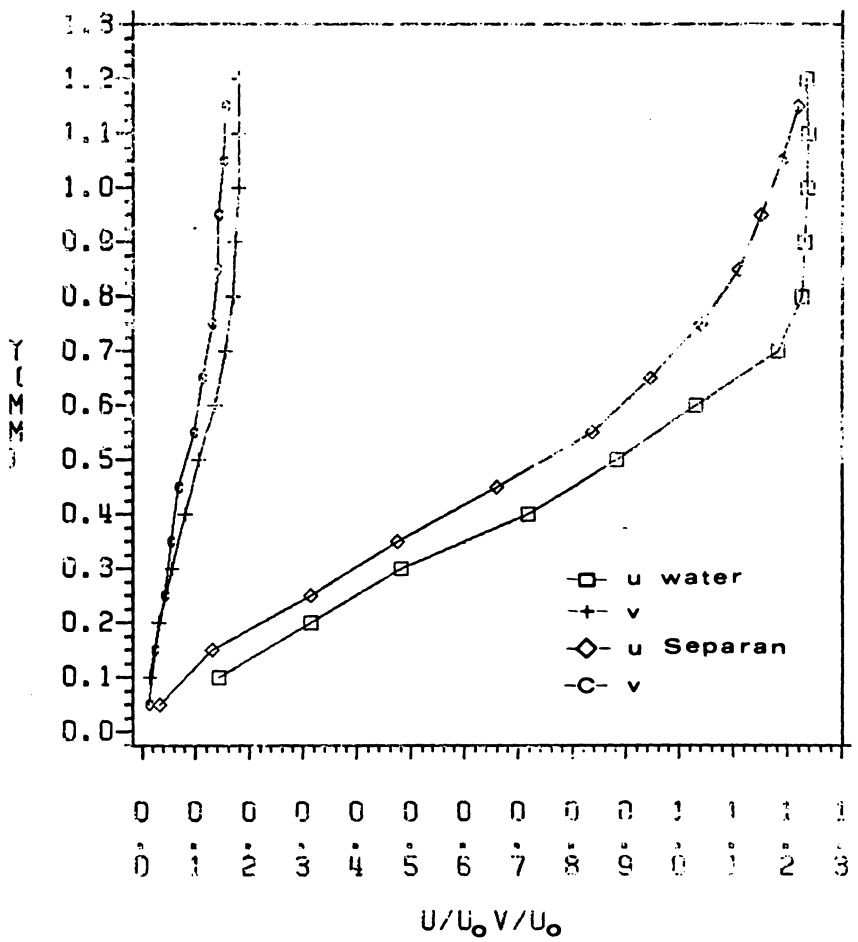

Figure 4.25 Boundary-layer velocity profiles at θ=82 degrees-Re=13,500 (water and 100 wppm Separan)

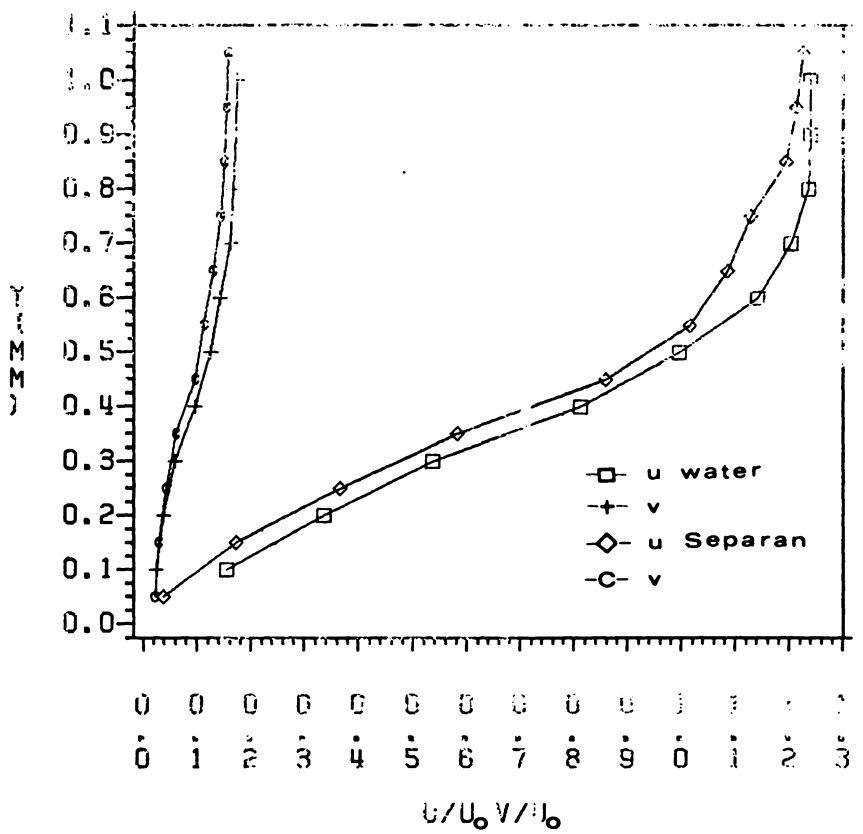

Figure 4.26 Boundary-layer velocity profiles at θ=82 degrees-Re=20,875 (water and 100 wppm Separan)

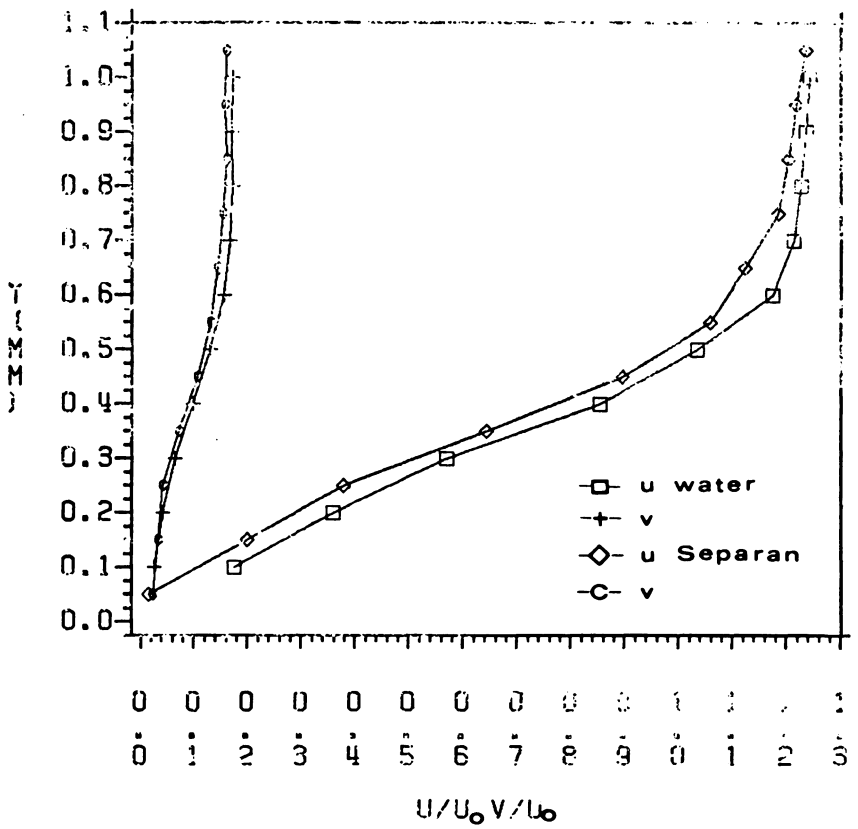

Figure 4.27 Boundary-layer velocity profiles at θ=82 degrees-Re=27,500 (water and 100 wppm Separan)

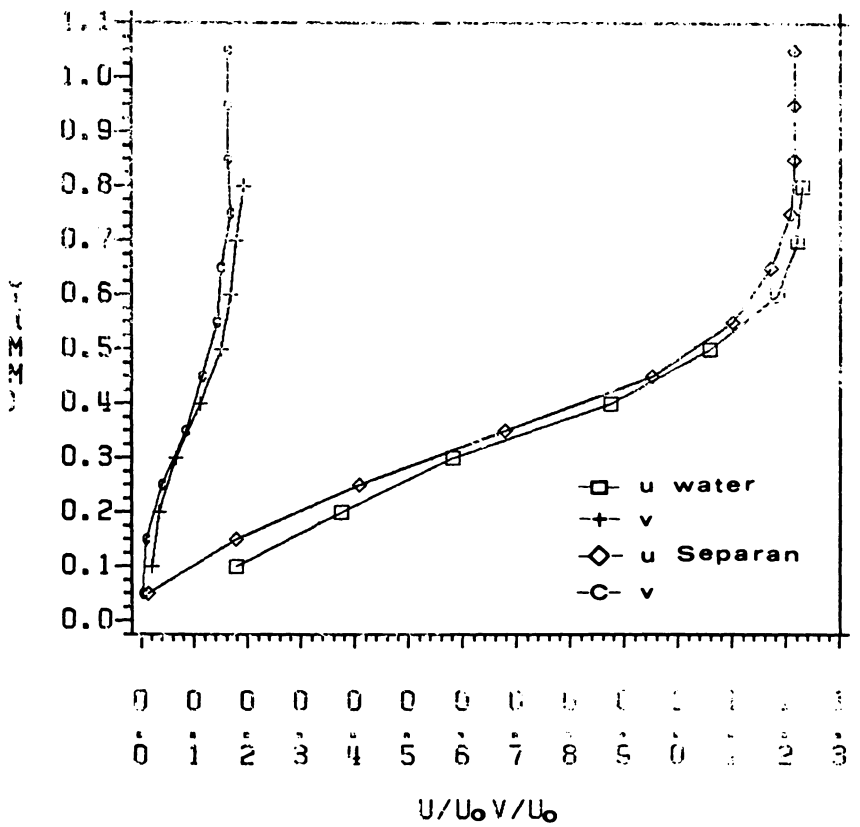

Figure 4.28 Boundary-layer velocity profiles at θ=82 degrees-Re=34,300 (water and 100 wppm Separan)

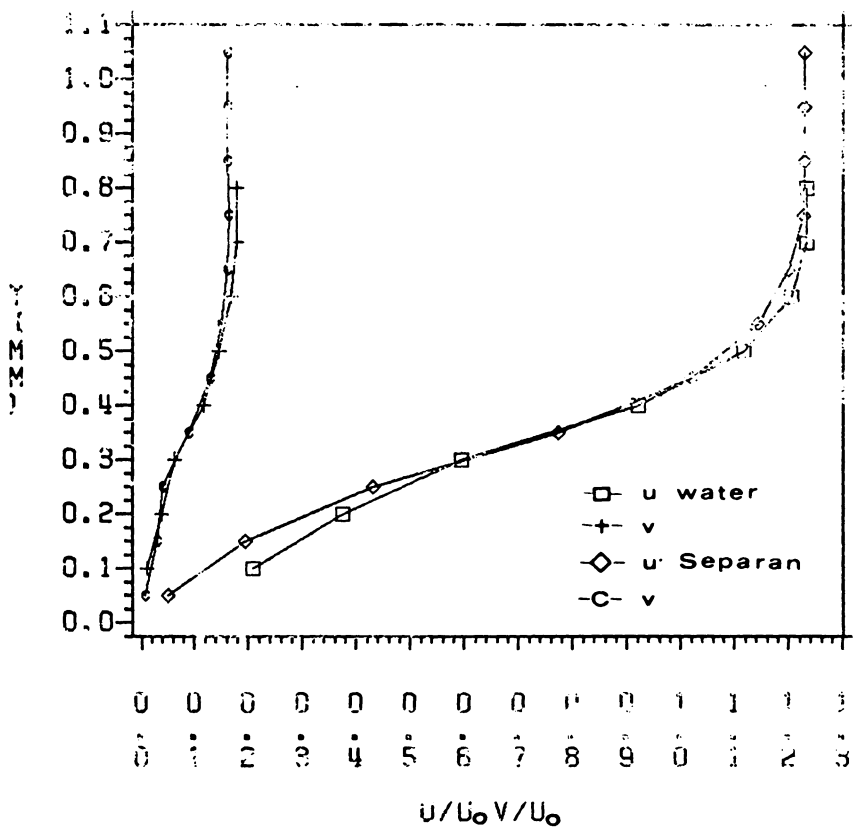

Figure 4.29 Boundary-layer velocity profiles at θ=82 degrees-Re=41,200 (water and 100 wppm Separan)

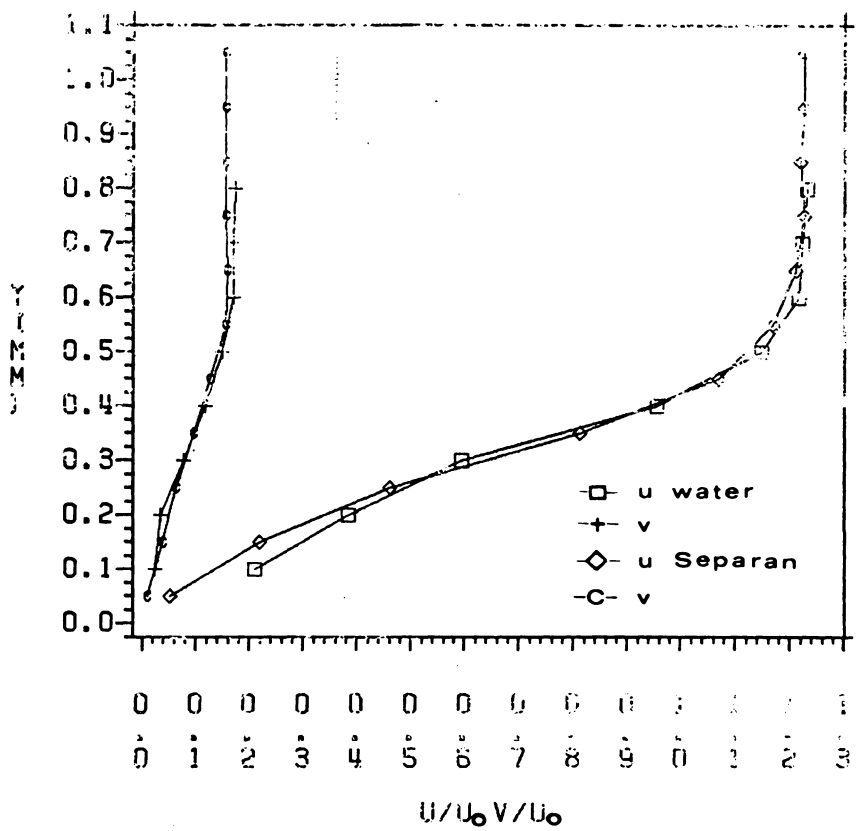

Figure 4.30 Boundary-layer velocity profiles at θ=82 degrees- Re=48,060 (water and 100 wppm Separan)

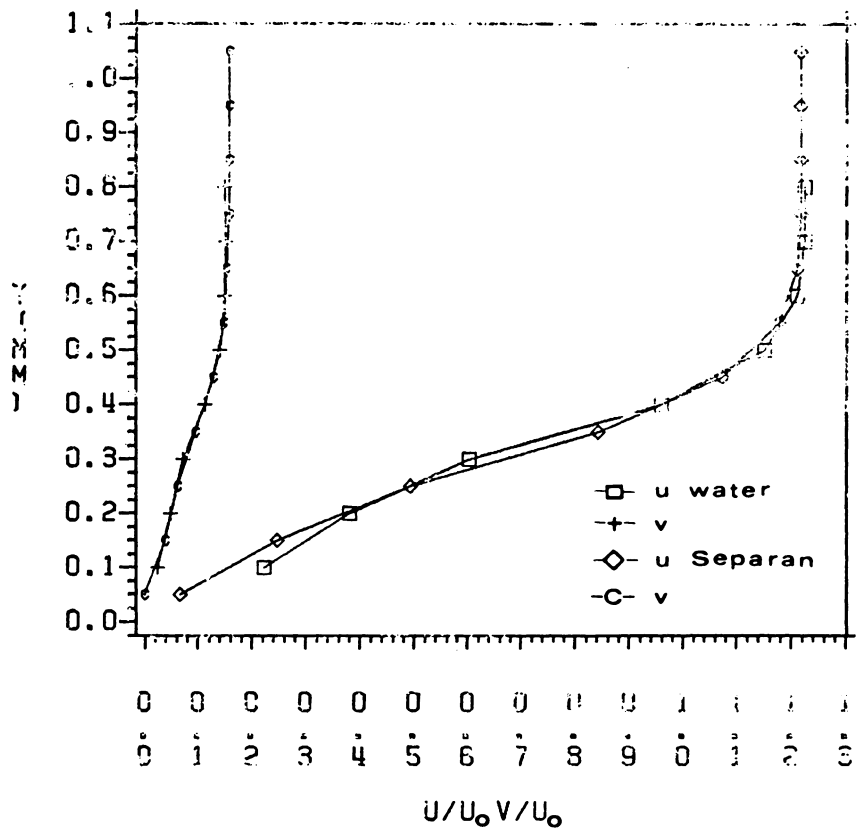

Figure 4.31 Boundary-layer velocity profiles at θ=82 degrees-Re=55,000 (water and 100 wppm Separan)

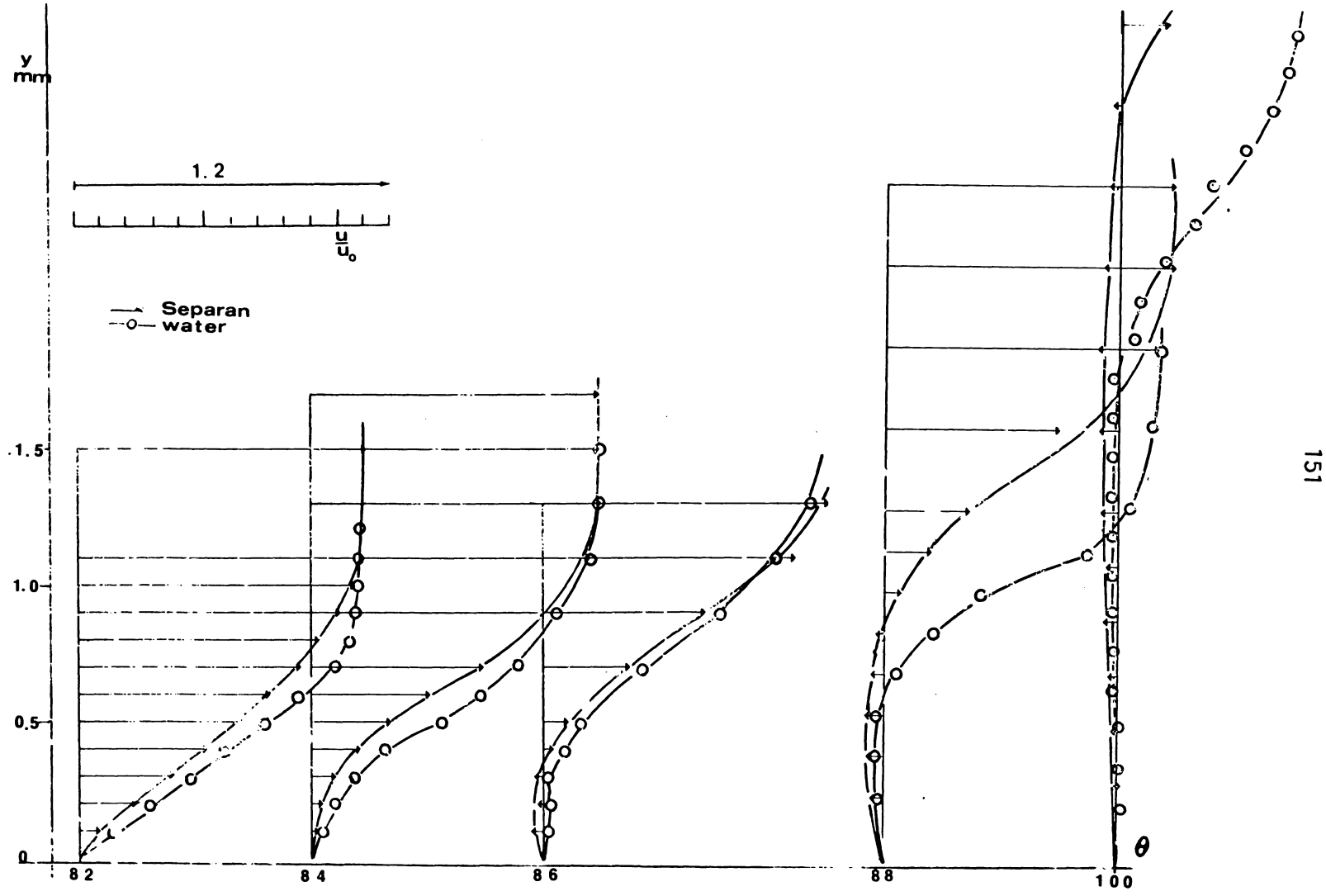

Figure 4.32a u-velocity profiles near and downstream of separation(water and 100 wppm Separan, Re=20,875)

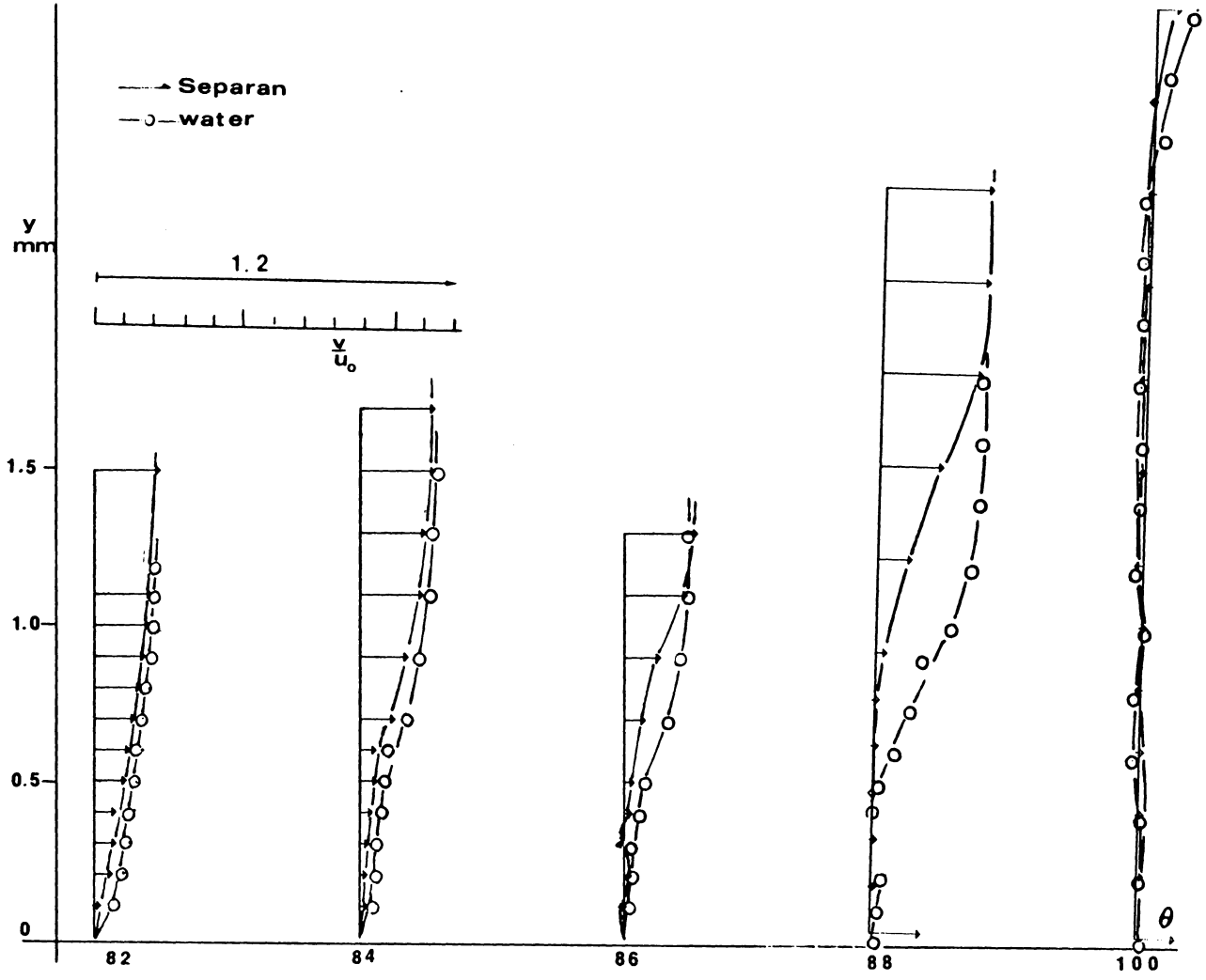

Figure 4.32b v -velocity profiles near and downstream of separation(water and 100 wppm Separan, Re=20,875)

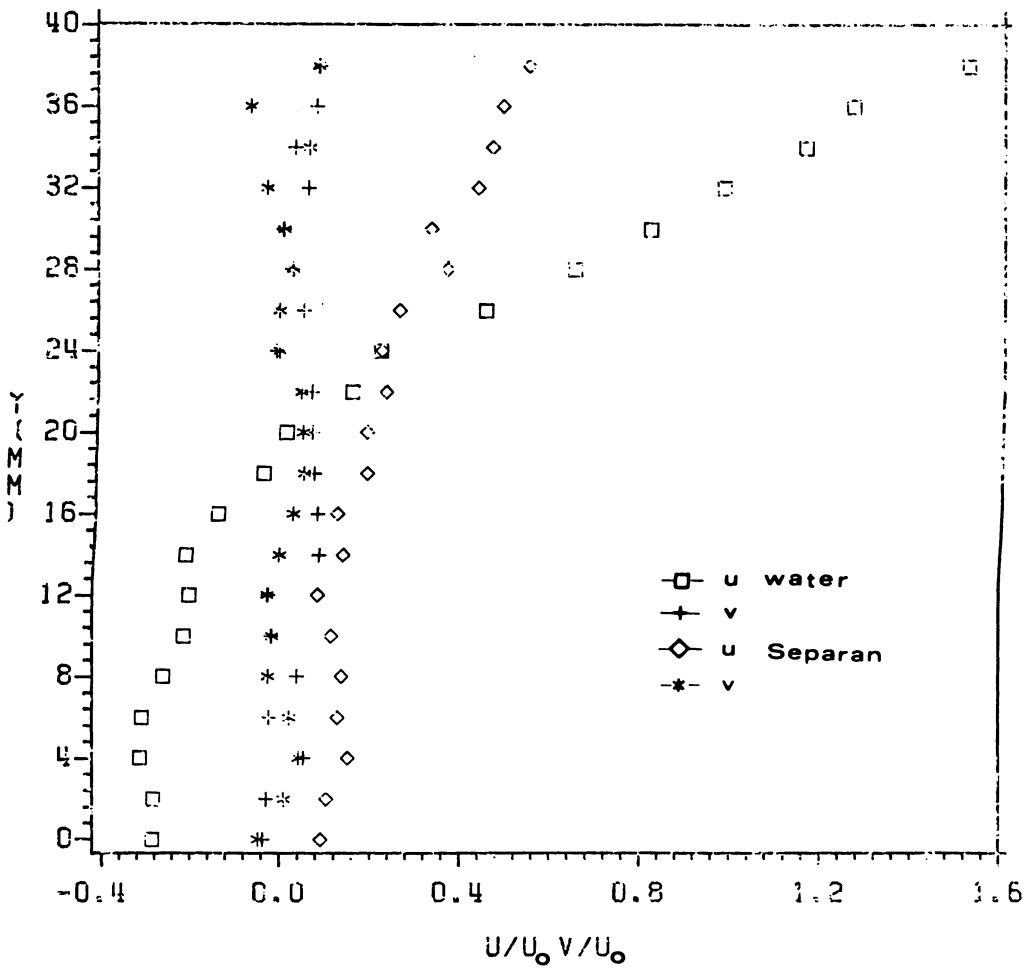

Figure 4.33 Wake velocity profiles
(water and 100 wppm Separan, Re=20,875)

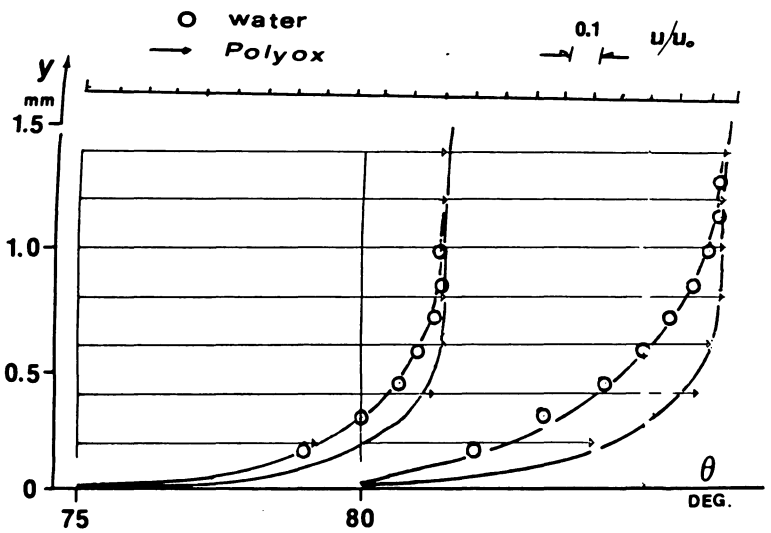

Figure 4.34 Laminar velocity profiles at θ=75 and 80 degrees-Re=25,000

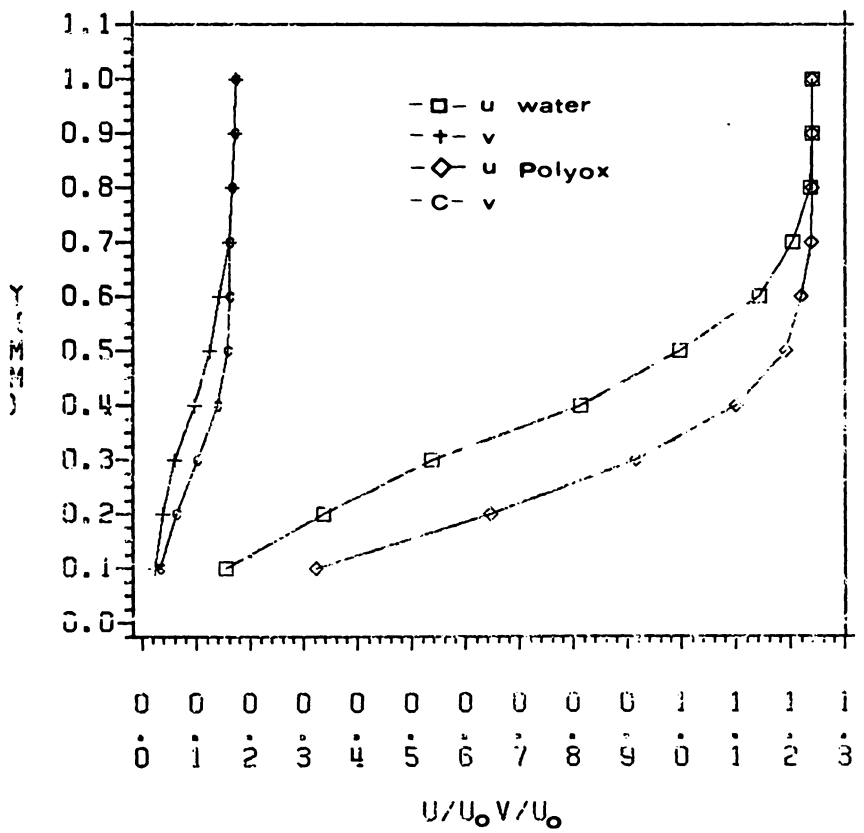

Figure 4.35 Laminar velocity profiles at θ=82 degrees-Re=20,875

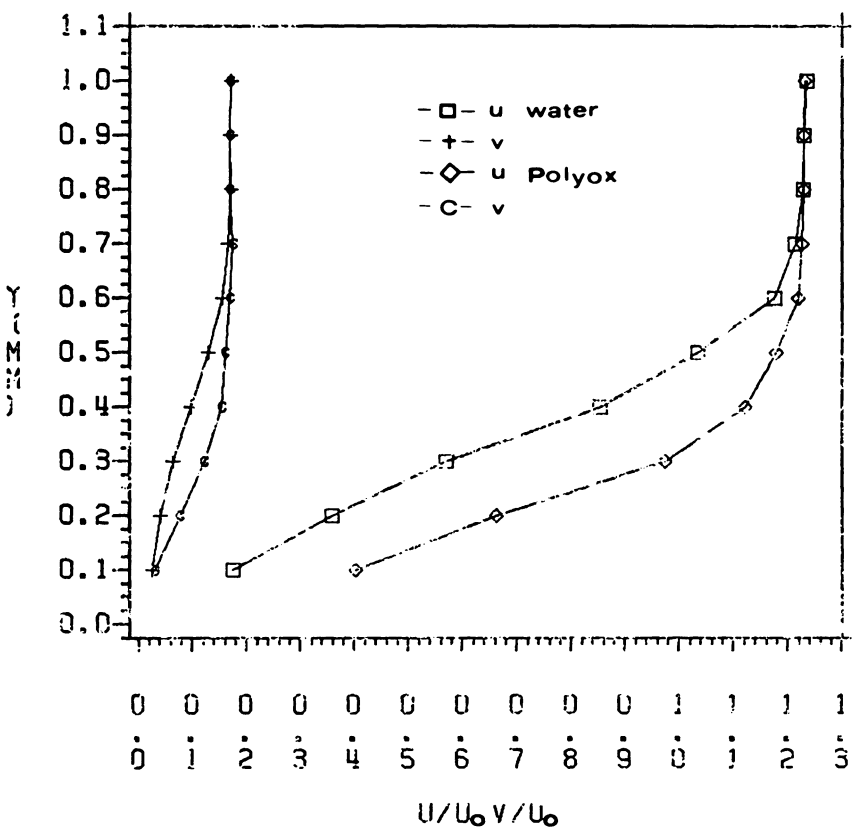

Figure 4.36 Laminar velocity profiles at θ=82 degrees-Re=27,500

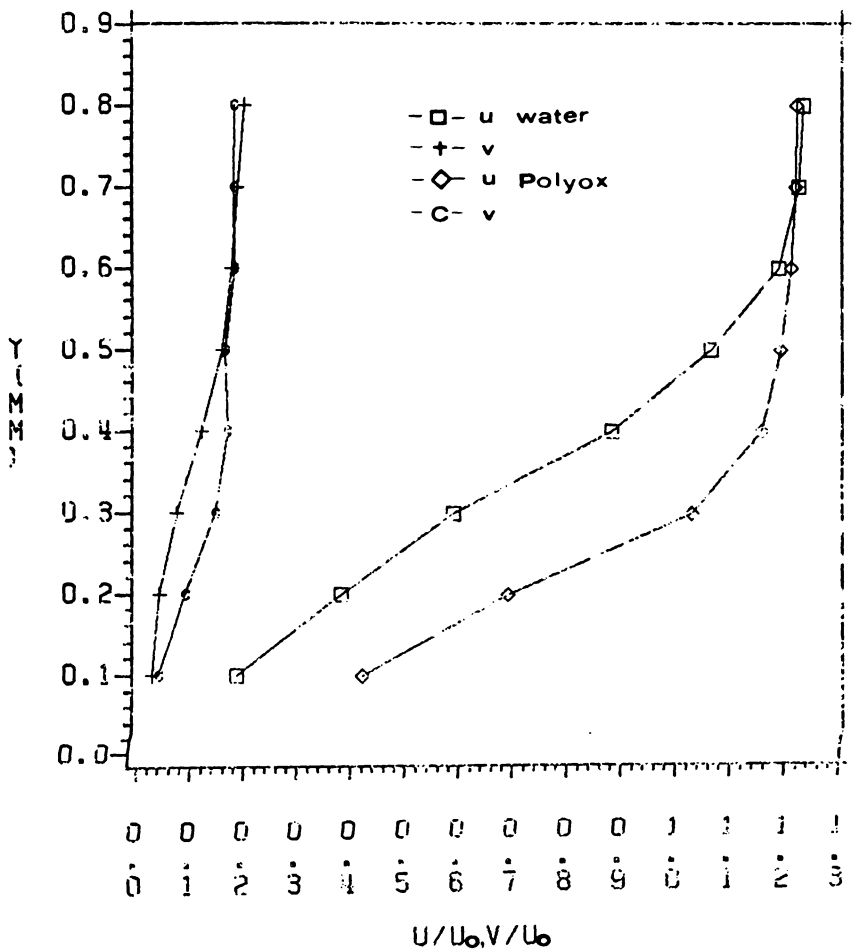

Figure 4.37 Laminar velocity profiles at θ=82 degrees-Re=34,300

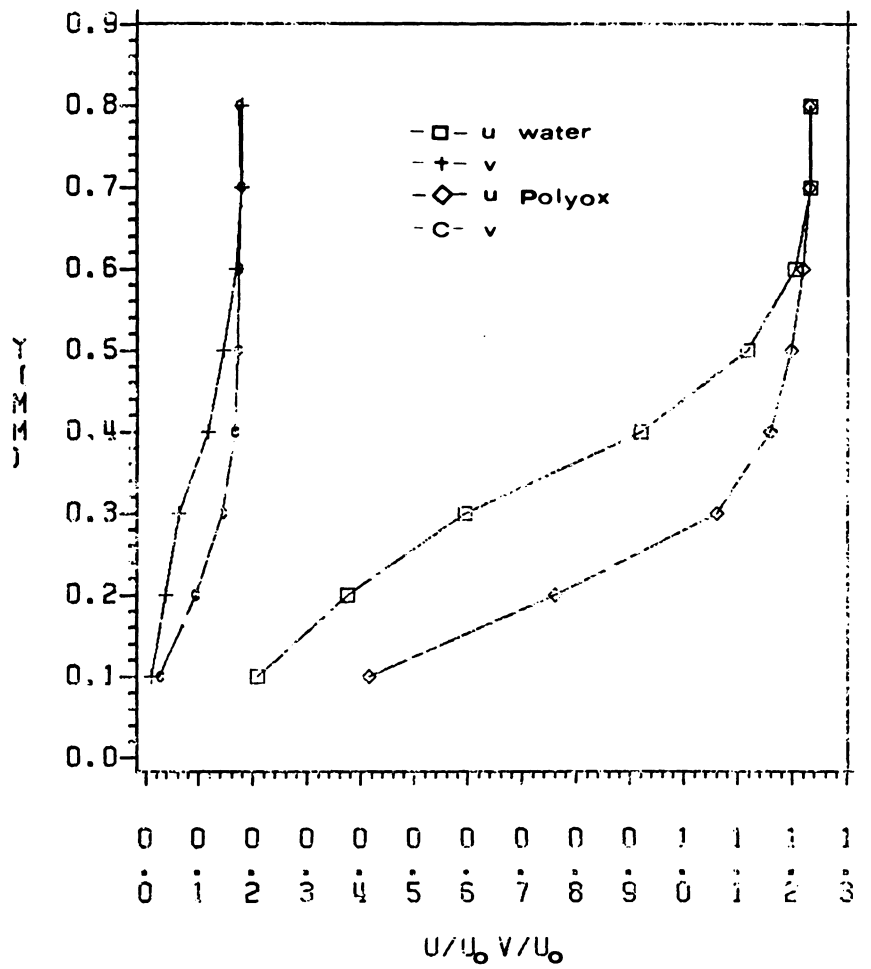

Figure 4.38 Laminar velocity profiles at θ=82 degrees-Re=41,200 (water and 100 wppm Polyox)

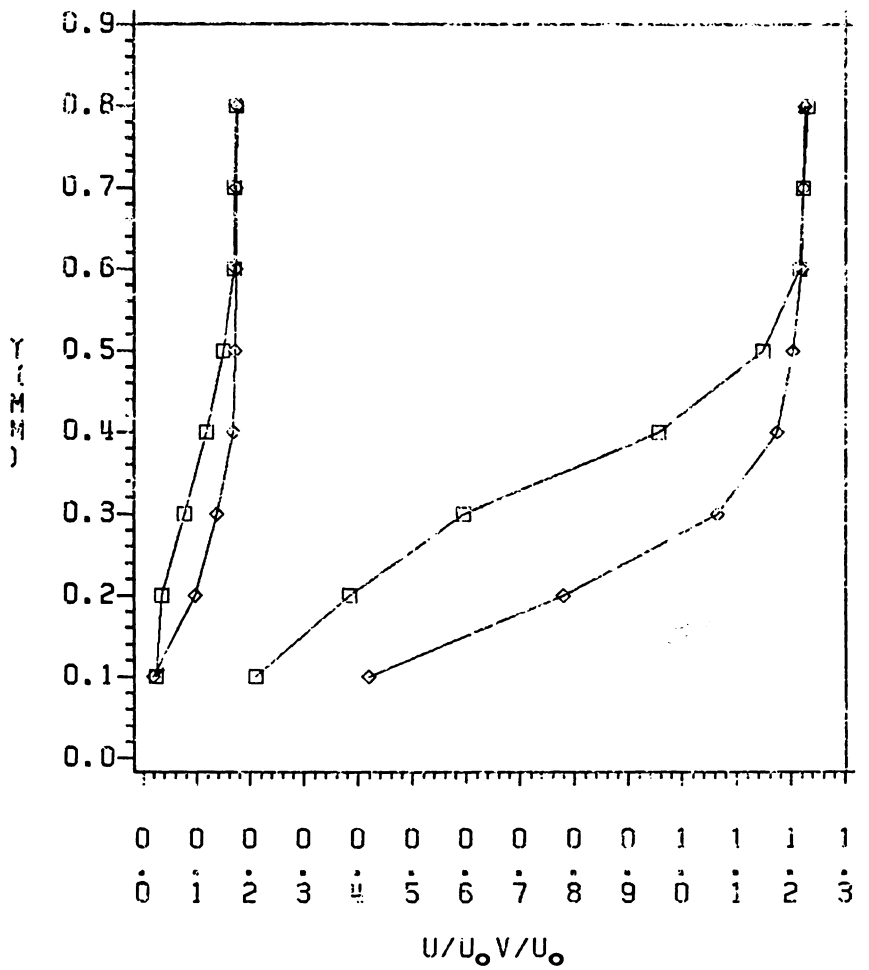

Figure 4.39 Laminar velocity profiles at θ=82 degrees-Re=48,060 (water and 100 wppm Polyox)

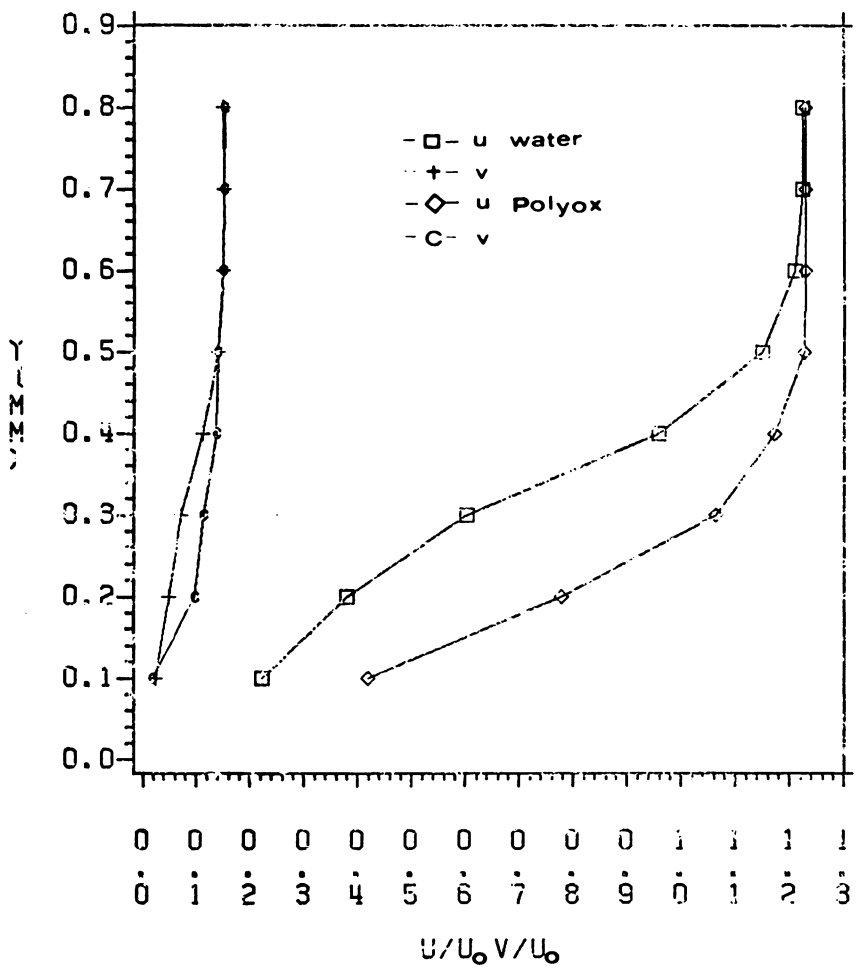

Figure 4.40 Laminar velocity profiles at θ=82 degrees-Re=55,000 (water and 100 wppm Polyox)

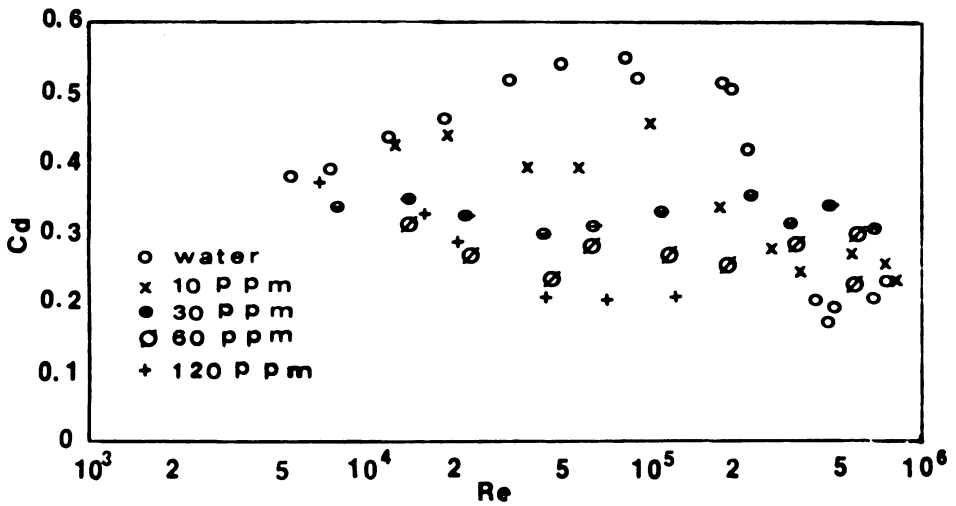

Figure 4.41 The drag of sphere in Polyox solutions (White 1962)
(water and 100 wppm Polyox)

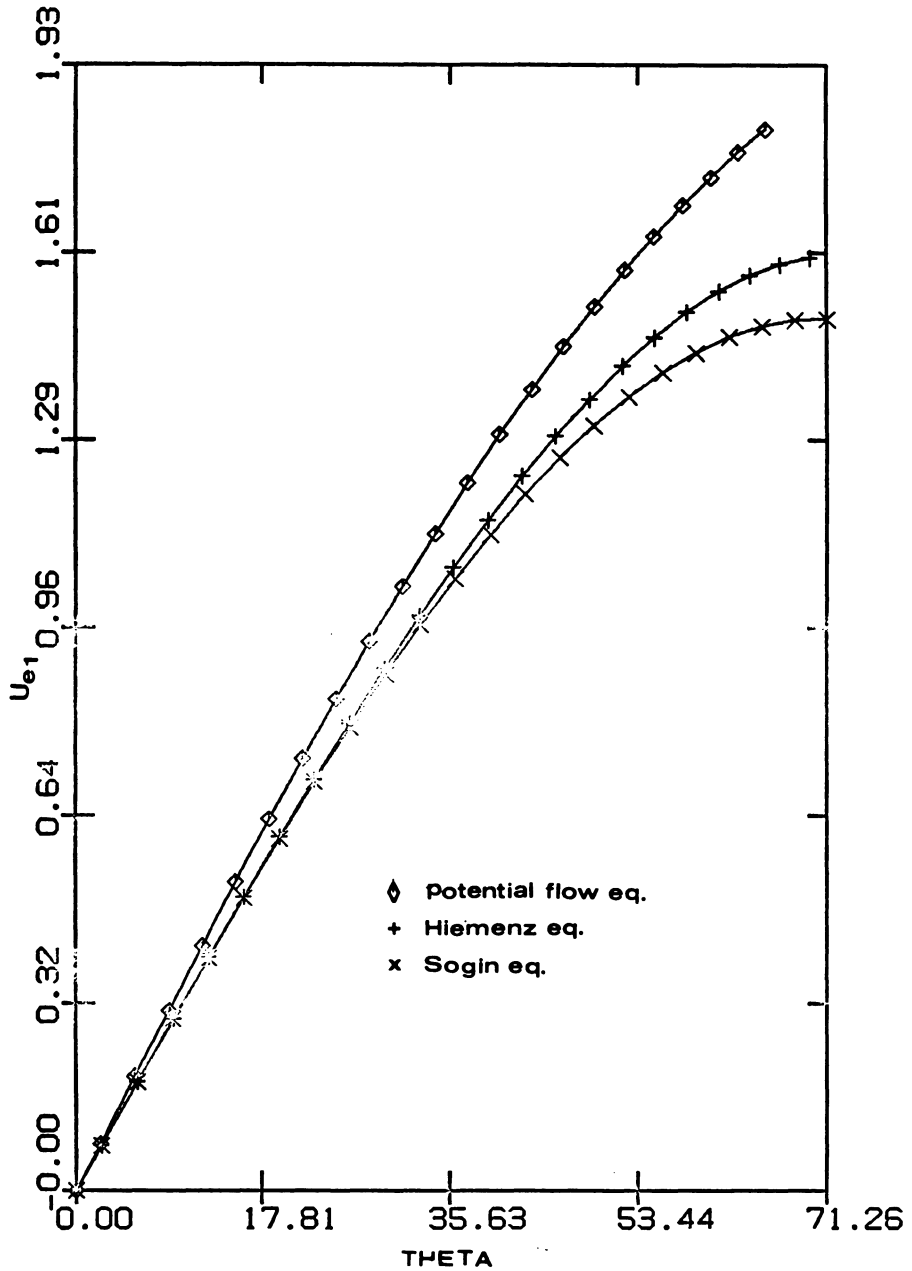

Figure 5.1 Typical outer flow velocity distributions around a circular cylinder in crossflow

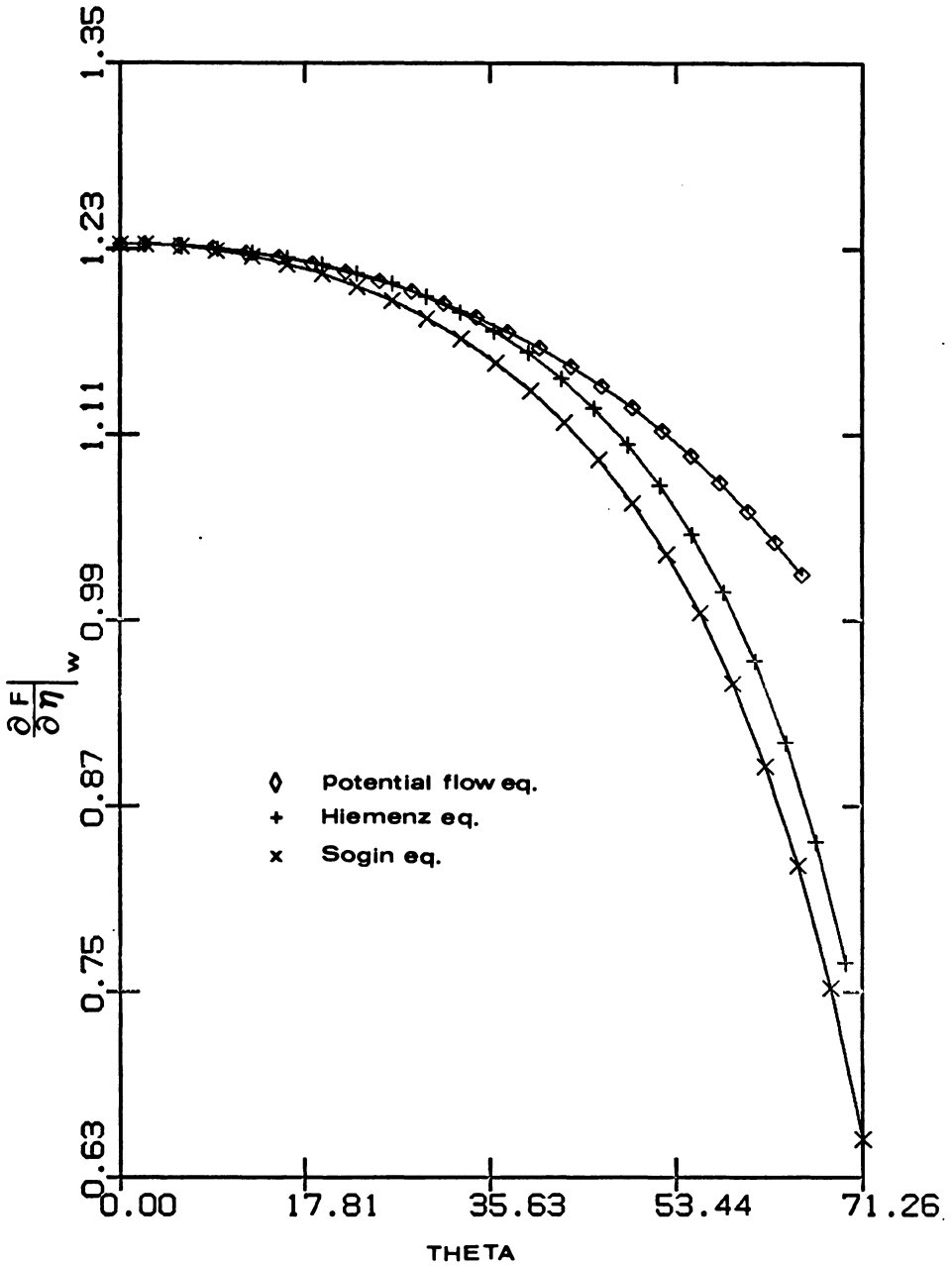

Figure 5.2 Wall velocity gradient corresponding to the outer flow of Fig. 5-1

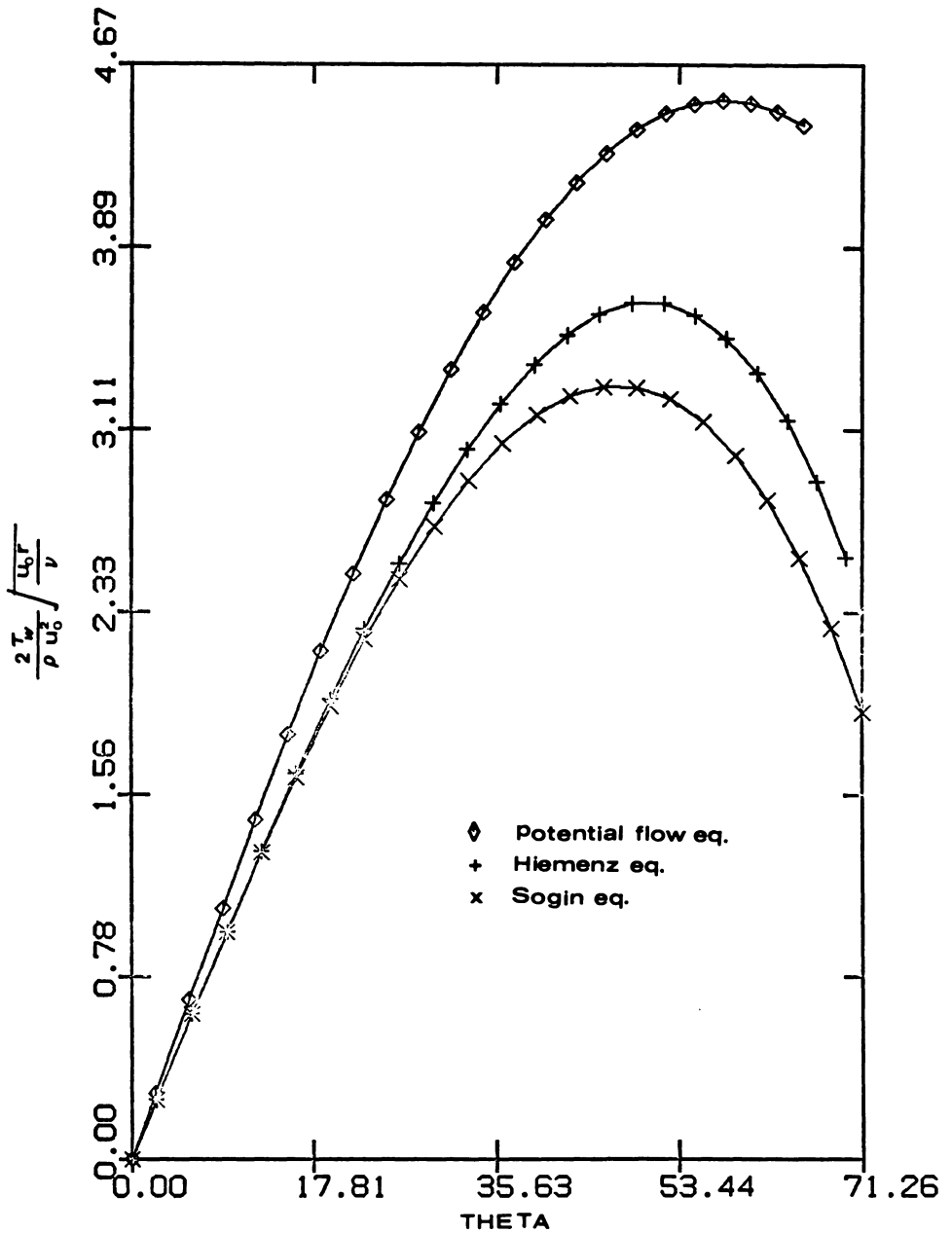

Figure 5.3 Skin frictiopn corresponding to the outer flow of Fig. 5-1

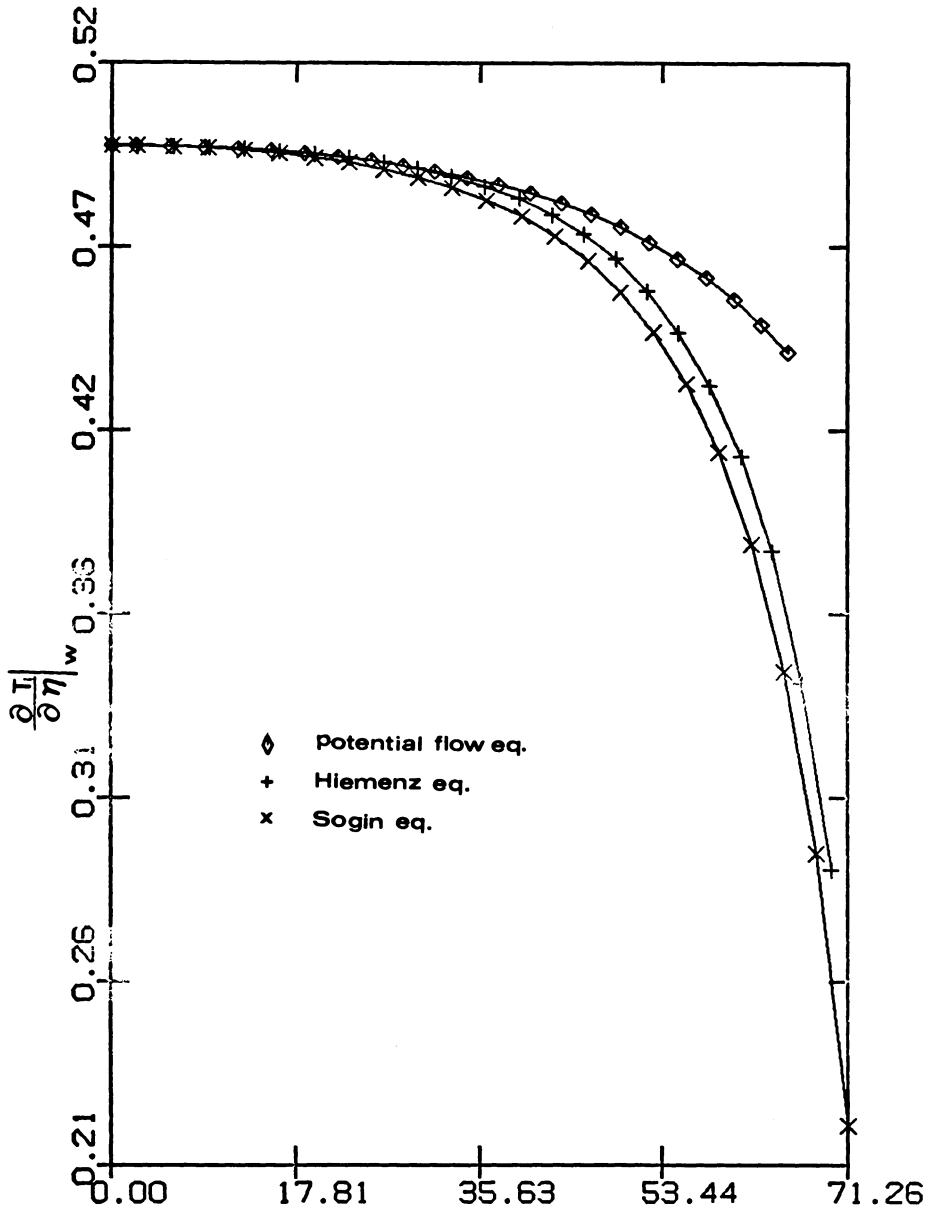

Figure 5.4 Wall temperature gradient corresponding to the outer flow of Fig. 5-1

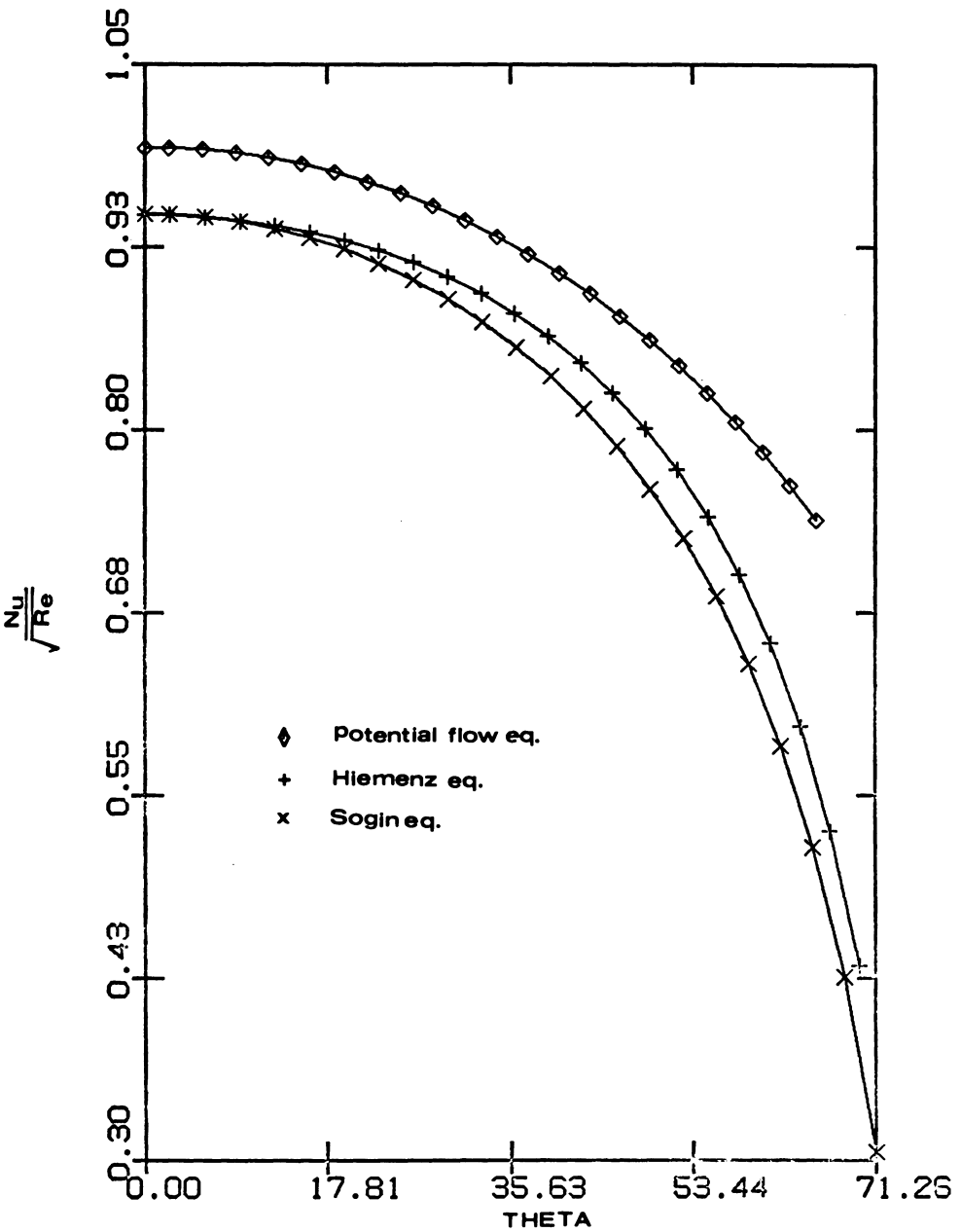

Figure 5.5 Local rate of steady heat transfer corresponding to the outer flow of Fig. 5-1

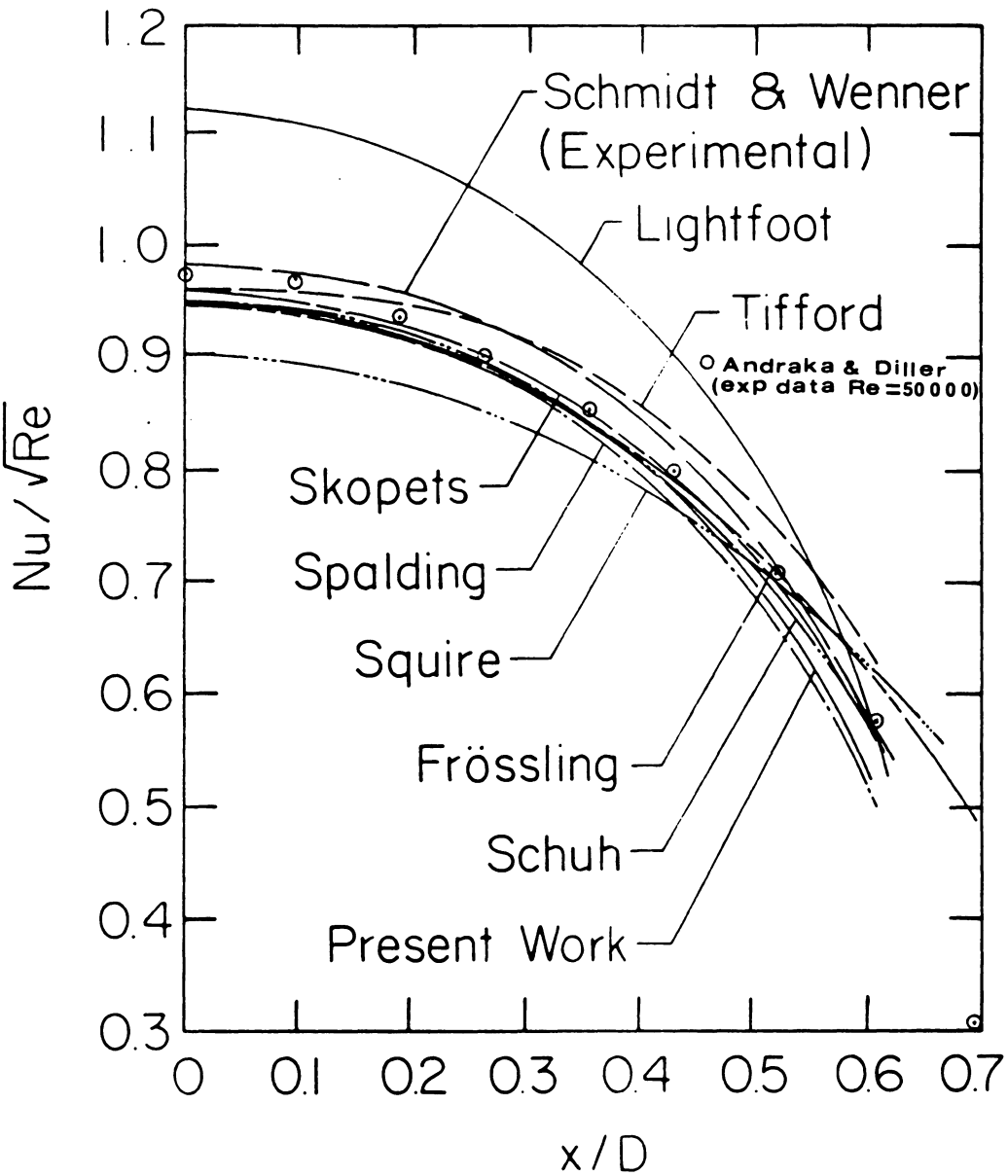

Figure 5.6 Overview of steady heat transfer

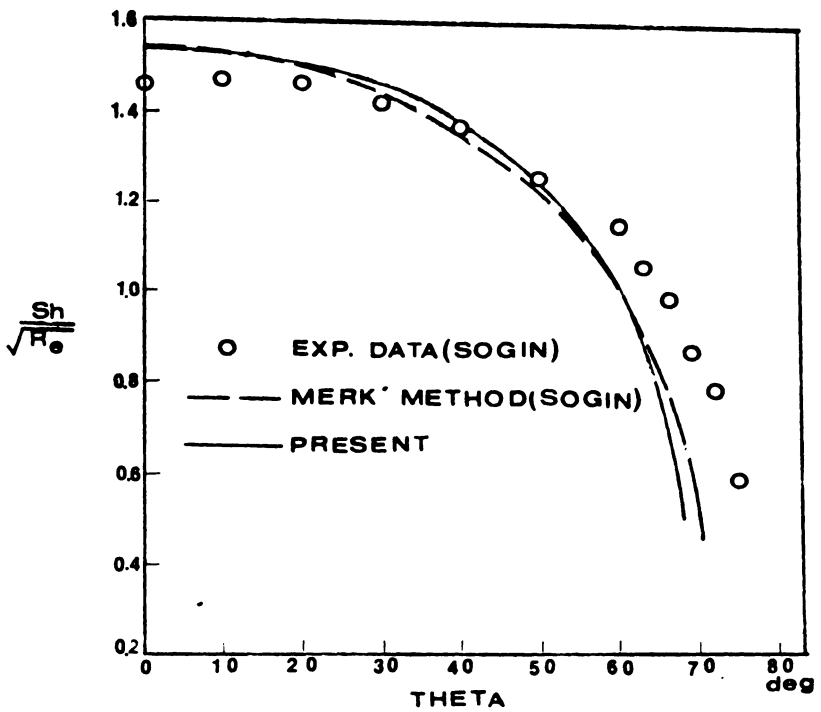

Figure 5.7 Local rate of mass transfer
(Sublimation of naphthalene into air)

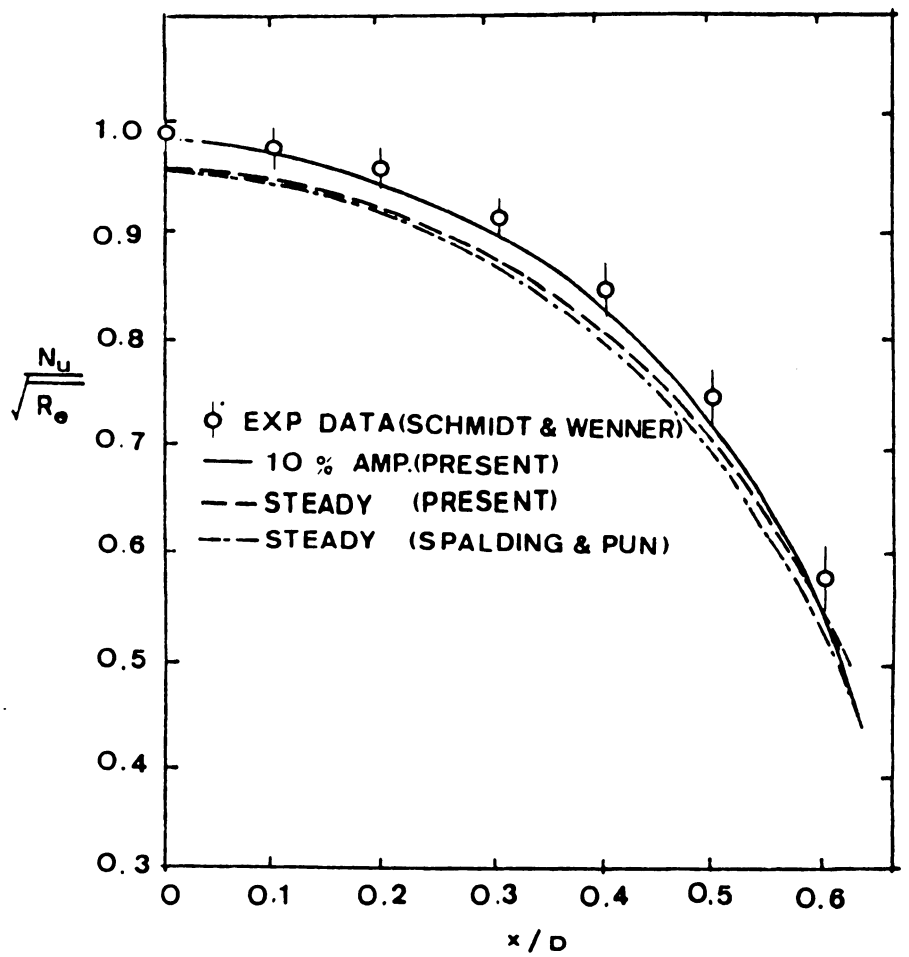

Figure 5.8 Periodic mean rate of heat transfer with 10% free stream amplitude(St=.21)

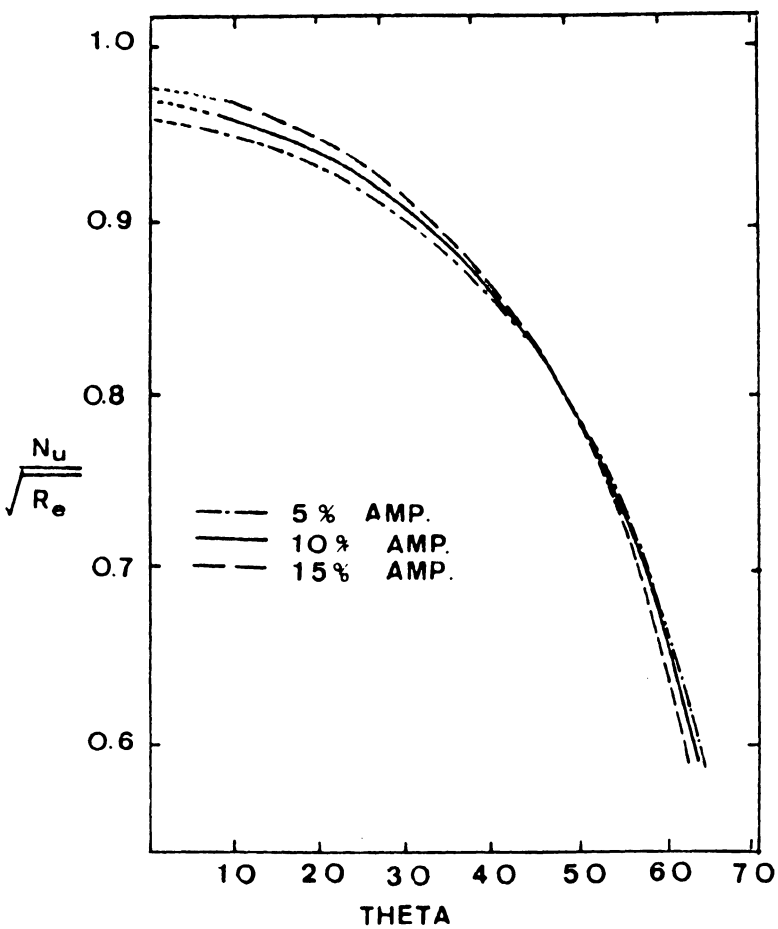

Figure 5.9 Periodic mean rate of heat transfer as a function of free stream amplitude(St=.21)

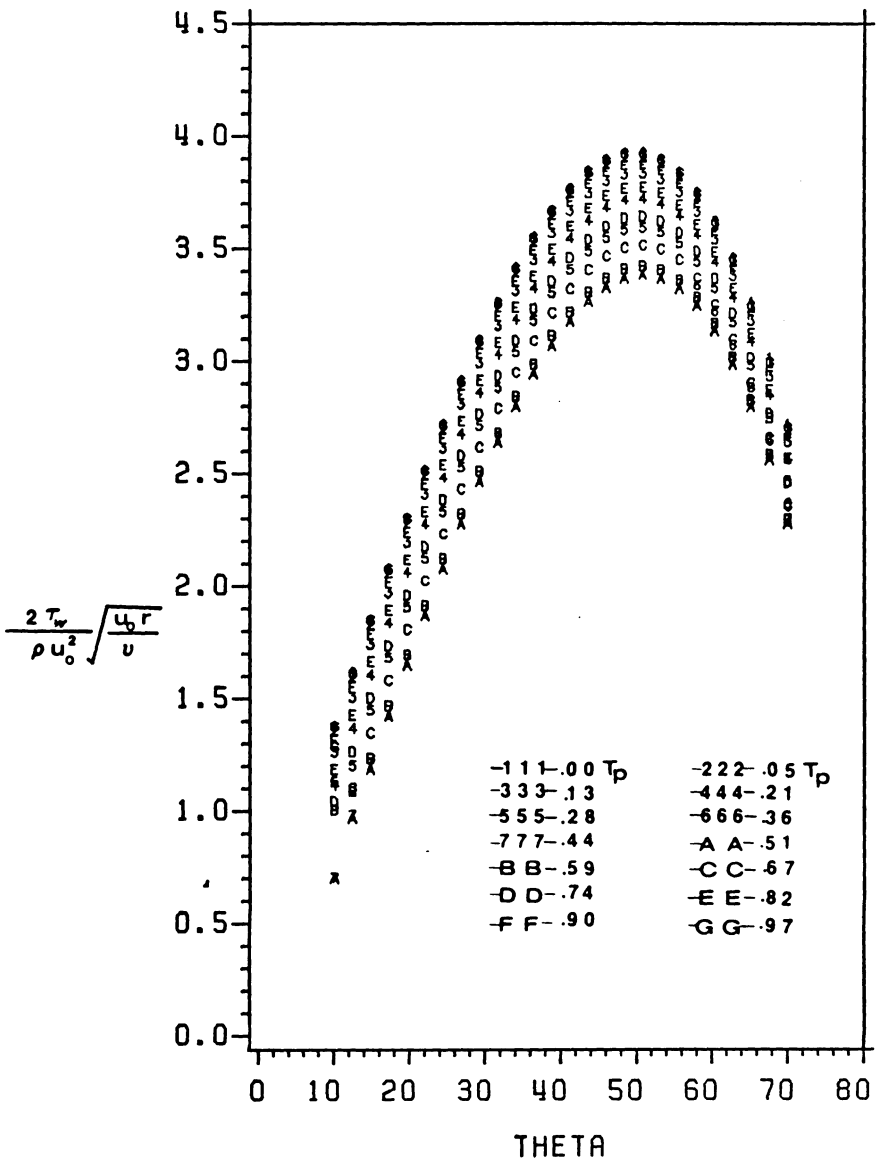

Figure 5.10 Periodic variation of skin friction

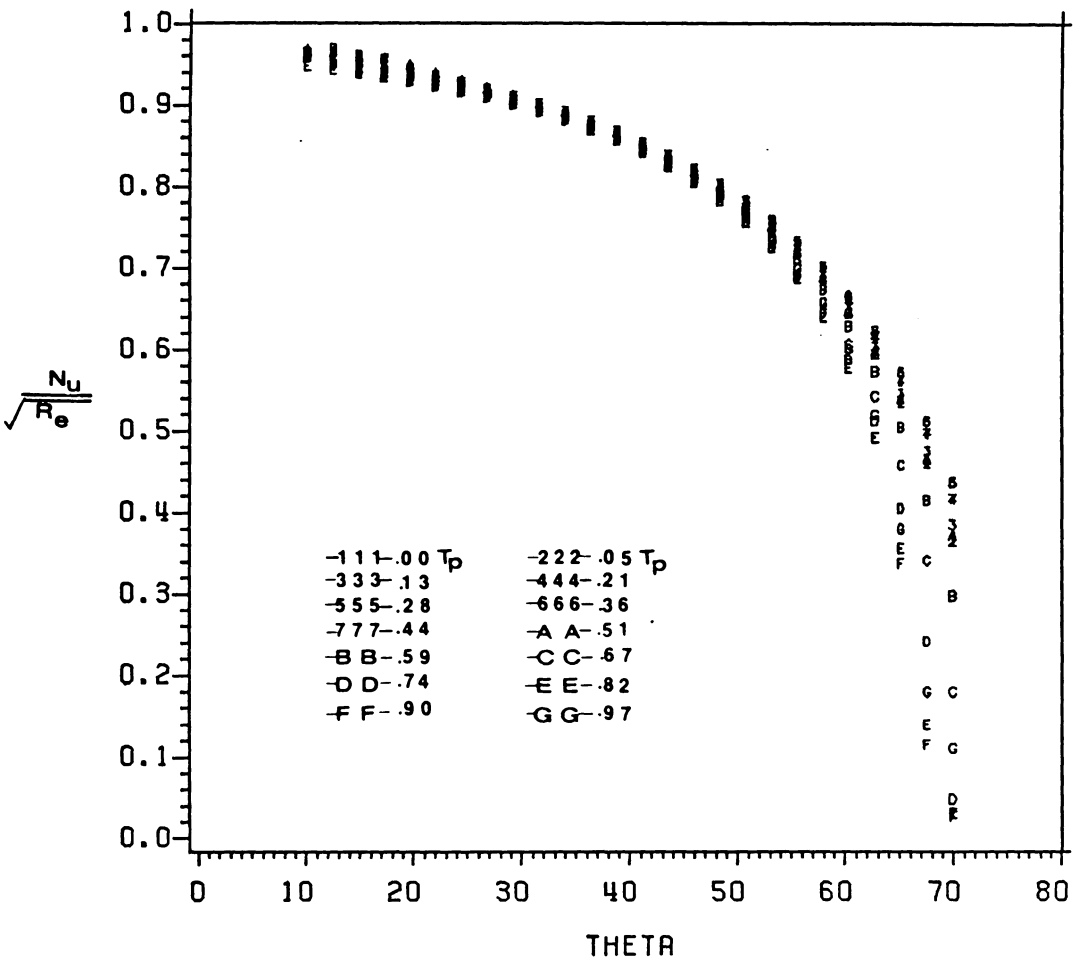

Figure 5.11 Periodic variation of local heat transfer

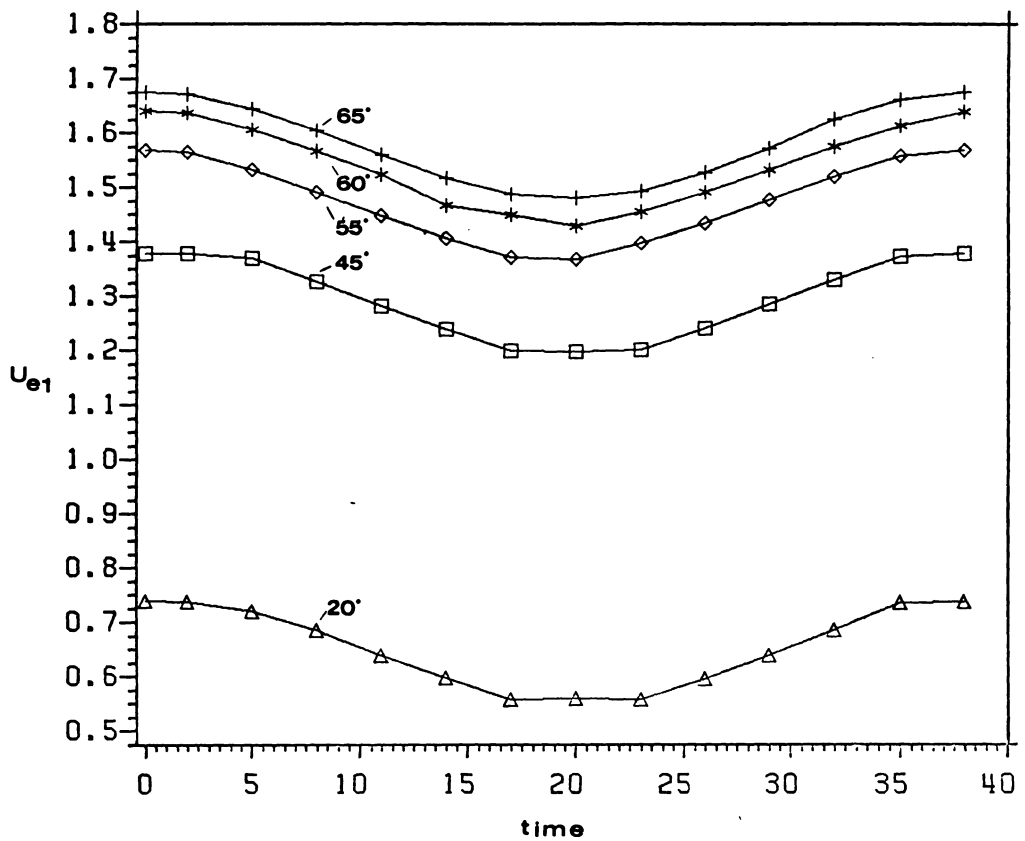

Figure 5.12 Periodic variation of outer flow at selected angles

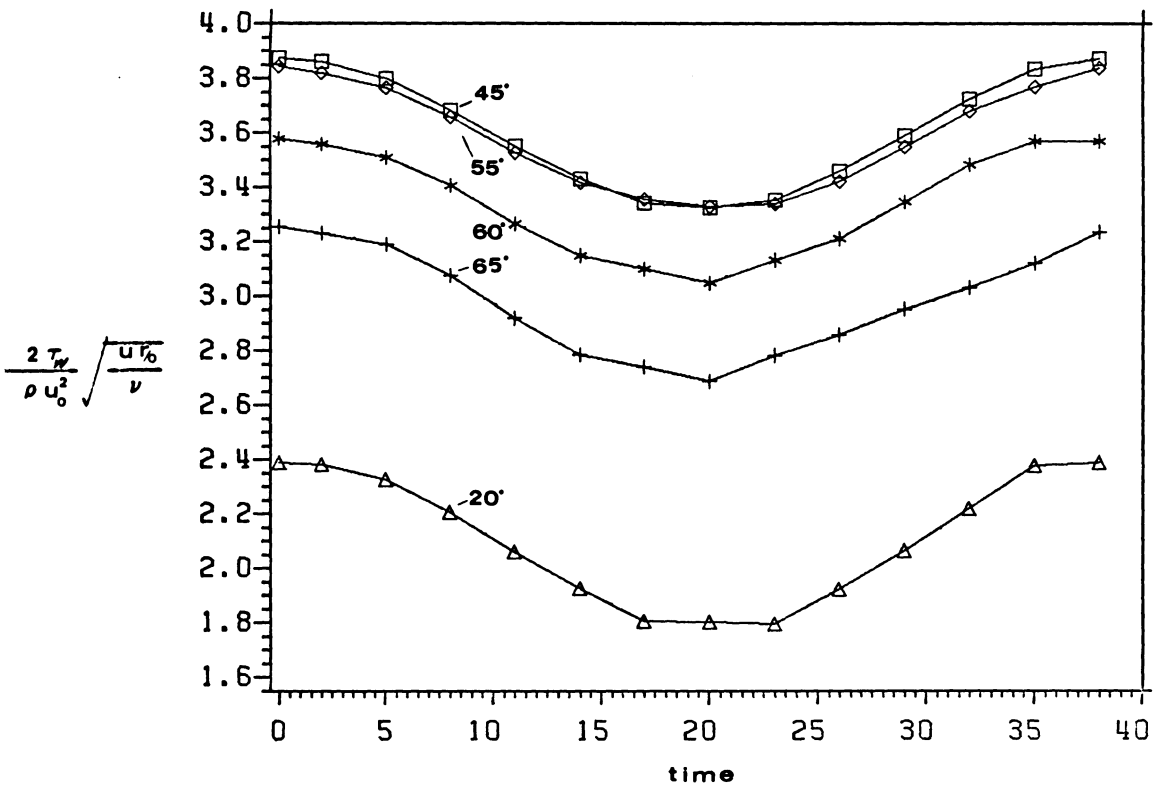

Figure 5.13 Periodic variation of skin friction selected angles

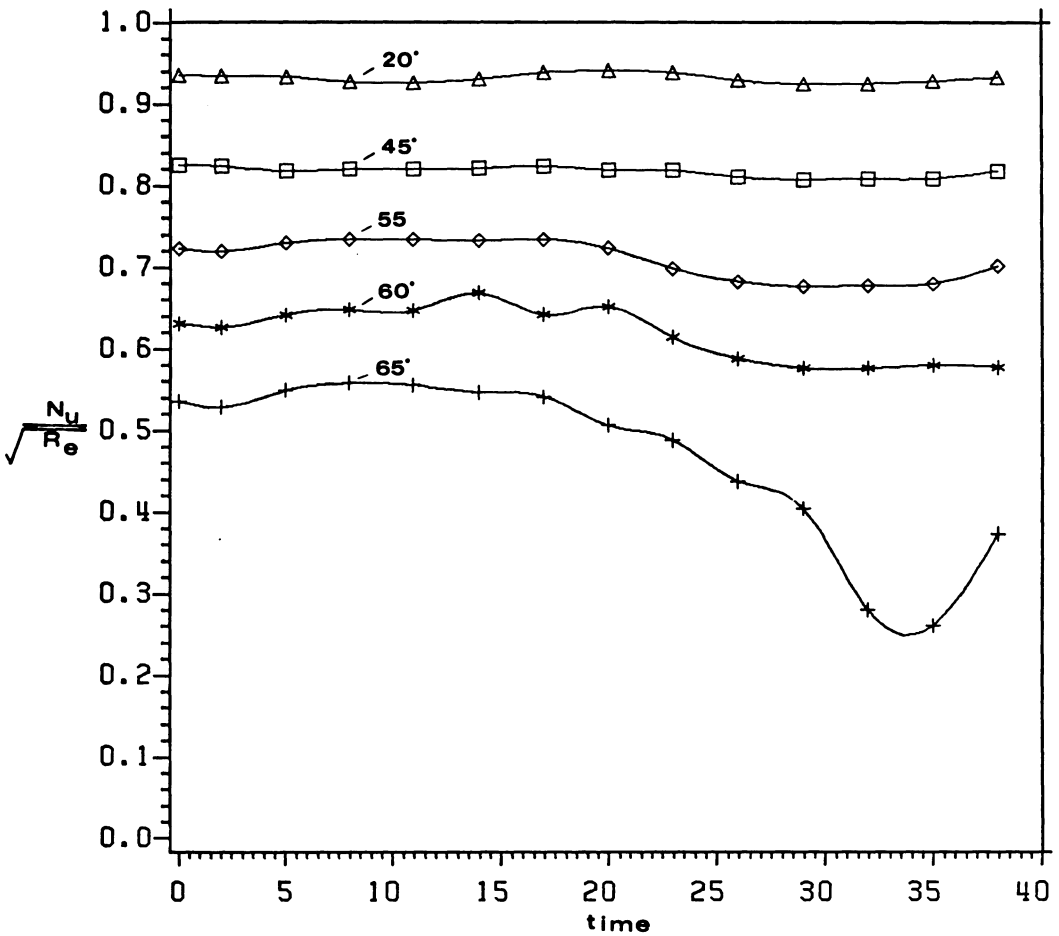

Figure 5.14 Periodic variation of heat transfer at selected angles

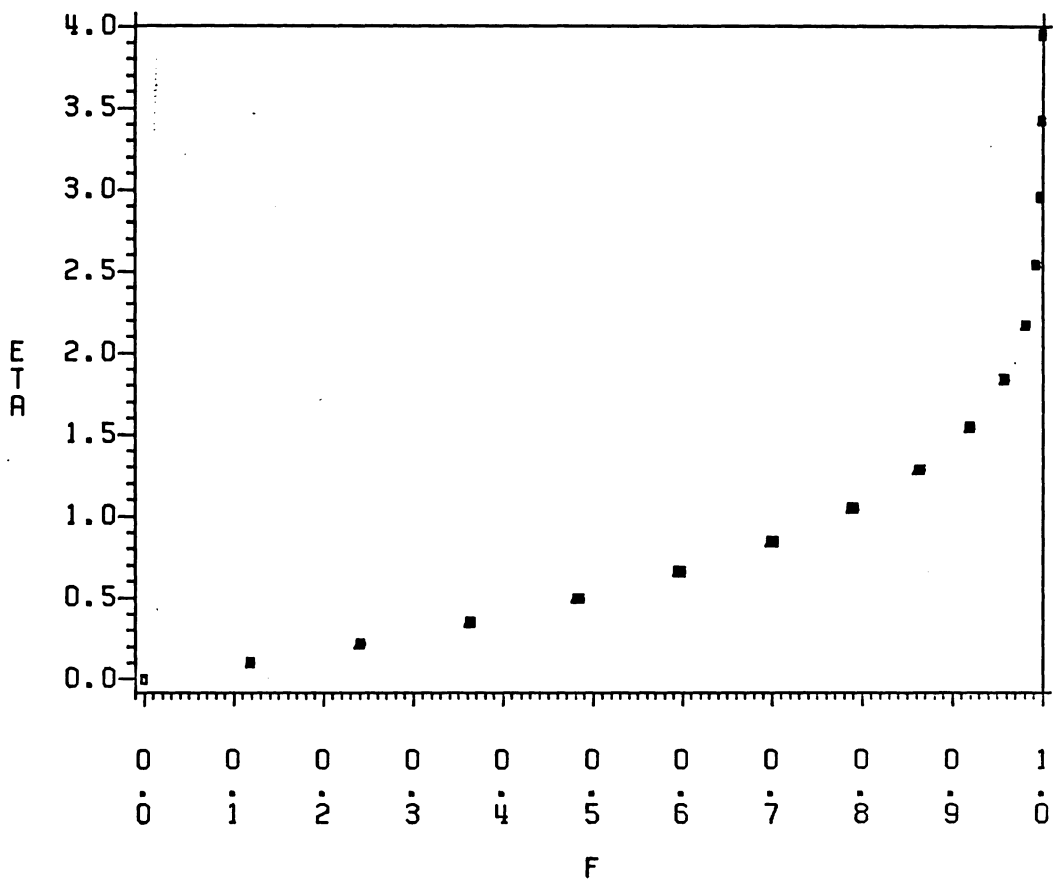

Figure 5.15 Boundary-layer velocity amplitude at θ=20 degrees

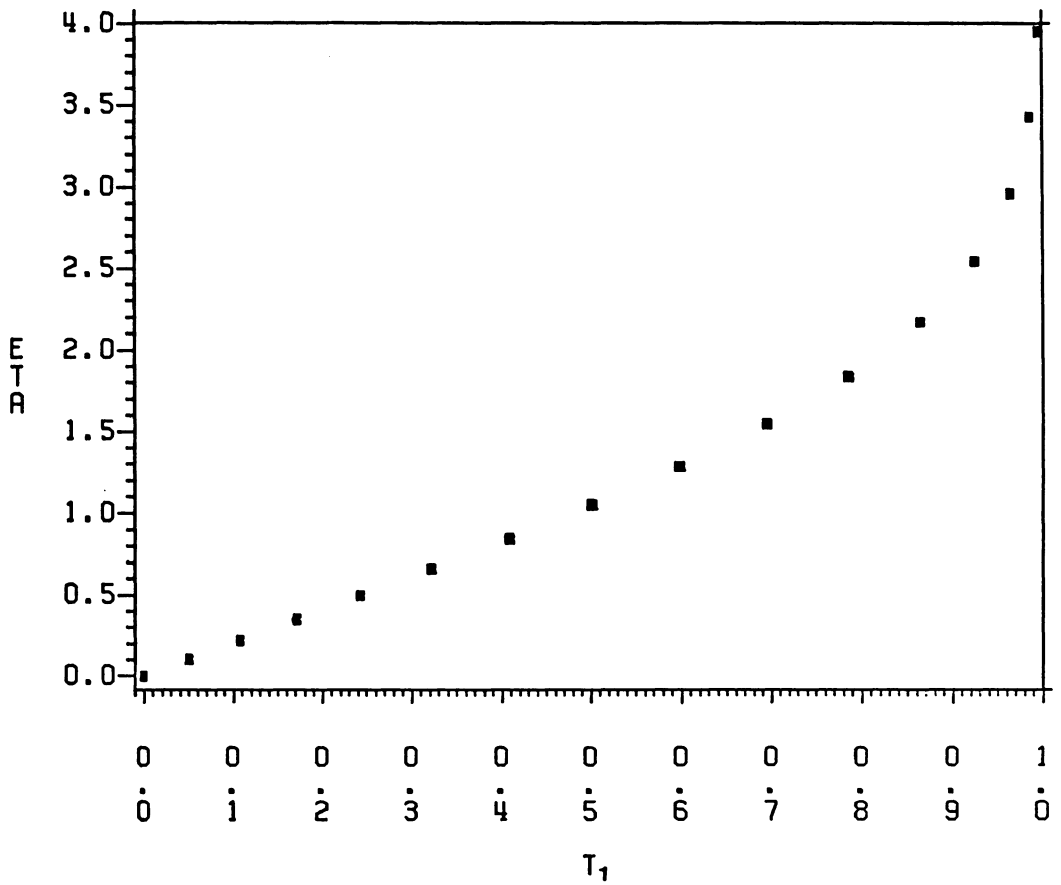

Figure 5.16 Boundary-layer temperature amplitude at θ=20 degrees

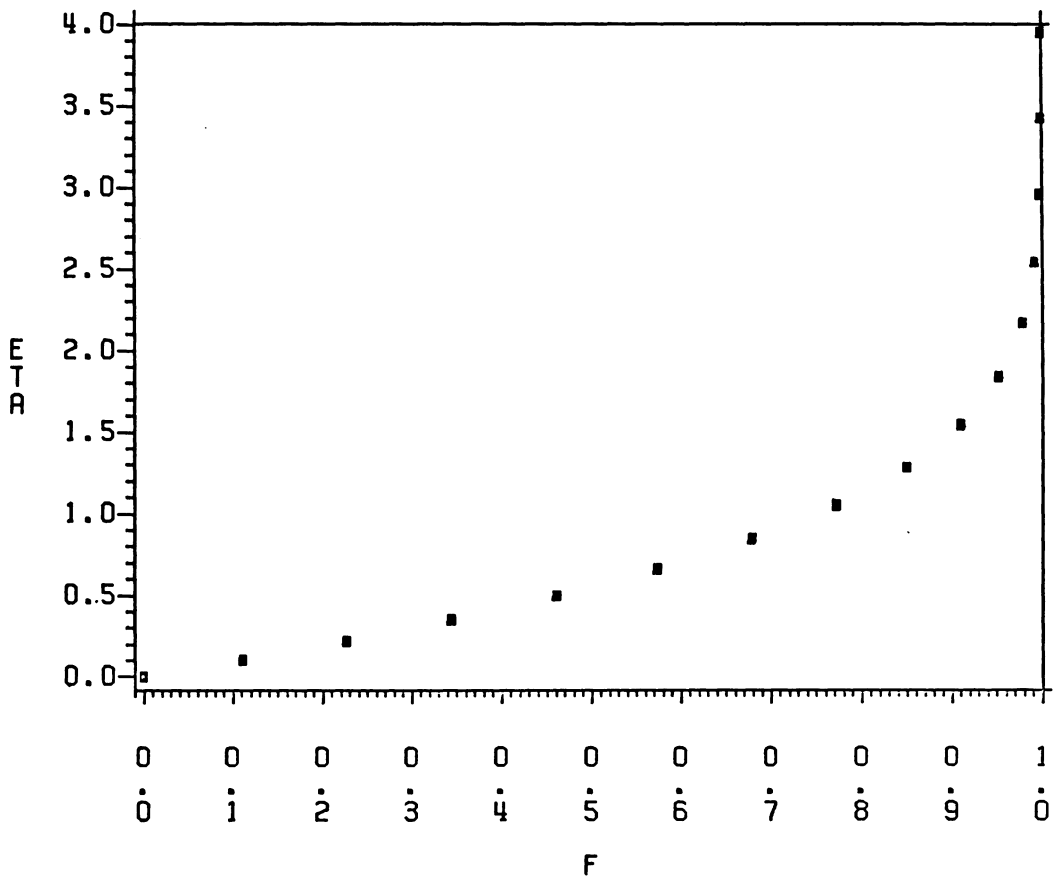

Figure 5.17 Boundary-layer velocity amplitude at θ=45 degrees

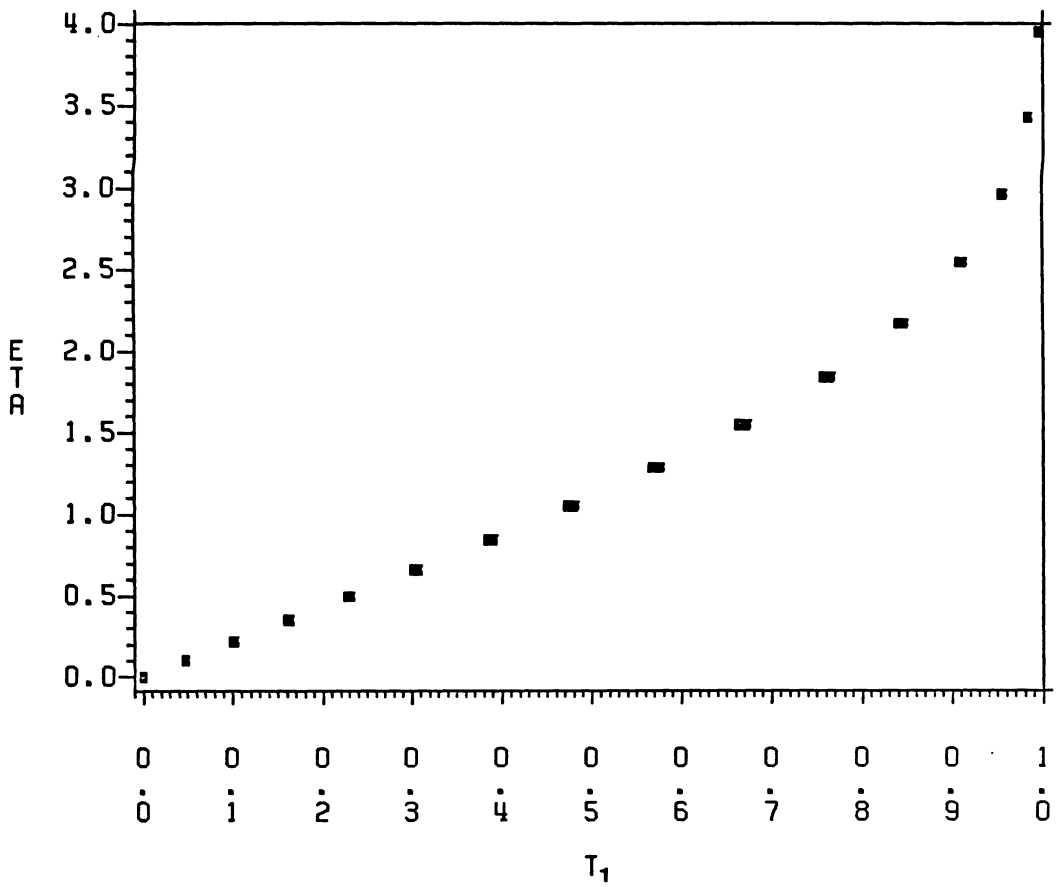

Figure 5.18 Boundary-layer temperature amplitude at θ=45 degrees

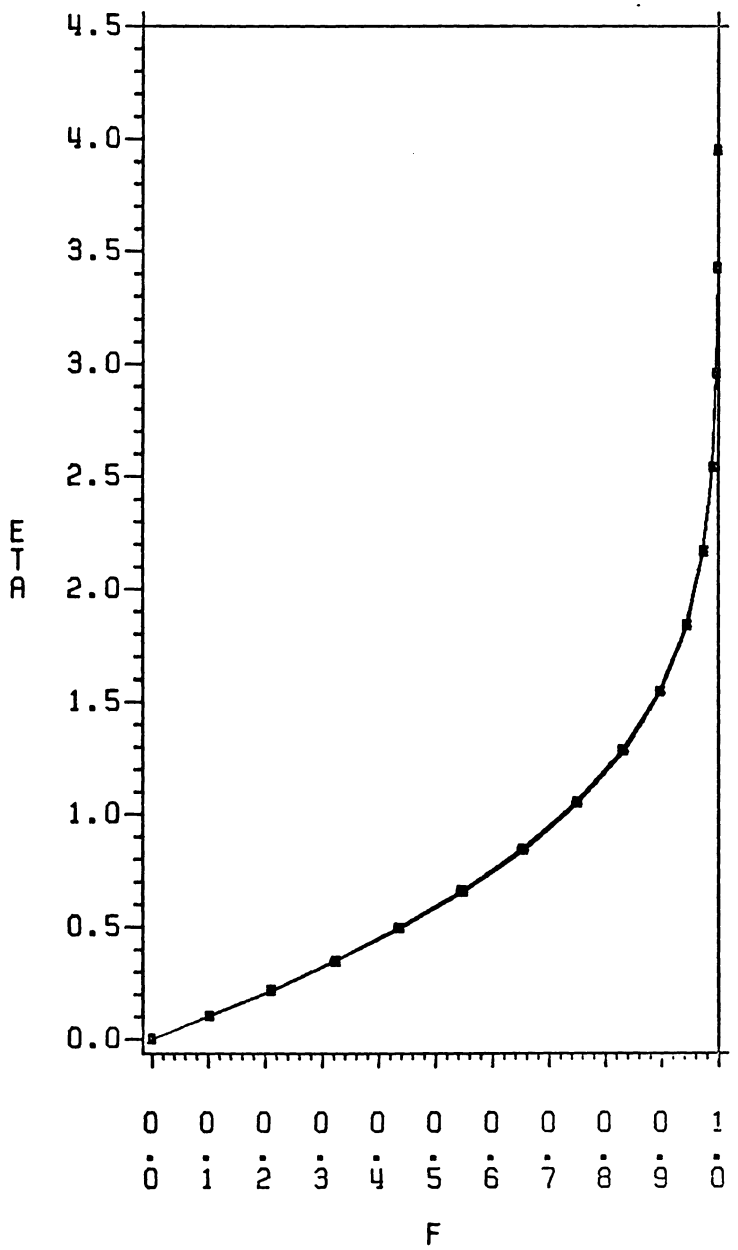

Figure 5.19 Boundary-layer velocity amplitude at θ=55 degrees

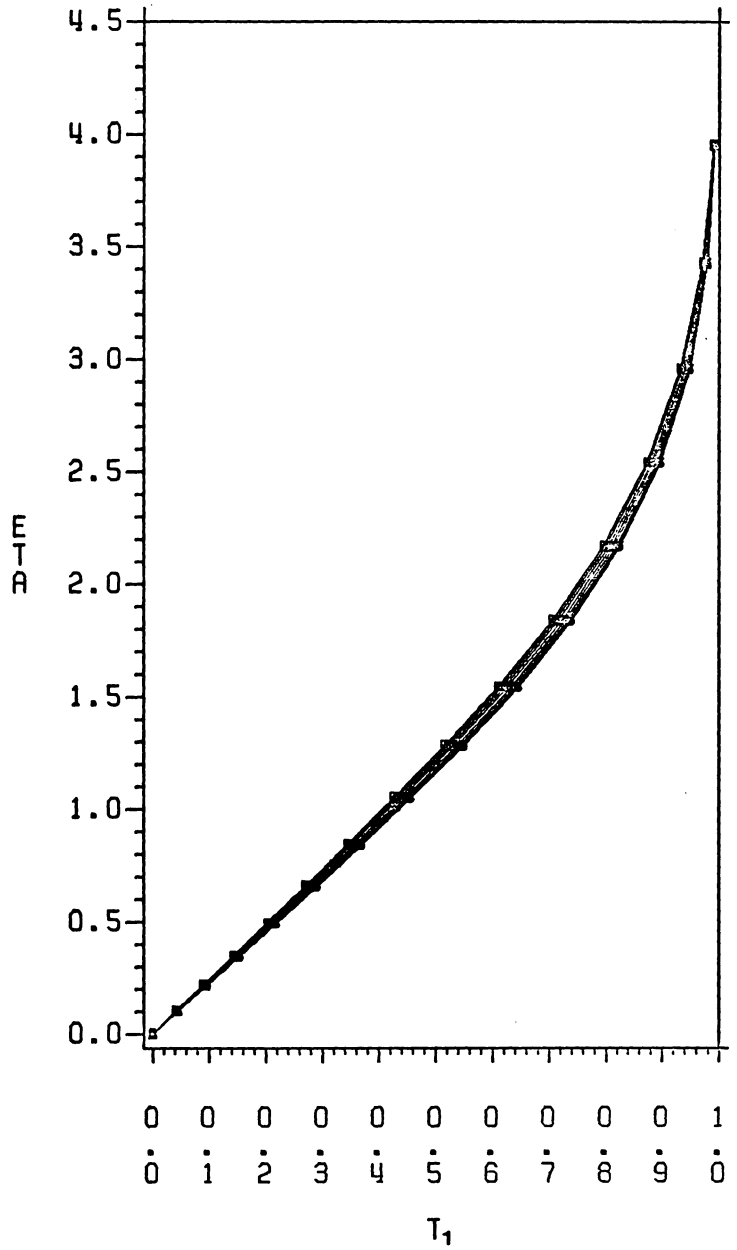

Figure 5.20 Boundary-layer temperature amplitude at θ=55 degrees

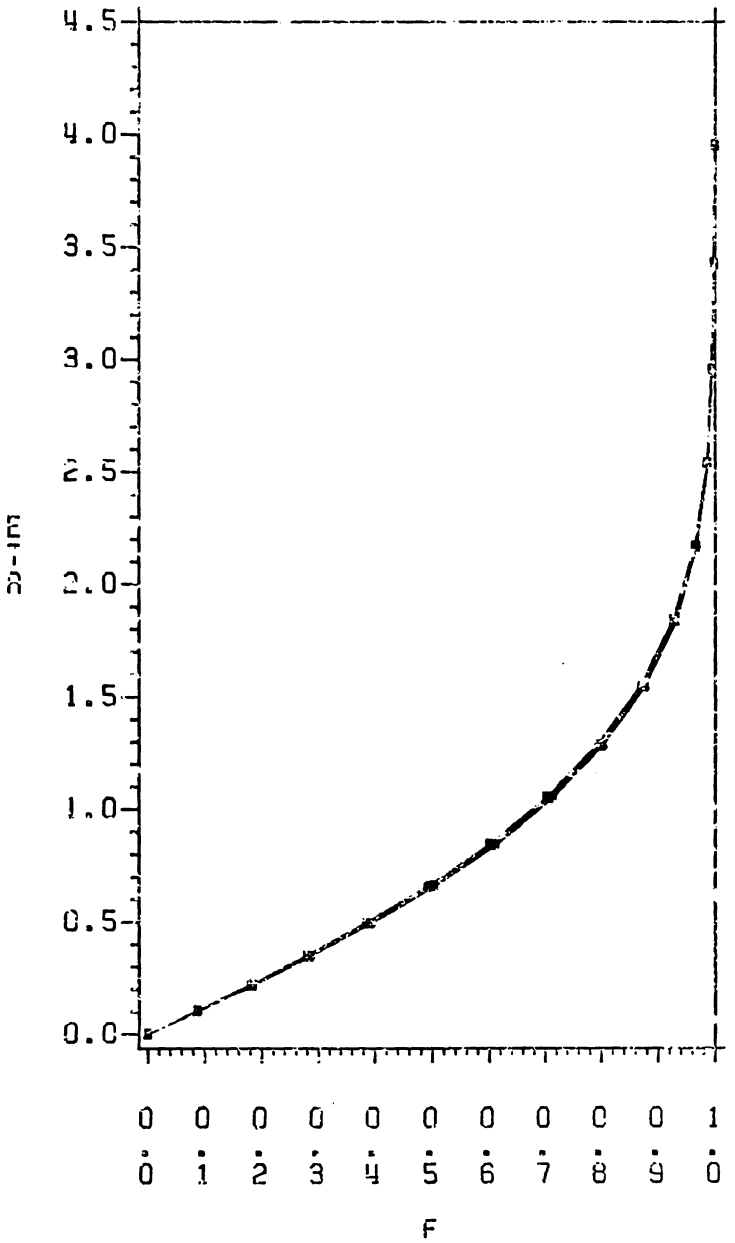

Figure 5.21 Boundary-layer velocity amplitude at θ=65 degrees

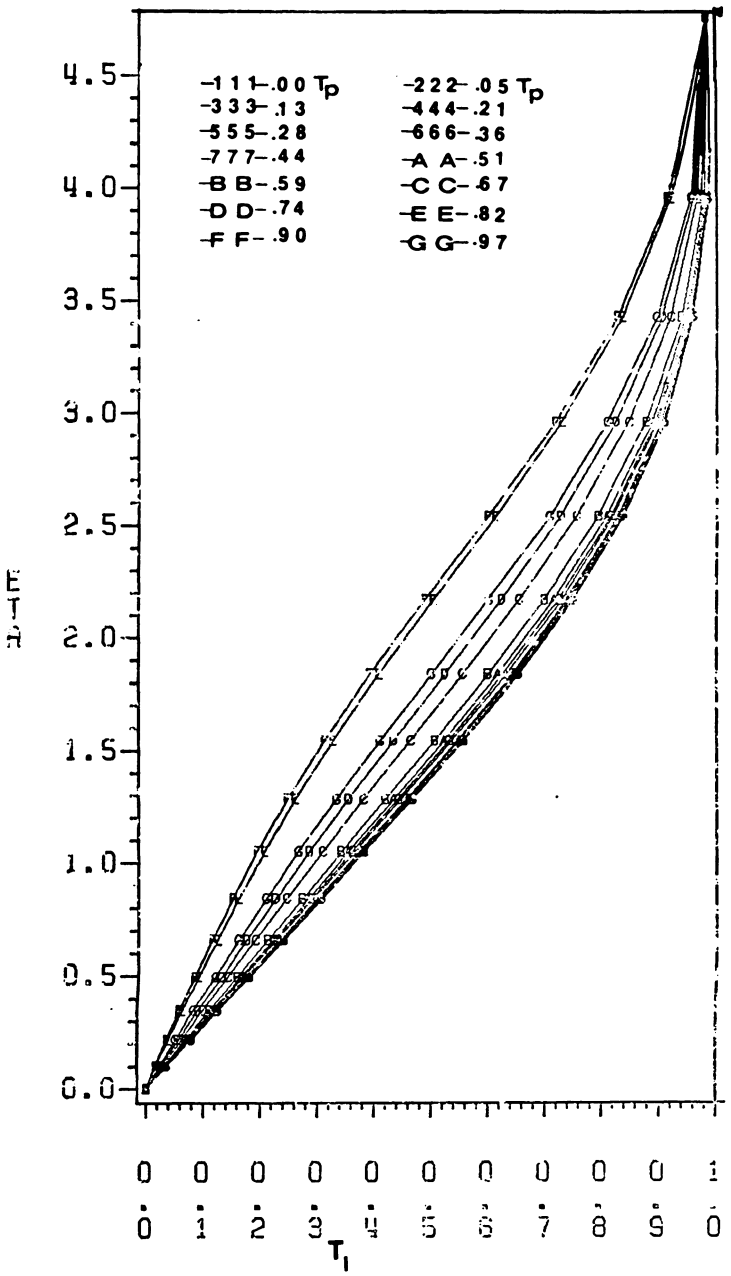

Figure 5.22 Boundary-layer temperature amplitude at θ=65 degrees

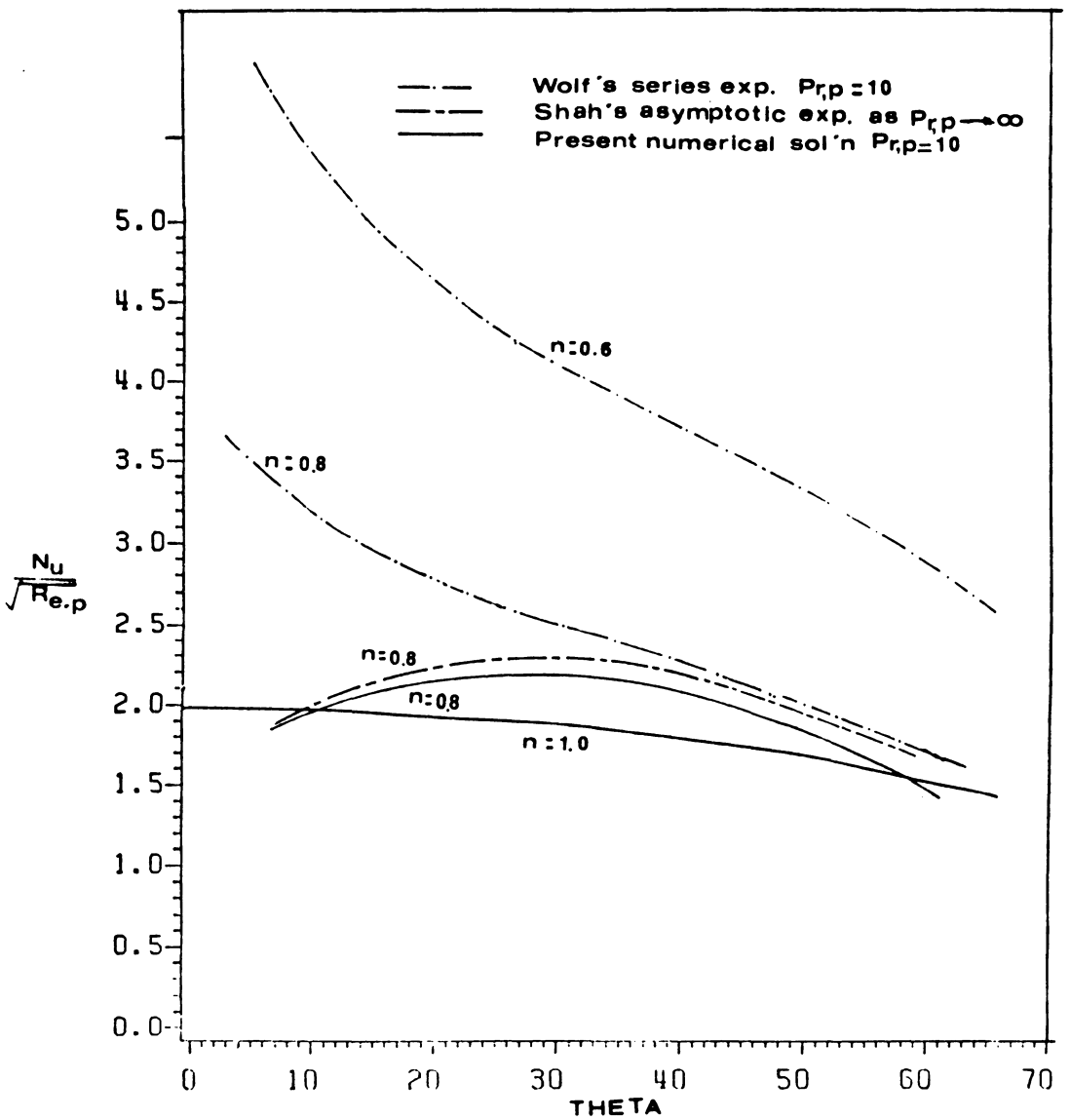

Figure 5.23 Local rate of heat transfer for pseudoplastic materials(n=0.8)

(n=0.8

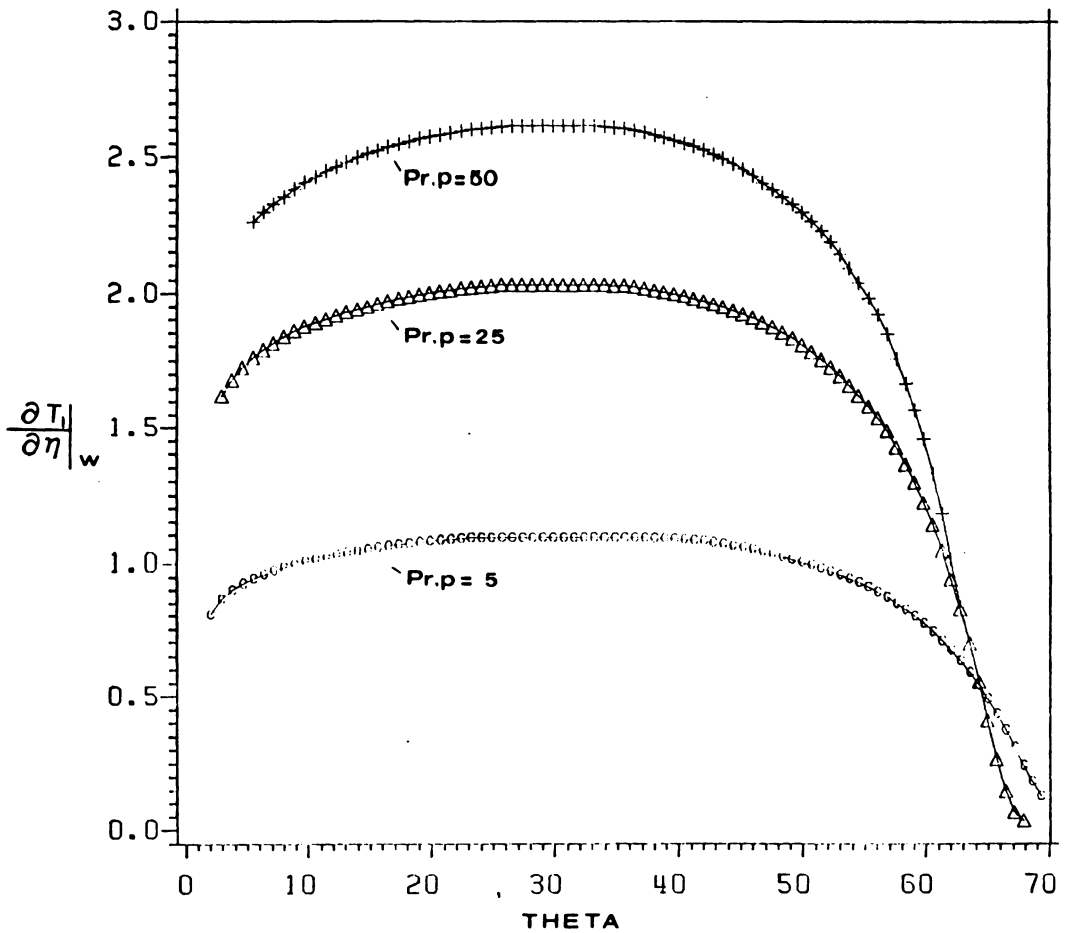

Figure 5.24 Wall temperature gradient of pseudoplastic materials as a function of the generalized prandtl number(n=0.8)

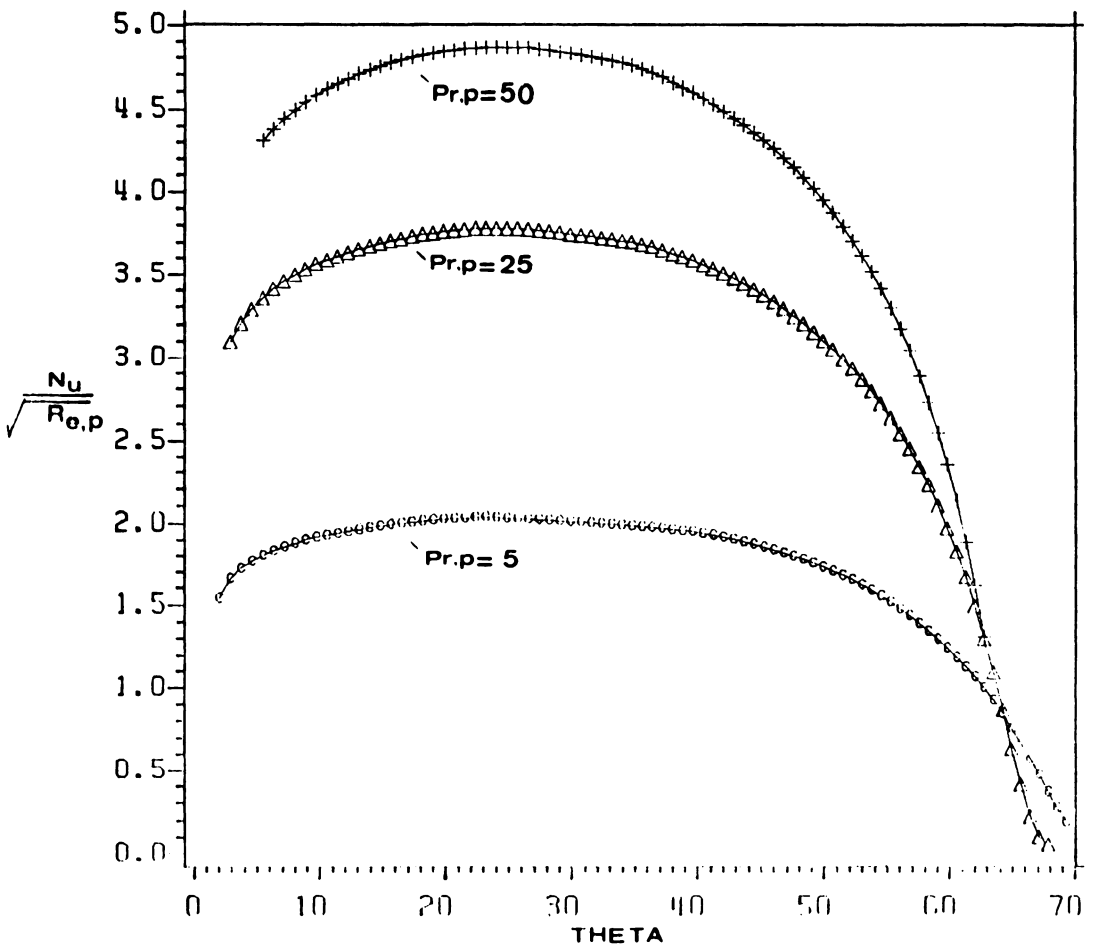

Figure 5.25 Local rate of heat transfer of pseudoplastic materials as a function of the generalized prandtl number(n=0.8)

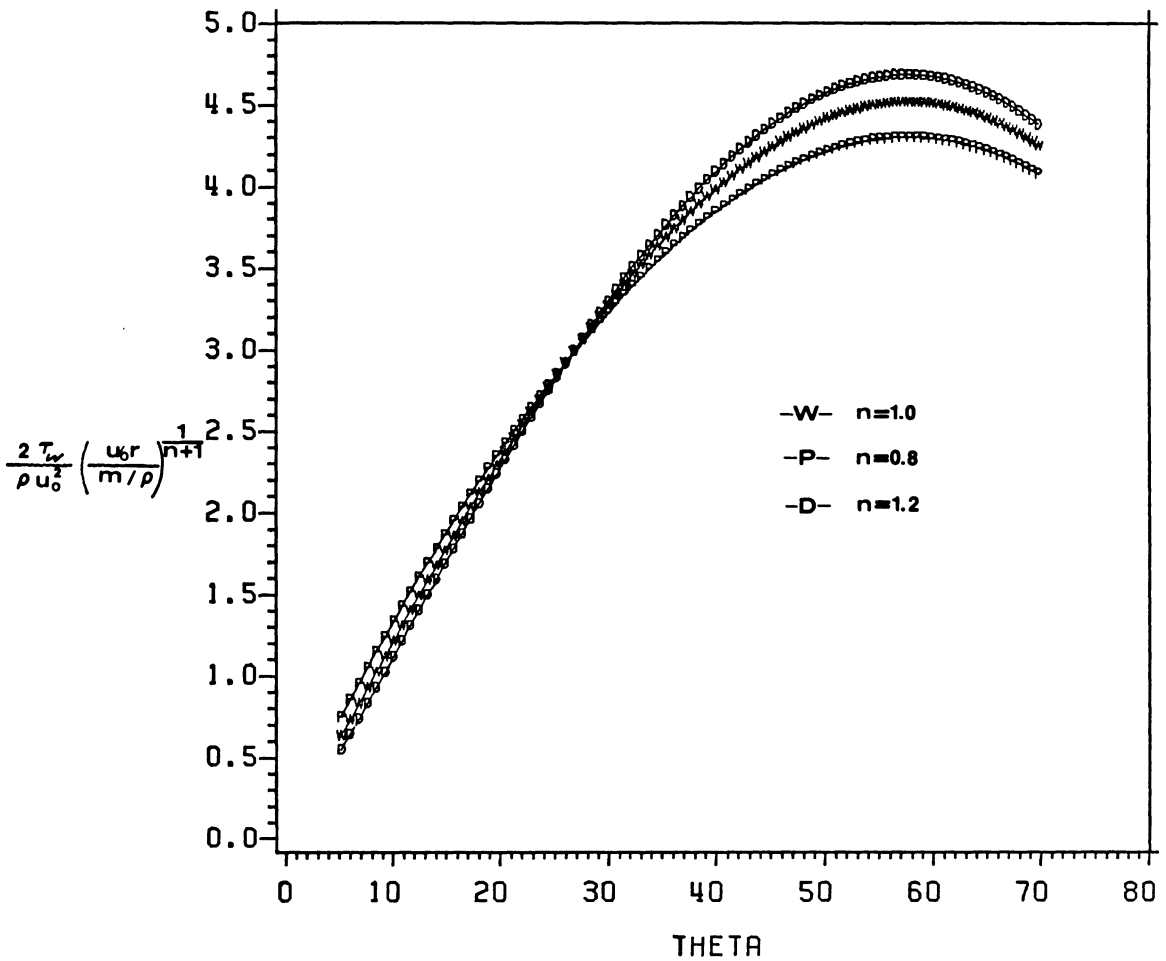

Figure 5.26 Skin friction of power-law materials predicted with potenrial flow equation

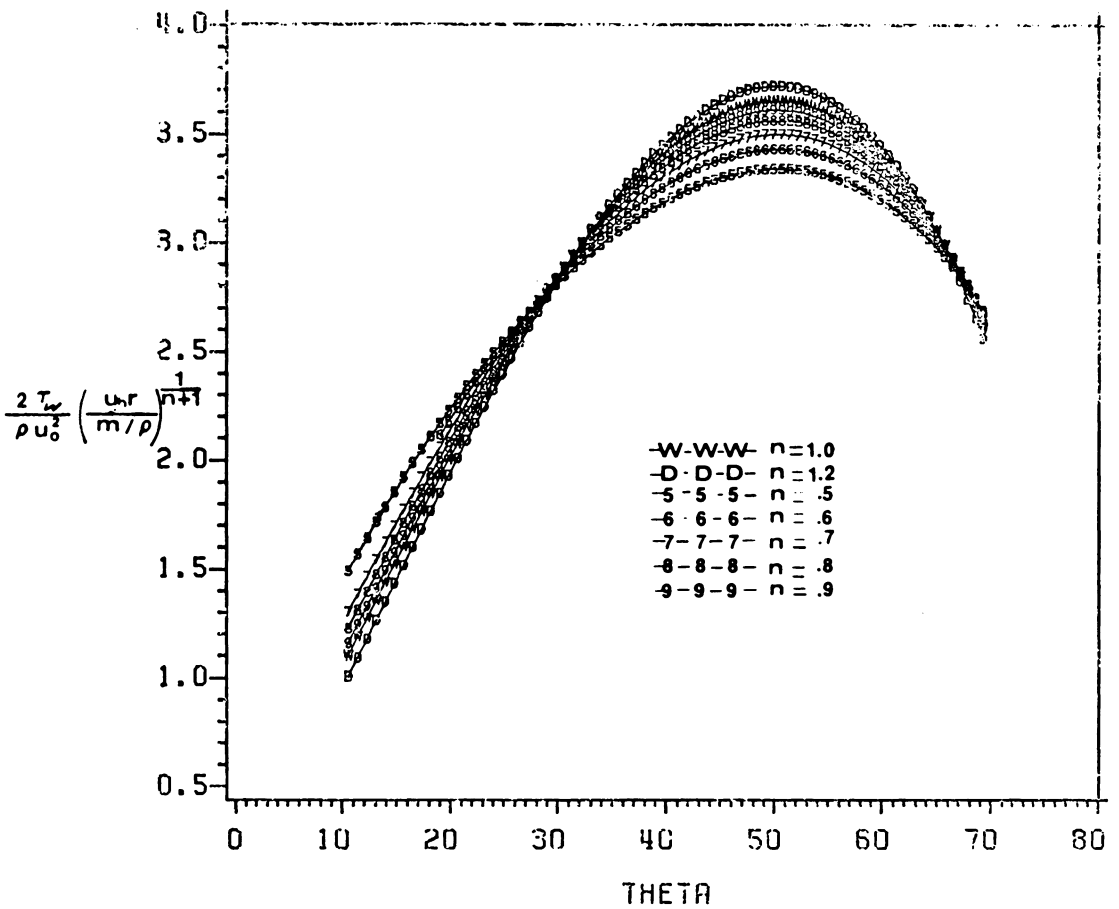

Figure 5.27 Skin friction of power-law materials predicted with Himenz' outer flow equation

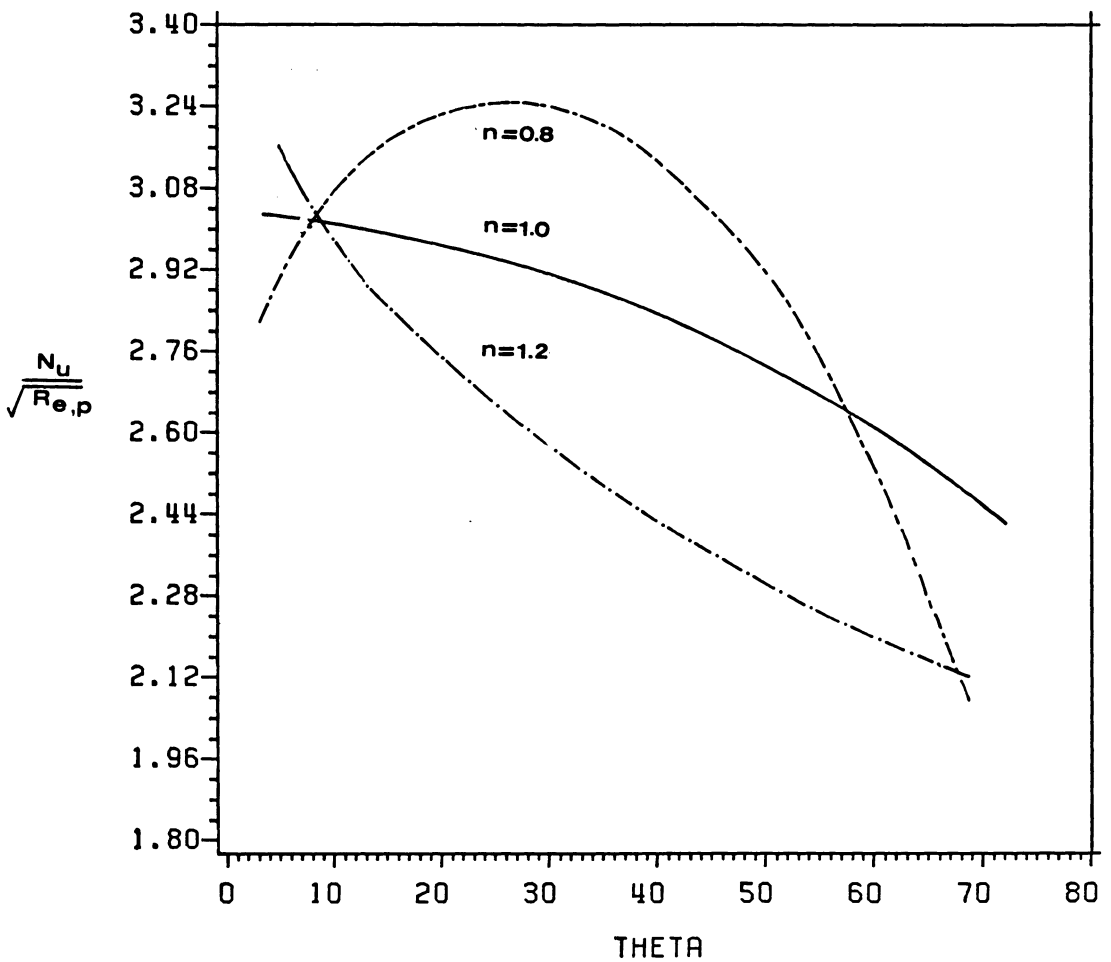

Figure 5.28 Heat transfer of power-law materials predicted with potenrial flow equation

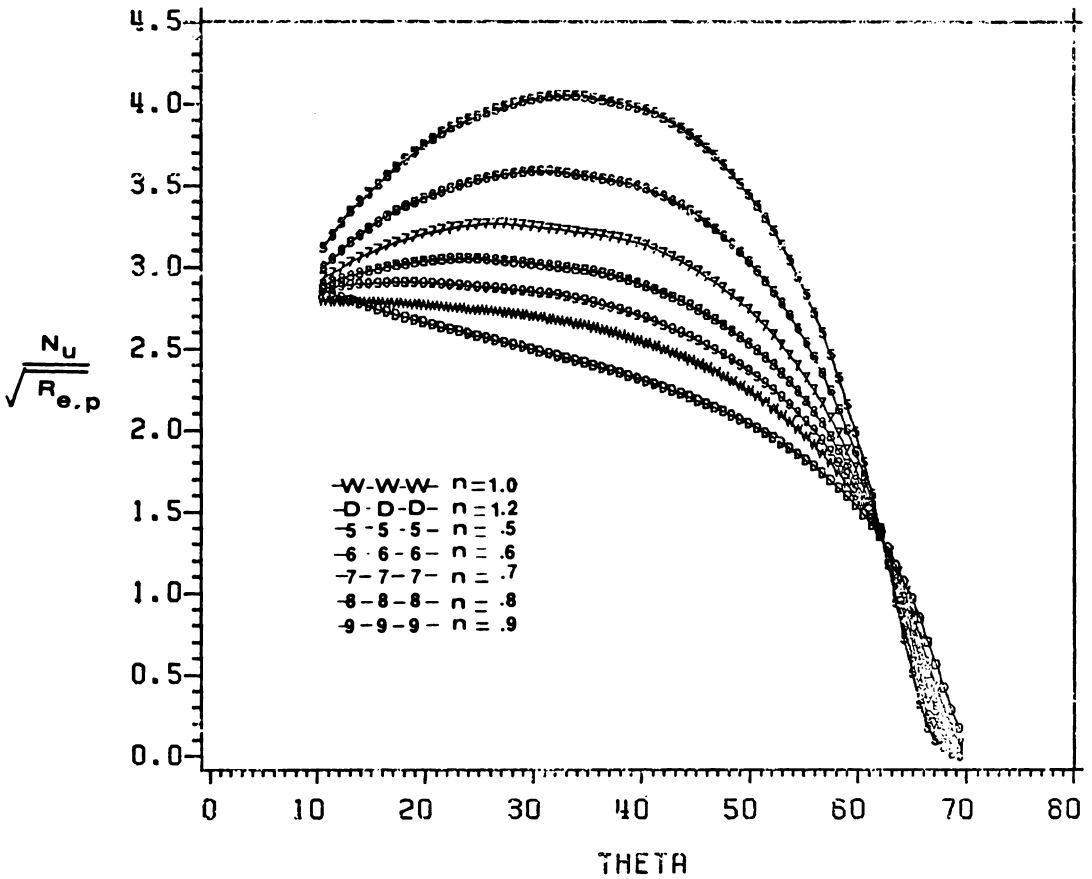

Figure 5.29 Heat transfer of power-law materials predicted with himenz' outer flow equation

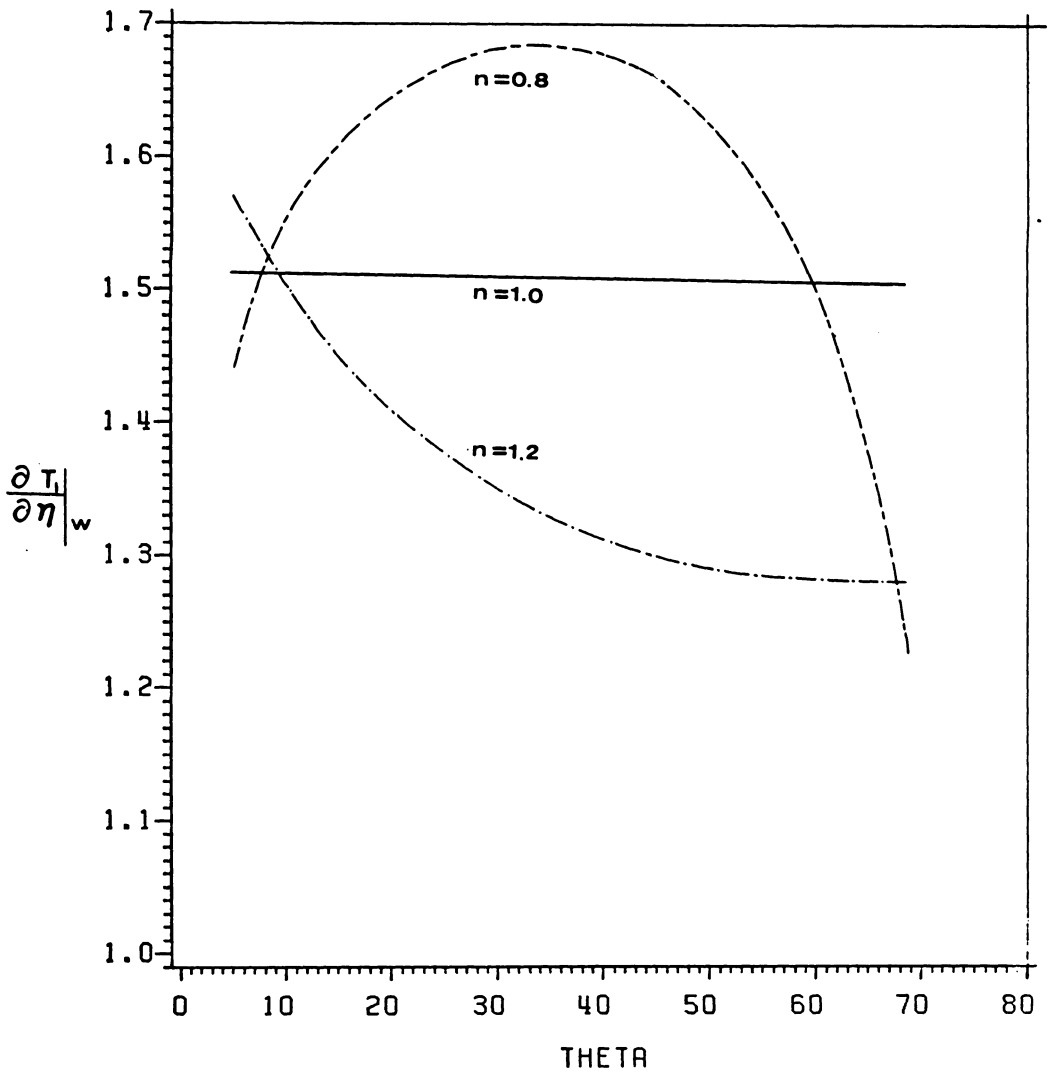

Figure 5.30 Wall temperature gradient of power-law materials predicted with potential flow equation

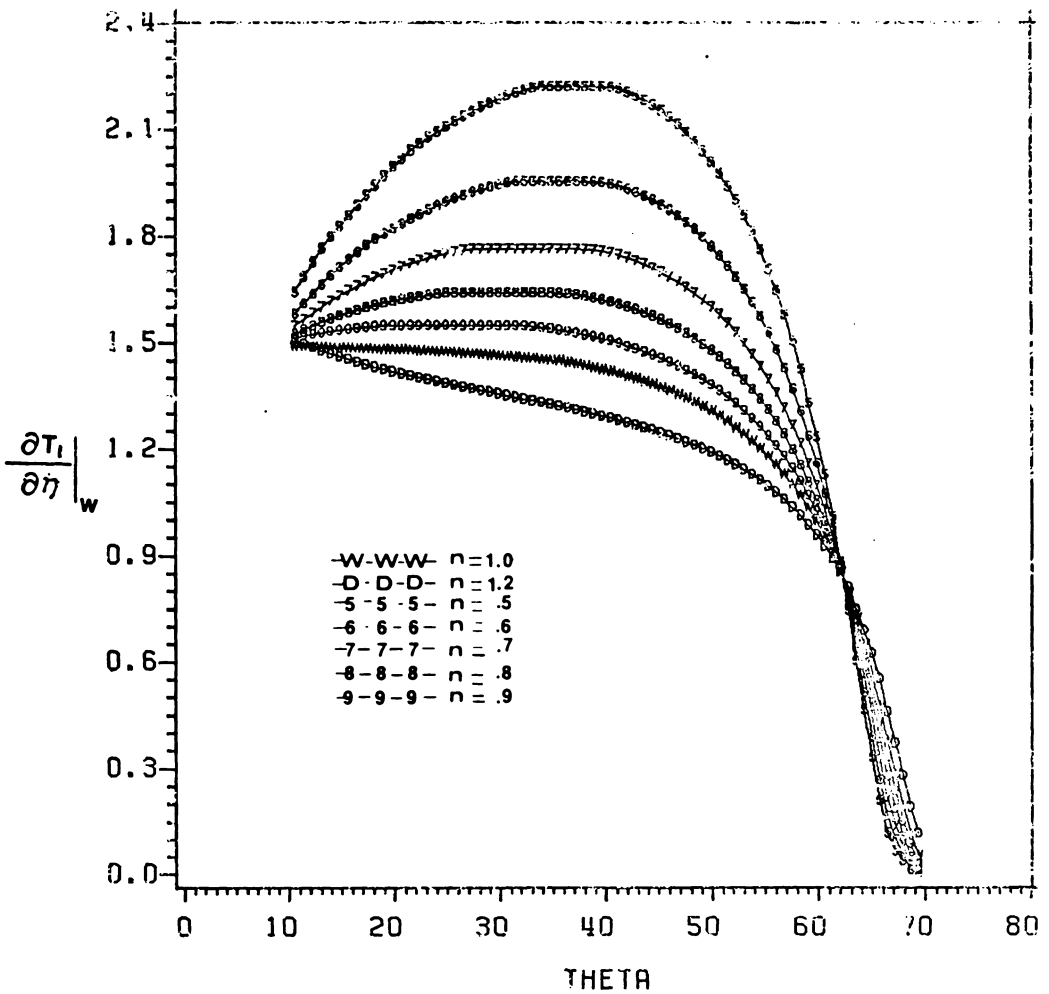

Figure 5.31 Wall temperature gradient of power-law materials predicted with Himenz' outer flow equation

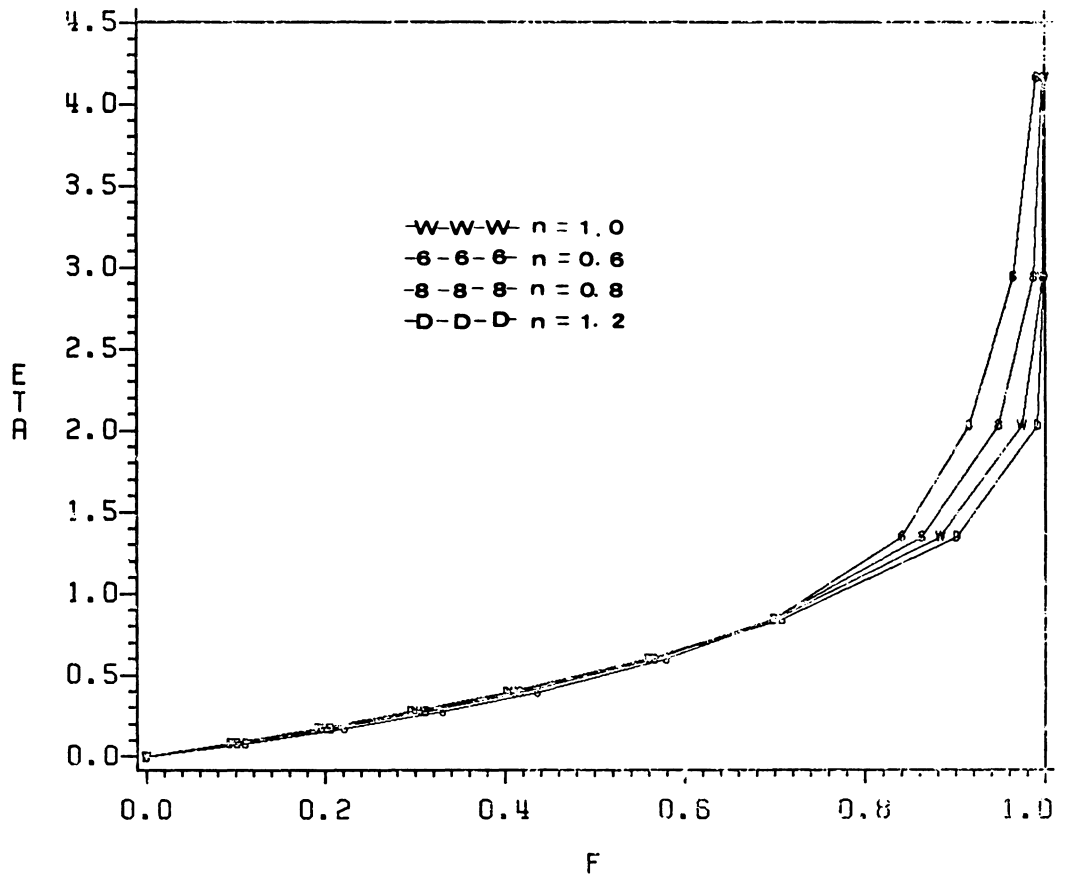

Figure 5.32 Boundary-layer velocity distributions of power-law materials at θ=20 degrees

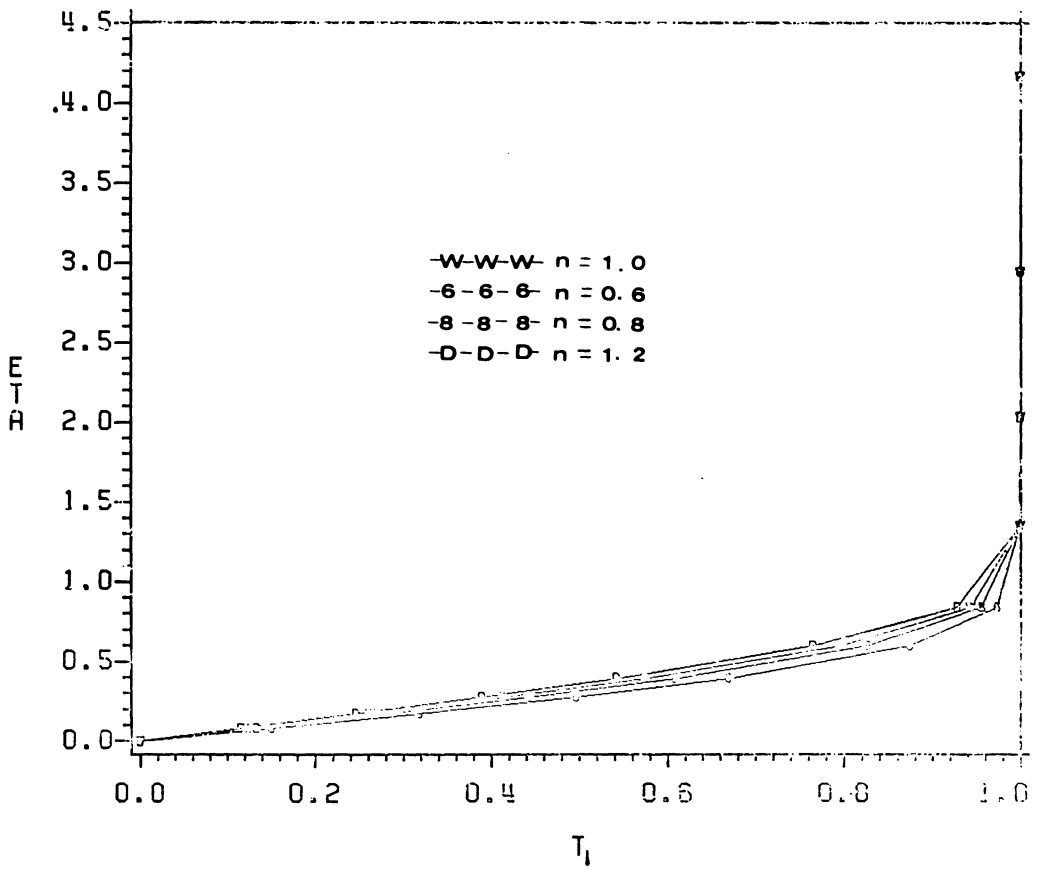

Figure 5.33 Boundary-layer temperature distributions of power-law materials at θ=20 degrees

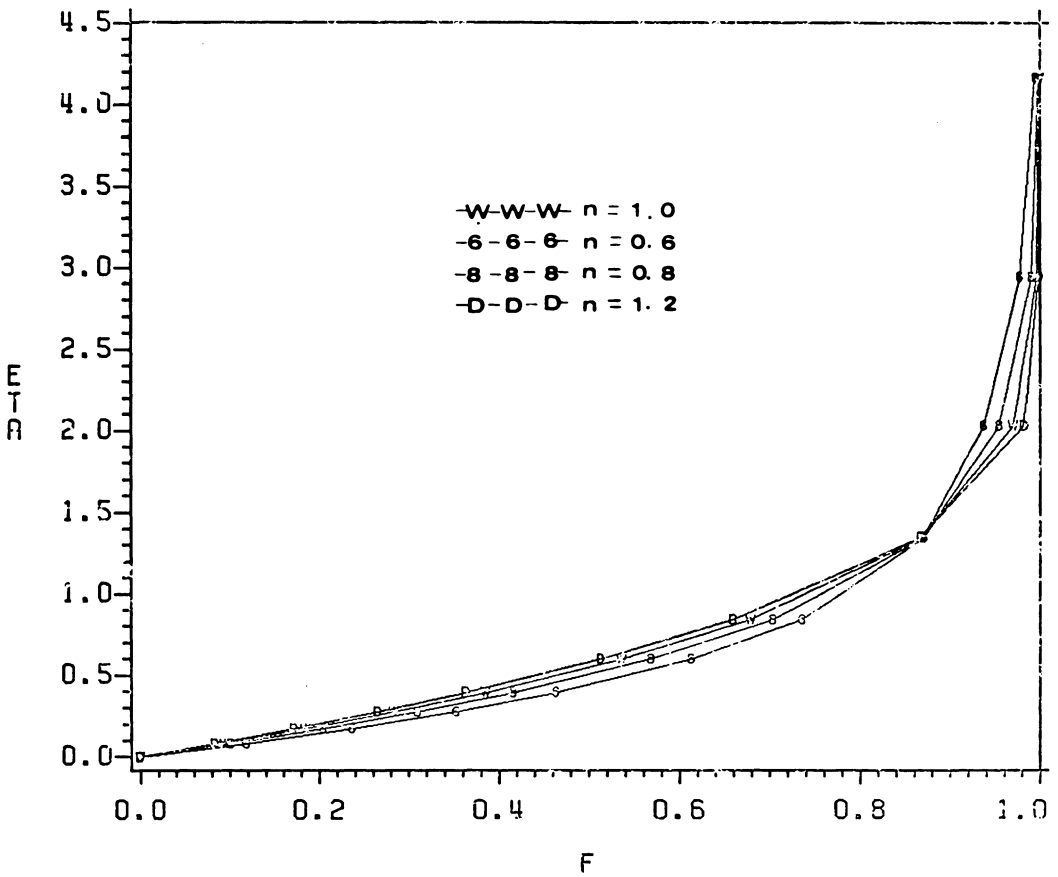

Figure 5.34 Boundary-layer velocity distributions of power-law materials at θ=45 degrees

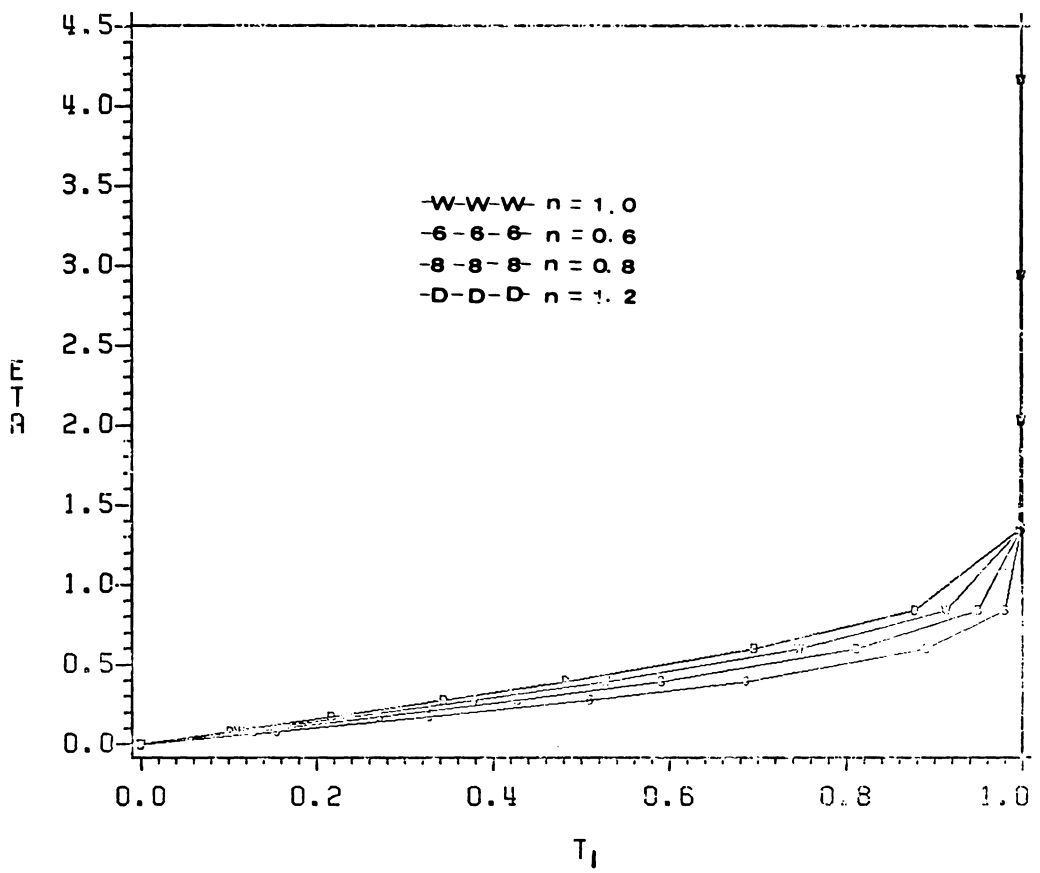

Figure 5.35 Boundary-layer temperature distributions of power-law materials at θ=45 degrees

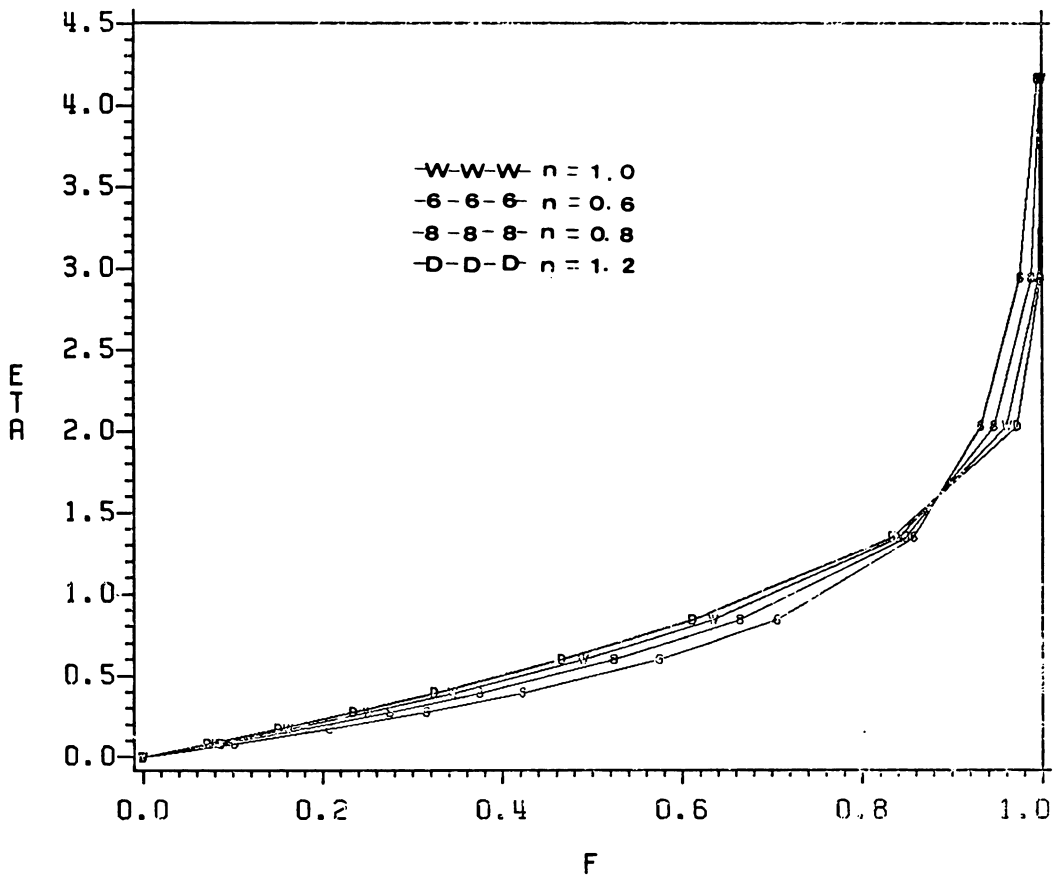

Figure 5.36 Boundary-layer velocity distributions of power-law materials at θ=60 degrees

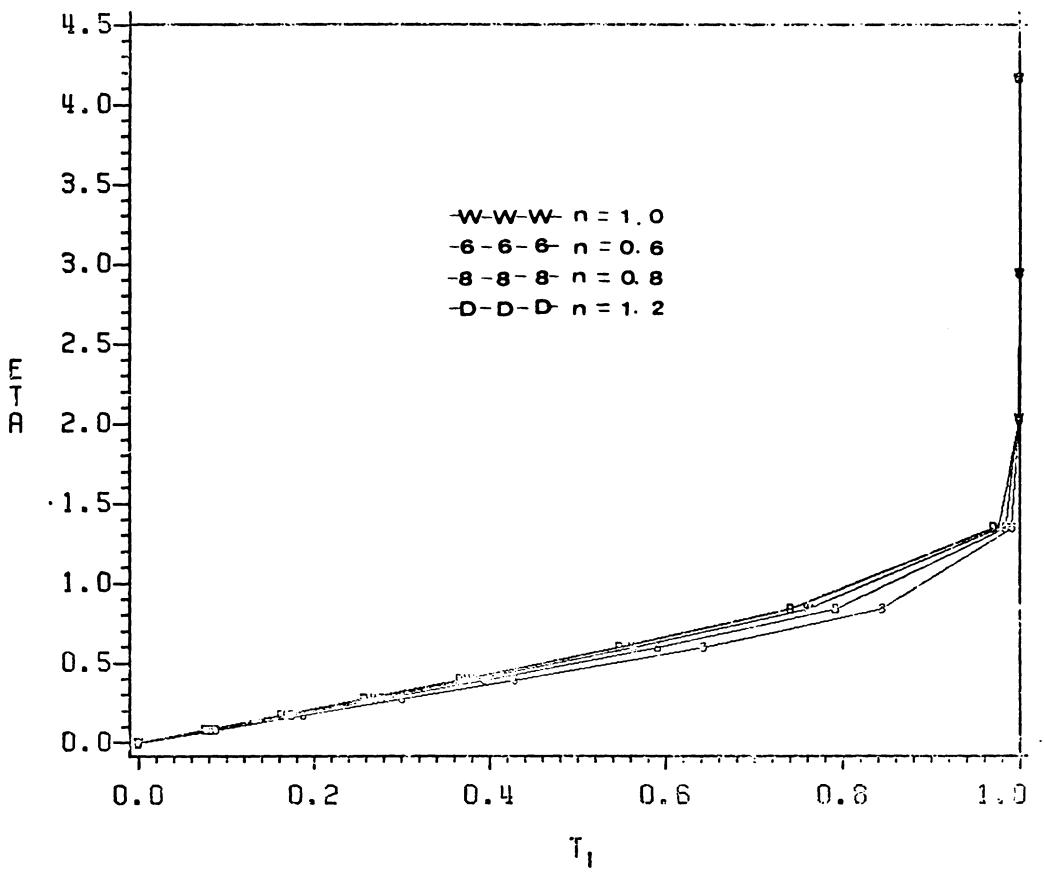

Figure 5.37 Boundary-layer temperature distributions of power-law materials at θ=60 degrees

Table 4.1 The Steady plane Stagnation Flow Solution

Y	F		F'		F''	
	present	Howarth	present	Howarth	present	Howarth
0.0	0.0	0.0	0.0	0.0	1.23259	1.3120
0.20000	0.02332	0.0233	0.22661	0.2266	1.03445	1.0345
0.40000	0.08806	0.0881	0.41446	0.4145	0.84633	0.8463
0.60000	0.18670	0.1867	0.56628	0.5663	0.67517	0.6752
0.80000	0.31242	0.3124	0.68594	0.6859	0.52513	0.5251
1.00000	0.45923	0.4529	0.77787	0.7779	0.39801	0.3980
1.20000	0.62203	0.6220	0.84667	0.8467	0.29378	0.2938
1.40000	0.79665	0.7967	0.89681	0.8968	0.21100	0.2110
1.60000	0.97978	0.9798	0.93235	0.9323	0.14735	0.1474
1.80000	1.16886	1.1689	0.95683	0.9568	0.09996	0.1000
2.00000	1.36197	1.3620	0.97322	0.9732	0.06583	0.0658
2.20000	1.55776	1.5578	0.98385	0.9839	0.04204	0.0420
2.40000	1.75525	1.7553	0.99055	0.9905	0.02602	0.0260
2.60000	1.95381	1.9538	0.99463	0.9946	0.01560	0.0156
2.80000	2.15300	2.1530	0.99705	0.9970	0.00905	0.0090
3.00000	2.35256	2.3526	0.99842	0.9984	0.00508	0.0051
3.20000	2.55233	2.5523	0.99919	0.9992	0.00275	0.0028
3.40000	2.75221	2.7522	0.99959	0.9996	0.00144	0.0014
3.60000	2.95215	2.9521	0.99980	0.9998	0.00073	0.0007
3.80000	3.15212	3.1521	0.99991	0.9999	0.00036	0.0004
4.00000	3.35211	3.3521	0.99996	1.0000	0.00017	0.0002
4.20000	3.55210	3.5521	0.99998	1.0000	0.00008	0.0001
4.40000	3.75210	3.7521	0.99999	1.0000	0.00003	0.0000
4.60000	3.95210	3.9521	1.00000	1.0000	0.00001	0.0000

Table 4.1 Flow Parameter Characteristics of the Wind Tunnel

driving frequency	amplitude	St	Re
3.4(Hz)	.015	.105	53,400
5.0	.021	.071	53,400
6.8	.029	.055	53,400
10.0	.043	.042	53,400
16.0	.055	.046	66,400
19.2	.066	.051	66,400
23.5	.149	.034	36,000
29.0	.184	.034	36,000
31.5	.200	.034	36,000
31.5(high)	.200	.045	36,000
34.0	.216	.037	36,000
39.5	.251	.039	36,000

Table 4.2 The Time-Averaged Point of Separation From Flow Visualization

Re,D	8,000	30,000	60,000
% Tur.(water)	3.4	1.5	0.8
time-averaged point of separation(degrees)			
water	87	84.5	81.5
Separan(100 wppm)	86	85.	84.

Table 5.1 Outer Flow Velocity Distributions

$$Ue1 = A\ x_1 - A\ x_1^3 + A\ x_1^5$$

	A_1	A_3	A_5	Re
potential flow	2.0	0.333	0.016	
Hiemenz	1.814	0.271	0.047	18,400
Sogin and Subramanian	1.820	0.400	0.0	122,000
Shah et al	0.920	0.131	0.0	50,000

Data : Evans(1968) and Shah et al(1969)

The vita has been removed
from the scanned document